

**Development of a light-sheet fluorescence microscope
employing an ALPAO deformable mirror to achieve
video-rate remote refocusing and volumetric imaging.**

Terence George Wright

**Photonics Group
Department of Physics
Imperial College London**

Thesis submitted in partial fulfilment of the requirements
for the degree of Doctor of Philosophy (Ph.D.)
Imperial College of Science, Technology and Medicine

Abstract

There are numerous situations in microscopy where it is desirable to remotely refocus a microscope employing a high numerical aperture (NA) objective lens. This thesis describes the characterisation, development and implementation of an Alpao membrane deformable mirror-based system to achieve this goal for a light-sheet fluorescence microscope (LSFM).

The Alpao deformable mirror (DM) DM97-15 used in this work has 97 actuators and was sufficiently fast to perform refocus sweeps at 25 Hz and faster. However, a known issue with using Alpao deformable mirrors in open-loop mode is that they exhibit viscoelastic creep and temperature-dependent variations in the mirror response [4, 5]. The effect of visco-elastic creep was reduced by ensuring that the mirror profile was on average constant on timescales shorter than the characteristic time of the visco-elastic creep. The thermal effect was managed by ensuring that the electrical power delivered to the actuators was constant prior to optimisation and use. This was achieved by ensuring that the frequency and amplitude of oscillation of the mirror was constant prior to optimisation, so that it reached a thermal steady state, was approximately constant during optimisation and constant during use.

The image-based optimisation procedure employed used an estimate of the Strehl ratio of the optical system calculated from an image of an array of 1 μm diameter holes. The optimisation procedure included optimising the amount of high-NA defocus [1] and the Zernike modes from Noll indices 4 to 24. The system was tested at 26.3 refocus sweeps per second over a refocus range of -50 to 50 μm with a 40x/0.85 air objective and a 40x/0.80 water immersion objective. The air objective enabled a mean Strehl metric of more than 0.6 over a lateral field of view of 200x200 μm^2 and for a refocus range of 45 μm . The water objective achieved a mean Strehl metric of more than 0.6 over a lateral field of view of 200x200 μm^2 over a larger refocus range of 77 μm .

The DM-based refocusing system was then incorporated into a LSFM setup. The spatial resolution of the system was characterised using fluorescent beads imaged volumetrically at 26.3 volumes per second. The performance of the system was also demonstrated for imaging fluorescence pollen grain samples.

Author Declaration

The work presented in thesis is the author's own, unless labelled, with the following exceptions:

The aluminium mount used to support the illumination and imaging objectives in the iSPIM arrangement was designed by Dr Hugh Sparks.

Terence George Wright

.....

Copyright

The copyright of this thesis rests with the author. Unless otherwise indicated, its contents are licensed under a Creative Commons Attribution-Non Commercial 4.0 International Licence (CC -BY-NC).

Under this licence, you may copy and redistribute the material in any medium or format. You may also create and distribute modified versions of the work. This is on the condition that: you credit the author and do not use it, or any derivative works, for a commercial purpose.

When reusing or sharing this work, ensure you make the licence terms clear to others by naming the licence and linking to the licence text. Where a work has been adapted, you should indicate that the work has been changed and describe those changes.

Please seek permission from the copyright holder for uses of this work that are not included in this licence or permitted under UK Copyright Law.

Acknowledgements

I would like to thank my PhD supervisor Prof. Chris Dunsby for showing me how to plan and conduct an experiment – and in general showing me how to do science. This has been a very interesting and exciting journey, again thank you Chris for all of your help and patience!

I would also like to thank Hugh Sparks – who helped me a lot particularly at the beginning of my work. Also thanks to Martin and Simon from the Photonics workshop and also Judith, Marcia and Sanja for administrative help and support.

I would also like to thank Daniel, Nathan, and Sunil for some excellent conversations.

Contents

Abstract.....	2
Author Declaration.....	3
Copyright.....	4
Acknowledgements.....	5
List of abbreviations.....	9
Table of figures	11
List of Tables	23
Chapter 1: Thesis overview	24
Chapter 2 : Background information	27
2.1 Introduction	27
2.2 Microscope objectives	28
2.3 Fluorescence microscopy.....	31
2.4 Volumetric imaging and optical sectioning.....	33
2.4.1 Confocal microscopy	34
2.4.2 High speed confocal microscopy	35
2.4.3 Multiphoton microscopy.....	36
2.4.4 Deconvolution microscopy	36
2.4.5 Structured illumination microscopy.....	37
2.4.6 Light-sheet fluorescence microscopy	37
2.4.6.1 Gaussian beams	40
2.4.6.2 Other types of light sheet	41
2.4.7 Common light-sheet configurations	43
2.4.8 Single objective light-sheet microscopy	45
2.4.8.1 Highly-inclined and laminated microscopy.....	45
2.4.8.2 Oblique plane microscopy	45
2.4.8.3 Swept confocally-aligned planar excitation (SCAPE) microscopy	46
2.4.8.4 Axial plane optical microscopy.....	46
2.4.8.5 Reflected beam light-sheet microscopy	47
2.4.9 Extended depth of field microscopy	47
2.6 Adaptive optics in microscopy	48
2.6.1 Remote refocusing.....	51
2.6.2 High-NA defocus	53

2.6.3	Zernike modes.....	56
2.6.4	Electrically tunable lenses.....	60
2.6.5	Spatial light modulators (SLM).....	62
2.6.6	Deformable Mirrors	63
2.6.7	Choosing the DM.....	65
2.7	Summary	66
Chapter 3 : DM characterisation		68
3.1	Introduction	68
3.2	Alpao DM97-15 membrane DM.....	68
3.3	Optical setup for characterising the DM.....	74
3.4	DM scale transformation	76
3.5	Alignment of the optical axis of the beam with the centre of the DM.....	76
3.6	Strehl ratio	79
3.7	Estimating the background	80
3.8	Estimated Strehl ratio	80
3.9	Assessment of aberrations through the system	84
3.10	Flattening the mirror with a Shack Hartman Wavefront Sensor	88
3.11	Creep/hysteresis with the DM	92
3.12	Characterisation of visco-elastic creep	94
3.13	Characterisation of thermal creep	97
3.14	Summary	99
Chapter 4: Optimisation of the DM for volumetric scanning		101
4.1	Introduction	101
4.2	Setup of the Optical System.....	102
4.3	Refocusing using high-NA defocus.....	103
4.4	Static optimisation by optimizing high-NA defocus and also Zernike modes.....	108
4.5	Reducing the set of Zernike Modes	113
4.6	Quasi-Dynamic Optimisation	114
4.7	Dynamic Optimisation.....	117
4.7.1	Initial approach with discrete DM pose changes.....	117
4.7.2	Improvements to dynamic optimisation with discrete DM pose changes	120
4.7.3	Asymmetric staircase pose sequence	126
4.7.4	Dynamic optimisation with continuous linearly interpolated DM sweep profile.....	127
4.8	Summary	137
Chapter 5 : Deformable Mirror based Light Sheet Fluorescent Microscope		138
5.1	Introduction	138

5.2	Deformable-mirror-based light-sheet fluorescence microscope	138
5.3	Imaging sub-system	141
5.4	Illumination sub-system.....	144
5.5	Light-sheet dimensions	146
5.6	Alignment of the illumination subsystem	146
5.7	Combining and aligning the illumination and the imaging subsystems	148
5.8	Timing of the DM, Camera and Galvo.....	160
5.9	Imaging corn pollen	163
5.10	Imaging sunflower pollen.....	165
5.11	Resolution estimation using beads	166
5.12	Summary	167
	Chapter 6: Future work and conclusions	170
	Published work and proceedings	174
	References	175
	Appendix	183

List of abbreviations

API	Application programming interface
AOD	Acousto-optic deflector
AO	Adaptive optics
BP	Band pass
CCD	Charge coupled device
DM	Deformable mirror
DSLIM	Digitally scanned light-sheet microscope
ETL	Electrically tunable lens
FOV	Field of view
FWHM	Full width half maximum
HILO	Highly-inclined and laminated microscopy
iSPIM	Inverted SPIM
NA	Numerical aperture
ND	Neutral density
LSFM	Light-sheet fluorescence microscope
mSPIM	Multidirectional SPIM
MuVi-SPIM	Multi-view SPIM
OPM	Oblique-plane microscopy
OS-SIM	Optically sectioning structured illumination
OTF	Optical transfer function
OPL	Optical path length
PMT	Photomultiplier tube
PSF	Point spread function
ROI	Region of interest
sCMOS	Scientific complementary metal oxide silicon
SCAPE	Swept confocally aligned planar excitation microscopy
SDK	Software development kit
SHWFS	Shack-Hartmann wavefront sensor
SIM	Structured illumination

SLM	Spatial light modulator
S/N	Signal to noise ratio
SPIM	Single plane illumination microscopy
SR-SIM	Super-resolution structured illumination
STED	Stimulated emission depletion microscopy
TPLSFM	Two-photon light-sheet fluorescence microscopy

Table of figures

Figure 1 Early microscope objectives made up of 2 lens modules. (a) The Lister objective had 2 achromatic doublets and the spacing between them allowed spherical aberration to be reduced. (b) The Petzval objective was also made of 2 doublets, the front objective corrected for spherical aberration and also introduced coma which was corrected by the rear group. The position of the aperture stop could be used to achieve a flatter field. (c) The Amici objective introduced an aplanatic lens which increased the NA. (d) The Abbe lens used 2 aplanatic singlets following the aplanatic condition along with a doublet and cemented triplet.	29
Figure 2 The Boegehold objective [8] included a thick meniscus lens into the rear group which could correct for Petzval curvature to achieve a flat field.	30
Figure 3 The Shoemaker objective [9] was the first example of a three module objective. All modern objectives have a three module design.	30
Figure 4 A Jablonski diagram showing two electronic energy levels, each composed of many vibrational energy levels. A photon will cause the fluorophore to transition to a higher energy electronic energy level, which decays by vibrational relaxation to the lowest vibrational level in E1, which then decays to E0 through the emission of a fluorescence photon.	32
Figure 5 Schematic of a wide-field fluorescence microscope. The excitation light is reflected by a dichroic mirror and illuminates the sample. The emitted fluorescence is then gathered by the same objective, the light passes through the dichroic mirror and then through an emission filter which filters out the excitation light where it is brought to focus by a tube lens onto camera.	32
Figure 6 A schematic of a confocal fluorescence microscope. The illumination pinhole is conjugate to the detection pinhole, behind which is a photo-multiplier tube. Light from out-of-focus planes is not admitted by the detection pinhole and so the image is optically sectioned.	35
Figure 7 Schematic of a light-sheet fluorescence microscope. Fluorophores are excited by a thin light-sheet (possibly produced by passing a laser beam through a cylindrical lens). The fluorescence is then imaged by an objective arranged to be normal to the light-sheet and in wide field configuration.	37
Figure 8 Key parameters for the focus of a Gaussian beam (blue), showing the beam waist ($z=0$) and the Rayleigh range (z_R). The black diagonal lines indicate the ray optics approximation to the Gaussian beam.	40
Figure 9 Cross section of a Bessel beam showing the log of the intensity - showing significant energy in the side rings. When a Bessel beam is used to create a digitally scanned light sheet – the emission for the side lobes will create out of focus blur.	43
Figure 10 This figure shows schematics of different arrangements of the illumination and imaging objectives in LSM. (a) shows a common arrangement where the sample is mounted in an agarose cylinder and can also be rotated about the y-axis, which permits several angular views to be combined into a view with more isotropic resolution. (b) mSPIM, where either side is sequentially illuminated and an image taken. These can be combined to reduce the effect of shadow artefacts. (c) open-top SPIM where the objectives view the sample through a water-filled prism that is matched with the refractive index of the medium used to mount the sample. This arrangement has much more room for the sample and can also be used with multi-well plates. (d) MuVi-SPIM in this variety the sample can be viewed from either side along with the illumination coming from both directions. This allows for a reduction in shadow artefacts and scattering of the light-sheet. (e) iSPIM the illumination and imaging objectives are tilted and above the sample – and enables samples to be conveniently mounted onto microscope slides. (f) Dual-illumination iSPIM, the sample is illuminated	

and imaged from 2 orthoganol directions and fused to produce a more isotropic resolution. In this figure, x and z are in the horizontal plane, and up is in the negative y direction.....	44
Figure 11 A schematic of an OPM system. L3 and L6 are arranged to make a remote, undistorted 3D image and a another objective L7 is arranged to be normal to the light sheet, and creates an optically sectioned image. Hence this is a single objective LSFM technique.	45
Figure 12 A schematic of an axial plane optical microscope, much like OPM an intermediate image is produced by L3. The mirror M1 transfers the lateral and the axial planes of the remote image. This allows the lateral and axial planes to be simultaneously imaged.	46
Figure 13 Schematic of reflected beam light-sheet microscope. The light-sheet is reflected into a direction perpendicular to the axis of the objective. Volumetric imaging can take place is the objective is moved axially.	47
Figure 14 Creating an undistorted 3D image by arranging 2 objectives such that the back focal plane of one objective is imaged onto the other. With correct choice of M1 and M2 a 3D stigmatic image is produced.	73
Figure 15 Panel (a) shows a microscope L3 imaging an arbitrary plane in the image created by L2. Panel (b) uses a plane mirror to image planes from the aerial image created by L2.	73
Figure 16 If it is the case that any ray leaving F1 and reaching F2 obeys the Sine Condition which is given by eq. 8, then it is guaranteed that a small lateral patch at F1 is perfectly imaged to F2, within the assumptions of Geometrical Optics.....	65
Figure 17 An optical system which obeys the Sine Condition is equivalent to using Principal Spheres centred at each focal point rather than using Principal Planes as in Geometrical Optics, as shown in (a). (b) shows the case for an infinity corrected objective in which the second Principal Sphere is a plane.	65
Figure 18 For a point object displaced by z along the optical axis where $z \ll f$, the rays leaving this point can be imagined to be approximately parallel to those leaving F, and so to obey the Sine Condition. Additionally the OPL is shown, which produces an expression for high-NA defocus in the objective's pupil.	76
Figure 19 When the object point is displaced by z and by x from F then the result is high-NA defocus and also tilt added to the OPL.....	77
Figure 20 When the object point is displaced by z and by x from F then the result is high-NA defocus and also tilt added to the OPL.	547
Figure 21 Comparison between high-NA defocus and approximations of successively more Zernike polynomials with even degree n, which correspond to defocus, spherical aberration and higher orders of spherical aberration. The plot shows that the root mean square difference between high-NA defocus and the approximation of principal defocus and spherical aberration is below the Strehl limit.	37
Figure 22 A schematic of an ETL produced by Optotune. It consists of a container which contains an optical fluid. An elastic polymer membrane changes the curvature of its central region in response to pressure around the outer ring. This allows the add optical power to the beam.....	60
Figure 23 Axial displacement needed for the RMS difference between high-NA defocus and primary defocus to break the diffraction limit. This shows the limit of an ETL to correct for high-NA defocus. The dotted line shows the maximum axial displacement for a system with NA=0.75, which was used in this paper. The blue curve is for a water immersion objective and the red is for an air objective .	61
Figure 24 (a) shows a schematic of a MEMS DM based on electrostatic forces, such as sold by Boston Micromachines Corporation. The profile of the diaphragm is changed by the electrostatic field produced by the electrodes. The mirror surface is attached to the diaphragm. (b) shows a schematic of a MEMS DM based on electromagnetic forces such as sold by Alpao and Imagine Optic.	

The reflective membrane is moved by the forces from the interactions between the actuator coil and permanent magnets.....	65
Figure 25 Positions of actuators (labelled by actuator number) on the Alpao DM97-15 membrane deformable mirror.	68
Figure 26 Structure of the Alpao DM97-15. Magnetic forces between the actuator coils and magnet apply a force to a linkage which then applies a push or pull to the silver-coated mirror surface.	69
Figure 27 Panel(a) influence function for actuator 60, command value has been set to 1. Panel (b) The surface profile when actuator 62 is set to -1.	70
Figure 28 This figure shows a schematic of the influence functions and how they compose to form the influence matrix. Three examples of influence functions are shown on the left. To make an influence function, a command value of 1 is applied to each actuator and an image taken with a Shack Hartmann Wavefront Sensor which for the purposes of this example is assumed to have a 4x4 lenslet array. The map of the surface has been simplified and represented by 2 colours. Each influence matrix is reorganised into a horizontal vector (the columns of the influence matrix are shown in the top example of influence function). These are then packed to produce the influence matrix.	70
Figure 29 The error between 50 μm of high-NA defocus for an Olympus 40x/0.80W objective and the surface obtained through the manufacturer supplied Alpao DM 97-15 influence matrix.	72
Figure 30 A plot showing for an Olympus 40x/0.80 water immersion objective, the RMS error between the high-NA defocus and the surface obtained using the manufacturer supplied Alpao DM97-15 influence matrix for different amounts of defocus. The plot also shows the maximum absolute command value sent to the mirror's actuators. These values take the values -1 to 1.	73
Figure 31 Light from an LED is imaged by asphere lenses AL1 and AL2 onto a Lambertian diffuser which illuminates a star-test mask (STM) consisting of 1 μm holes in a chrome-coated glass slide. Light is then collected by objective O1. The back focal plane of this objective is relayed by tube lenses TL1 and TL2 to the DM which applies a correction for the defocus of the STM. Light is then brought to focus by TL3 onto the sCMOS camera. The position of the STM is adjusted by a motorised stage.	74
Figure 32 Panel (a) shows a close-up of the Star Test Mask (STM) which consists of 1 μm diameter holes separated by 20 μm gaps in a chrome-coated glass slide. Panel (b) shows a raw image of the STM (brightness enhanced to make the pinholes more visible), the lateral magnification of the system is 22.2x.	74
Figure 33 The incident light with a circular cross section intercepts the plane of the DM pupil as an ellipse before reflecting back into a circle. This essentially stretches in one axis in the phase pattern (vertical direction shown in the image) whilst keeping the other the same. To allow for this the pattern applied to the DM needs to be appropriately stretched.	76
Figure 34 Panel (a) shows the Zernike terms (OSA indexing) for a centred high-NA defocus pattern. Panel (b) shows the Zernike expansion when the pattern is slightly displaced.	77
Figure 35 Panel (a) shows the pupil of O1 (larger blue filled circle) overlaid with the image of the aperture of the DM (smaller yellow unfilled circle). The pattern applied to the DM needs to be shifted so that the centre of the pattern lies on the centre of the optical system rather than the centre of the DM. Panel (b) shows a schematic of the image of a single star-test mask star in image space. If a high-NA defocus of 8 μm and then -8 μm is applied to the DM the result is that the pinholes will displace by an amount which grows larger the more the DM is misaligned from the optical axis.	78
Figure 36 Displacement of the central pinhole as 8 μm and then -8 μm of high-NA defocus is added to the DM. When the displacement is minimised then the centre of the pattern of high-NA defocus	

applied to the mirror should be very close to the position of the optical axis. Hence the procedure describe determines the position of the optical axis on the DM.	79
Figure 37 Panel (a) shows the annulus of pixels around each pinhole used to estimate the background. Panel (b) shows a map of background estimates over for field of view, where each hexagon corresponds to the background estimate associated with each pinhole.	80
Figure 38 Example raw image of the star-test mask (the contrast of the image has been increased to improve visibility of the pinhole images) recorded with the star-test mask in the focal plane of the 40x/0.85 NA air objective. The inset shows a zoomed-in region of the pinhole within the blue square. The yellow circle in the inset shows the circular bounding area around that pinhole. The perimeter of the yellow circle was used to find the local level of background light in the image for that pinhole and the values within the yellow circle were used to estimate the Strehl ratio. (b) False-colour Strehl map where each hexagon shows the Strehl metric calculated for a particular pinhole. The estimate for the Strehl ratio for the pinhole inside the blue circle in (a) is reported by the hexagon in the blue circle in (b).....	82
Figure 39 Plot comparing the results of simulations where the estimated Strehl ratio obtained from a point source (blue circles) is compared with an estimate obtained from simulated images of 1 micron pinholes (red crosses).	83
Figure 40 Plots showing that the Mean Strehl either across the full Field of View or the central third of the Field of View is independent of the LED drive current.....	83
Figure 41 The STM was imaged by the objective (O which was an Olympus 40x/0.85) and L1 (150, 200, 250 mm achromatic doublet), onto the camera. The Strehl maps are shown (a), (b), (c). Then L1 was replaced with a 200 mm tube lens and the Strehl maps shown in (d). Mean Strehl is the mean of the Strehl ratios across the full field of view. The scale bar is 200 μm	84
Figure 42 The STM was imaged by the objective (O which was an Olympus 40x/0.85) which produces an intermediate image by L1 which is the related to the camera by L2 and L3. This is equivalent to regarding L1 and L2 as producing an intermediate image of the pupil of the objective which is then imaged by L3. Initially L1,2,3 where achromatic doublets 100, 150, 200 mm, with the resulting Strehl map (a). These were replaced with tube lenses, initially 200, 100, 200 mm with Strehl map (b) and then 100, 200, 200 mm with Strehl map (c). Mean Strehl is the mean of the Strehl ratios across the full field of view. The scale-bar is 200 μm	86
Figure 43 Light from the STM was collected by the objective (O which was an Olympus 40x/0.85). L1 and L2 imaged the pupil of the objective onto either a $\lambda/10$ flat dielectric mirror or the DM, which folded the optical axis through 20 degrees. The image of the pupil was imaged by L3. The system schematic is shown in (d) which is the same as Figure 7 and is the used in chapter 4 as a test rig . The Strehl map for the $\lambda/10$ flat is shown in (a), the results for the factory flat DM is shown in (b) and for the DM after being flattened using the Shack Hartman wavefront sensor is shown in (c). The mean Strehl is the mean of the Strehl ratios across the full field of view. The scale-bar is 200 μm . The components and manufacturers are shown in Table 2.	87
Figure 44 Shack Hartman wavefront sensor (SHWFS) setup for flattening the DM. White light from the halogen light source is coupled into the fibre F and then reflected by the broadband dielectric mirror M where it is then collimated by achromatic doublet L1 and then reflected by the non-polarising beam splitter BS to the DM. The light is reflected back to the BS and then passes through the de-magnifying telescope made of L2 and L3 and then reaches the SHWFS.	88
Figure 45 Schematic of a Shack Hartman wavefront sensor (SHWFS). The perturbed wavefront is sampled by the lenslet array. For a slightly perturbed wavefront, the wavefront is approximately planar at each lenslet. These microlenses focus the wavefront into a spot (which is an image of the fibre), which is displaced by an amount related to the tilt of the wavefront. Hence each lenset	

produces an estimate of the local tilt of the wavefront and this can then be integrated to give an estimate of the wavefront itself.	89
Figure 46 Raw image taken from the SHWFS showing the spots corresponding to each microlens (spatial sampling of 110 μm).	90
Figure 47 Wavefront measured by the Shack Hartman wavefront sensor (SHWFS) on consecutive days, 1 hour after being switched on after being off all night. The variation in surface is likely due to changes in ambient temperature and humidity. Note the scales of (a) and (b) are different.	91
Figure 48 SHWFS image taken after 10 iterations of the procedure to flatten the mirror. Standard deviation = 0.014 μm , Diffraction limit = 0.036 μm	91
Figure 49 Raw images of the central pinhole of the STM with the mirror in the best flat. Images taken over 3 consecutive days with the DM constantly on an held when not used (e.g. at night) in the best flat.	92
Figure 50 Panel (a) The DM is set flat for 240 s from -300 s to -60 s on the time axis, an initial image is taken with the camera at -60 s. Then 100 μm of high-NA defocus is applied to the mirror for 60 s until 0 s, and the DM is then set to flat. Images are captured every 5 s after the DM is flattened. Panels (b), (c), (d) show raw images of the pinholes demonstrating visco-elastic creep.....	94
Figure 51 Timing diagram for experiment demonstrating that the characteristic time of the visco-elastic creep depends on the length of time that the DM is held in a particular pose. Top: the amount of high-NA defocus applied to the DM as a function of time. The DM is held flat from -1000 s to -500 s, and then an image taken. The DM should now be free from visco-elastic creep. The DM is then held with 80 microns of high-NA defocus for 500 s before returning to flat and an image is captured every 5 s for 1000 s. Middle: the procedure is repeated for the case where the mirror is held at 80 microns for 100 s. Bottom: the timings of the camera trigger for both experiments is shown.	94
Figure 52 Estimation of the 4th moment about the centroid of the image of the pinhole.	95
Figure 53 This plot compares the 4 th moment about the image of the central pinhole after the mirror has been held for 80 μm of high-NA defocus for 100 s (blue line) compared with 80 μm for 500 s (red line). The dashed line shows the 4 th moment of the central pinhole for the initially flattened DM. The 100 s step test takes about 200 s to return to flat compared to the 500 s step test, which takes about 1000 s to return to flat.	95
Figure 54 Experiment to show the difference in characteristic time between setting the DM to 50 microns for 1000 s compared with oscillating from 50 to -50 microns with the DM being on average flat, with each pose held for 200 ms, for a period of 1000 s. In both the constant and oscillating tests the mirror is initially held flat for 1000 s in order to ensure that there is no visco-elastic creep remaining and the mirror is flat, and an initial flattened image is taken. Then the mirror is either kept at a fixed displacement or oscillated for 1000 s and then the mirror is returned to flat and an image taken every 5 s for 1000 s.	96
Figure 55 Plots showing the results of the oscillating mirror (brown) compared to the fixed mirror position (blue). It shows that the characteristic time for the oscillating mirror is much smaller than for the fixed mirror position, of the order of 1000 s compared to 100 s. This shows that the visco-elastic creep can be reduced by ensuring that the average pose of the mirror is flat.	97
Figure 56 The oscillating mirror experiment is repeated with different amplitudes of oscillation (10,30,50,70,90,110 μm), where each pose was held for 200 ms. (a) shows the amplitude for 50 μm of high-NA defocus and (b) for 10 μm	98
Figure 57 Normalised mean Strehl metric of the central 200 microns of the field of view against time for different amplitudes of oscillation, where the mirror was oscillated for 1000 s. These plots show that the time taken to return to flat increases as the amplitude of oscillation increases. This is due to the extra heat generated by the mirror causing thermal creep.	98

Figure 58 Plot showing the time taken for the DM to return to flat (relaxation time), after oscillating for 1000 s for different amplitudes of high-NA defocus. The relation time increase as the high-NA defocus increases until high-NA defocus of about 70 microns in which case the relaxation time levels off.	99
Figure 59 Optical setup used to optimise and test the deformable mirror for rapid refocusing. AL – aspheric lens; O – microscope objective, TL, tube lens; DM, deformable mirror. Light from the LED was imaged by aspheric lenses AL1, AL2 onto a Lambertian diffuser which illuminates a star test mask (STM). Light from the STM was collected by the objective O1 whose back focal plane was relayed lenses TL1, TL2 to the deformable mirror which applied a phase correction before tube lens brought the light to focus on the sCMOS camera.	102
Figure 60 Panel (a) shows the Strehl map for high-NA defocus set to 30 μm for a STM placed at a physical defocus of 30 μm . Panel (b) shows the Strehl map with 34 μm of high-NA defocus applied to the DM and the stage at a physical defocus of 30 μm . The patterns observed in both panels are consistent with the presence of field curvature.	104
Figure 61 Strehl maps when high-NA alone is applied to the DM. The stage was moved from -50 μm to 50 μm in 5 μm intervals. Each pose was held for 60 s prior to taking an image (stage positions at multiples of 10 μm are shown in the figure). Results obtained using the air 40x/0.85 NA objective lens.	105
Figure 62 The stage was moved from -50 μm to 50 μm . High-NA defocus was applied to the mirror corresponding to each stage position. Then the stage was displaced in steps of 1 μm from -10 μm to 10 μm and a Strehl map obtained for each new stage position. For each stage position the displacement required to maximise each pixel in the Strehl map was used to create the images shown in the figure. They show the amount of field curvature present at each stage position and corresponding high-NA defocus applied to the mirror. Results were obtained using the air 40x/0.85 NA objective lens.	106
Figure 63 Estimated field curvature for Botcherby high-NA defocus for the 40x/0.85 air objective lens. Estimate was obtained by comparing best focus of the centre of the STM to best focus at the righthand edge of the STM image.	106
Figure 64 The stage was moved from -50 μm to 50 μm . High-NA defocus was applied to the mirror corresponding to each stage position. Then the stage was displaced in steps of 1 μm from -10 μm to 10 μm and a Strehl map obtained for each new stage position. The Strehl maps shown in the figure were obtained by taking the best Strehl value at pixel through the stack of 21 Strehl maps corresponding to each stage position. It shows the performance of the system if the field curvature could somehow be managed.	107
Figure 65 Strehl maps obtained for different amounts of high-NA defocus applied to the DM for the case where the amount of defocus has been chosen to maximise the mean Strehl metric obtained over the central 100x100 μm of the FOV.	107
Figure 66 Comparison of high-NA alone, with optimised high-NA defocus, and the maximum Strehl projection obtained for each STM defocus position.	108
Figure 67 The search to find the best pose for the DM can be regarded as a search through Zernike space. Initially, the nominal amount of high-NA defocus is applied. The DM pose is then optimised as described in the previous section to produce the point marked as optimised high-NA defocus. Further optimisation then takes place along each dimension in turn. The whole procedure is then repeated in order to close in on an improved local optimum.	109
Figure 68 Optimisation of Z4 by applying different amounts of Z4 to the mirror, choosing the best 7 scores about the maximum and fitting a parabola to estimate the optimum.	110

Figure 69 Optimisation thrown off course when the optimised rectangle of pinholes does not contain the optic axis, the white rectangle shows the region used to find the mean Strehl score. ..	111
Figure 70 Flow chart for the static optimisation procedure.....	112
Figure 71 Strehl maps for the stage positions -50 μm to 50 μm after the DM was statically optimised firstly for high-NA defocus and for the Zernike modes {Z4 ... Z28}.....	112
Figure 72 Comparison of DM statically optimised for high-NA alone compared with {high-NA defocus, Z4 ... Z28}. The error bars show the standard deviation calculated from two independent measurements. The high-NA defocus at the nominal stage position curve is the same data as shown in Figure 66.	113
Figure 73 Comparison of the static optimisation results for {high-NA defocus, Z4..Z28} compared with the reduced set optimised {high-NA defocus, linear, Z4,5,6,7,14} and simply applying high-NA defocus for the stage position.	114
Figure 74 Timing diagram for quasi-dynamic optimisation. The DM is oscillated through 300 ramps of defocus and then, when the mirror reaches the target pose on the last ramp cycle, an image of the STM is acquired by the camera when the mirror is defocused by the amount that is currently being optimised.	115
Figure 75 Flowchart for the quasi-dynamic optimisation procedure.	116
Figure 76 Panel (a) shows the results of quasi-dynamic optimisation with an interpose of 10ms (9 Vol/sec). Prior to the acquisition of each STM image, the DM is oscillated 300 times in order to achieve a thermal steady state. Panel (b) shows the static optimisation results for these defocus positions taken from Figure 13 for comparison.	117
Figure 77 Symmetric saw-tooth of DM poses correcting for defocus of the stage for positions {50, 40, ..., -50, ... , 40} μm . Red line shows amount of defocus applied to the DM and the blue line is to guide the eye. Blue points indicate where the DM pose is changed.	118
Figure 78 Timing diagram showing the DM defocus compared with the camera exposures. The DM is set to oscillate and the Flash takes images are timed to occur for a particular DM defocus. During the first phase, varying amplitudes of a given Zernike mode were added to the particular pose that is being optimised. After capturing the optimisation images, the optimum is found during the second phase. The optimum is then tested through the acquisition of evaluation images during the third phase to check that the score does improve. If it does, then the change in pose is accepted. Otherwise it is rejected.	119
Figure 79 Flowchart for the dynamic optimisation procedure where the DM is continually oscillating through a set of discrete poses.....	119
Figure 80 Results of dynamic optimisation for a set of discrete poses for an interpose time of 20 ms (5 Vol/sec), and an exposure time of 5 ms. The exposure was taken 12 ms after the pose change.	120
Figure 81 Wiring diagram for TTL pulse selector. A TTL pulse is output by the DM on each pose change. The desired DM pose change is selected by the AND gate when the output from the NI USB 6008 DAQ is high. Hence the DAQ can be used to enable the camera to receive only specific TTL pulses from the DM.	121
Figure 82 Timing diagram showing the symmetric staircase of poses being applied to the DM (blue). Each pose change is accompanied by a TTL output pulse (red). The DAQ is set to output a logical 1 for a period before and after the desired pose change. This causes the DM trigger to be transmitted through AND gate to trigger an image acquisition by the Orca Flash.	121
Figure 83 Sequences of 23 images taken consecutively (10ms exposure time, 20ms interpose time) by the Orca Flash with a 1 s delay between sequences. Each row corresponds to a sequence. After the 4th sequence, a thermal steady state has been reached by the camera. The cap was on during this experiment.	122

Figure 84 Strehl maps that show that near to a pose change a letterboxing artefact occurs – this is due to the rolling shutter of the Orca Flash. The interpose time was 25 ms and the exposure time was 2 ms. Note that in the Strehl map in Panel (a), the black stripe in the image at 0 ms is in a similar spatial location to the red stripe at 24 ms. It corresponds to part of the image corresponding to one pose and the rest corresponding to the next pose. However only one pose is in focus and has a good Strehl value. This is further illustrated by Panel (b) which is a raw image and only shows a horizontal stripe of in focus pinholes.....	123
Figure 85 The Global Exposure output trigger of the Flash is used to control an LED illumination source. In this way the LED is on only whilst the whole camera chip is being exposed.....	124
Figure 86 Average Strehl of the central 100 micron square as the time between the pose change and the exposure is varied. The mirror takes approximately 5 ms to settle.	125
Figure 87 The effect of the settling of the mirror on the performance of the optimisation algorithm. The image was taken 2 ms before the end of the interpose interval and the exposure time was 1 ms.	126
Figure 88 Sawtooth sequence of defocus positions, {50,40,30, ... -30,-40,-50,-30 -10,10,30} μm ...	127
Figure 89 Command poses (blue dots) are explicitly optimised. The poses inbetween are linearly interpolated (blue line). The DM surface is updated with a new pose every 65 μs	128
Figure 90 Panel (a) shows the saw-tooth of command values sent to the actuator during a discontinuous staircase sequence of poses where the mirror is moved and held. Panel (b) shows the saw-tooth command values for continuous movement of the mirror surface where the positions between the command values are linearly interpolated. In both (b) and (c) the return poses are used to apply a bias in order to ensure that the average command value is zero.	129
Figure 91 The DM is set to repeatedly play a sequence of commands corresponding to a full refocus sweep. At the beginning of the sequence, the DM outputs a TTL trigger pulse (red line on the DM timing diagram), which was used to trigger an exposure on the camera. The camera was set to introduce a delay between receiving the trigger from the DM in order to take an image of the mirror in the desired pose.....	129
Figure 92 The output pulse from the Orca Flash is reduced from 1 ms to 0.3 ms by the NI 6363 DAQ. Figure shows the final electronic system used for linearly interpolated dynamic optimisation.....	131
Figure 93 Results obtained from dynamic optimisation of the DM at 26.3 Hz with the 40 \times /0.85 air objective and coverslip. a) False-colour Strehl maps (upper row) and small ROI of raw star test mask image from the centre of the camera's FOV (lower row) for DM poses optimised to provide defocuses of -50 to 50 μm in 10 μm steps (top to bottom). For clarity, the brightness of each raw star-test mask image has been individually scaled to the maximum for that image. For each optimised DM pose, data is shown for star test mask defocus positions Δz of -2 to 2 μm in 0.5 μm steps away from the defocus position used during DM optimisation (left to right). b) False-colour map of best Strehl value for each pinhole taken over all Δz values. c) False-colour map showing Δz location in units of μm of the best Strehl value for each pinhole, i.e. showing the curvature of the field imaged.	133
Figure 94 Results for dynamic optimisation of the DM at 26.3 Hz for the 40 \times /0.80 water dipping objective with ultrasound gel as the immersion medium. a) False-colour Strehl maps (upper row) and small ROI of raw star-test mask image from the centre of the camera's FOV (lower row) for DM poses optimised to provide defocuses of -50 to 50 μm in 10 μm steps (top to bottom). For clarity, the brightness of each raw star-test mask image has been individually scaled to the maximum for that image. For each optimised DM pose, data is shown for star-test mask defocus positions Δz of -4 to 4 μm in 1 μm steps away from the defocus position used during optimisation (left to right). b) False-colour map of best Strehl value for each pinhole taken over all Δz values. c) False-colour map	

showing Δz location in units of μm of the best Strehl value for each pinhole, i.e. showing the curvature of the field imaged.	134
Figure 95 Maximum Strehl (a) and mean Strehl (b) of the central $200 \times 200 \mu\text{m}$ square of the field of view for the statically optimised Olympus 40x/0.85 air objective, as well as the dynamically optimised (26.3 refocus sweeps/sec) Olympus 40x/0.85 air objective and Olympus 40x/0.80W water immersion objective. The dashed line shows the diffraction limit.....	135
Figure 96 Plots showing the amplitude of the high NA defocus mode and Zernike modes (indexed by Noll index), for each defocus. Blue curve shows results for the 40x/0.85 lens with coverslip. Red curves show results for the 40x/0.8 water lens with ultrasound gel as the immersion medium. The black dashed lines show the Strehl limit above which the RMS wavefront aberration for that mode alone exceeds the diffraction limit of $\lambda/14$	135
Figure 97 Schematic showing how the STM is moved towards the imaging objective at $6 \mu\text{m/s}$ at the imaging objective is volumetrically refocused at a rate of 26.3 sweeps/sec through a range of -50 to $50 \mu\text{m}$	136
Figure 98 Image sequence acquired from every defocus position as a function of time as the star-test mask is translated at a constant velocity of $6 \mu\text{m s}^{-1}$ towards the microscope objective. Data was acquired using the 40x/0.80W objective with ultrasound gel as the immersion medium. Refocus sweeps were performed at 26.3 Hz. Each column shows a sequential set of sCMOS images acquired at each of the 11 control poses of the DM, which correspond to refocus positions over the range -50 to $50 \mu\text{m}$. Non-consecutive DM sweeps/volumes are shown moving left to right across the figure.	136
Figure 99 Panel (a) shows a schematic of the deformable-mirror-based light-sheet fluorescence microscope. Light at a wavelength of 488 nm produced by a laser diode is coupled to a mono-mode fibre and then collimated by an Olympus 10x/0.25 objective (O1). The light is then passed through a 50 mm focal length cylindrical lens CY which creates an focused line of illumination on the galvo mirror. This is then relayed via a pair of plössl lenses (L1 and L2) to the back focal plane of the Nikon 10x/0.3W (O2) illumination objective which creates the light sheet in the sample. The emitted fluorescence is then collected by the Olympus 40x/0.8W imaging objective (O3) whose back focal plane is relayed by a telescope composed of 100 mm (L3) and 200 mm (L4) tube lenses to the DM and a phase correction is made before the image is focussed onto the sCMOS camera by a 200 mm focal length tube lens (L5). Panel (b) shows the V-shape iSPIM arrangement of the illumination and imaging objectives attached to an aluminium mount.	139
Figure 100 The LSFM in its optimisation mode. The imaging objective (O3) is unbolted from the aluminium mount and rotated to face the Star Test Mask (STM). The back focal plane of O3 is folded through 90° by M2 and then relayed to the DM by L3 and L4. The optimisation procedure of Chapter 4 is used to find the sequence of surfaces to apply to the DM in order to refocus the objective at video frame rates.	140
Figure 101 View along the z-axis of the opto-mechanics of the optical system as it was configured for the work described in Chapter 4.	141
Figure 102 Changes in the opt-mechanics of the imaging arm showing the cage converter, rotating cage segment, right-angled mirror and z-axis translation mount.	141
Figure 103 Panel (a) shows the Strehl maps obtained after the DM was optimised at 26.3 vol/sec with the imaging arm in the same configuration as Chapter 4 and shown in Figure 95. Panel (b) shows the results of optimisation with the rotating cage segment and fold mirror L2 as shown in Figure 96. These results show that there is a slight deterioration in the Strehl maps at each defocus after introduction of the fold mirror.	142
Figure 104 Figure shows that as the imaging objective (O3) is rotated (through angle θ), the virtual image of the sample is also rotated through θ	142

Figure 105 As the imaging objective (O3) moves from its optimisation position ($\theta = 270$ deg) to its position in a LSM configuration ($\theta = 41.4$ deg), the centre of the image of the pupil of O3 changes. It was found that the pupil walked 0.1 mm in the y direction and 0.6 mm in the x direction.	143
Figure 106 Panel (a) A schematic of the imaging arm in the focusing plane of the cylindrical lens CY. Light from a mono-mode fibre is collimated by O1 then focused by the cylindrical lens CY onto the Galvo G. The Galvo is made conjugate to the back focal plane of O2 using a pair of plossl lenses. Panel (b) shows the imaging arm in the non-focusing plane of CY.	144
Figure 107 Schematic of the opto-mechanics of the illumination arm	145
Figure 108 Schematic of the illumination arm showing how the aluminium mount is attached to the right-angled mirror mount.	145
Figure 109 Schematic of the light-sheet showing the intensity variation within the focal plane of the imaging objective O3. The intensity is maximum at the centre of the ellipse with a FWHM of $132\ \mu\text{m}$ in direction of propagation of the light-sheet (which is the confocal parameter of the Gaussian beam in the non-focusing plane of the cylindrical lens), and $460\ \mu\text{m}$ in the perpendicular direction (which is the confocal parameter in the focusing plane of the cylindrical lens).	146
Figure 110 Panel (a) shows the setup for aligning the position of the galvo so that it at the focus of L1. Panel (b) shows the setup for aligning the position of the cylindrical lens CY so that the galvo is at its line focus. Further details of the procedure are in the text.	147
Figure 111 SolidWorks model showing the arrangement of the illumination and imaging objectives attached to the aluminium mount. This arrangement maximises the working distance of the system. (image credited to Dr. Hugh Sparks).....	148
Figure 112 Schematic showing the silicone structure which contains a fluorescent sea along with the relative positions of the illumination and imaging objectives.	149
Figure 113 Image showing an in-focus image of the light-sheet collected by objective O3. The long in-focus shadow artefacts indicate that the light-sheet is in the front focal plane of the imaging objective. FOV is $600 \times 600\ \mu\text{m}$	149
Figure 114 Shadow artefact are longer when the light-sheet is (a) parallel to the focal plane of the imaging objective compared with (b) a tilted light sheet which will result in shorter shadow artefacts.	150
Figure 115 Raw camera image showing signal from the fluorescent sea (top left) and the slide (black, bottom right). The edge of the slide can be used to align the light-sheet. FOV is $600 \times 600\ \mu\text{m}$	150
Figure 116 Panel (a) shows that the working distance of the system is limited by the illumination objective. Panel (b) shows that the working distance is limited by the imaging objective.	151
Figure 117 Schematic showing the alignment of the waist. In Panel (a) the waist is not aligned and as a result the axial resolution is worse than in the case of Panel (b); hence the edge of the slide is blurrier in the case of (a) than (b).	152
Figure 118 (a) Diagram defining the inclination of the imaging arm θ . (b) illustration of how θ defines the angle of the image of the edge of a slide (black) with a fluorescent sea above (green) on the camera.	152
Figure 119 Images show the edge between the slide of the fluorescent sea for different voltages applied to the galvo. FOV of $600 \times 600\ \mu\text{m}$	153
Figure 120 Panel (a) shows that measurements of the x and x' positions of the edge of the slide on the camera as the light-sheet moves from A to A' enables the displacement d of the edge of the slide to be determined. Panel (b) shows how this is related to the axial displacement of the objective O3, z.	153
Figure 121 Relationship between the galvo voltage and the displacement z of the slide as viewed by O3.....	154

Figure 122 Different ways in which the light-sheet can be misaligned. Panel (a) shows a defocused light-sheet, Panel (b) shows a tilted light-sheet and Panel (c) shows misalignment of the waist of the light-sheet.	155
Figure 123 Top: cartoon of the image acquired when imaging beads in agarose on a microscope slide. Bottom: side-on view cartoon of a cluster of beads positioned into the focal plane and on the optical axis of the imaging objective.....	155
Figure 124 Panels (a) and (b) show the light-sheet being moved axially along the imaging axis until the cluster of beads has maximum intensity. At this point the propagation axis of the light-sheet is assumed to intercept with the focal point of the imaging objective.	156
Figure 125 Schematic of the image of the beads when the light-sheet is correctly aligned, running along the focal plane of the imaging objective and normal to the optical axis of the imaging objective.....	157
Figure 126 Schematic of the image if the light-sheet is displaced in the axial direction of the illumination object, as shown in Figure 116 (c).	157
Figure 127 Panel (a) shows a schematic of the appearance of the beads if the light-sheet is defocused compared to (b) where the light-sheet is in the focal plane. In (a) there is an absence of in-focus beads along the central diagonal. In (b) there is an absence of out-of-focus beads along the central diagonal.	158
Figure 128 Raw image of fluorescent beads in agarose once the light-sheet has been aligned. The intensity and contrast of the image has been changed to make the beads more visible. FOV was 600x600 μm	159
Figure 129 Timing diagram showing the relationship of the sequence of poses used to scan a volume to the TTL pulse produced by the DM; which is used for electronic timing in the system. ..	161
Figure 130 Schematic showing the how the different elements of the system are connected. The DM produces a single pulse for each volume scan which triggers the NI DAQ 6363 to produce a sequence of commands for the galvo and also triggers the camera and switches on the laser for the desired exposure time.	161
Figure 131 Pulse from the NI DAQ 6363 which shows that the rising edge of the pulse triggers the camera and the length of the pulse is used to modulate the output of the laser and determines the length of time that it is switched on.	162
Figure 132 System timing diagram for the DM refocusing LSFM. The DM emits a TTL pulse prior to playing a sequence of poses corresponding to scanning a single volume. A voltage ramp is applied to the galvo mirror and a single image is taken at the same time within each volume.	162
Figure 133 System timing diagram for the DM refocusing LSFM. The DM emits a TTL pulse prior to playing a sequence of poses corresponding to scanning a single volume. A voltage ramp is applied to the galvo mirror and a sequence of images acquired by the camera. The images can be taken at any stage within the capturing of the volume as the DM and Galvo are synchronised with each other.	163
Figure 134 Optically-sectioned images of corn pollen (which is auto-fluorescent) taken with the DM refocusing the LSFM in strobe mode at 26.3 volts/sec. The exposure time of the camera was 2 ms and the laser was set to maximum power of 40 mW. Used in a strobe mode the system captures a single image per volume and so the entire FOV of the LSFM can be examined. The figure shows just the central 160x160 μm region of the camera FOV. The yellow rectangle in the image at -20 μm corresponds to the FOV used in Figure 129 where a series of 10 images were taken per volume. ..	164
Figure 135 Optically-sectioned images of corn pollen taken with the DM refocusing the LSFM at 26.3 vol/sec. In each volume a series of 10 images equally spaced from axial range -50 μm to 50 μm were acquired with an exposure time of 2 ms. Due to bandwidth limits of the USB 3 connection between the Orca Flash and the PC the FOV was limited to the central 75x38 μm , which corresponds to 256x128 pixels. The FOV in this figure is identified in Figure 128 by the yellow rectangle.....	164

Figure 136 Central 120x120 μm ROI with the system in strobe mode with one camera frame acquired per sweep with LSFM operating at 26.3 vol/sec and with an exposure time of 2 ms.....	165
Figure 137 Sunflower pollen with the LSFM volumetrically imaging at 26.3 vol/sec capturing 10 images per volume equally spaced between -50 μm to 50 μm . Panel (a) and (b) show images of the central 70x38 μm from 2 different preparations of sunflower pollen. The FOV is limited by the bandwidth of the USB 3 connection between the Orca Flash sCMOS camera and the PC.	166
Figure 138 The lateral spatial resolution of the system was estimated with 200 nm fluorescent beads. The FWHM was estimated from the 40 beads with minimum FWHM within the central 100x100 μm at each defocus position.	167

List of Tables

Table 1 The first 22 Zernike modes tabulating the Noll index, radial and azimuthal index, functional form and classical aberration name.	58
Table 2 A list of components used in the test-rig shown in Figure 31.	75
Table 3 Components used in Figure 41, where the objective is used with a single lens.	85
Table 4 Components used in Figure 42 which use lenses L1 and L2 to make an intermediate image of the pupil, which is then images onto the sCMOS camera by L3.	86
Table 5 Components list for Figure 44, using a SHWFS to image the surface of the DM.	89
Table 6 Components list for Figure 99, DM based LSFM schematic.....	139

Chapter 1: Thesis overview

This thesis documents the development and characterization of a light-sheet fluorescence microscope (LSFM) that can perform sustained high speed 3D imaging at video frame rates (26.3 volumes/sec). This system uses a membrane deformable mirror (DM) under open loop control to refocus a high-NA objective (Olympus 40x/0.80W), to axially scan 11 optically sectioned images each separated by 10 μm per volume. The instrument achieves a mean Strehl ratio of at least 0.6 over a field of view in the sample of 200x200 μm and a defocus range of 77 μm , such an instrument could be used to study high speed biological processes such as the propagation of calcium and voltage signalling in and between cardio-myocytes in heart tissue. This instrument is the first DM based LSFM that can operate in a sustained way at video frame rates.

A LSFM (described in detail in 2.4.6) can produce optically sectioned images by using a light-sheet to illuminate a thin slither inside the sample and then collecting the fluorescence produced with an objective arranged normal to the plane of the light-sheet. Restricting the excitation light to the focal plane results in less photo-toxicity and photo-bleaching, and with the objective in a wide field configuration acquiring a full field of view with each camera exposure means that the technique is much faster than other approaches such as confocal microscopy. A 3D stack of images can be produced by changing the axial position of the light-sheet and by refocusing the objective to match the plane of the light-sheet. The refocusing can be achieved by moving the objective or the sample, however this can potentially vibrate and disturb the sample. Remote refocusing is where an objective is refocused without moving the objective. In reference [1] remote refocusing was achieved by using a pair of objectives, the second objective matched to the first to create an undistorted intermediate 3D image which was then further imaged by another objective – which could then be moved to create a 3D stack of images. Another approach is to use an adaptive optical device to provide a phase correction in the Fourier plane of the objective to compensate for the defocusing of the object plane. In reference [2] an electrically tunable lens (ETL) was used to refocus a low NA objective as part of a LSFM. As shown in Chapter 2, an ETL only corrects for primary defocus and is not able to compensate for the more complicated phase profile required for a high-NA objective (referred to as high-NA defocus). Deformable mirrors can operate at kHz rates with sufficient degrees of freedom in the mirror surface [3] to be able to correct for the defocus of a high-NA objective. The phase correction for the defocus of a high-NA objective is called high-NA defocus and is described analytically in [1]. These facts suggest that a DM should be capable of refocusing the objective at video frame rates. Membrane DMs however are known to experience hysteresis [4,5] – so that previously applied mirror profiles will affect its future response. The first goal of this project was to develop a simple and robust compensation strategy for this hysteresis. Next it was necessary to develop an algorithm to optimize

the surface of the deformable mirror for high-NA defocus for different axial displacements. Finally, a light-sheet fluorescence microscope was built utilizing the DM refocusing system to achieve video-rate 3D imaging, and its performance characterised with fluorescent beads and pollen grains.

This work is an advance on prior art such as reference [6] where membrane DM had been used under open loop control to provide higher-order defocus correction for rapid adaptive focusing and also compensation for sample aberrations on a multiphoton microscope to image a labelled pollen grain and also a live fruit fly brain. This system achieved 10 optically sectioned images axially separated by 5 μm for the pollen grain and 5 optically sectioned images separated by 5 μm for the fruit fly brain at a rate of 2 volumes/sec.

In [7] a high speed extended depth of field system (EDOF) is presented using a DM to axially sweep the focus through a single exposure and then apply deconvolution to recover the 3D image. The authors imaged 4 μm fluorescent beads with a 40x/0.8NA objective at 472 volumes/sec with an extended depth of field of 41 μm . In this work each camera image is processed into a volume, which results in a far greater number of volumes imaged each second than other LSFM approaches that require an axial stack of images. However, deconvolution is required which requires significant computation and can be less than optimal with thickly labelled samples.

The remainder of this first chapter consists of a chapter by chapter summary of the thesis. Chapter 2 provides background information relevant to the project. It begins by describing the development of microscope objectives – which are the key and most sophisticated component of optical microscopes. Next, different types of optical sectioning microscopes are discussed with particular attention paid to LSFM. Adaptive optics (AO) can be used to remotely refocus a high-NA objective as well as to correct for aberrations in a system or sample. AO technologies including ETLs, DMs and spatial light modulators (SLM) are discussed in the context of optical microscopy. Finally, the decision making for the DM used in this project, the Alpao DM97-15 is outlined.

Chapter 3 characterises the Alpao DM97-15 in a more detail. The linearity of the response of the mirror is described along with the influence matrix – which together are used in the process of instructing the mirror to take on a particular surface profile (or pose). The test-rig used for DM characterization is described – this is the same as the arrangement used to optimize the mirror for high-NA defocus used in later chapters. Alpao membrane DMs are known to experience hysteresis and interferometer-based correction strategies have previously been developed to handle the issue [4,5]. In this chapter, two kinds of mirror creep, visco-elastic and thermal creep are characterized and simple strategies were developed to manage the problem.

Chapter 4 is about optimizing the DM so that it can remotely refocus the objective at video frame rates. It describes the development of an optimisation procedure employing a metric based on the Strehl ratio. The optimisation procedure is initially used to optimize the mirror in a static manner, without rapid refocusing. Next, the mirror is optimized while it is moved in steps between different values of high-NA defocus. In order to avoid visco-elastic creep as well as thermal creep, the optimisation had to proceed with the DM oscillating at the desired refocusing rate for volumetric imaging. This procedure was then developed further into a continuous form of oscillation of the mirror where a stream of commands continually change the mirror surface so that at any particular moment the DM is optimized for refocus by a particular amount. This dynamic optimisation procedure achieved a refocus sweep rate of 26.3 vol/sec over a defocus range of -50 to 50 μm and was used an Olympus 40x/0.85 NA air objective as well as an Olympus 40x/0.80 NA water immersion objective.

Chapter 5 presents the development of a DM-based LSFM where the DM was optimized for volumetric imaging in the manner described in Chapter 4. The light-sheet was created using a cylindrical lens and scanned through the sample using a galvo mirror. The system was arranged so that the objective could be moved into one position where the DM could be optimized for volumetric scanning and then to another where it could be used as a LSFM. The performance of the system was evaluated by imaging 200 nm fluorescent beads as well as corn and sunflower pollen.

Chapter 6 summarises the achievements of the project as a whole and describes opportunities for future work including various research approaches for improvement of the instrument.

Chapter 2 : Background information

2.1 Introduction

Progress in biology has gone hand in hand with improvements in optical microscopy. Classical optical microscopes can typically achieve a diffraction-limited resolution of about 250 nm [8, 133, 134], which has allowed for the imaging of many important biological structures within cells and has led to tremendous advances in cell biology. In the simplest optical microscopes an objective lens creates an intermediate image of the sample (which can be at infinity in an infinity-corrected microscope), and then a second lens (tube lens, typically a triplet) projects a real image of the sample onto the camera. Each object point in the sample produces rays that are collected by the objective and sent through the system. The steeper the rays with respect to the optical axis that are collected from each point in the sample by the objective then the higher the resolution of the image. The resolution of an optical system is determined by the numerical aperture (NA), which is a function of the steepest ray captured from an on-axis object point. If n is the refractive index of the immersion medium and α is the angle of the steepest ray from an on axis point that passes through the entrance pupil of the system, then the NA is given by eq.1, [8],

$$NA = n \sin(\alpha) \quad eq. 1$$

All of this refraction has to be done in a such a way as to minimise aberrations – and this leads to the sophistication of the optical design of modern objectives. Enormous advances have been made over the last two centuries and now modern objectives typically have a field number of 25 mm (which means the diameter of the intermediate image formed by the objective), and can achieve diffraction-limited performance across the field of view (FOV), whilst maintaining a flat field over a wide range of visible wavelengths [9].

Optical imaging can take place in a number of ways including trans-illumination, reflection and via fluorescence. Trans-illumination seeks to exploit contrast through spatial variations in absorption and scattering within the structures of the sample. When imaging in reflection, image contrast is generated using back-scattered photons. Fluorescent labels can be used to tag specific molecules, and fluorescent probes can report a wide range of intracellular parameters such as calcium ion concentration and voltage. Fluorescence imaging has therefore become very widely used in biological research. The ability to accurately tag and track structures within cells and to produce images with high signal to noise ratio (S/N) using fluorescent reporters has allowed for quantitative and non-destructive study of biological processes both in vitro and in vivo. It is also desirable to be able to study distributions of molecules or processes in 3D within a cell, and this can be achieved using microscopy

techniques capable of optically sectioned imaging, as acquiring a stack of optically-sectioned images enables volumetric, i.e. 3D, imaging [10]. In addition, cells have been shown to exhibit different behaviours in 3D than in 2D [11], in terms of the cellular environment as well as intercellular relationships, and this presents a further need for 3D imaging. There is also a range of fast biological phenomena such as calcium and voltage signaling in and between cardiomyocytes in heart tissue. Here it is useful to be able to record biological processes in 3D at video rates. The goal of this work is to produce a light-sheet fluorescence microscope (LSFM) capable of video-rate volumetric imaging through the use of a deformable mirror (DM) to rapidly refocus the detection optical system. This chapter provides a summary of the key concepts to do with fluorescence microscopy and adaptive optics relevant to this goal.

2.2 Microscope objectives

This project will involve using a deformable mirror to change the axial position of in-focus plane imaged by the objective without moving the objective or the sample, this is also known as remote refocusing. Objectives are optimised to minimise aberrations when the sample is in the focal plane. Using the objective outside of its design conjugate will introduce aberrations. This section provides a brief summary of the optical design of microscope objectives.

Objective lenses are the key and most sophisticated component in an optical microscope, in references [12,13] the authors reviewed the patent literature and summarized the general principles of modern objective design. Significant historical milestones in objective design start with Lister's two-doublet design as shown in Figure 1 (a). This design consisted of two separated achromatic doublets and the spacing between them allowed spherical aberration to be reduced. The Lister objective enabled many early discoveries about the structure of plant and animal cells [14].

The Petzval objective, shown in Figure 1 (b) also consisted of two lens modules. The front doublet corrected for spherical aberration but introduced coma, which was corrected by the second group. The position of the aperture stop and also the separation between the two doublets could optimise the amount of astigmatism – and help to achieve a flatter field. This was followed by Amici's introduction of an aplanatic lens [9, 15] shown in Figure 1(c) to increase the NA of the objective at the cost of increasing field curvature. Abbe's design in 1886 and shown in Figure 1 (d) was a significant improvement in performance; it used two singlets both following the aplanatic condition in order to minimize spherical aberration, coma and astigmatism whilst bending rays through large angles. The residual field curvature and lateral colour introduced by this first group of lenses was then corrected by a second group of lenses comprised of a doublet and cemented triplet.

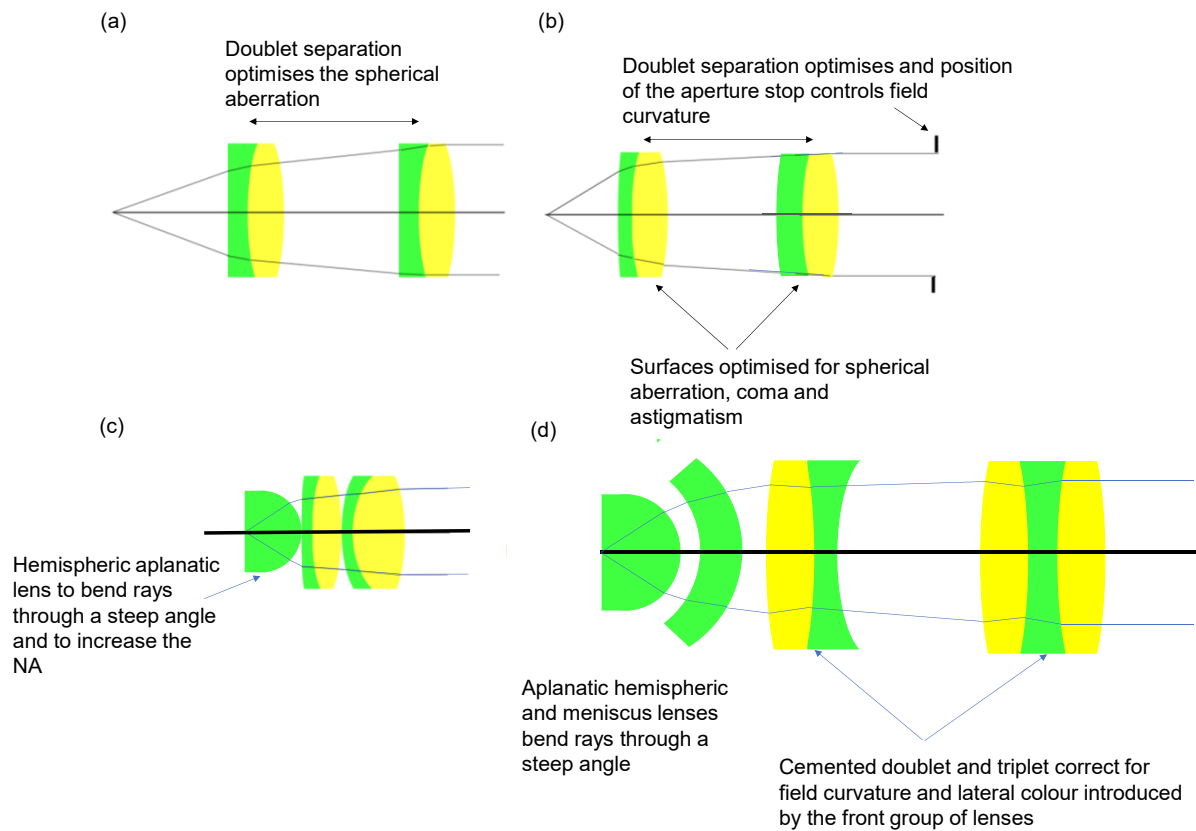


Figure 1 Early microscope objectives made up of 2 lens modules. (a) The Lister objective had 2 achromatic doublets and the spacing between them allowed spherical aberration to be reduced. (b) The Petzval objective was also made of 2 doublets, the front objective corrected for spherical aberration and also introduced coma which was corrected by the rear group. The position of the aperture stop could be used to achieve a flatter field. (c) The Amici objective introduced an aplanatic lens which increased the NA. (d) The Abbe lens used 2 aplanatic lenses following the aplanatic condition to increase the NA and a rear group made up of a cemented doublet and triplet which corrected for field curvature and lateral colour.

In 1938, Boegehold [12,16] developed a 2 group objective which used a thick meniscus lens to correct for Petzval curvature, as shown in Figure 2. The front group of lenses was used to correct for spherical and longitudinal chromatic aberration and the rear group has a thick meniscus lens to correct for lateral colour and field curvature.

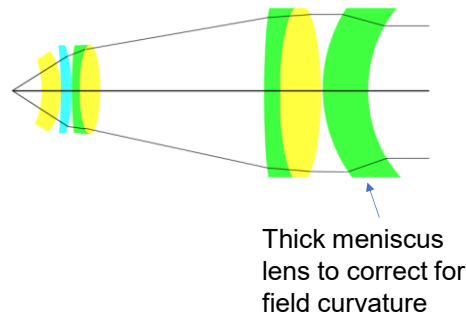
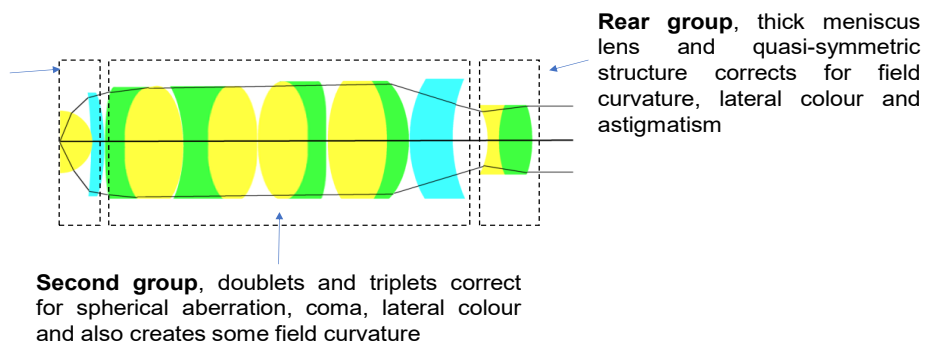


Figure 2 The Boegehold objective [16] included a thick meniscus lens into the rear group which could correct for Petzval curvature to achieve a flat field.

In 1972 Shoemaker (shown in Figure 3), developed a three-group apochromatic oil-immersion objective [12, 17], which has been the basic structure for high-NA objectives since. Typically, in a three-group design the front group consists of several aplanatic meniscus lenses which bend the light through large angles. The aplanatic condition cannot be perfectly fulfilled and will result in residual spherical aberration, coma, field curvature, lateral colour and slight astigmatism. The middle group which is made up of several cemented doublets and triplets corrects for spherical aberration and coma and creates a negative Petzval curvature. The rear group corrects for field curvature and usually has a thick meniscus lens or uses a quasi-symmetric structure [15], or a combination of both. This group is optimized to correct for lateral colour and reduce astigmatism.

First group, aplanatic meniscus lenses bends light through a steep angle however creates some residual spherical aberration, coma, field curvature, lateral colour



Rear group, thick meniscus lens and quasi-symmetric structure corrects for field curvature, lateral colour and astigmatism

Second group, doublets and triplets correct for spherical aberration, coma, lateral colour and also creates some field curvature

Figure 3 The Shoemaker objective [17] was the first example of a three module objective. All modern objectives have a three module design.

Development after 1970 is described in references [9, 12, 13]. Objectives tended to be divided into those used for biomedical research and those used in the semiconductor industry. Developments included objectives for biomedical research with a correction function to correct for variation in the thickness of the coverslip used to mount the specimen. Zeiss produced the first objectives capable of working with multiple types of immersion fluid in 1975. After 1980, all manufacturers turned to infinity optics that allowed additional optical components to be inserted into the infinity space between the objective and the tube lens without introducing significant aberration.

Fluorescence microscopy motivated further developments in objective design from the 1980s to deal with UV excitation light, and new kinds of glasses were created which did not autofluoresce and which enabled better colour correction. Similarly, confocal microscopy led to developments in the rear lens group to achieve a very flat field.

Microscope objectives are highly optimized devices engineered to perform optimally at their design conjugates. Typical modern objectives correct for primary and higher orders of spherical aberration, coma, astigmatism, field curvature and axial and lateral colour. The goal of this project will be to refocus a high-NA objective in order to achieve video-rate volumetric scanning by means of a deformable mirror. Not using the objective at its design conjugates will throw the carefully balanced objective away from its optimal performance and will result in the introduction of aberrations. The deformable mirror itself will introduce at least field curvature into the system. The spherical aberration terms produced by defocusing the sample can be collected together into an expression called high-NA defocus (described in 2.6.2), which can be corrected by the deformable mirror. However, field dependent aberrations such as coma, astigmatism and field curvature cannot be corrected by a single correction device in a Fourier plane and will provide a limit to the performance of the system.

2.3 Fluorescence microscopy

In fluorescence microscopy it is fluorescence light emitted by fluorophores that is imaged [18]. These fluorophores are often attached directly to structures of interest within the sample. The sample might be genetically modified to express a fluorescent protein, or there might be natural autofluorescence present. Fluorophores can be grouped into categories that include fluorescent proteins and chemical dyes; both can be used to label live cells, to target different parts of a cell or to report specific properties, e.g. Ca^{2+} reporters such as the fluorescent protein GCaMP [19] and chemical dye Fluo4 [20]. Fluorescent proteins – such as the green fluorescent protein (GFP) that was originally isolated from the *Aequorea victoria* jellyfish [21-24] – can be expressed by cells through genetic engineering. Alternatively, fluorophores can be attached to antibodies which then bind a specific antigen. In primary immunostaining, a fluorescent tag is attached to the antibody whereas in secondary immunostaining the tag is attached to a secondary antibody which targets a primary antibody. This provides enormous versatility and the ability to target any protein of interest for which there is a suitable antibody.

In fluorescence, a fluorescent molecule is initially excited to a higher electronic energy level through the absorption of a photon. After excitation, the fluorophore then decays to the lowest vibrational energy level associated with that electronic state before relaxing to the ground electronic state

through the emission of a fluorescence photon. Once in the ground electronic state, the fluorophore may undergo further vibrational relaxation. Because of the vibrational relaxation, when it decays to the ground electronic energy level the photon emitted has a lower frequency and hence longer wavelength than the one that was originally absorbed. This increase in wavelength is known as the Stokes shift. This process is often shown using a Jablonski diagram, see in Figure 4.

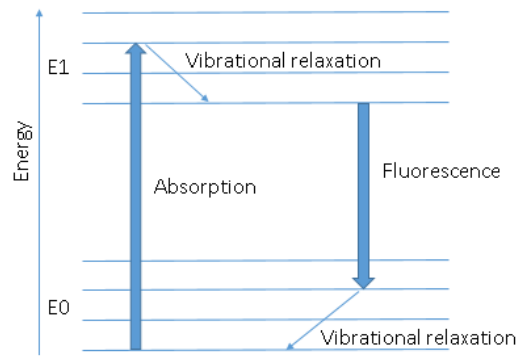


Figure 4 A Jablonski diagram showing two electronic energy levels, each composed of many vibrational energy levels. A photon will cause the fluorophore to transition to a higher energy electronic energy level, which decays by vibrational relaxation to the lowest vibrational level in E1, which then decays to E0 through the emission of a fluorescence photon.

The Stokes shift means that the absorption spectrum and the emission spectrum are displaced from each other. Hence, a suitably chosen filter or filters can be used to block out the excitation light and only allow the emission light through. This is the basis of wide-field fluorescence microscopy.

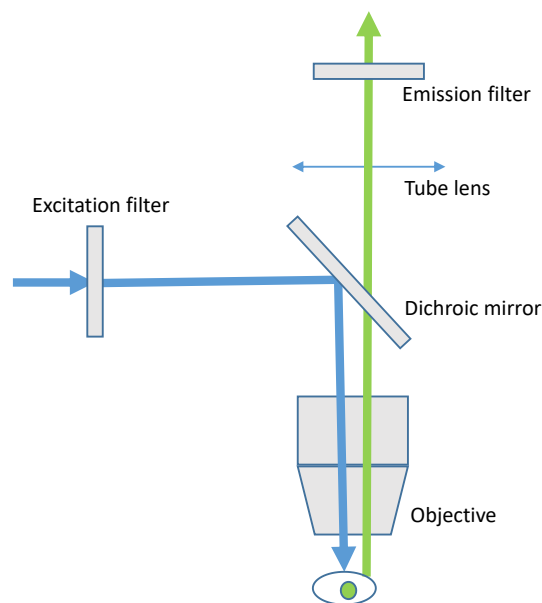


Figure 5 Schematic of a wide-field fluorescence microscope. The excitation light is reflected by a dichroic mirror and illuminates the sample. The emitted fluorescence is then gathered by the same objective, the light passes through the dichroic mirror and then through an emission filter which filters out the excitation light and it is then brought to focus by a tube lens onto a camera.

In a wide-field fluorescence microscope, as shown in Figure 5, the sample is approximately uniformly illuminated by excitation light that excites the fluorophores. The resulting fluorescence is then captured by the imaging lens, passes through a dichroic mirror (which selectively transmits or reflects light based on wavelength), filtered by an emission filter and then the tube lens forms the image. The same objective is used to illuminate/excite the sample as well as to capture the fluorescence. Due to the Stokes shift of fluorescence emission and the high out-of-band blocking provided by modern excitation and emission bandpass filters, the excitation light is blocked from reaching the camera and fluorescence signal can be recorded with very low background, to the extent that it is routinely possible to perform fluorescence imaging of single molecules [25].

2.4 Volumetric imaging and optical sectioning

In a wide-field fluorescence microscope, the wide-field illumination will excite any fluorophores throughout the entire field of view of the microscope, and this is independent of the axial plane within the sample that the objective is focused. Fluorophores located away from the focal plane of the objective will be extended (blurred) in the image plane. Collectively, out-of-focus fluorophores add significant background light to the in-focus image of fluorophores in the focal plane and so reduce the contrast of the in-focus image.

As an example, for an oil immersion objective with an NA of 1.3 the depth of field is of the order of 300 nm, while a typical human T cell by comparison has a thickness of about 10 μm . This means that most of the cell is out of focus and so will contribute to the out-of-focus blur. This means that it is not possible to be sure that the fluorescence gathered by a particular pixel comes from a particular axial location in the sample. It also shows that a significant improvement in the level of contrast could be achieved if the out-of-focus light from above and below the focal plane were to be reduced.

Fluorescence images can also be degraded by the presence of scattered light. This is light that has been reflected/refracted/diffracted on its way to the objective. The result is that it will seem to have been emitted from somewhere other than the true point of emission. The deeper the fluorophore is in the sample then the greater the chance of a scattering event. Out-of-focus fluorescence along with scattering and also sample absorption are the main obstacles to high-contrast imaging of 3D objects.

The goal of optical sectioning is to collect light from only the in-focus region of the object. The term optical sectioning is used in an analogous way to physical sectioning of samples with a physical knife blade. There are many approaches to optical sectioning in fluorescence microscopy such as confocal microscopy, light-sheet microscopy, structured illumination microscopy, multiphoton microscopy as

well as computational approaches such as deconvolution applied to wide-field fluorescence microscopy [26].

2.4.1 Confocal microscopy

The method of confocal microscopy [27] is illustrated in Figure 6, which is a technique widely used in biological research. The illumination is structured to produce a point of light in the sample. Regions near the focus of this excitation beam will experience a significantly higher intensity than further away and as a result produce more fluorescence. A confocal aperture (pinhole) in front of the detector (typically a photo-multiplier tube) is made conjugate with the illumination spot in the sample. The image of the detection pinhole in the sample (which for an infinitely small pinhole would be the intensity PSF of the imaging optics), gives the probability of fluorescence being captured by the detector. Hence the detected light is also structured. An object point outside of the focal plane will produce a large defocused image on the pinhole and so the light from the object point that gets through the pinhole is greatly attenuated. Only light from the focal plane is not significantly attenuated and so the confocal microscope achieves optical sectioning. Another bonus with confocal microscopy is that it also slightly improves the lateral spatial resolution in the focal plane compared with the conventional wide-field fluorescence microscope [28,29]. In order to create a 3D image, the imaged point has to be scanned in sequence in a raster fashion through the sample. This can be achieved by moving the object across the objective lens, or by moving the objective lens and keeping the object stationary. For biological samples however, any vibration or movement has the potential to affect the specimen – causing it to move and reduce resolution in the image. Therefore, an alternative approach is to use a scanning head attached to the microscope. Such devices employ a beam scanning mechanism, such as galvanometer (galvo) mirrors and/or acousto-optic deflectors, to scan the excitation laser beam across the sample and to also de-scan the fluorescent light onto the stationary confocal detection pinhole, therefore keeping the object and objective at rest [30].

Due to the fact that the pinhole rejects the fluorescence signal from out-of-focus planes, fluorescence signal from out-of-focus planes is wasted and this leads to unnecessary phototoxicity and photobleaching of the sample when acquiring a 3D image volume. In addition, in typical non-resonant galvo-mirror-based confocal microscopes, the scanning process occurs at line acquisition rates of a few hundred Hz which also influences the rate of volumetric imaging.

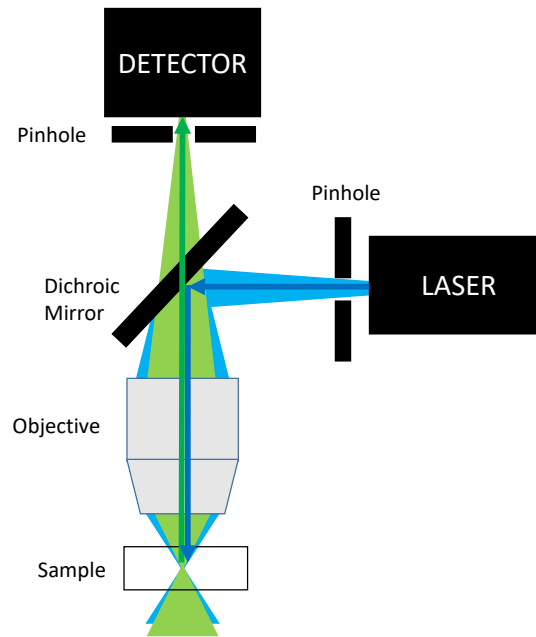


Figure 6 A schematic of a confocal fluorescence microscope. The illumination pinhole is conjugate to the detection pinhole, behind which is a photo-multiplier tube. Light from out-of-focus planes is not admitted by the detection pinhole and so the image is optically sectioned.

2.4.2 High speed confocal microscopy

There are various strategies to overcome the relatively slow scanning procedure in standard confocal microscopy. One approach is to speed up the scanning procedure by using acousto-optic deflectors (AOD) [31,32], where travelling sound waves within the lattice of a crystal act as a diffraction grating with a variable period so as to deflect light by a variable angle. The scanning rate can be increased this way at the expense of system complexity and cost. In general, the image acquisition rate cannot be increased by simply increasing laser power, as the photobleaching and phototoxicity mechanisms typically scale non-linearly with peak intensity at the sample [33].

Line-scanning confocal microscopy [34] uses line illumination and a slit and pixelated 1D detector array rather than a pinhole, which reduces the requirement for scanning from 2D to 1D. The confocal slit detection will reject out-of-focus light in the direction perpendicular to the line but not parallel to the line. The scanning speed is therefore faster than a standard confocal however at the expense of reduced optical sectioning performance. One convenient way to implement line-scanning confocal microscopy is through the rolling shutter property of a sCMOS camera, which records signal only in one a line at a time. The rolling shutter can be synchronized with scanned line illumination, which eliminates the requirement for scanning optics in the detection path [35].

Spinning disk confocal microscopy, or Nipkow spinning disk microscopy, utilizes a disk of pinholes in order to perform parallelized confocal microscopy [36,37]. This allows for faster capture of 2D images than standard confocal microscopy. However, it is possible for fluorescence excited by light passing

through one pinhole to be detected through another pinhole. This crosstalk can effectively raise the background and can reduce contrast. The greater the fill-factor of holes within the disk, the higher the unwanted background level rises.

2.4.3 Multiphoton microscopy

In multiphoton microscopy [38] a fluorophore is excited by the absorption of two or more photons each with an energy lower than that required to excite the fluorophore alone. In 2-photon excitation, the frequency of the excitation light is half that of the equivalent single-photon excitation. Exciting fluorophores through the near-simultaneous absorption of multiple photons is less likely than single-photon excitation, and so a greater intensity of excitation light is required in order to achieve a useful level of fluorescence signal. Because of the need for two absorption events, two-photon excitation occurs with a probability proportional to the square of the excitation intensity [39]. This non-linear excitation probability leads directly to the useful observation that fluorescence excitation is restricted to small spot in the focal plane, therefore giving rise to optically sectioned imaging. An advantage of two-photon excitation compared to confocal microscopy is that a detection pinhole is no longer required, as all fluorescence is known to have been emitted from the same fluorescing region. The high intensity required in order to achieve an acceptable amount of fluorescence typically requires the use of laser pulses such as can be achieved by mode-locked lasers. A common choice is a Ti-sapphire laser that produces 100 fs pulses at a wavelength about 800 nm (repetition rate of 80 MHz) with a peak power of 50 kW. This can supply high peak power without significant average power and thermal heating of the sample. Typically, red and near-IR are used for excitation light in two-photon microscopy, which is within the low absorbing/scattering 'biological window', and as a result two-photon microscopy can image deeper into tissue compared to confocal microscopy [40]. Two photon light-sheet microscopy (TPLSM) has an inherent sectioning ability, less photo-damage and better penetration ability than confocal imaging however at the greater complexity of requiring a mode-locked laser.

2.4.4 Deconvolution microscopy

Computational optical sectioning microscopy, or deconvolution microscopy, is another method of optically sectioning and volumetric imaging. In these approaches, mathematical models of the image formation process are used to estimate optically sectioned images from a raw non-sectioned image stack. A good review article of 3D deconvolution microscopy is provided by reference [41], as well as a description of commonly used algorithms provided in [42]. One way to classify the various approaches to deconvolution are those where the PSF is known (to some extent), such as maximum likelihood estimation, the Lucy-Richardson algorithm and the constrained Tikhonov-Miller algorithm,

compared to those where the Point Spread Function (PSF) is not known – the blind deconvolution algorithms (e.g. maximum likelihood blind deconvolution, Ayers-Dainty algorithm). Deconvolution methods fail with thickly labelled samples due to the ambiguity of determining which photon came from which spatial location due to the reduced signal to background ratio.

2.4.5 Structured illumination microscopy

Structured illumination microscopy can be used to achieve optical sectioning (OS-SIM) [43], and also super-resolution imaging (SR-SIM) [44]. OS-SIM exploits the fact that higher spatial frequencies are attenuated as they pass through an optical system of a defocused objective and low spatial frequencies are suppressed to a lower degree. The DC component can pass through the optical system independently of defocus and so the DC component is not optically sectioned. If the object did not have a DC component, then it would be possible to achieve optically sectioned imaging. This can be achieved in practice for any sample by projecting a grid onto the sample. Illuminating the sample with a grid means that some regions of the sample will not receive any light. Hence typically three images of the sample are needed each with the grid shifted across the field of view by a third of the illumination period. These 3 images can then be combined to create an optically sectioned image. The approach was subsequently extended to achieve super-resolution (SR-SIM) where the lateral resolution was doubled compared to wide-field microscopy [45].

2.4.6 Light-sheet fluorescence microscopy

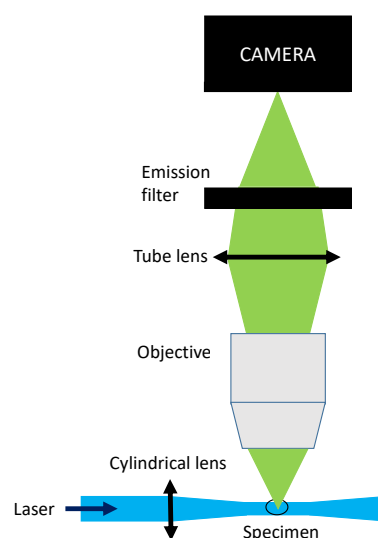


Figure 7 Schematic of a light-sheet fluorescence microscope. Fluorophores are excited by a thin light-sheet (possibly produced by passing a laser beam through a cylindrical lens). The fluorescence is then imaged by an objective arranged to be normal to the light-sheet and in wide field configuration.

The basic design of a light-sheet microscope originated with work by Siedentopf and Zsigmondy [46] with the ultra-microscope, which was used to improve the understanding of colloidal gold. Light was introduced into the microscope perpendicular to the observation axis. The method did not catch on due to the short working distances of the high-NA objectives of the time limiting the use of the device to colloidal suspensions. Interest resurfaced in the early 1990s as the light-sheet could be used to reduce the excitation volume [47]. In reference [48] a light-sheet created by a cylindrical lens was used to view water born bacteria.

Modern light-sheet fluorescence microscopy (LSFM, illustrated in Figure 7) originates from the 2006 paper by Huisken et al. [49] and was then called selective-plane illumination microscopy (SPIM). The term SPIM is particularly used to refer to the configuration developed in [49] with light-sheet fluorescence microscopy (LSFM) being a more general term describing all techniques which use a light-sheet. In light-sheet microscopy, an illumination objective lens is used to produce a single plane of excitation light that illuminates a plane within the sample; fluorophores within this plane then emit fluorescence. The generated fluorescence is collected by the imaging objective, which is arranged to be normal to the light sheet. Usually, the illumination objective and the imaging objective are arranged to be at 90° to each other and the system is designed so that only the region being imaged is the region which is illuminated by the excitation beam. The imaging system is a wide-field configuration and therefore captures the entire field of view in one go. Significantly, only the plane being imaged is illuminated, unlike confocal microscopy, and this means that the sample does not need be exposed to as much light and so there is less photobleaching and phototoxicity. This means that light-sheet microscopy can be used for time-lapse imaging. Keller et al. [50-52] demonstrated the low phototoxicity of light-sheet fluorescence microscopy by imaging the development of a zebrafish embryo at 3 minute intervals for 58 hours. They referred to the resulting dataset as a digital embryo. Another example of the low photobleaching and phototoxicity was provided in [53], where the authors imaged a beating zebrafish heart. Development of LSFM has occurred with the use of recently-available low-cost CCD and sCMOS cameras, along with a wide range of frequency-doubled solid-state laser sources covering the entire visible spectrum.

Ideally in LSFM, a perfectly thin light sheet would illuminate the focal plane resulting in a perfectly thin optically sectioned image with no unwanted contributions from out-of-focus fluorescence. However, diffraction causes changes in the thickness of the light-sheet along its propagation length; the thinner the light-sheet then the smaller the distance – and hence field of view – over which the thickness of the light-sheet is approximately constant. For example a Gaussian light sheet with a thickness of $6\ \mu\text{m}$ (half width at intensity $1/e^2$) can support a field of view of $110\ \mu\text{m}$ (from eq. 6), which would be

adequate for imaging single larger cells or groups of smaller cells, whereas a light-sheet with a thickness of 12 μm can typically support fields of view of 500 μm .

In a light-sheet system, the lateral resolution achieved is defined by the lateral resolution of the imaging optical system used for fluorescence collection. For the axial resolution of the system, it is first important to determine how the axial resolution is defined. Two useful measures are the axial full width at half maximum through the centre of the overall point spread function (PSF) and the full width at half maximum of the optical sectioning strength of the system (the variation in image intensity with defocus of a thin fluorescent sheet) [26]. The first of these is determined by a combination of the light-sheet thickness as well as the axial resolution of the imaging optical system. This can be modelled in the following way. Let the intensity of the detection PSF in the axial direction be approximated by a Gaussian $\exp\left(-\left(\frac{z}{\Delta z}\right)^2\right)$ and the profile of the illumination sheet intensity be approximated by a second Gaussian $\exp\left(-\left(\frac{z}{w_{LS}}\right)^2\right)$, where Δz and w_{LS} are standard deviations and are the parameters controlling the width of these functions. The product of these PSFs gives the PSF for the light-sheet system,

$$\exp\left(-\left(\left(\frac{1}{\Delta z}\right)^2 + \left(\frac{1}{w_{LS}}\right)^2\right)z^2\right) \quad eq. 2$$

and so this gives a standard deviation of the resulting Gaussian distribution, that is to say the width parameter for the system, as

$$w_{\text{system}} = \sqrt{\frac{1}{\left(\frac{1}{\Delta z}\right)^2 + \left(\frac{1}{w_{LS}}\right)^2}} \quad eq. 3$$

This shows that the axial PSF FWHM ($\text{FWHM} = 2.355\sigma$ for a Gaussian), depends on both the light-sheet thickness and the axial PSF FWHM of the detection optics. The effect of the light sheet on the system axial PSF FWHM becomes significant when the FWHM of the light-sheet is about the same size or smaller than the axial FWHM of the detection optics. For example, using eq.3 if the imaging FWHM and size of the light-sheet FWHM are of about the same size, then the resulting axial resolution would be improved by a factor of $\sqrt{2}$.

If the thickness of the light-sheet is larger than the detection PSF FWHM then deconvolution will be beneficial and will be able to reassign detected photons to their original position and will be able to improve contrast.

The second metric for the axial resolution – the FWHM of the optical sectioning strength – depends on the thickness of the illumination light sheet and is independent of the PSF of the detection optical system [26, 28, 29].

2.4.6.1 Gaussian beams

A common implementation to generate a static light sheet is by passing a Gaussian beam through a cylindrical lens; the applied astigmatism creates a light sheet with the desired width and length.

A Gaussian beam is the TEM_{00} output of a laser and also a good approximation to the mode emitted from a single mode fibre and is the solution to the Helmholtz equation with an additional paraxial constraint [54] – it is generally considered to be accurate as long as rays stay shallower than 30° . The output of a laser can be a real or virtual waist (a virtual waist is inside the laser). Any cross section of a Gaussian beam has a Gaussian intensity. The propagation characteristics of a Gaussian beam can be characterized by its beam waist at a particular position along the optical axis $w(z)$, which can be defined as the radius at which the beam intensity falls to $1/e^2$ (13.5%) of the axial intensity, as shown in Figure 8.

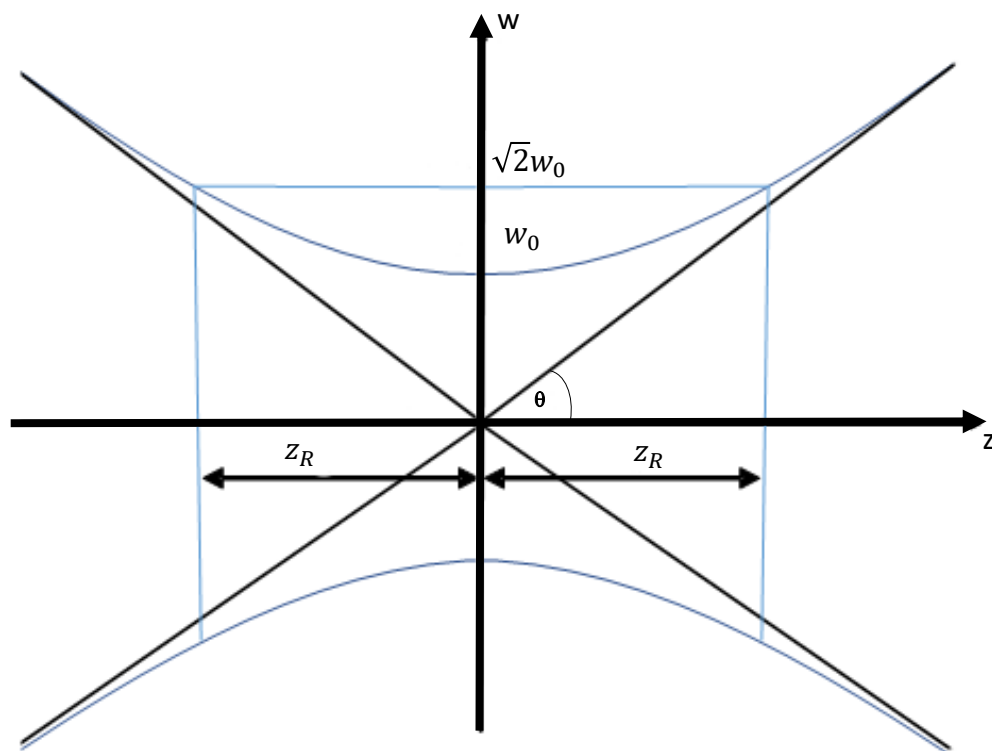


Figure 8 Key parameters for the focus of a Gaussian beam (blue), showing the beam waist ($z=0$) and the Rayleigh range (z_R). The black diagonal lines indicate the ray optics approximation to the Gaussian beam.

The beam waist is described by,

$$w(z) = w_0 \sqrt{1 + \left(\frac{\lambda z}{\pi w_0^2}\right)^2} \quad eq. 4$$

where w_0 is the radius of the $1/e^2$ intensity contour at the plane where the wavefront is flat and is the beam waist radius. The intensity of the Gaussian beam in the plane perpendicular to the propagation direction is given by,

$$I(r) = I_0 e^{-2r^2/w^2} \quad eq. 5$$

where r is radial distance in the x-y plane perpendicular to the propagation direction z . The Rayleigh range, z_R , is defined as the distance over which the beam radius spreads by a factor of $\sqrt{2}$ and the axial intensity falls by a factor of 2 from the value at the beam waist.

$$z_R = \frac{\pi w_0^2}{\lambda} \quad eq. 6$$

A useful property of Gaussian beams (which is not described by Geometrical Optics) is that if the waist of a beam is situated at the front focal plane of a thin lens then there will be another waist at the back-focal plane. The waists are related by the formula,

$$w_2 = \frac{f\lambda}{\pi w_1} \quad eq. 7$$

where w_1, w_2, z_R, f are the beam waist at the back focal plane, front focal plane, Rayleigh range and the focal length of the lens respectively.

2.4.6.2 Other types of light sheet

Although a Gaussian beam is simple to achieve in practice, the relationship between the beam waist and field of view achieved can be restrictive. The illumination intensity also varies across the light sheet in the plane of the illumination and perpendicular to the propagation direction. Another method is to scan a beam (typically a Gaussian beam from a laser) in the direction perpendicular to the detection optics. This approach provides a more uniform intensity of the light sheet over the direction scanned and is called a digitally-scanned light-sheet microscope (DSLM) [52]. The resulting virtual light sheet creates a more uniformly illuminated field of view and is spatially incoherent, which has the benefit of reducing interference effects such as stripe artefacts in scattering or absorbing samples. DSLM can also allow for other approaches such as structured illumination to be achieved by varying the intensity of the illumination beam as it is scanned [34]. In the work by Keller et al. [51], the intensity of the beam was modulated as it was scanned in order to achieve optical sectioning

structured illumination. The DSLM-SI showed an average 533 % increase in contrast compared with DSLM, also the improvement did not come as a result of any reduction in penetration depth.

More sophisticated beam-shaping techniques can be used to create Bessel beams [55]. These beams are referred to as non-diffracting, which means that they keep the same cross section regardless of propagation distance. This means they can be used to create longer light sheets than Gaussian beams at the expense of energy distributed outside the main light sheet. Bessel beams have a self-healing ability and they can recover from scattering events which would affect Gaussian beams [55-57]. This can reduce the effect of shadow artefacts, which is where scattering of the light sheet in the sample results in shadows that partially cover the field of view of the image and produce undesirable non-uniformities in the final image [58]. A disadvantage of Bessel beams is that they have a significant amount of energy in the side lobes (as shown in Figure 9) and this results in light from out-of-focus planes being recorded by the detector, reducing the optical sectioning and image contrast. This is not a problem for two-photon excitation implementations with a Bessel beam [57], as the non-linear excitation efficiency means that only the central lobe has sufficient probability to produce fluorescence. The effect of the side-lobes can be reduced for one-photon Bessel beam excitation by employing confocal line-scanning illumination in combination with a line detector [59,60] where, much like in slit-scanning confocal microscopy, light is rejected from the region above and below the focal plane. Another method is to use deconvolution to correct for the effects of the out-of-focus light.

The Airy beam is another kind of non-diffracting beam [61,62] which has a curved trajectory and has self-healing characteristics like a Bessel beam. It is produced by a cubic phase profile and can produce a longer field of view than the Bessel beam. However, the Airy beam has larger side lobes than the Bessel beam, which often requires the use of deconvolution to suppress their effect.

It has been shown that is possible to create 'designer' diffraction free beams that can move through arbitrary paths through the sample and can also have their intensity changed along the beam [63-66] to deal with the effects of absorption. All of these approaches are variants of the light-sheet idea with the decoupling of the illumination subsystem from the imaging subsystem, and as the complexity increases more parameters are introduced to adjust and tune the form of the illuminating beam.

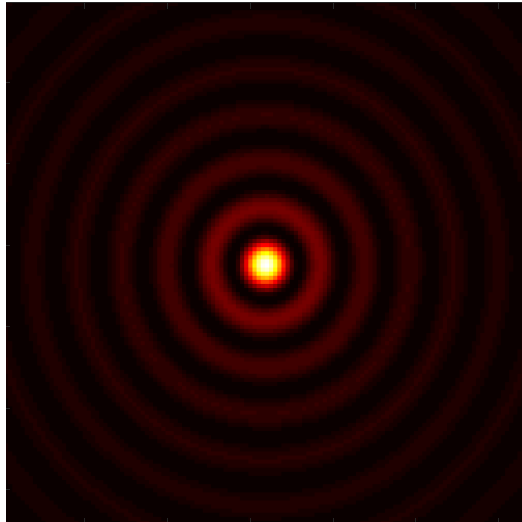


Figure 9 Intensity of a cross section of a Bessel beam - showing significant energy in the side rings. When a Bessel beam is used to create a digitally scanned light sheet – the emission for the side lobes will create out of focus blur.

2.4.7 Common light-sheet configurations

In order to image volumetrically it is necessary to produce an axial stack of optically sectioned images along the optic axis of the detection objective. Therefore, it is necessary to both reposition the focal plane of the imaging objective and the light-sheet relative to the object. The former can be achieved using a motorized stage to move the sample or an actuator to move the objective. This suffers from the problem of inducing mechanical vibrations into the sample that are likely to reduce the spatial resolution achieved. Another approach is to refocus the detection optics using adaptive optics, and this will be covered later in this chapter. The repositioning of the light sheet relative to the object can be achieved by applying tilt to the illumination beam via a galvo-mirror arranged to be conjugate via relay lenses to the back focal plane of the illumination objective. The illumination objective then converts the tilt applied by the galvo into up and down displacement of the illumination sheet along the direction of the optical axis of the imaging arm. A recurring issue when using two objectives in light-sheet microscopy is that the space between the objectives is limited, and this places constraints on the types of sample mounting methods that can be employed. Figure 10(a) shows a common SPIM arrangement where the sample is mounted in an agarose cylinder which can also be rotated about the y axis and different angular views being combined to create a more isotropic resolution. Where the light sheet is scattered in the sample the result can be shadow artefacts [67]. These shadow stripes have high spatial frequency components and so are not effectively removed by multi-view fusion approaches. Arranging two objectives to produce two counter-propagating illumination beams and sequentially illuminating from each direction within the exposure time of the camera results in a reduction in shadow artefacts; this is called mSPIM [68], see Figure 10(b). Another variation called MuVi-SPIM [69, 70], see Figure 10(d), is to view the sample from either side as well as being

illuminated from both directions, which helps deal with the fact that the image quality degrades as one moves further from the focal plane. Inverted SPIM (iSPIM, Figure 10(e)), is a convenient way to mount the objectives which are positioned above the sample and is the method used for LSFM in this work, see Chapter 5. In dual-illumination iSPIM (Figure 10(f), [71, 72]), the sample is illuminated and imaged from two orthogonal directions in order to produce a more isotropic resolution; this comes at the price of a more complicated setup. Open-top SPIM (Figure 10(c), [73]), has much more room for the specimen and can be used with a conventional 96-well plate. The water-filled prism reduces the aberrations as the angled light-sheet passes into the medium used to mount the sample.

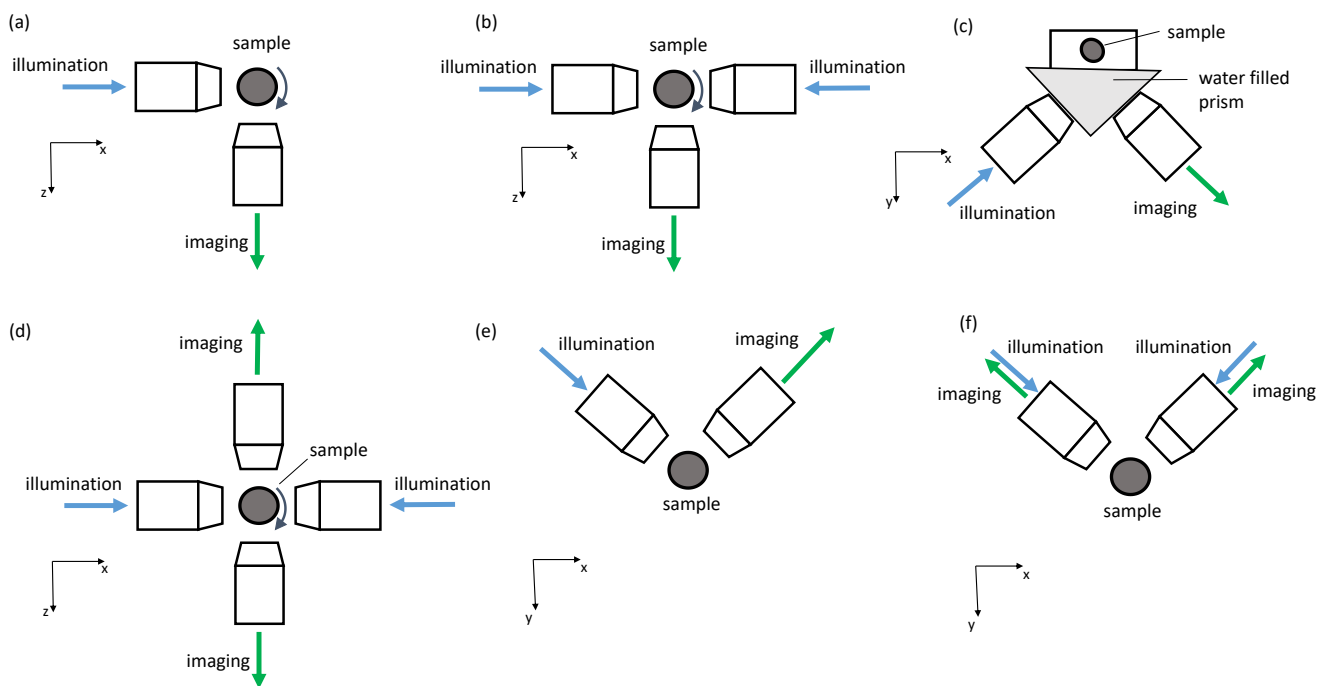


Figure 10 This figure shows schematics of different arrangements of the illumination and imaging objectives in LSFM. (a) shows a common arrangement where the sample is mounted in an agarose cylinder and can also be rotated about the y-axis, which permits several angular views to be combined to give a more isotropic resolution. (b) mSPIM, where either side is sequentially illuminated and an image taken. These can be combined to reduce the effect of shadow artefacts. (c) open-top SPIM where the objectives view the sample through a water-filled prism that is matched with the refractive index of the medium used to mount the sample. This arrangement has much more room for the sample and can also be used with multi-well plates. (d) MuVi-SPIM, where the sample can be viewed from either side along with the illumination coming from both directions. This allows for a reduction in shadow artefacts and scattering of the light-sheet. (e) iSPIM the illumination and imaging objectives are tilted and above the sample – and enables samples to be conveniently mounted onto microscope slides. (f) Dual-illumination iSPIM, the sample is illuminated and imaged from 2 orthogonal directions and fused to produce a more isotropic resolution. In this figure, x and z are in the horizontal plane, and up is in the negative y direction.

2.4.8 Single objective light-sheet microscopy

2.4.8.1 Highly-inclined and laminated microscopy

A highly-inclined and laminated microscope (HILO) [74] uses a single high-NA objective to produce a light-sheet that emerges from the objective at an inclined angle, and the resulting fluorescence is collected by the same objective. In this configuration only a single line in the final image from within the illuminated sheet is in focus at any one time.

2.4.8.2 Oblique plane microscopy

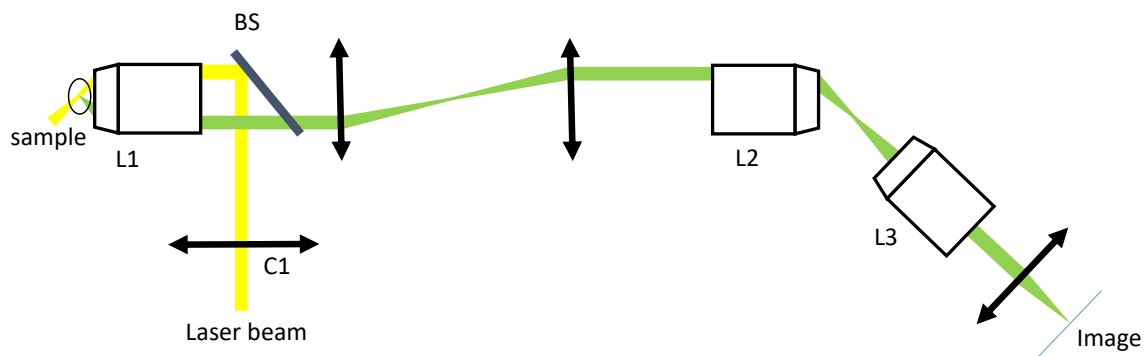


Figure 11 A schematic of an OPM system. L1 and L2 are arranged to make a remote, undistorted 3D image. Another objective, L3, is then arranged to be normal to the light sheet and creates an optically sectioned image. Hence this is a single objective LSFM technique.

In oblique-plane microscopy (OPM, illustrated by Figure 11) [75], a single high NA objective L1 sends a light-sheet to the sample and also collects fluorescence. In this approach, the sample is illuminated with an inclined light-sheet. Remote refocusing, as described by Botcherby et al., [1, 76] and introduced in more detail below, uses a second objective L2 aligned so that its back pupil is matched to the image of the back pupil of the imaging objective. This creates an undistorted intermediate 3D image; most of the aberrations introduced by using the imaging objective to collect light from an object away from the design conjugate are cancelled out by the remote refocusing objective and so the intermediate image can be diffraction limited over an extended 3D volume. A third microscope objective L3 is then arranged with its optical axis normal to the light sheet image and projects an image of the tilted illuminated plane onto the camera. OPM can be used to image 3D volumes at video frame rate and, unlike the standard light-sheet configuration employing two objectives arranged at 90°, it does not require any special sample preparation or mounting. This approach has been used to image cardiomyocytes [77, 78] at high speed. A weakness of the approach is the fact that the inclined nature of L3 has an acceptance cone which only selects a portion of the light emitted by L2 and so has the effect of reducing the NA of the system.

2.4.8.3 Swept confocally-aligned planar excitation (SCAPE) microscopy

In SCAPE microscopy [79] a polygonal mirror is inserted into a plane conjugate with the pupil of the primary objective of an OPM-like setup. Rotation of the mirror changes the lateral position of the light sheet emerging from the objective. Multiple images are acquired with each sweep that are used subsequently to create a 3D volume. The technique has been used to image neuronal circuits within a mouse brain.

2.4.8.4 Axial plane optical microscopy

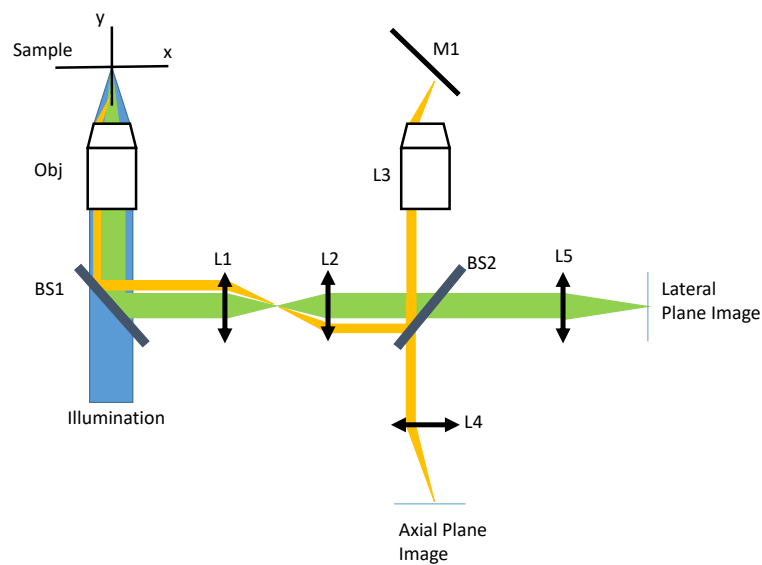


Figure 12 A schematic of an axial plane optical microscope, much like OPM an intermediate image is produced by L3. The mirror M1 transfers the lateral and the axial planes of the remote image. This allows the lateral and axial planes to be simultaneously imaged.

Axial plane optical microscopy [80] (illustrated in Figure 12), is equivalent to an OPM system where the optical system is folded by placing a mirror at the focal plane of L2 in Figure 12 or L3 in Figure 13. By tilting the mirror M1 at an angle of 45 deg it is possible for the detection optical system to view the sample at 90 deg to the optical axis of the primary objective. The lens L4 produces an axial plane image and L5 produces a lateral plane image. Unfortunately, the effective pupil of the whole system is reduced due to the high tilt angle, which lowers the NA and collection efficiency that can be achieved.

2.4.8.5 Reflected beam light-sheet microscopy

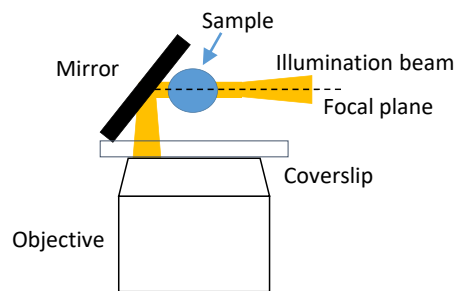


Figure 13 Schematic of reflected beam light-sheet microscope. The light-sheet is reflected into a direction perpendicular to the axis of the objective. Volumetric imaging can take place as the objective is moved axially.

In reflected beam light-sheet microscopy [81] (illustrated in Figure 13), a mirror is placed at 45° next to the sample, which enables a light-sheet to be produced passing through the sample with the plane of the light-sheet normal to the objective. Moving the objective axially causes the focal plane to move axially in the sample, but the position of the light-sheet waist will translate across the image FOV. An electrically tunable lens (ETL) can be used to keep the light-sheet waist central to the field of view as the sample is scanned.

2.4.9 Extended depth of field microscopy

One could imagine summing a z-stack of images obtained with an optical sectioning technique such as confocal or light-sheet microscopy in order to produce a single image. It would be as if this image had been obtained from an instrument with an extended depth of field and would display information from the whole range of sample depths at the same time [82]. Before CCDs the authors of [83] suggested taking an axially integrated photographic image by leaving the shutter open and smoothly changing the focus and then to deconvolve the image with the optical transfer function (OTF) of the integrated system. The key point was that for sufficiently long focus changes (longer than twice the extent of the sample) the OTF is depth independent with defocus. This simplifies the process of deconvolution. A summary of the various methods for extending the depth of field is provided in reference [84].

Botcherby et al. [85] used remote refocusing (described later in the chapter) in order to sweep the effective focal plane through an axial range during a single camera acquisition. Alternative methods to sweep the focus are to use an electrically tunable lens (ETL) or a deformable mirror (DM) [7, 86]. The 3D PSF of the system can then be used to remove background haze by deconvolution. This means that a single exposure of the camera can acquire a single extended depth of field image through the volume. For high-speed volumetric imaging it is usually the case that the camera is the key bottle neck

and so this approach provides a solution, however at the price of achieving just a single 2D image rather than a full 3D volume.

Normally, the OTF of an objective lens rapidly decreases for higher frequencies with defocus. By placing an appropriate phase mask into the back focal plane of the objective, it is possible to prevent this collapse and to retain approximately the same OTF through a wide range of defoci. A cubic phase mask that is either cubic in the x and y directions or cubic in the radial direction is effective at producing a constant OTF with defocus. The cubic phase mask causes object points to be equally blurred independently of their defocus position. Hence, the deconvolution can be accomplished with a single step after measurement of the extended PSF of the system. This approach of using a mask combined with digital image restoration creates a digital-optical microscope system; the pupil encodes the optical wavefront so that a computer algorithm can recover the image; this approach is known as wavefront coding [87]. In reference [88], wavefront coding techniques allowed a light-sheet system to volumetrically image at > 70 vol/sec. The main disadvantage of wavefront coding compared with standard wide-field imaging is that it relies on sparse fluorescent labelling of the sample, and as the labelling becomes more dense then the signal to noise of the raw images will limit the ability for the algorithm to extract closely-spaced features.

2.6 Adaptive optics in microscopy

Adaptive optics originated as a method in astronomy to correct for atmospheric disturbance of light from an astronomical object caused by turbulence in the atmosphere. Before light from a distant object can reach the telescope, it has to pass through large volumes of moving air which alter the wavefront and can affect the quality of the image. Atmospheric distortion typically limits the resolution of large aperture telescopes to that of a 40 cm telescope aperture [89].

In order to correct for aberrations, it is necessary to measure them. In the case of astronomy, light from a natural guide star near to the observation direction is directed to a wavefront sensor such as a Shack Hartman wavefront sensor (SHWFS, which is described in more detail in Chapter 3). The SHWFS will measure the phase of the received wavefront, which is then used to inform the compensation applied on the wavefront shaping device. In the absence of a natural guide star, an artificial guide star can be produced by exciting sodium atoms in the upper atmosphere (conveniently, the upper atmosphere contains sodium from meteors burning up on entry). Sensing the wavefront with e.g. a SHWFS and then using the information to apply a wavefront correction using an adaptive element is called closed-loop control.

In microscopy there are many sources of optical aberration and any optical system will be optimized for best performance within a specific set of parameters; variation from these is likely to lead to aberrations. For example, a well-corrected water-dipping objective will focus light to a diffraction-limited spot in water; however, if the sample varies in refractive index from water then this will change the phases and directions of the rays resulting in optical aberrations and the loss of diffraction-limited performance. Biological samples are heterogeneous. For example, cells have various components, e.g. proteins, lipids, nuclear acids, membranes, each with a slightly different refractive index that is different to the immersion media [90]. Refraction at boundaries will cause distortion to the wavefront that results in sample-induced aberrations. As well as aberrations which originate from the sample itself, aberrations can also be produced by the system caused by imperfections in the alignment and the optics themselves.

Adaptive optics approaches can be used to overcome these effects and they employ some form of programmable optical element to correct for the aberrations induced by the sample and/or system. If the aberration is known, the correction device can be used to compensate for the distortion in the wavefront. This can be performed by pre-compensating a wavefront used for illumination prior to it being passed into an aberrating lens and/or sample. It can also be used to correct light emitted by a sample after it is aberrated by the lens and/or sample on its path to the detector. Correcting for aberrations by a correction device has the effect of reducing the effect of the aberration.

In the case of confocal microscopy, the final image quality is affected by aberrations in both the excitation and emission beams, and the use of adaptive optics to correct both the illumination and detection beam paths was demonstrated by Booth et al. [91]. Adaptive optics has also been applied to multiphoton microscopy [92], for example to correct for depth induced aberrations [93] or to achieve adaptive motion compensation [94]. In the case of light-sheet microscopy, the quality, thickness and uniformity of the light-sheet can affect the system spatial resolution; as an example changes in the refractive index of a sample can have the effect of deflecting the light-sheet out of the focal plane of the imaging objective and so degrading performance. In reference [95] an adaptive optics approach was used to try to maintain the position of the light-sheet within the focal plane of the detection objective. In addition, aberrations affecting the emitted light can affect the lateral resolution. Adaptive optics approaches to LSFM have involved correcting aberrations in both the illumination as well as in the collection optics [96]. Adaptive optics in light-sheet microscopy is reviewed in [96, 97].

The type of compensating device used in adaptive optics depends on the nature of the aberration to be corrected; for a simple aberrations such as primary defocus an electrically tunable lens (ETL) will

suffice, and for more complex aberrations deformable mirrors (DM) as well as spatial light modulators (SLM) can be used to produce the required correction. Some systems can have several adaptive optical elements, for example one to correct for low spatial frequencies and another for high spatial frequencies in a woofer-tweeter arrangement [98]. The choice of adaptive optical component will depend on the complexity of the aberration as well as the time constant that it is required to operate.

There are rarely naturally occurring guide stars in biological tissue. Small fluorescent beads or the back scattering of excitation light from a point scatterer can be used to provide a guide star. In the work by Azucana et al. [99] fluorescent beads were injected into *Drosophila* embryos and the aberration induced by the sample was then measured with a SHWFS and the wavefront corrected by a SLM. In the work by Jorand et al. [100] fluorescent beads were included into a multicellular tumor spheroid in order to enable aberration correction in a light-sheet system.

Indirect wavefront measurement approaches (also called wavefront sensor-less approaches) seek to use features within an image, for example brightness, sharpness or contrast, in order to provide an adaptive optic correction. In reference [96], the authors used a metric based on the contrast within different regions of the image to provide correction via a deformable mirror for imaging a transgenic zebrafish in a standard SPIM arrangement. Hill climbing and genetic algorithms are often used to find the best correction and in reference [101] a range of algorithms were examined with each using sensor-less adaptive optics to reduce aberrations in multiphoton and confocal microscopy. In general, metrics based on image brightness work well for samples with bright fluorescence, but for dimmer or fluctuating signals metrics based on contrast and spatial frequency are more effective. These iterative approaches can require many raw image acquisitions, which have issues with regard to photo-bleaching and photo-toxicity of the sample.

‘Modal’ approaches use an adaptive optic device such as an SLM or a DM to introduce a known aberration (often amounts of different Zernike modes), and then measure the effect on various image-based metrics such as brightness etc. The metrics are chosen to be sensitive and informative towards the amount of aberration applied. Through a series of images, relationships are determined between the modal aberrations and the image-based statistics. Once determined, these relationships are then used in reverse to estimate the amount of each aberration introduced by the sample. These approaches require fewer images than genetic or hill climbing approaches. This approach was used by Booth et al. [102] to improve the image quality of confocal microscopy. Débarre et al. [103] improved the contrast in two-photon fluorescence microscopy in a mouse embryo. Bourgenot et al. [96] improved the aberrations introduced by glass or plastic pipettes sample holders when imaging zebrafish.

Phase-retrieval and phase-diversity [104] are similar to the modal approach, where a series of defocused images can be used to estimate an aberration-free image as well as the aberration. In references [105, 106] the phase diversity approach was used to estimate a 3D image as well as the aberrations, however the procedure required a coherent or quasi-coherent image.

Indirect wavefront-sensing methods requiring multiple images are therefore in general slower than direct wavefront sensing methods. In both cases however, the size of the isoplanatic patch (region of the FOV where the wavefront errors are closely correlated) ultimately decides the potential effectiveness of the approach. The size of this region depends on factors such as local refractive index and sample shape; the size of the patch can range from 100s μm e.g. in mouse brain [107, 108], to patches which are only relevant to the site of measurement in the case of *C.elegans* or zebrafish larvae [109, 110].

2.6.1 Remote refocusing

If high-NA defocus (see section 2.6.2) is applied to the back focal plane of an objective then the result is that it will form an image point at the correctly defocused point. The work by Botcherby et al. [1] refocuses light optically by arranging a pair of objectives such that the back focal plane of the first objective is matched to the back focal plane of the second. Provided that the lateral magnification of the system is chosen to be equal to the ratio of the refractive index of the immersion media of the first and second lenses, the result is that the 3D image created by the second objective is undistorted. The aberrations created by the first objective due to defocus, as well as field dependent aberrations caused by off axis object points, are largely undone by the second objective to create a non-aberrated image point, see Figure 14.

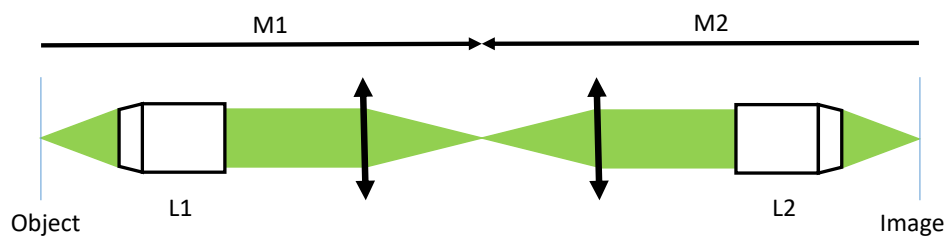


Figure 14 Creating an undistorted 3D image by arranging 2 objective such that the back focal plane of one objective is imaged onto the other. With correct choice of M1 and M2 a 3D stigmatic image is produced.

The image formed by the second objective can now be imaged by another microscope objective L3 as shown in Figure 15 (a), which can be used to image any plane in this image at any particular angle.

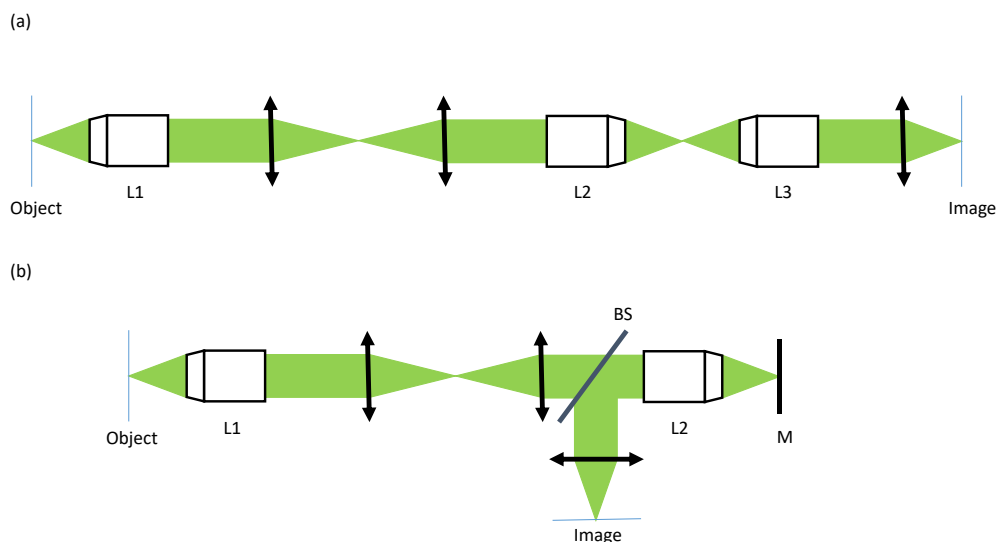


Figure 15 Panel (a) shows a microscope L3 imaging an arbitrary plane in the image created by L2. Panel (b) uses a plane mirror to image planes from the aerial image created by L2.

The configuration shown in Figure 15 (a) can be folded about L2 as shown in Figure 15 (b). The mirror makes a virtual image of the desired plane which is then imaged by L2 and tube lens onto the camera. By moving the mirror along the optic axis the virtual image is translated and so L2 will image a different plane onto the camera. If that particular plane is illuminated and optically sectioned by a light sheet, and the mirror and the light-sheet are synchronized then L2 will volumetrically image the sample. This folded configuration has the advantage that the mass of the moving mirror can be much smaller than the mass of L3 that needs to be moved in the unfolded configuration.

Both the unfolded and folded configurations allow the sample to be imaged volumetrically without needing to move L1 or the sample, thus preventing vibration of the sample and a consequent reduction in resolution and/or image contrast.

The folded remote-refocusing approach was used to refocus a light-sheet system at video frame rates in the work by Sparks et al. [111]. A disadvantage of this approach is that a comparatively large amount of light is lost at the two additional microscope objectives L2 and L3; typical microscope objectives have a peak transmission of 90%. In addition, the folded configuration required the use of a polarizing beamsplitter that only accepts 50% of the signal in the case of fully unpolarized fluorescence from the sample. Together, these effects reduce the collected signal to 40% of that after L1. Refocusing the system with a DM offers the potential to achieve a better throughput of light.

When the sample is displaced axially from the focal plane of the objective – a wavefront error is introduced to the pupil of the objective. By applying a suitable phase correction by an adaptive optic in a location conjugate to the back focal plane of the objective it is possible to refocus a high-NA

objective. This is known as remote refocusing – and means that neither the sample nor the objective needs to be physically moved.

2.6.2 High-NA defocus

The goal of the project is to refocus a microscope employing a high-NA objective by applying a phase correction to its pupil, and to sweep the amount of defocus through a specified range at video frame rate. Under the paraxial approximation, defocus can be regarded as quadratic wavefront aberration. A quadratic surface applied to the wavefront error of the pupil of the objective would be sufficient to refocus the shallow ray angles found in the focal plane of a low-NA objective. For high-NA objectives, which generate steep rays at focus, a higher-order correction is required. Most microscope objectives are designed to obey the Sine Condition [8, 15, 112, 113, 114]. Under the assumptions of Geometrical Optics, it can be shown that for an optical system obeying the Sine Condition, a small lateral region at the object focal plane is perfectly and stigmatically imaged [8]. This is shown in Figure 16.

$$\frac{\sin(\theta_1)}{\sin(\theta_2)} = \frac{n_1}{n_2 M} \quad \text{eq. 8}$$

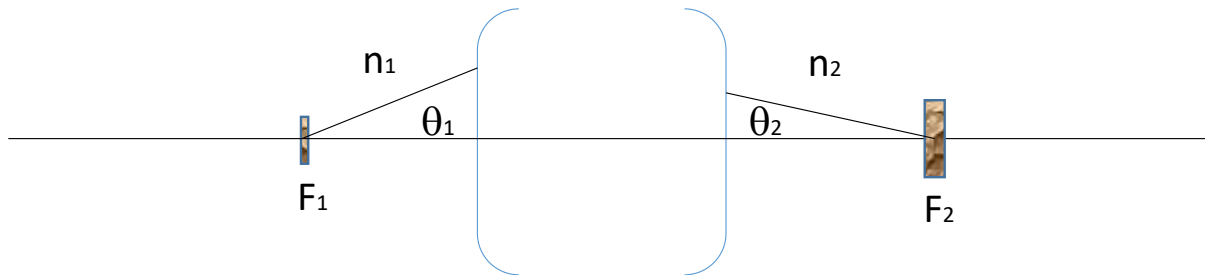


Figure 16 If it is the case that any ray leaving F1 and reaching F2 obeys the Sine Condition which is given by eq. 8, then it is guaranteed that a small lateral patch at F1 is perfectly imaged to F2, within the assumptions of Geometrical Optics.

It can also be shown that such a system will also be free from all orders of coma [8, 112, 113]. For this reason, the Sine Condition is often used as a starting point in objective design. Microscope objectives contain many lenses which are carefully balanced to offset and minimize aberrations at the design conjugates; which in most cases are the focal plane of the objective and infinity. The Sine Condition can be shown to be equivalent to using Principal Spheres instead of Principal Planes [112]. This Sine Condition-based model of an objective – using Principal Spheres (although one sphere has an infinite radius and is a plane), is used extensively throughout this thesis, see Figure 17(a). For an infinity-corrected objective, this model becomes one of a spherical first/front Principal Surface and a planar second/back Principal Surface, see Figure 17(b).

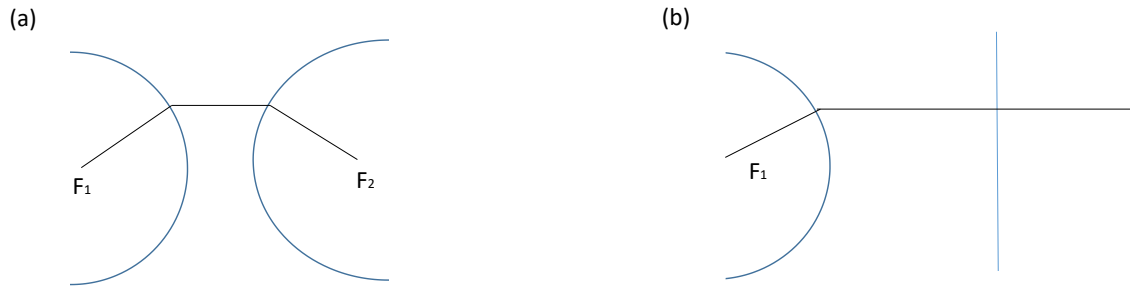


Figure 17 An optical system which obeys the sine condition is equivalent to using Principal Spheres centred at each focal point rather than using Principal Planes as in Geometrical Optics, as shown in (a). (b) shows the case for an infinity corrected objective in which case the second Principal Sphere is a plane.

One can use this Sine Condition-based model of an objective to estimate the difference in optical path length between an object at the front focal point and a point displaced slightly from the front focal point. If the displacement is much smaller than the focal length of the objective, then we can make the approximation that the ray from the front focal point to a point on the front Principal Sphere and a ray from a displaced point to the same point on the Principal Sphere are parallel, and therefore also obey the Sine Condition (as shown in Figure 18).

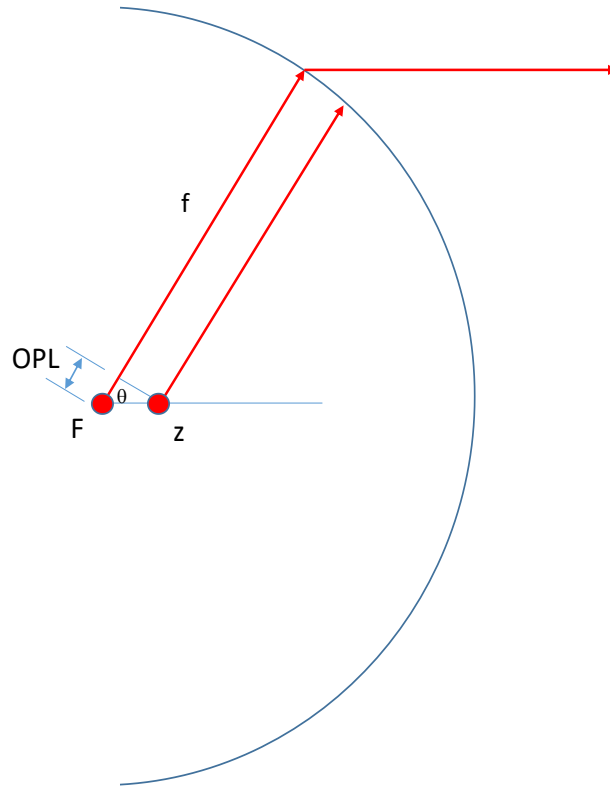


Figure 18 For a point object displaced by z along the optical axis where $z \ll f$, the rays leaving this point can be imagined to be approximately parallel to those leaving F , and so obey the Sine Condition. Additionally the OPL is shown, which produces an expression for high-NA defocus in the objective's pupil.

The difference in optical path length between these two points, where z is the axial displacement of the displaced point and θ is the angle of the rays with respect to the optical axis is then,

$$\text{for } z \ll f \quad \text{OPL} = nz \cos(\theta)$$

$$\text{OPL} = nz\sqrt{1 - \sin^2(\theta)} \quad \text{eq. 9}$$

Using ρ for the normalized pupil radius, and if α is the maximum acceptance angle of the objective with numerical aperture NA , manipulation of the Sine Condition shown in (eq.10) results in a convenient expression for the OPL, i.e. high-NA defocus expressed in terms of the normalized pupil radius (eq.11).

$$\frac{\sin(\theta)}{\sin(\alpha)} = \rho \quad (\text{Sine Condition}) \quad \text{eq. 10}$$

$$\text{OPL} = nz\sqrt{1 - \sin^2(\alpha)\rho^2} = z\sqrt{n^2 - NA^2\rho^2} \quad \text{eq. 11}$$

For an object displaced laterally by a small amount x compared to f , the extra OPL is shown in Figure 19 and corresponds to a tip term (eq.12).

$$OPL = z\cos(\theta) + x\sin(\theta) \quad eq. 12$$

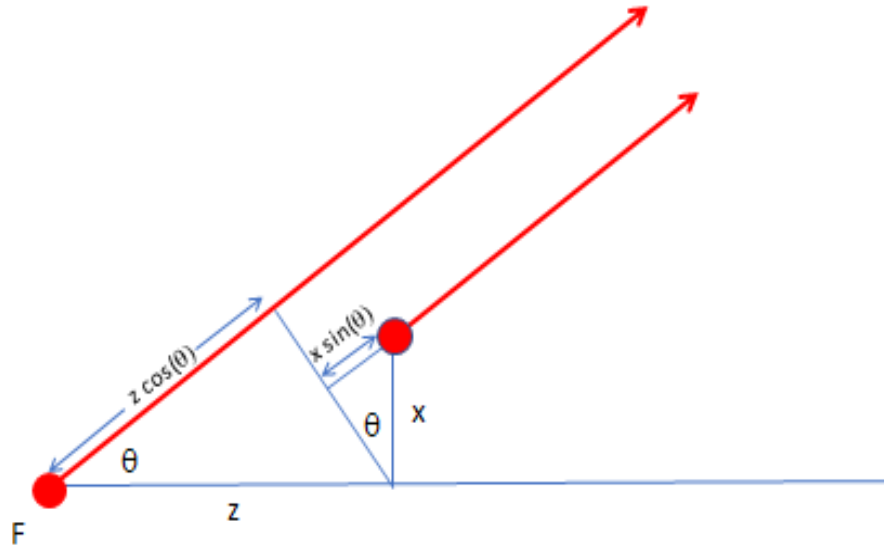


Figure 19 When the object point is displaced by z and by x from F then the result is high-NA defocus and also tilt added to the OPL.

Now consider the situation where an adaptive-optic device is placed in a plane conjugate to the back focal plane of the microscope objective and used to apply a high-NA defocus of distance $-z$. The OPL applied by the adaptive optics would cancel out the high-NA defocus terms in eq.11 above just leaving the tip and tilt terms.

This expression for high-NA defocus can be expressed as a Taylor expansion (eq.13). This shows that the expression is composed of principal defocus (ρ^2) and decreasingly small amounts of primary spherical aberration and higher orders of spherical aberration ($\rho^4, \rho^6, \rho^8, \dots$). For low-NA objectives, the terms of order greater than principal defocus are negligible and so a parabolic correction suffices. For higher NA lenses, a higher-order correction is required.

$$\begin{aligned} OPL &= nz\sqrt{1 - \sin^2(\alpha)\rho^2} \\ &= nz\left(1 - \frac{1}{2}\sin^2(\alpha)\rho^2 - \frac{1}{8}\sin^4(\alpha)\rho^4 - \frac{1}{16}\sin^6(\alpha)\rho^6 - \frac{5}{128}\sin^8(\alpha)\rho^8 + \dots\right) \quad eq. 13 \end{aligned}$$

2.6.3 Zernike modes

Any continuous function on the unit disk can be expanded into Zernike modes [115] shown in Figure 20. Zernike modes are a set of polynomials defined over the unit disk that form a complete

set, which means that through linear combination they can be used to construct any continuous and differentiable function over the unit disk. The number of Zernike polynomials required to effectively approximate a particular surface depends on the complexity of the surface and the error required and is discussed in reference [116]. There are many such sets of functions which can be used to represent continuous functions on the unit disk, however an advantage of Zernike polynomials/modes is that they can be identified with standard aberrations in optics such as spherical aberration, astigmatism etc.

The Zernike mode is characterized by a pair of integers: n which is the radial degree and m which is the azimuthal degree and $m \leq n$ with $n - |m| = \text{even}$, e.g. if $n = 3$, then $m = 1, 3$. Each azimuthal degree m has an even and odd mode. Even Zernike modes are defined as,

$$Z_n^m(\rho, \phi) = \sqrt{n+1} R_n^m(\rho) \sqrt{2} \cos(m\phi), \quad \text{when } m \neq 0 \quad \text{eq. 14}$$

Odd Zernike modes are defined as,

$$Z_n^m(\rho, \phi) = \sqrt{n+1} R_n^m(\rho) \sqrt{2} \sin(m\phi), \quad \text{when } m \neq 0 \quad \text{eq. 15}$$

Also,

$$Z_n^0(\rho, \phi) = \sqrt{n+1} R_n^0(\rho) \sqrt{2} \sin(m\phi), \quad \text{when } m = 0 \quad \text{eq. 16}$$

$$R_n^m(\rho) = \sum_{k=0}^{\frac{n-m}{2}} (-1)^k \binom{n-k}{k} \binom{\frac{n-m}{2}}{k} \rho^{n-2k}, \quad \text{with } R_n^m(1) = 1 \text{ by definition} \quad \text{eq. 17}$$

The even modes are often represented by a negative m , and odd modes by a positive m . e.g. Z_1^{-1} is even (cosine mode) and Z_1^1 is odd (sine mode) for $n=1$ and $m=1$. As well as being indexed by n and m , the Zernike polynomials can be indexed by a single index j . In Noll indexing [117] (which is also called Standard Zernike Coefficients in Zemax), j starts at 1 and the even j have cosine and odd j have sine azimuthal terms. Table 1 tabulates the functional form of the first few Zernike modes up to Z_{22} .

j	n	m	Functional form of the Zernike mode	Common name
1	0	0	1	Piston
2	1	1	$2r \cos(\theta)$	Tilt
3	1	1	$2r \sin(\theta)$	Tilt
4	2	0	$\sqrt{3}(2r^2 - 1)$	Defocus
5	2	2	$\sqrt{6}r^2 \sin(2\theta)$	Astigmatism
6	2	2	$\sqrt{6}r^2 \cos(2\theta)$	Astigmatism
7	3	1	$\sqrt{8}(3r^3 - 2r) \sin(\theta)$	Coma
8	3	1	$\sqrt{8}(3r^3 - 2r) \cos(\theta)$	Coma
9	3	3	$\sqrt{8}r^3 \sin(3\theta)$	
10	3	3	$\sqrt{8}r^3 \cos(3\theta)$	
11	4	0	$\sqrt{5}(6r^4 - 6r^2 + 1)$	spherical aberration
12	4	2	$\sqrt{10}(4r^4 - 3r^2) \cos(2\theta)$	
13	4	2	$\sqrt{10}(4r^4 - 3r^2) \sin(2\theta)$	
14	4	4	$\sqrt{10}r^4 \cos(4\theta)$	
15	4	4	$\sqrt{10}r^4 \sin(4\theta)$	
16	5	1	$\sqrt{12}(10r^5 - 12r^3 + 3r) \cos(\theta)$	
17	5	1	$\sqrt{12}(10r^5 - 12r^3 + 3r) \sin(\theta)$	
18	5	3	$\sqrt{12}(5r^5 - 4r^3) \cos(3\theta)$	
19	5	3	$\sqrt{12}(5r^5 - 4r^3) \sin(3\theta)$	
20	5	5	$\sqrt{12}r^5 \cos(5\theta)$	
21	5	5	$\sqrt{12}r^5 \sin(5\theta)$	
22	6	0	$\sqrt{7}(20r^6 - 30r^4 + 12r^2 - 1)$	

Table 1 The first 22 Zernike modes tabulating the Noll index, radial and azimuthal index, functional form and classical aberration name.

Noll modes have a normalization with an RMS amplitude of 1 radian. The orthogonality and normalization is expressed by,

$$\int d^2r \frac{1}{\pi} Z_{j_1} Z_{j_2} = \delta_{j_1, j_2} \quad eq. 18$$

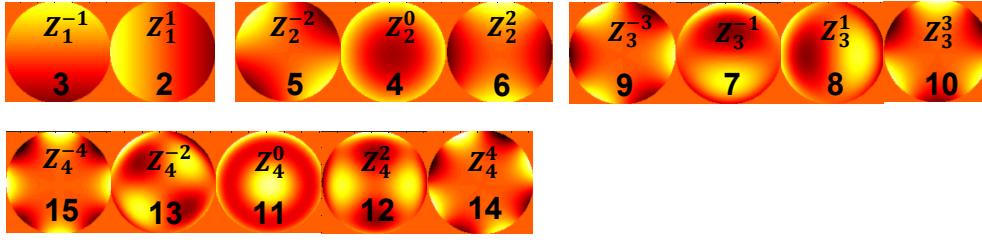


Figure 20 Zernike modes for $n = 1, 2, 3, 4$. The bottom number is the Noll index for the mode the label at the top of the mode provides the values of n (bottom) and m (top). If m is negative then it means the even (cosine) mode, if it is positive then it means the odd (sine) mode.

To determine the number of Zernike modes required to adequately approximate high-NA defocus, 30 μm of high-NA defocus for an Olympus 40x/0.85 air objective corresponding for was expanded into radial Zernike modes. The non-zero modes correspond to an even radial degree (n) and an azimuthal degree (m) of zero such as defocus ($n = 2$), spherical aberration ($n = 4$), secondary Zernike spherical aberration ($n = 6$), tertiary Zernike spherical aberration ($n = 8$), and so on. As can be seen in Figure 21, three radial modes are quite sufficient to ensure that the RMS error between the true high-NA defocus function and the truncated series of defocus and spherical Zernike aberration is below the Strehl limit for 550 nm wavelength light. Primary defocus and spherical aberration do reduce the RMS error close to the Strehl limit but extra correction would be needed to ensure diffraction limited performance.

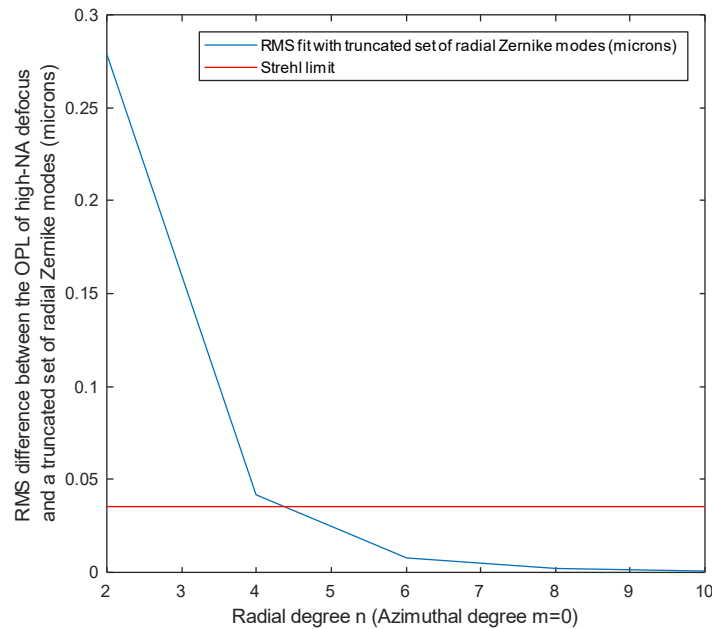


Figure 21 Comparison between high-NA defocus and approximations of successively more Zernike polynomials with even degree n , which correspond to defocus ($n=2$), spherical aberration ($n=4$) and higher orders of spherical aberration for 30 μm of defocus with a $\text{NA}=0.85$ air objective with wavelength 550 nm.

2.6.4 Electrically tunable lenses

An electrically tunable lens (ETL) uses electronic control to change its focal length. These lenses have successfully been used for remote refocusing in multiphoton microscopy [2], light-sheet microscopy [118] and confocal microscopy [119]. The tunable lenses produced by Varioptic (owned by Corning) are liquid-based lenses. A sealed unit contains two different and immiscible liquids which have different refractive indices. The curved shape of the boundary between the two liquids adds optical power to the rays passing through the system. An electric field changes the radius of curvature of the boundary and so focal length. The tunable lenses produced by Optotune are made up of a container which contains an optical fluid which is sealed off with an elastic polymer membrane (a schematic is shown in Figure 22). Pressure applied to the outer ring of the elastic polymer membrane can change the curvature of the central region of the membrane which acts as the lens. The pressure can be applied by an electromagnetic actuator. These devices can operate at kHz.

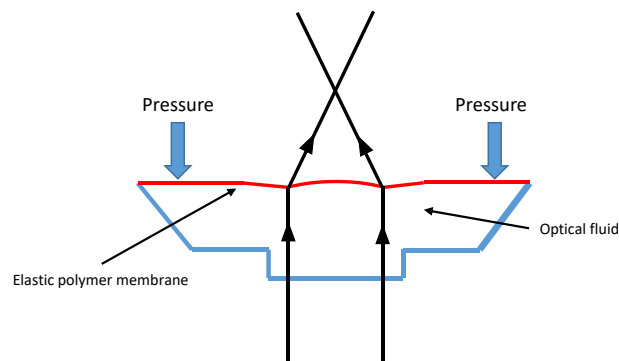


Figure 22 A schematic of an ETL produced by Optotune. It consists of a container which contains an optical fluid. An elastic polymer membrane changes the curvature of its central region in response to pressure around the outer ring. This allows the add optical power to the beam.

The Optotune ETL in reference [118] was able to scan 17 planes within a zebrafish heart at 30 volumes per second. The authors used a medium/low NA objective lens which was corrected for primary defocus by the ETL. They reported that astigmatism, coma and field curvature restricted the use of the lens to the central region of the field of view and that these aberrations increased towards the limits of the ETL focal range. ETLs in general only provide low-order quadratic primary defocus wavefront correction whereas spherical aberration and higher orders are required to remotely refocus high-NA objectives [1, 120]. The proposed bi-actuator design of a liquid ETL in reference [121] consisting of 2 concentric piezo rings was able to provide simultaneous correction for defocus and spherical aberration. However, more degrees of freedom are required for greater aberration correction of high-NA lenses and in inhomogeneous media. In reference [122], hysteresis associated with the ETLs produced by Optotune was characterised. They report that the hysteresis could be up to 1D of optical power and was dependent on the history of the current applied to refocus the lens.

Their calibration scheme requires driving the ETL back to its minimum or maximum value after applying each focus in order to avoid creep effects. This would complicate the use of this kind of ETL in high speed volumetric imaging.

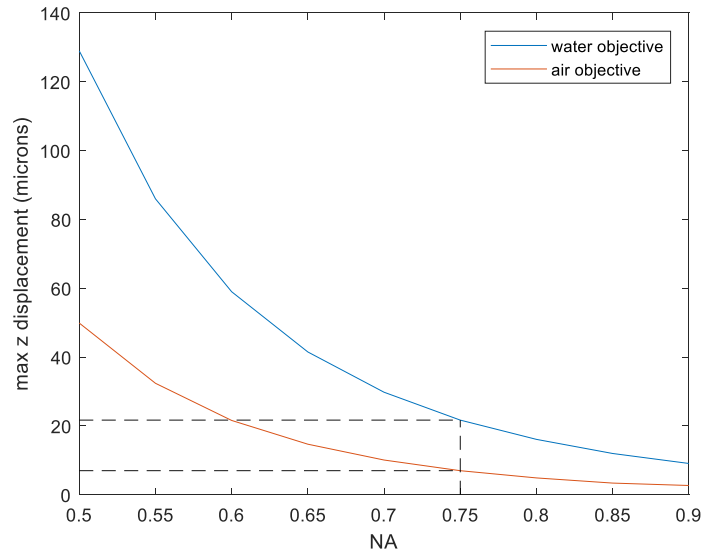


Figure 23 Axial displacement needed for the RMS difference between high-NA defocus and primary defocus to break the diffraction limit for 500 nm wavelength light. This shows the limit of an ETL to correct for high-NA defocus. The dotted line shows the maximum axial displacement for a system with NA=0.75, which was used for this work. The blue curve is for a water immersion objective and the red is for an air objective. Figure reproduced from [134].

Since an ETL generally applies only primary defocus, it is limited in its ability to refocus high-NA lenses. Figure 23 shows a plot of the maximum diffraction-limited refocus that can be achieved as a function of NA when applying only quadratic defocus wavefront correction for water and air immersion media with the Strehl limit calculated for 500 nm wavelength light. Analytic expressions for the optimal amount of primary defocus needed to achieve a given high-NA defocus, the standard deviation of the difference between the optimum primary defocus and the high-NA defocus and also the maximum diffraction-limited defocus that can be achieved with primary defocus correction alone are given in the Appendix. The dashed line in Figure 23 shows that for an NA of 0.75 (which corresponds to the effective NA of the system used in this project), the application of primary defocus alone only allows a diffraction-limited remote refocus distance of 22 μm with a water immersion objective, and only 7 μm with an air objective. This corresponds to diffraction-limited defocus ranges of 44 μm and 14 μm respectively.

The lack of degrees of freedom of control for an ETL limits its usefulness for refocusing a high-NA objective, although it can be usefully used to refocus a low NA objective at high speed. With a correction device with more degrees of freedom it would be possible to correct for high-NA defocus,

system aberrations and also sample-based aberration, as well as providing average corrections to certain field dependent aberrations such as field curvature. Spatial light modulators and deformable mirrors are adaptive optic correction devices which do have a large number of degrees of freedom and can also operate at high speed.

2.6.5 Spatial light modulators (SLM)

Spatial light modulators (SLM) are electro-optical modulation devices which are composed of pixels that can be instructed to change their optical transmission properties [123]. The absorption, phase or retardance of light can be independently changed at each pixel. Typically, they can modify the phase of a wavefront at a rate of 60 to 1400 frames per second, which would be fast enough for video-rate volumetric imaging. SLMs have been used for aberration correction in microscopy [124] as well as super-resolution microscopy techniques such as structured illumination microscopy (SR-SIM) [125] and stimulated emission depletion microscopy (STED), such as the work of Auksoy et al. [126] and also [127, 128].

A common type of SLM is the liquid-crystal SLM where the voltage applied to each pixel results in change in birefringence that can be used to modulate the phase and/or amplitude of the wavefront. Liquid-crystal SLMs are constructed using nematic or smectic types of liquid crystal. In nematic liquid crystals, the ellipsoidal molecules of the liquid crystal material have their centres randomly located throughout the volume whereas in smectic the liquid crystals are arranged in parallel but in layers. It is the ellipsoidal shape of the molecules which causes them to show optical birefringence; the refractive index in the direction of the major axis of the molecule is higher than the minor axis. In the nematic phase, when a sufficient voltage is applied then a dipole moment is induced in the molecule which results in a torque that can change the orientation of the molecules. Thus, the birefringence can be controlled. Typically, the voltage is applied to two glass plates which have been coated with a transparent conductor (for example indium tin oxide), with the liquid crystal layer between them. Application of an electric field can modulate the amplitude, phase or polarization of the incident light.

In order to apply an arbitrary phase to an incident wavefront it is necessary to create a phase-wrapped profile for the SLM – which means dividing the desired optical path into modulo 2π . Errors in the phase profile can be produced by the finite size of the pixels and discontinuities between adjacent pixels.

SLMs can be highly efficient, high-speed, high-fidelity phase-correction devices – however are not as fast as some deformable mirrors. SLMs are also polarization sensitive and operate over a narrow range of wavelengths. Deformable mirrors are achromatic and do not require the additional complexity of phase wrapping.

2.6.6 Deformable Mirrors

Deformable mirrors provide electronic control over the shape of the mirror surface in order to modify the phase of an incident wavefront [3]. The first deformable mirror was proposed by Babcock in 1953 [129] and also introduced the concept of adaptive optics as a way of correcting atmospheric disturbance in astronomy. The design consisted of a thin layer of oil which covered a reflecting mirror. Electric charges were put onto the surface of the film, and electrostatic forces distorted the surface of the oil depending on the charge spatial pattern. This proposed device was slow, sensitive to the environment and operated over a narrow bandwidth.

Generally speaking, deformable mirrors can be divided into 2 groups: segmented mirrors and continuous faceplate mirrors. Segmented mirrors are formed of many flat mirror segments, where each can be moved either with piston alone, or with piston as well as tip and tilt. These segments will change the average phase over the area of each segment. These mirrors are independent of each other, which helps to approximate an arbitrary correction to a wavefront. However, sharp edges between plane segments can result in scattering and diffraction effects. In continuous faceplate mirrors, a thin deformable membrane has its shape adjusted by discrete actuators. The shape of the mirror surface is determined by the positioning and forces from the actuators, and also the shape and elastic properties of the material used to form the faceplate. The advantage of a continuous faceplate is that it allows for a smooth wavefront control.

The key parameters for classifying a deformable mirror are the actuator pitch, actuator mechanical stroke and temporal response. The actuator pitch determines how accurately a particular surface can be applied to the DM. The actuator mechanical stroke determines the amplitude of the wavefront that a DM can correct. The temporal response is of particular importance for developing a microscope capable of video-rate refocusing. Additionally, the DM would ideally be insensitive to environmental conditions such as temperature and humidity. Finally, low-voltage DMs are preferable, as they would reduce the size of cable bundles as well as requiring the control electronics to dissipate less heat.

The development of DM technologies is described in the review article [3]. Military contracts motivated the development of deformable mirrors in the 1970s and were based on the use of ferroelectric (piezoelectric and electrostrictive) materials. These kinds of materials are able to deliver a large amount of force with high accuracy and with a fast response. These were used for bimorph DMs and continuous faceplate stacked array DMs in astronomy. In the 1990s voice coil actuators were introduced to change the shape of the DM. In the late 1990s the development of micro electro-mechanical systems (MEMS) technology led to light-weight, compact and low-voltage DMs that were lower cost due to economies of scale.

Bimorph DMs are made of two wafers of piezoelectric material bonded together with an array of electrodes placed between. The top and bottom of the wafers are connected to ground. A glass plate is attached to the top and bottom surfaces, one is made reflective and the other used to control the temperature dependence of the structure. By changing the voltages of the electrodes in the centre of the structure strain forces from the piezoelectric material can change the profile of the mirror surface. Bimorph DMs are in principle simple however require high driving voltages, have resonances in the range of a few hundred Hz and also experience creep caused by the ferroelectric material.

In a stacked array DM, an array of ferroelectric actuators are attached to a continuous faceplate. The actuators themselves are made of stacks of disks or plates of ferroelectric material with electrodes deposited between each plate. The array of actuators is glued onto the faceplate. Application of a voltage changes the length of the actuator which applies a force to the faceplate – changing its profile. Usually these actuators are driven with a voltage between 0 and 150 V and are capable of producing a 10 μm stroke. They are usually quite stiff structures with a comparatively high first resonant frequency (>10 kHz) and can operate with a fast (ms and higher) response time. An advantage is the flexibility of design and positioning of the actuators in terms of the number and arrangement of the actuators, their large stroke and high accuracy. However, disadvantages are the bulky electronics and the creep associated with ferroelectric materials.

Voice actuator coil DMs consist of a dense array of voice actuator coils attached to a thick metallic plate (cold plate) on one side, which is used to dissipate heat, and a very stable glass plate (reference body) on the other. A thin optical shell (< 2mm thick) has an array of attached permanent shell magnets and this structure floats on the magnetic field created by the actuator coils. This thin shell acts as the deformable mirror. The average distance of the thin shell to the reference body is 50 to 70 μm . Typical response times are of the order of 1 ms, and they can provide excellent accuracy, long-term stability and can have strokes of around 50 μm . The main disadvantages of this kind of device are the high power consumption (2.5 kW), and the brittleness of the structure.

A MEMS-based DM uses technology based on the silicon computer industry (schematics of electrostatic and magnetic based MEMS DMs are shown in Figure 24). Most MEMS deformable mirrors use a thin mirror membrane attached to a flexible support which is moved by electrostatic or magnetic forces. The DMs produced by Boston Micromachines Corporation have a continuous reflective membrane attached to a diaphragm. The profile of the diaphragm is controlled by an electrostatic field produced by electrodes. Another approach is where the reflective surface of the DM is made up of individual segments each supported by 3 pivots; 3 electrodes produce electric fields which allow for tip, tilt and piston of each segment. These electrostatic-field-based DMs require voltages of the order

of 200 V to get a 5 to 8 μm stroke and a response time of 1 ms. Another MEMS DM technology uses a continuous membrane faceplate with attached flexures each with a permanent magnet which are located above magnetic actuators. For DMs which use magnetic fields to deform the membrane, strokes of the order of 50 μm are obtained for 1 V of control voltage. Typically, they have a response time of the order of 1 ms. MEMS technology has led to DMs with thousands of actuators with sub-mm pitch, the latest devices from Boston Micromachines (which use electrostatically driven actuators), have 4092 actuators.

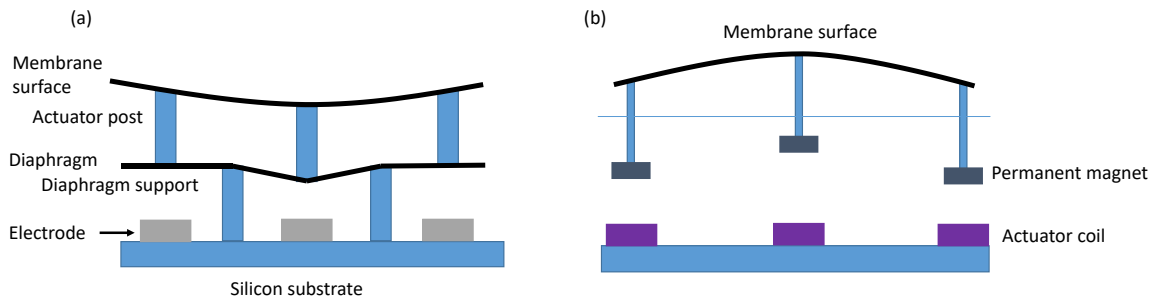


Figure 24 (a) shows a schematic of a MEMS DM based on electrostatic forces, such as sold by Boston Micromachines Corporation. The profile of the diaphragm is changed by the electrostatic field produced by the electrodes. The mirror surface is attached to the diaphragm. (b) shows a schematic of a MEMS DM based on electromagnetic forces such as sold by Alpao and Imagine Optic. The reflective membrane is moved by the forces from the interactions between the actuator coils and permanent magnets.

2.6.7 Choosing the DM

In order to achieve high speed volumetric imaging, the deformable mirror needs to be sufficiently fast. It also needs to provide as large a stroke as possible in order to provide as large a possible refocusing depth range. In the paraxial limit and treating the DM as a spherical mirror where the maximum radius of curvature is determined by the stroke s , the maximum amount of defocus z is given by,

$$z = \frac{4\pi^3}{NA^2} \left(\frac{R_p}{R_{DM}} \right)^2 s \quad eq. 19$$

where R_p and R_{DM} are the radius of the image of the pupil of the objective and DM respectively [7]. Clearly, the radius of the DM pupil should not be smaller than the radius of the objective pupil otherwise light from the image would be lost. Also, if R_{DM} is larger than R_p then parts of the DM surface would not be used hence the best arrangement is when R_p and R_{DM} are equal. Hence, assuming that relay optics can always be chosen to project the pupil of the objective identically onto the DM, then the size of the stroke will determine the degree of refocus.

A second consideration is that a large number of actuators and small pitch between actuators is also desirable in order to be able to correct higher-order aberrations. MEMS DMs can have sub mm pitch

and this suggests the best choice for the high-speed refocusing of an objective is a MEMS continuous membrane mirror DM with magnetic actuators.

The companies Mirao and Alpao both produce deformable mirrors with a high reflectivity (>96.5%) silver coated polymer membrane controlled by electromagnetic actuators with similar prices. The Mirao52e has 52 actuators and is specified to apply a maximum tip/tilt of 50 μm . The Alpao DM97-15 has 97 actuators and a maximum specified tip/tilt of 60 μm . The Mirao52e has a pupil of 15 mm compared to the Alpao DM 97-15 with a diameter of 13.5 mm. If the image of the pupil of the objective is perfectly matched to the pupil of the DM, then the size of the DM pupil is irrelevant; however the Alpao DM will have a greater fidelity due its larger number of actuators and will be able to correct for higher order aberrations. The Alpao also has a larger stroke (comparing tip/tilt for each), and so should be able to refocus the objective to a greater depth. Using influence matrices provided by these manufacturers, simulations of using both the Alpao and Mirao DMs to produce high-NA defocus was performed. The maximum amount of diffraction-limited high-NA defocus, determined by root-mean-square difference between the simulated surface of the mirror and the desired surface for refocusing a Nikon 25x/1.1W objective, was then calculated. The Alpao DM97-15 had a range of $\pm 17 \mu\text{m}$ compared to $\pm 13 \mu\text{m}$ for the Mirao52e. Both mirrors can operate at kHz. Hence, the Alpao DM97-15 was chosen for this project.

2.7 Summary

This chapter has presented background information relevant for the development of a video-rate LSFM using a deformable mirror to refocus the detection optical system. The chapter began with a brief overview of the development of microscope objectives – which showed that they were highly sophisticated and optimized devices – and a discussion of how using them outside of their design conjugate would introduce aberrations to the system. Then, fluorescence microscopy along with various approaches to optical sectioning were described including the main approaches to LSFM. In particular, the lateral resolution of a light-sheet system is determined by the imaging objective. The axial resolution can be parameterized by the PSF axial FWHM, which is determined by both the thickness of the light sheet as well as the axial resolution of the imaging system and also by the FWHM of the optical sectioning response, which is only determined by the thickness of the light sheet. The system used in this project generates its light-sheet by passing a laser beam through a cylindrical lens, so the general features of Gaussian beams were described. The chapter then turned to introduce adaptive optics and described how a defocused high-NA objective produces high-NA defocus which could be corrected by an adaptive optic device in order to remotely refocus the system. Various adaptive optic devices were considered; ETLs, SLMs, DMs. ETLs were shown to be limited as they only

correct for primary defocus – which means they can only effectively be used to refocus low-NA objectives or high-NA objectives through a narrow axial range. Both SLMs and DMs can operate at high-speed however DMs are slightly faster, achromatic and do not require phase wrapping. Out of the different kinds of DM that could be used MEMS magnetic actuator-based DMs offered the largest stroke and could operate with sufficient response time. Finally, the Alpao DM97-15 and the Mirao52e were compared. These devices have similar prices and specifications. It was found through simulation that the Alpao DM97-15 should be able to achieve a larger diffraction limited axial range of defocus – and hence was chosen for this project.

As it turned out, the Alpao DM97-15 suffers from visco-elastic creep as well as thermal hysteresis due to the heat generated by the actuator coils. This is discussed, along with a strategy to deal with these problems in the next chapter. The Mirao52e does not appear to have either of these problems, and in retrospect the Mirao52e might have been a better choice.

Chapter 3 : DM characterisation

3.1 Introduction

This chapter characterises an Alpao DM97-15 membrane deformable mirror (DM) and shows how it can be used to refocus a microscope employing an Olympus 40x/0.85 air objective. A metric – the estimated Strehl ratio – is introduced and is used to characterize the aberrations within the DM refocusing optical setup. This metric is used later on in this work to optimize the shape of the DM in order to achieve a saw-tooth refocus profile at video rates. The DM has 2 forms of hysteresis/creep which can change the response of its actuators to commands; they are visco-elastic creep which has a timescale of 100s of seconds and thermal creep with a timescale of 10s of seconds. These forms of creep are characterised and a strategy is developed to reduce their effects.

3.2 Alpao DM97-15 membrane DM

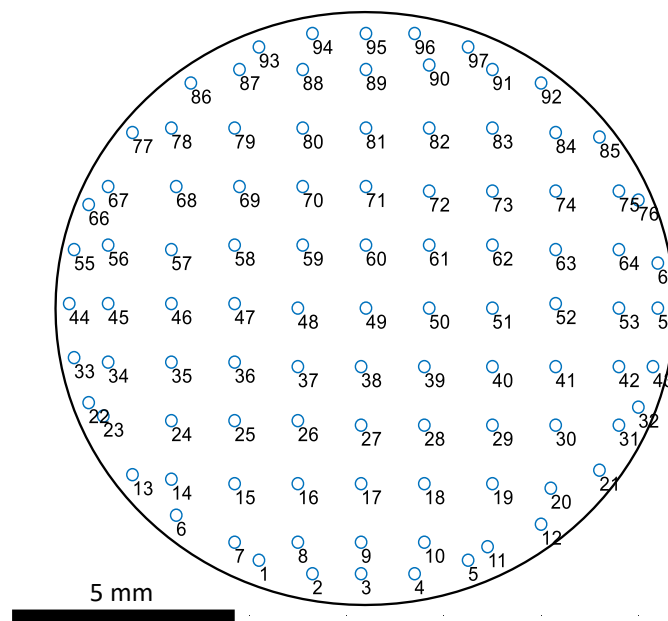


Figure 25 Positions of actuators (labelled by actuator number) on the Alpao DM97-15 membrane deformable mirror.

The Alpao DM97-15 membrane DM is an adaptive optical mirror with a 13.5 mm diameter protected-silver-coated surface with 97 actuators (with an average separation or pitch of 1.5 mm), see Figure 25. It is pinned at the margin which will create an error at the edge if the full aperture is used. In this project the full aperture was not used and the edge effects were not significant. Each actuator applies a force to the flexible surface in order to alter its profile. The maximum stroke of any particular actuator depends on the overall surface being applied to the DM. From the Alpao test report for this

mirror [131] for tip/tilt the maximum actuator stroke is $73.22\text{ }\mu\text{m}$ (PV), and for defocus it is $62.75\text{ }\mu\text{m}$ (PV) and for astigmatism it is $59.89\text{ }\mu\text{m}$ (PV). The report states that this mirror has a settling time (to within $\pm 10\%$ of the steady-state position) of 0.39 ms , hence that it can operate at kHz rates. As shown in Figure 26, each actuator has a magnet associated with it which experiences a force due to current flowing in the actuator coil.

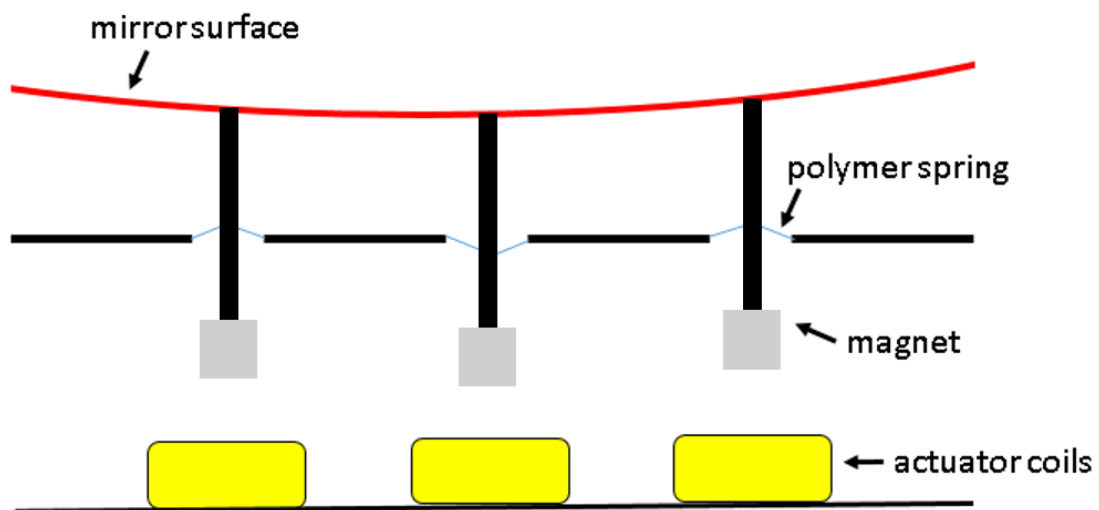


Figure 26 Structure of the Alpao DM97-15. Magnetic forces between the actuator coils and magnet apply a force to a linkage which then applies a push or pull to the silver-coated mirror surface.

The mirror test report also states that the change in mirror surface position is linear with a linearity error measured to be at most 0.34% . Linearity is an important property and means the resulting mirror profile obtained from a set of actuator commands can be obtained by separately adding together the mirror profile resulting from each individual actuator command. This kind of situation can be modelled very conveniently with linear algebra.

Each actuator takes a control signal on the interval -1 to 1 . One could imagine setting each actuator in turn to 1 (leaving the rest at 0), and then capturing mirror's surface profile (e.g. using a Shack Hartman Wavefront Sensor, SHWFS). The spatial profile of the mirror surface height in response to an actuator command of 1 is called the Influence Function for that actuator (Figure 27), and this typically approximates a 2D Gaussian.

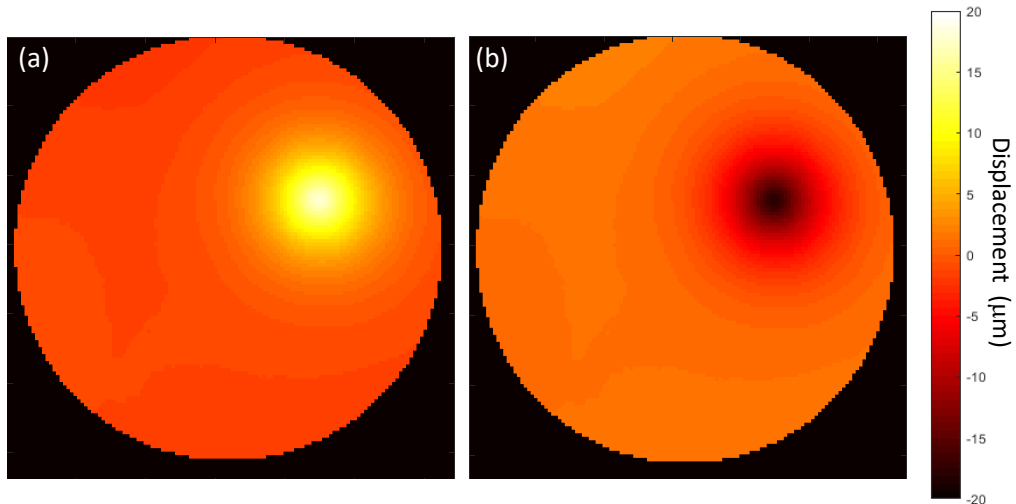


Figure 27 Panel (a) influence function for actuator 60 measured when its command value has been set to 1. Panel (b) The surface profile when actuator 62 is set to -1.

The 2D array of measured surface heights that form the Influence Function can be flattened into a vector associated with each actuator and then all of the resulting vectors packaged into a matrix. The resulting matrix is known as the Influence Matrix (illustrated in Figure 28).

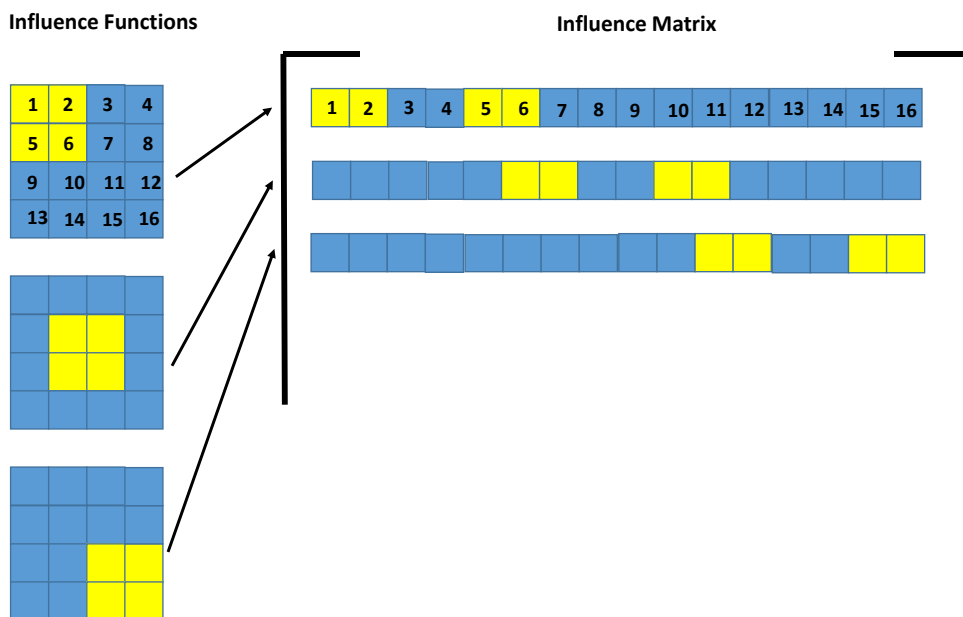


Figure 28 This figure shows a schematic of the influence functions and how they compose to form the influence matrix. Three examples of influence functions are shown on the left. To make an influence function, a command value of 1 is applied to each actuator and an image taken with a Shack Hartmann Wavefront Sensor which for the purposes of this example is assumed to have a 4x4 lenslet array. The map of the surface has been simplified and represented by 2 colours: yellow indicates a high surface and blue indicates no displacement. The location of each actuator is at the centre of each yellow region. Each influence matrix is reorganised into a horizontal vector (the columns of the influence matrix are shown in the top example of influence function). These are then packed to produce the influence matrix.

The response of the mirror to any particular set of commands can be found by scaling each of the influence functions by their respective actuator command value and then summing. Matrix multiplication can perform this procedure very neatly, as shown with Einstein's summation convention by eq. 20 where M is the Influence Matrix, the vector c is the command values associated with each Influence Function and vector s is the estimated resulting surface on the deformable mirror assuming linearity in its behavior.

$$s_j = M_{i,j}c_j \quad eq. 20$$

The inverse of the influence matrix can be used to reverse this procedure and will produce an estimate for command values for a particular mirror surface as shown in eq.21.

$$c_j = (M^{-1})_{j,i}s_i \quad eq. 21$$

The space of surfaces created by adding together linear combinations of the influence functions is a subset of the space of all surfaces, so there is no guarantee of being able to find commands for an arbitrary surface profile. Also, there is no guarantee that these actuator commands obtained by applying the inverse matrix will all be in the interval $[-1 \ 1]$ allowed physically by the mirror, and in many cases they will not. In practice, this method is often acceptable for continuous and differentiable surfaces which do not have too much curvature. The code associated with this project automatically clamps actuator commands within the interval $[-1 \ 1]$. Figure 29 shows the error across the pupil when high-NA defocus is applied to the mirror. It shows the difference between the high-NA defocus function (for an Olympus 40x/0.80W objective with water as the immersion medium) and the mirror surface which has been obtained using the Alpao DM97-15's influence matrix for 50 μm of defocus. The RMS error is well within the diffraction limit. The Figure 29 shows a pattern of error near to each actuator location repeats itself in a similar way across the area of the pupil, with the larger errors

occurring near to the edge of the pupil which is where the high-NA defocus function is largest, and the mirror is pinned at the edge.

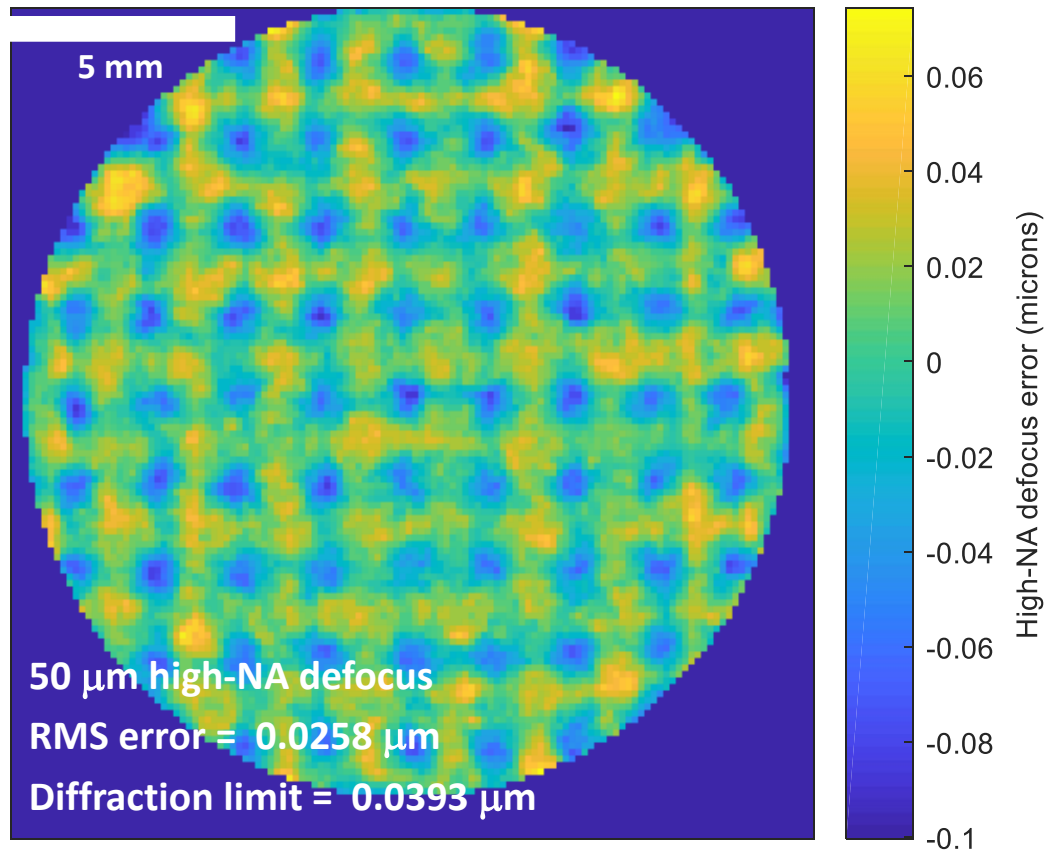


Figure 29 The error between 50 μm of high-NA defocus for an Olympus 40x/0.80W objective and the surface obtained through the manufacturer-supplied Alpao DM 97-15 influence matrix.

Due to the mirror's linear response, the surfaces that the mirror can fit are those that are linear combinations of the influence functions. For surfaces which are not linear combinations the surface which minimizes the root-mean square error would be selected. The clearly structured error in Figure 29 shows that the desired surface is not within the space of surfaces that the mirror can directly reach via linear combinations of the influence functions. The slight non-linear response of the mirror could also be responsible for this error. Figure 30 shows a plot of the RMS error in the surface (left y-axis) with high-NA defocus and also the maximum absolute actuator command value (right y-axis). It shows that the RMS error exceeds the diffraction limit at 88 μm of high-NA defocus. This is despite the actuator commands still being able to provide additional stroke. This shows that there is a limit to the

amount of diffraction limited correction for high-NA defocus that the mirror can provide caused by the fidelity of its representation of the mirror.

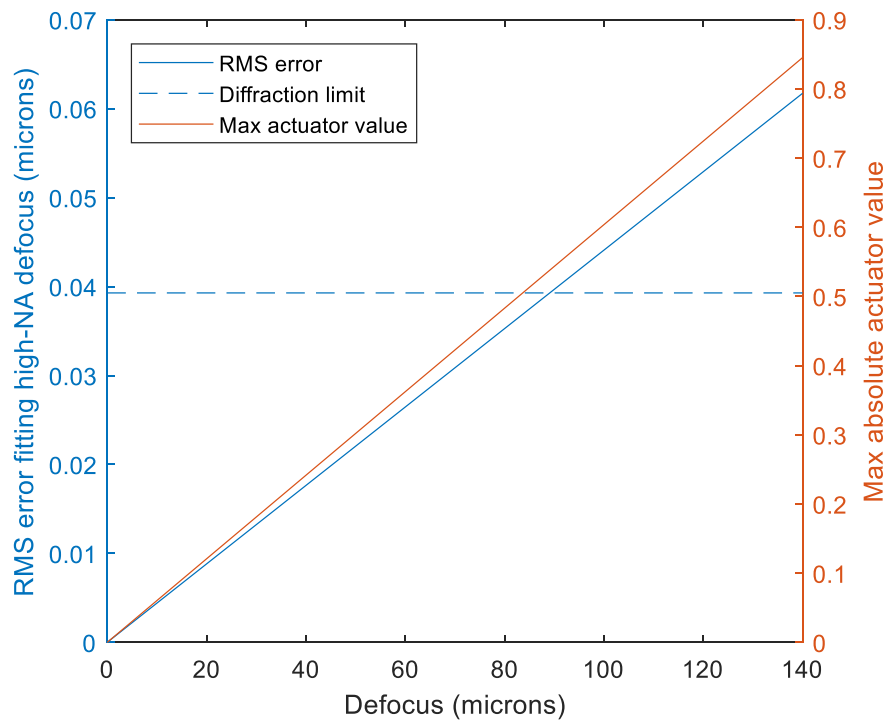


Figure 30 A plot showing the RMS error between the high-NA defocus and the surface obtained using the manufacturer supplied Alpao DM97-15 influence matrix for different amounts of defocus. The plot also shows the maximum absolute command value sent to the mirror's actuators. These values take the values -1 to 1 for an Olympus 40x/0.85 water immersion objective.

As with all matrices, the influence matrix will transform a vector of zeros to a vector of zeros. This is equivalent to the mirror being flat when driven with a set of zeros as actuator commands. However, the mirror does not necessarily adopt a flat shape when every actuator command is set to zero. A set of actuator commands required to flatten the mirror was measured at the Alpao factory, and this will be referred to as the factory flat. When the DM electronic control box is turned on, the factory flat is automatically uploaded and applied to the mirror – and the factory flat cannot subsequently be altered. It was found to be necessary to better flatten the mirror (explained later in this chapter) – as daily temperature variation altered the actuator commands needed to achieve the best flat surface.

3.3 Optical setup for characterising the DM

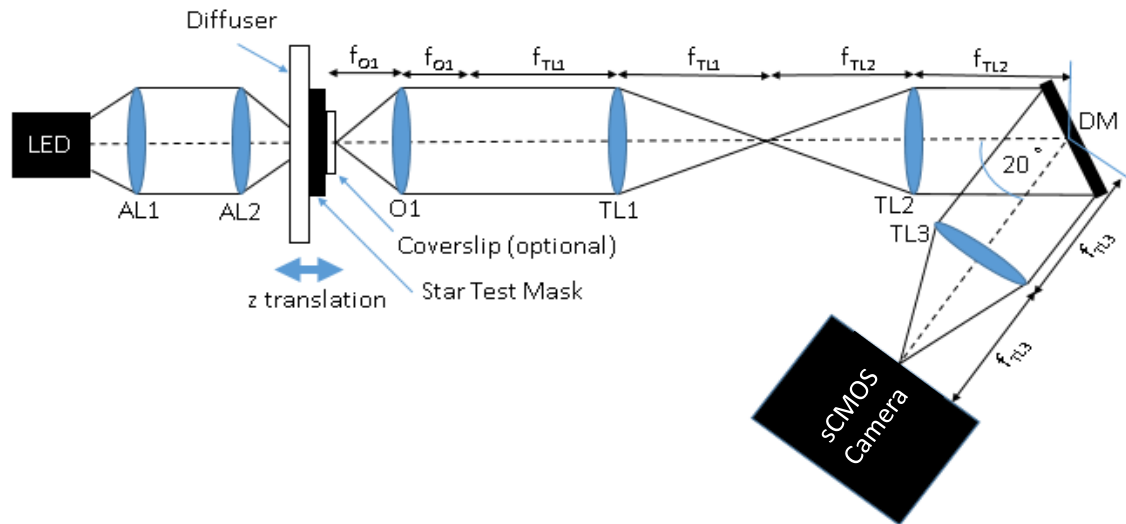


Figure 31 Light from an LED is imaged by asphere lenses AL1 and AL2 onto a Lambertian diffuser which illuminates a star-test mask (STM) consisting of $1\ \mu\text{m}$ holes in a chrome-coated glass slide. Light is then collected by objective O1. The back focal plane of this objective is relayed by tube lenses TL1 and TL2 to the DM which applies a correction for the defocus of the STM. Light is then brought to focus by TL3 onto the sCMOS camera. The position of the STM is adjusted by a motorised stage. Figure reproduced from [134].

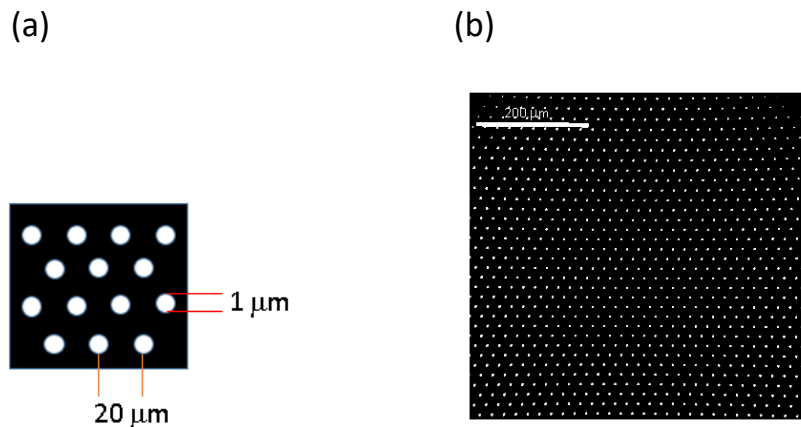


Figure 32 Panel (a) shows a close-up of the Star Test Mask (STM) which consists of $1\ \mu\text{m}$ diameter holes separated by $20\ \mu\text{m}$ gaps in a chrome-coated glass slide. Panel (b) shows a raw image of the STM (brightness enhanced to make the pinholes more visible), the lateral magnification of the system is 22.2x. Figure reproduced from [134].

LED	625 nm	Thorlabs, M625L3
AL1, AL2	Aspheric lenses	Geltech/Thorlabs 320230
Motion controller	Motion controller, to control stage	Newport, ESP 100
Diffuser	Lambertian diffuser	Comar, 50 DO 50
STM	Star Test Mask	JD Photo Data
O1	Olympus 40x/0.85 NA objective	Olympus, 1-UB827
TL1	100 mm tube lens	Thorlabs, TTL100A
TL2, TL3	200 mm tube lens	Thorlabs, TTL200A
DM	Deformable mirror	Alpao, DM97-15
Camera	sCMOS camera	Hamamatsu, OrcaFlash3v4.0

Table 2 A list of components used in the test-rig shown in Figure 31.

The experimental setup developed here is shown in Figure 31 with part/manufacture information shown in Table 2. This was also the setup used in Chapter 4 for the optimisation of the DM surface profile. Light from the 625 nm LED is collected and concentrated by asphere lenses AS1 and AS2 respectively onto a Lambertian opal diffuser. The diffuser illuminates the star-test mask (STM), which acts as the object for the system. The star-test mask is a chrome-coated glass substrate with 1 μm diameter circular holes arranged in a hexagonal lattice with a period of 20 μm , see Figure 32(a). The use of a pinhole to provide a star test pattern to assess aberrations is described in reference [130].

Light transmitted by the star-test mask is collected by objective O1 and its exit pupil is imaged onto the DM by a 4-f relay consisting of TL1 and TL2. The DM (Alpao DM97-15) applied a phase correction to account for the high-NA defocus and TL3 brought the light to a focus on the chip of a sCMOS camera (Hamamatsu, Orca Flash 3v4.0). The DM was angled—rather than it being normal to the incident beam—in order to avoid the additional complexity of installing a beam splitter to separate the incident and reflected light. The axial position of the STM was controlled by a motorised stage (Newport ESP100). During the development of the system the lenses O1, TL1, TL2, TL3 were varied as explained later in the chapter, however the general approach of applying a phase correction to the pupil of the objective via a telescope and then imaging onto the camera remained the same.

3.4 DM scale transformation

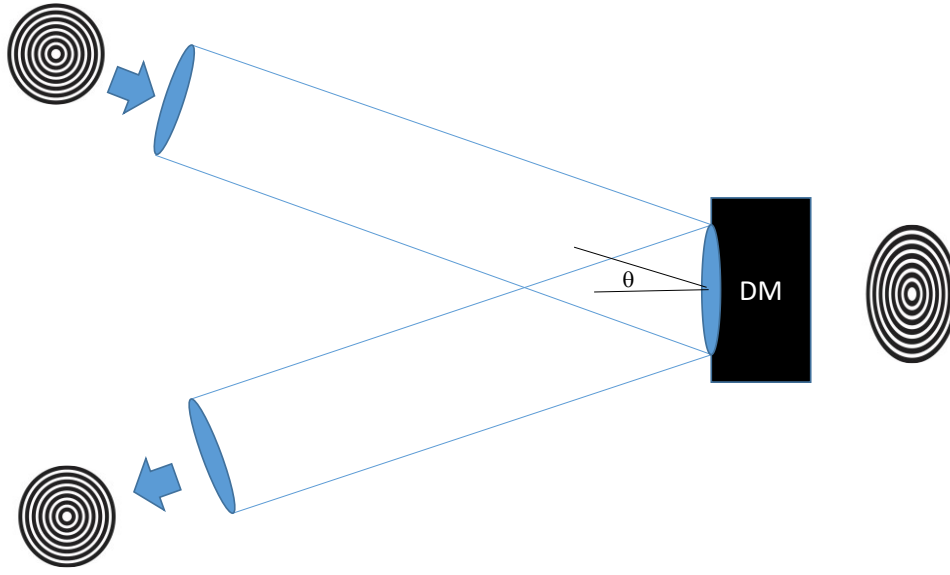


Figure 33 The incident light with a circular cross section intercepts the plane of the DM pupil as an ellipse before reflecting back into a circle. This essentially stretches in one axis in the phase pattern (vertical direction shown in the image) whilst keeping the other the same. To allow for this the pattern applied to the DM needs to be appropriately stretched.

Due to the 20° angle of incidence of the light onto the DM, the incident circular beam intercepts the DM surface as an ellipse and is then reflected back into a circular beam, due to the θ inclination of the optic axis to the normal of the mirror. To account for the angle of the DM, the phase on the DM was scaled by a factor of $1/\cos(\theta)$ in the plane parallel to that of the optical system. This is illustrated in Figure 33.

3.5 Alignment of the optical axis of the beam with the centre of the DM

If the centre of the DM is misaligned with the optical axis of the system, then the desired variation in OPL will not be applied to the correct parts of the pupil. First consider the case where there is no misalignment. For convenience, consider an objective of $NA = \frac{1}{\sqrt{2}} = 0.707$. The expression for high-NA defocus for $1\ \mu\text{m}$, for the objective used in air, is then given by,

$$OPL = \sqrt{1 - \frac{1}{2}(x^2 + y^2)} \quad eq. 22$$

This can be approximated by the first few terms of a Taylor series with powers of $r^2 = x^2 + y^2$ as,

$$OPL = 1 - \frac{1}{4}x^2 - \frac{1}{4}y^2 - \frac{1}{32}(x^2 + y^2)^2 + \dots \quad eq. 23$$

If this function is applied to the DM and the centre of the DM is aligned with the optical axis, then this will correct for high-NA defocus and will refocus the objective without introducing additional aberrations. If instead the centre of the DM is displaced by x relative to the optical axis by a small amount, say 0.1 (in the units of x), then a displaced correction would be applied at the pupil of O1. This would amount to,

$$\text{OPL} = \sqrt{1 - \frac{1}{2}((x - 0.1)^2 + y^2)} \quad \text{eq. 24}$$

The first few terms of the Taylor expansion for this expression are

$$\begin{aligned} \text{OPL} = & 0.997 + 0.0501x - 0.252x^2 - 0.251y^2 + 0.0126xy^2 + 0.0127x^3 - 0.0324x^4 - 0.0639x^2y^2 \\ & - 0.0315y^4 + 0.00483x^5 + 0.00475xy^4 + 0.00957x^3y^2 + \dots \quad \text{eq. 25} \end{aligned}$$

The introduction of the displacement has caused unwanted terms with odd powers to appear in the expansion and therefore the required phase correction applied at the pupil of O1.

The same can be seen when applying a Zernike expansion to a displaced high-NA defocus pattern. In Figure 34 (a), where the centre of the DM is aligned with the optical axis of the system, in the first 20 modes (OSA labelling) only modes 4 and 12 are significant – and these correspond to defocus and primary spherical aberration. When a displacement of the optical axis by 10% is introduced, the plot of Zernike mode amplitudes, see Figure 34 (b), shows a different picture. In particular, mode 7, which corresponds to vertical coma, is introduced. The introduction of unwanted additional Zernike modes will mean that a greater number of modes will need to be measured and optimized at each stage of the optimization of the mirror shape.

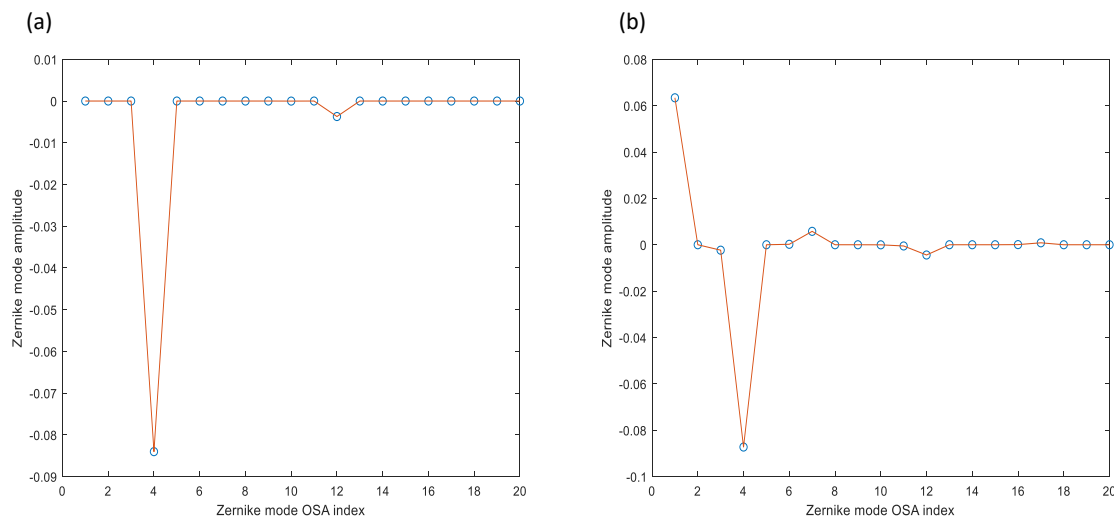


Figure 34 Panel (a) shows the Zernike terms (OSA indexing) for a centred high-NA defocus pattern. Panel (b) shows the Zernike expansion when the pattern is slightly displaced.

Ideally, an engineering solution would be used to ensure that the centre of the DM was aligned with the axis of the optical system, however as we were not able to achieve this in the timescale of the project, a software approach was used. The procedure involved applying $8\text{ }\mu\text{m}$ of high-NA defocus to the mirror and then taking an image of the star-test mask. This was followed by applying $-8\text{ }\mu\text{m}$ of high-NA defocus and the capture a second image of the star-test mask. Even though some defocus had been applied, the lateral shift in position of the centre of mass of the central pinhole in the star-test mask could be determined. If the DM is not aligned with the optical axis, then the high-NA defocus will produce an average tilt which has the effect of displacing the image of the pinhole. Changing the sign of the defocus changes the displacement of the pinhole. The displacement of the centre of mass of the pinhole as the high-NA defocus was changed from $8\text{ }\mu\text{m}$ to $-8\text{ }\mu\text{m}$ was taken to be an indication of the degree to which the optic axis was misaligned with the centre of the applied high-NA defocus surface, Figure 35.

Different amounts of lateral shift (labelled here as the x and y directions) were then applied to the high-NA defocus surface in the form of a grid search, and the corresponding displacement of the pinholes found for each shift. The x and y displacements that produced the minimal movement of the pinhole were taken to be the best estimate for the location of the optic axis on the DM. An exemplar set of data obtained from this procedure is shown in Figure 36.

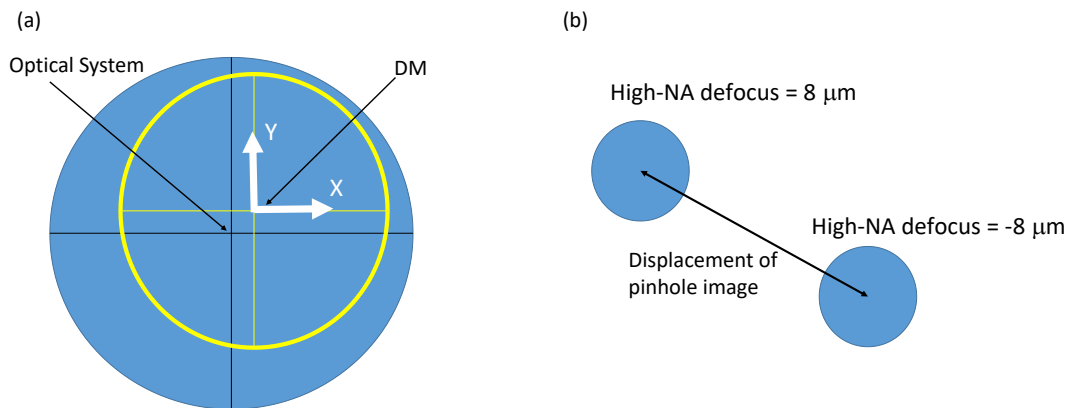


Figure 35 Panel (a) shows the pupil of O1 (larger blue filled circle) overlaid with the image of the aperture of the DM (smaller yellow unfilled circle). The pattern applied to the DM needs to be shifted so that the centre of the pattern lies on the centre of the optical system rather than the centre of the DM. Panel (b) shows a schematic of the image of a single star-test mask star in image space. If a high-NA defocus of $8\text{ }\mu\text{m}$ and then $-8\text{ }\mu\text{m}$ is applied to the DM the result is that the pinholes will displace by an amount which grows larger the more the DM is misaligned from the optical axis.

The displacement needed to minimize the shift of the STM on the application of defocus changed each time the optical setup was realigned.

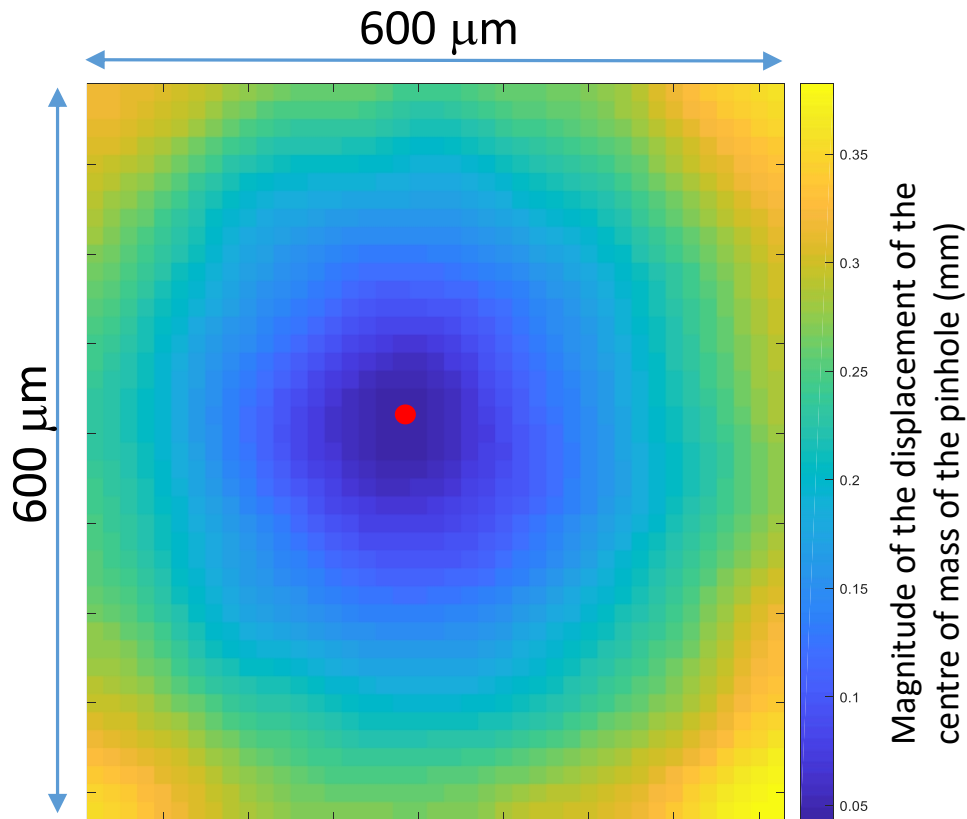


Figure 36 Displacement of the central pinhole as $8\ \mu\text{m}$ and then $-8\ \mu\text{m}$ of high-NA defocus is added to the DM. When the displacement is minimised then the centre of the pattern of high-NA defocus applied to the mirror should be very close to the position of the optical axis. Hence the procedure describe determines the position of the optical axis on the DM.

3.6 Strehl ratio

The Strehl ratio can be used to distinguish between those systems which can be regarded as being limited by diffraction to those which are aberration limited. The Strehl ratio as developed by Karl Strehl can be found by dividing the value of the on-axis intensity of the PSF of the optical system with the on-axis intensity of the PSF of the system that would be obtained if the system was limited only by diffraction [8]. A system is regarded as diffraction limited if the Strehl ratio is greater than 0.8 and is aberration limited otherwise. This limiting condition can also be expressed in terms of the RMS of the wavefront aberration: if the RMS wavefront aberration is larger than $\lambda/14$ then the system is aberration limited (derived in the Appendix). The definition of the Strehl ratio can be applied to consider the image of a point-like object at a particular position in the image field and the Strehl ratio can therefore be measured for many points in the image field.

3.7 Estimating the background

Estimation of the Strehl ratio depends to a very great extent on a good estimation of the background light in the image. The background light associated with each pinhole was found from regions of the image that should be darkest, i.e. those pixels furthest from the pinholes. For the STM employed in this work, the mean background for each pinhole was therefore estimated from an annulus of pixels centred on each pinhole with a radius equal to half of the inter-pinhole spacing and with an annulus thickness of 5 pixels. For very aberrated pinholes, light from the pinhole may spread out into the annulus of pixels used to determine the background and so create an erroneous estimate of the background. However, this bias will be greatest for aberrated pinholes images and least for unaberrated pinhole images. Therefore, this approach is valid provided the images of the pinholes are reasonably well focused. Figure 37 (a) shows the annuli used for the background estimation and (b) shows the estimate of background over the field of view.

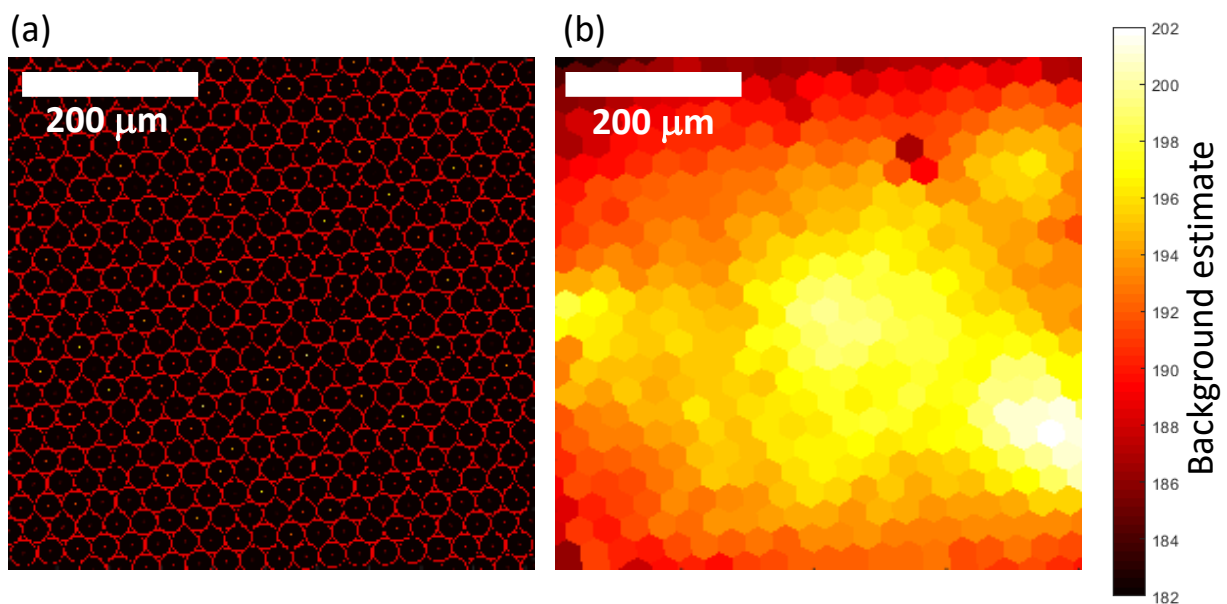


Figure 37 Panel (a) shows the annulus of pixels around each pinhole used to estimate the background. Panel (b) shows a map of background estimates over for field of view, where each hexagon corresponds to the background estimate associated with each pinhole.

3.8 Estimated Strehl ratio

The refocusing system needs to be able create as large as possible a volume over which a diffraction-limited image can be obtained. An estimate of the Strehl ratio was made for each pinhole and this value assigned to the pixels nearest to that pinhole in the form of a Voronoi diagram, to create a Strehl map. These Strehl maps could be used to assess aberrations across the field and were used in the DM optimisation procedure. Initially, the local background was obtained from the procedure described in the previous section and it was subtracted from the image. Next the positions of the centre of the

pinholes were found using the k-means algorithm [132]. This is a clustering algorithm which will group similar pixels together, in this case the pixels associated with the pinholes. The centroid of each group was taken to be the location of the centre of the pinhole. This algorithm allowed the system to automatically adapt to the changes in the position of the pinholes in the image, for example due to non-telecentric behavior and also aberrations such as distortion. With the position of the pinholes known, an estimate of the transverse magnification was made by finding the mean separation between the pinholes in the image.

For the wavelength of the LED (625 nm), the estimated transverse magnification and also the NA of the system (which was limited by the pupil of the DM to be 0.75) permitted an estimate of the theoretical PSF of the system to be calculated from the Fourier transform of the pupil [123 and also described in the Appendix].

Under the assumption of spatial incoherence, convolution between the theoretical PSF and the top-hat function of diameter 1 μm provided an estimate of the image of one pinhole in the star-test mask if the optical system was limited by diffraction alone. This image was then binned into rectangles of the same size as the pixels on the Hamamatsu Orca Flash camera, i.e. $6.5 \times 6.5 \mu\text{m}$. The resulting image was what would be expected if there was only diffraction and there were no aberrations in the system (as well as no significant shot noise and readout noise).

The Strehl ratio was then estimated for each pinhole using the following procedure. First, pixels within a circle with a radius of half the inter-pinhole spacing were selected for each pinhole, see blue circle in Figure 38 (a). Second, the *normalised maximum pixel value* for each pinhole was found by dividing the maximum pixel value within each circle by the sum of all pixel values within the circle. A Strehl metric was then estimated by dividing the normalised maximum pixel value by the theoretical diffraction-limited value for the normalised maximum pixel value in the absence of any aberration, which was calculated from the theoretical image described above. Finally, the Strehl metric for each pixel was displayed on a map (Voronoi diagram), where each hexagon corresponds to a specific pinhole; the Strehl metric for the pinhole marked with a blue circle in Figure 38 (a) is shown by the false-colour of the hexagon identified with a blue circle in Figure 38 (b).

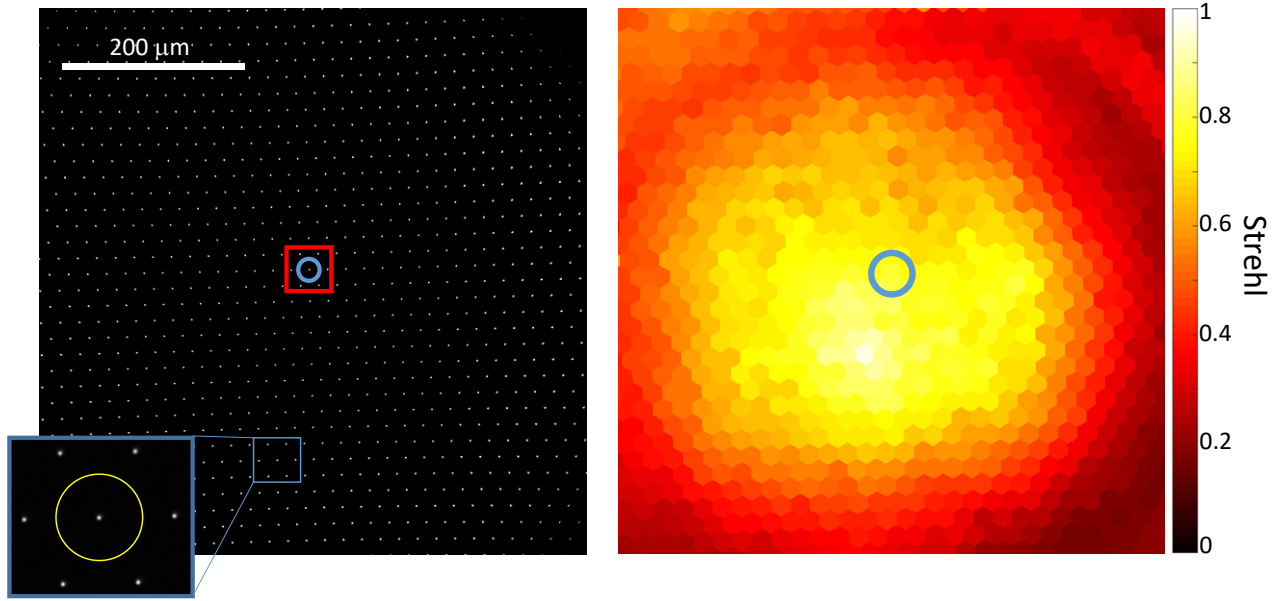


Figure 38 Example raw image of the star-test mask (the contrast of the image has been increased to improve visibility of the pinhole images) recorded with the star-test mask in the focal plane of the 40x/0.85 NA air objective. The inset shows a zoomed-in region of the pinhole within the blue square. The yellow circle in the inset shows the circular bounding area around that pinhole. The perimeter of the yellow circle was used to find the local level of background light in the image for that pinhole and the values within the yellow circle were used to estimate the Strehl ratio. (b) False-colour Strehl map where each hexagon shows the Strehl metric calculated for a particular pinhole. The estimate for the Strehl ratio for the pinhole inside the blue circle in (a) is reported by the hexagon in the blue circle in (b). Figure reproduced from [134].

The Strehl ratio is a comparison of the intensity of an aberrated image of a point object with an image of a point object limited by diffraction alone. However, the pinholes in the star-test mask employed were not true point objects and had a diameter of 1 μm . To check that the finite diameter of the star-test mask pinholes did not affect the measurement of the Strehl ratio, a simulation was carried out. The optical system was modelled as a 4-f system consisting of an objective and tube lens. The focal length of the first lens was taken to be that of the 40x/0.85 Olympus air objective ($f = 4.5 \text{ mm}$). The pupil in the Fourier plane was determined by the NA of the system, which yielded a diameter of 7.65 mm. The focal length of the second lens was taken to be 180 mm resulting in an optical system with a lateral magnification of 40x. To simulate the effects of aberrations, a random wavefront aberration function, $W(x, y)$ was introduced that consisted of a matrix of values drawn from the normal distribution $N(0, \sigma^2)$, where σ was the RMS wavefront error; and then the phase (aberration) of the pupil was then taken to be e^{ikW} . The value of the RMS wavefront error was increased and the Strehl ratio estimated from the intensity PSF alone (without convolution with pinhole) as well as the Strehl ratio estimated when including convolution with the pinhole. The results are shown in Figure 39. The estimate for the Strehl ratio including convolution with the pinhole is at most 6% above the true value based on the PSF. The difference is below 2% for Strehl ratios above 0.5. Therefore, the

Strehl ratio measured using the approach described here was taken to be a reasonable estimate of the actual Strehl ratio.

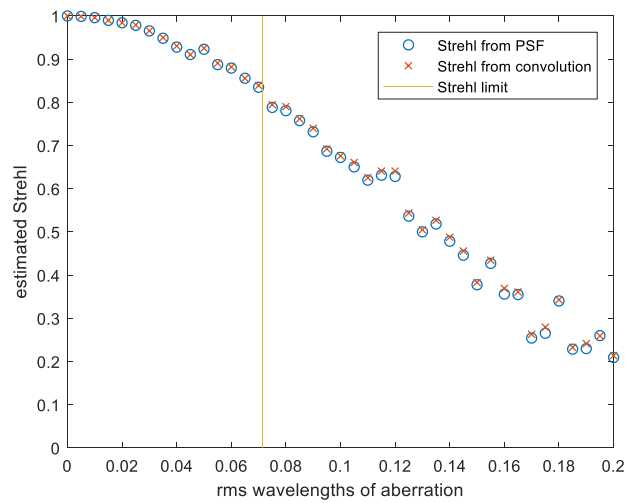


Figure 39 Plot comparing the results of simulations where the estimated Strehl ratio obtained from a point source (blue circles) is compared with an estimate obtained from simulated images of 1 micron pinholes (red crosses).

The Strehl ratio should be independent of the intensity of the light source used. To check this, experimental data was obtained with the star-test mask in a constant position with respect to O1 but with different LED drive currents. Figure 40 shows that the resulting Strehl estimates were independent of the brightness of the LED for drive currents above 0.1 A. For small drive currents the poor S/N can affect the reduce the estimate for the Strehl ratio. In order to maximize the illumination of the STM the drive current was set to 1.1 A.

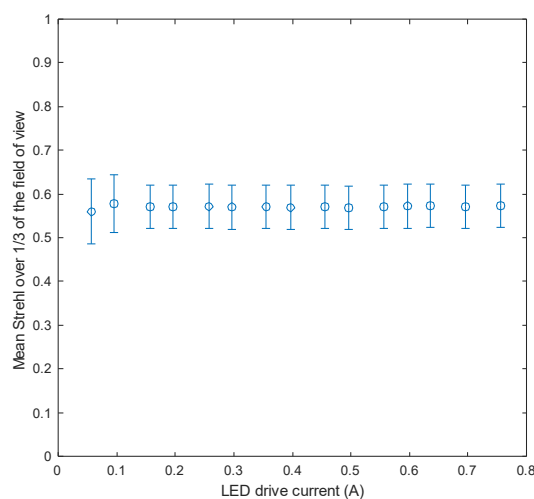


Figure 40 Plot showing that the Mean Strehl across the central third of the Field of View is independent of the LED drive current (error bars taken over 2 sets of results).

3.9 Assessment of aberrations through the system

Ideally, we would want the optical system to be as close as possible to diffraction limited so that the available stroke of the DM could be used to refocus the objective and to correct for sample aberrations rather than correct for system aberrations.

The system shown in Figure 31, was progressively set up, one optical element at a time, in order to analyse the accumulation of aberrations and a Strehl map produced at each stage. Initially the system was set up using achromatic doublets for the imaging and relay lenses and afterwards better corrected tube lenses were used. For each configuration of lenses the STM was moved from -5 to 5 μm in steps of 0.5 μm with a Strehl map obtained for each step. A maximum Strehl projection was then obtained for this stack which should be relatively unaffected by tip/tilt, defocus, field curvature, and distortion. These maximum Strehl maps were used to compare the accumulation of optical aberrations as the system was progressively constructed.

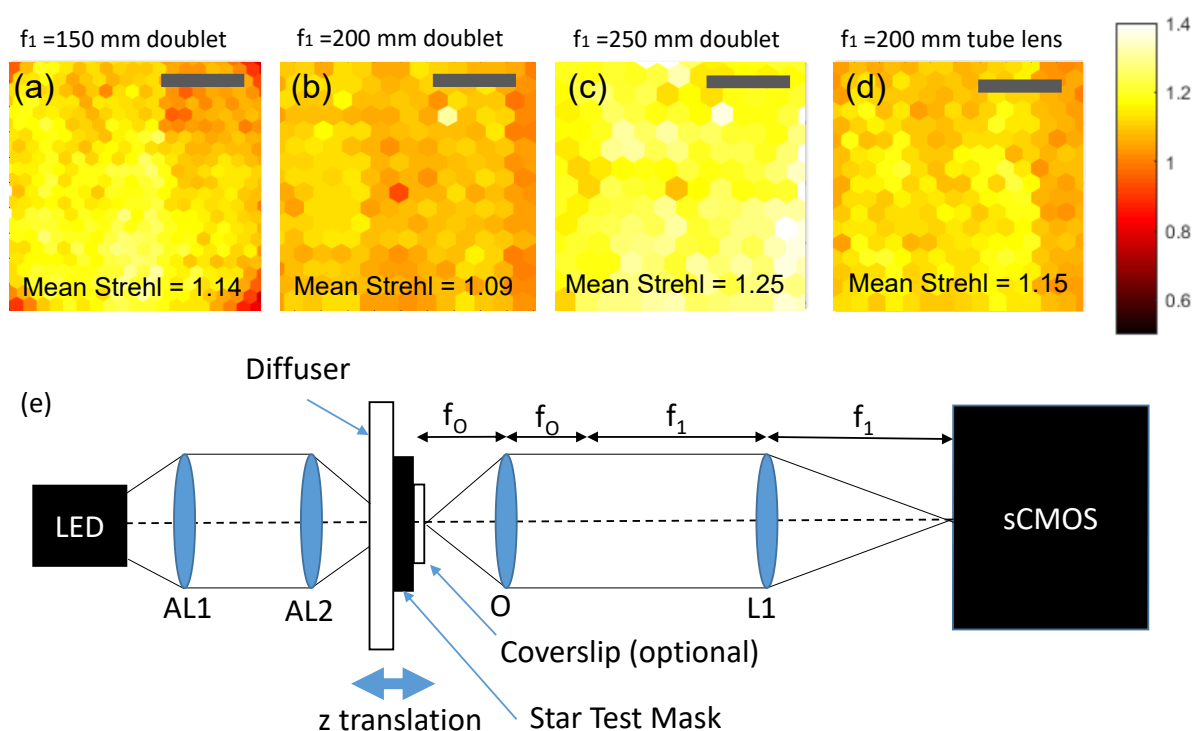


Figure 41 The STM was imaged by the objective (O which was an Olympus 40x/0.85) and L1 (150, 200, 250 mm achromatic doublet), onto the camera. The Strehl maps are shown (a), (b), (c). Then L1 was replaced with a 200 mm tube lens and the Strehl maps shown in (d). Mean Strehl is the mean of the Strehl ratios across the full field of view. The scale bar is 200 μm .

Olympus 40x/0.85NA objective	Olympus, 1-UB827
100 mm achromatic doublet	Thorlabs AC 254-100-A-ML
150 mm achromatic doublet	Thorlabs AC 254-150-A-ML
200 mm achromatic doublet	Thorlabs AC 254-200-A-ML
200 mm tube lens	Thorlabs TTL200A
sCMOS camera	Hamamatsu, OrcaFlash3v4.0

Table 3 Components used in Figure 41, where the objective is used with a single lens.

Initially the system consisted of an Olympus 40x/0.85 objective with a single lens to create an image of the STM on the camera as shown in Figure 41 and Table 3. In a first characterization step, achromatic doublets were used to create an image of the STM onto the camera. Next, the achromatic doublet was replaced with a better-corrected tube lens. The Strehl maps in Figure 41 show diffraction-limited performance across the field of view, with (a), (b), (c) showing the results for 150, 200, 250 mm doublets, and (d) showing a 200 mm tube lens. The fact that the estimated Strehl ratio is greater than 1 is likely due to tolerances in the estimate, such as the variation in diameter of the pinholes, and variation in magnification over the field of view. Sensitivity analysis shows that a 0.05 μm change in the radius of the pinhole would result in a change of 0.2 in the mean Strehl over the field of view. Also repeat measurements showed that typically the mean Strehl value across the field of view had a random error of 0.1. Despite these inadequacies, this estimate of the Strehl ratio along with the Strehl maps was still useful for contrasting the extra aberrations introduced by successive optical components.

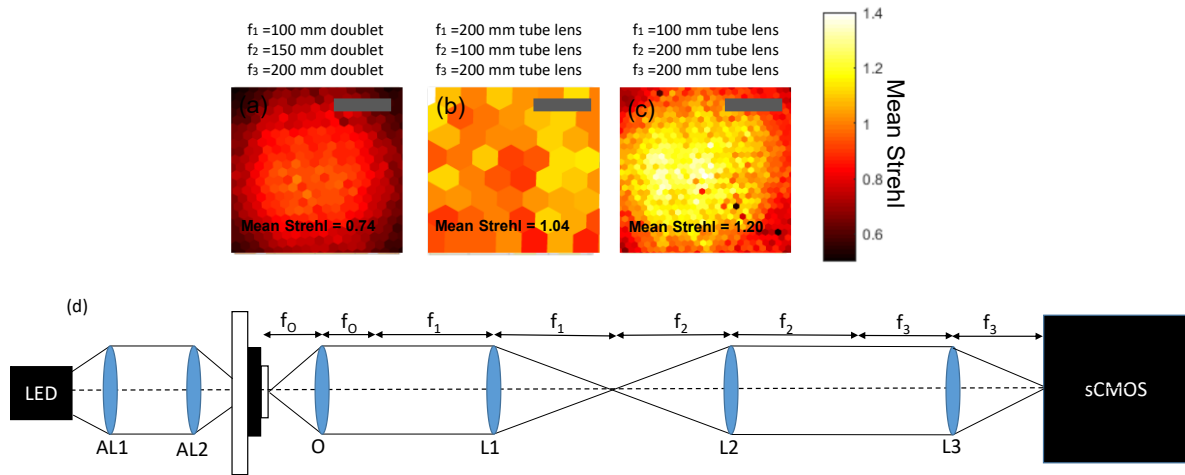


Figure 42 The STM was imaged by the objective (O which was an Olympus 40x/0.85) which produces an intermediate image by L1 which is the relayed to the camera by L2 and L3. This is equivalent to regarding L1 and L2 as producing an intermediate image of the pupil of the objective which is then imaged by L3. Initially L1,2,3 were achromatic doublets with focal lengths 100, 150, 200 mm, with the resulting Strehl map (a). These were replaced with tube lenses, initially 200, 100, 200 mm with Strehl map (b) and then 100, 200, 200 mm with Strehl map (c). Mean Strehl is the mean of the Strehl ratios across the full field of view. The scale-bar is 200 μm .

Olympus 40x/0.85NA objective	Olympus, 1-UB827
100 mm achromatic doublet	Thorlabs AC 254-100-A-ML
150 mm achromatic doublet	Thorlabs AC 254-150-A-ML
200 mm achromatic doublet	Thorlabs AC 254-200-A-ML
100 mm tube lens	Thorlabs TTL100A tube lens
200 mm tube lens	Thorlabs TTL200A tube lens
sCMOS camera	Hamamatsu, OrcaFlash3v4.0

Table 4 Components used in Figure 42 which use lenses L1 and L2 to make an intermediate image of the pupil, which is then images onto the sCMOS camera by L3.

Next, the pupil of the objective lens was relayed via 2 lenses to form an intermediate image (where later a phase correction would be applied by a DM), which was then imaged by another lens onto the camera as shown in Figure 42. Initially the 3 lenses were achromatic doublets, which were later replaced with better corrected tube lenses. With three doublets Figure 42 (a) shows a reduced diffraction limited field and (b) and (c) shows an increase in diffraction-limited performance with tube lenses purchased from Thorlabs.

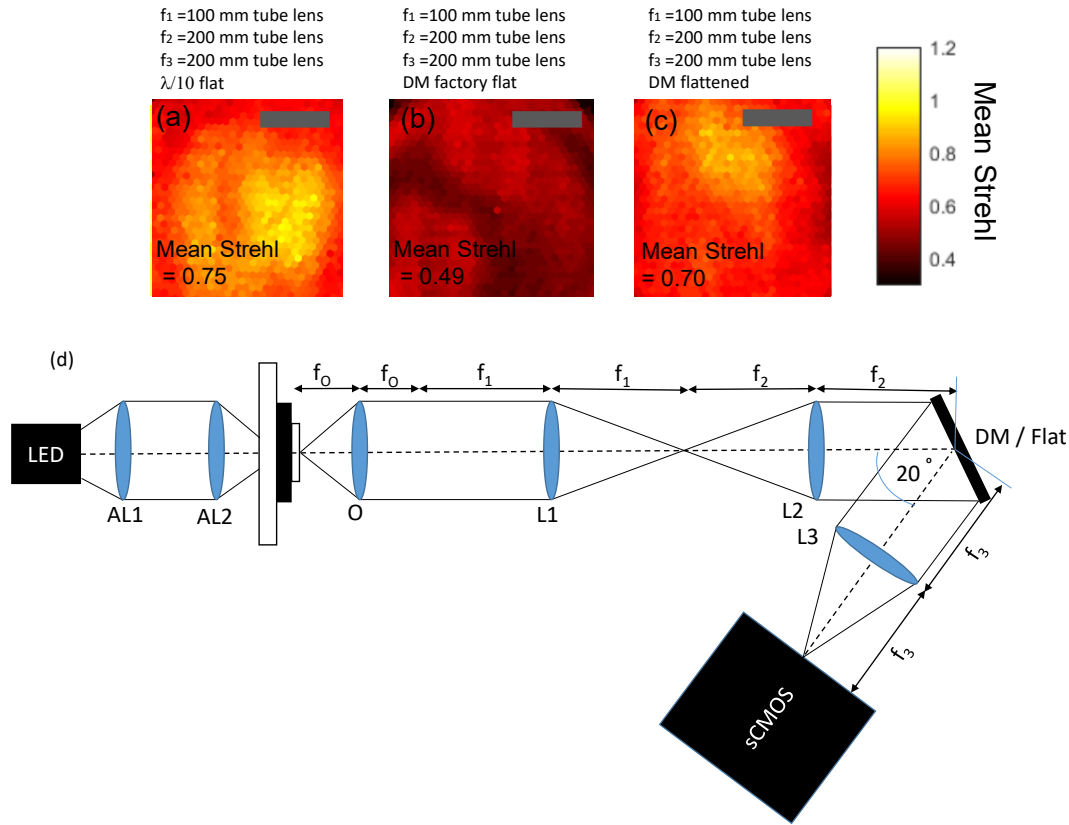


Figure 43 Light from the STM was collected by the objective (O which was an Olympus 40x/0.85). L1 and L2 imaged the pupil of the objective onto either a $\lambda/10$ flat dielectric mirror or the DM, which folded the optical axis through 20 degrees. The image of the pupil was imaged by L3. The system schematic is shown in (d) which is the same as Figure 7 and is used in chapter 4 as a test rig. The Strehl map for the $\lambda/10$ flat is shown in (a), the results for the factory flat DM is shown in (b) and for the DM after being flattened using the Shack Hartman wavefront sensor is shown in (c). The mean Strehl is the mean of the Strehl ratios across the full field of view. The scale-bar is 200 μm . The components and manufacturers are shown in Table 2.

Next, a $\lambda/10$ flat dielectric mirror or a DM was placed at the image of the pupil of the objective and the system was folded through 20° as shown by the schematic in Figure 43. The Strehl map for the $\lambda/10$ flat dielectric mirror shows a diffraction limited performance across the field of view and is comparable to the case of Figure 42 (c), indicating that the flat mirror and additional mechanical alignment did not add more aberrations to the system. In Figure 43 (b) shows the $\lambda/10$ flat dielectric mirror replaced with the DM set to the factory flat (which is where the DM is on and a set of zeros sent as commands to each actuator). There is a deterioration in performance showing that the DM is not acceptably flat. If the DM is not flat then any profile applied to the mirror surface (eg a Zernike mode), will result in an error of the order of the (factory flat - true flat). Hence it was necessary to develop a method to properly flatten the DM. This involved using a Shack Hartman wavefront sensor to physically measure the surface of the mirror and is described in the next sections. The results of the flattened DM are shown in (c) and are better than (b) but still worse than (a). That said the results show a diffraction-limited performance across the central third of the field of view.

3.10 Flattening the mirror with a Shack Hartman wavefront sensor

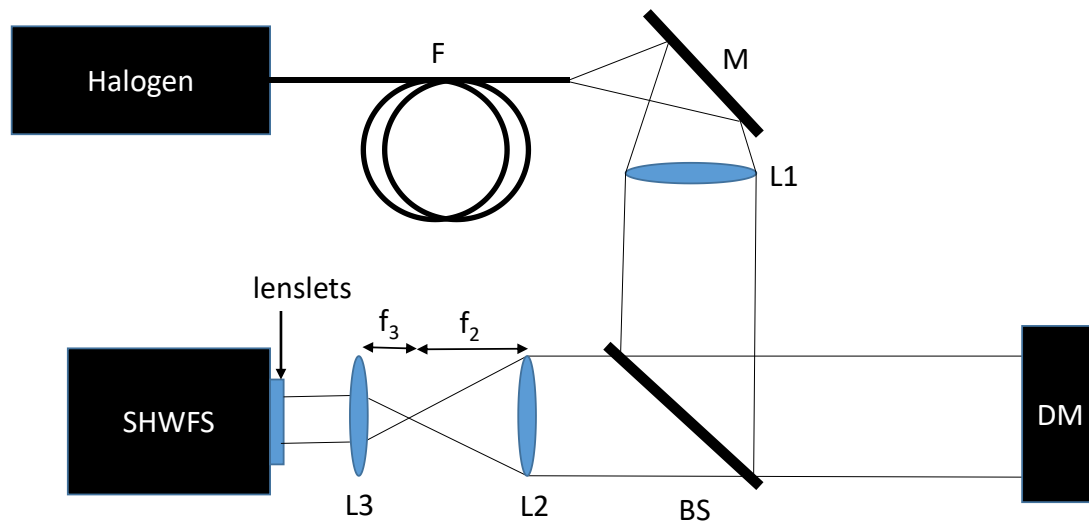


Figure 44 Shack Hartman wavefront sensor (SHWFS) setup for flattening the DM. White light from the halogen light source is coupled into the fibre F and then reflected by the broadband dielectric mirror M where it is then collimated by achromatic doublet L1 and then reflected by the non-polarising beam splitter BS to the DM. The light is reflected back to the BS and then passes through the de-magnifying telescope made of L2 and L3 and then reaches the SHWFS.

A Shack Hartman wavefront sensor, as shown in Figure 44, was added to the system in order to directly measure the surface profile of the deformable mirror. A halogen white-light source (6.7 mW) was coupled into multi-mode fibre (F, 400 μm 0.48NA) and then reflected through 90 deg. by a broadband dielectric mirror (M) where it was collimated by the achromatic doublet (L1). The collimated beam was reflected from a non-polarising beam splitter (BS) towards the deformable mirror (DM). The beam was aligned to be normal to the DM. The plane wavefronts of the collimated beam picked up the surface profile of the DM and it was reflected back towards and passed through the non-polarising beam splitter (BS). The beam was de-magnified by a factor of x4 from the telescope made up of L2 ($f=200$ mm) and L3 ($f=50$ mm). The wavefront before the lenslets was aligned to be conjugate to the surface of the DM. This was done by ensuring that a hex wrench placed directly across the pupil of the DM produced a sharp image on the Shack Hartman wavefront sensor. In this way the phase of the measured wavefront (allowing for double pass) is proportional to the surface profile of the deformable mirror.

L1	200 mm achromatic doublet	Thorlabs AC254-200-A-ML
L2	200 mm achromatic doublet	Thorlabs AC254-200-A-ML
L3	50 mm achromatic doublet	Thorlabs AC254-050-A-ML
BS	50:50 non-polarising beam splitter	Thorlabs CCM1-BS013/M
M	Broadband dielectric mirror	Thorlabs BB1-EOL
DM	Deformable mirror	AlpaoDM97-15
SHWFS	Shack Hartman Wavefront Sensor	Imagine Optic HAS04VIS
F	400 μm 0.48 NA step index fibre	FT030
Halogen	Halogen light source	OceanOptics HL-2000-FHSA

Table 5 Component list for setup shown in Figure 44.

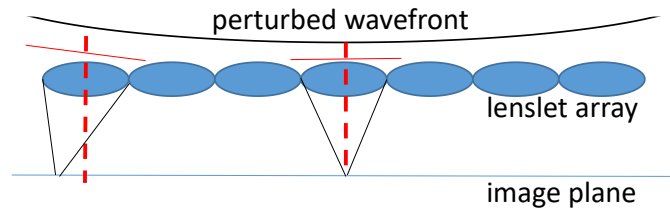


Figure 45 Schematic of a Shack Hartman wavefront sensor (SHWFS). The perturbed wavefront is sampled by the lenslet array. For a slightly perturbed wavefront, the wavefront is approximately planar at each lenslet. These microlenses focus the wavefront to a spot (which is an image of the fibre), which is displaced by an amount related to the tilt of the wavefront. Hence each lenslet produces an estimate of the local tilt of the wavefront and the results from all lenslets can then be integrated to give an estimate of the wavefront itself.

A Shack Hartman wavefront sensor consists of a grid of microlenses which sample the wavefront as shown in Figure 45. An example of the raw image acquired is shown in Figure 46. For slightly perturbed wavefronts, the wavefront is approximately planar in the vicinity of each microlens. The tilt of the wavefront can be found by the displacement of the focal spot produced by each lenslet. These wavefront gradients can then be integrated in order to infer the phase profile of the wavefront. The SHWFS was initially aligned by adding Thorlabs cage rods to the BS with a $\lambda/10$ flat placed at the end such that it was normal to the optical axis and also in the same location as the DM. This flat mirror would reflect the collimated light back to the sensor. The reconstructed surface was then used as a reference in order to flatten the DM.

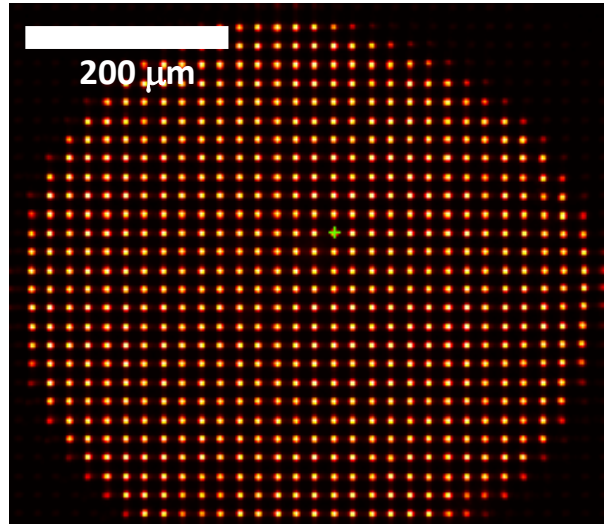


Figure 46 Raw image taken from the SHWFS showing the spots corresponding to each microlens (spatial sampling of 110 μm).

Figure 47 (a) and (b) show examples of the typical examples of the inferred DM mirror surface. These images were of the factory flat taken at the same time on two consecutive days. In each case the DM control box was switched on and the image captured after an hour of the DM being in its factory flat.

To flatten the DM the following procedure was followed. Initially, the mirror was set to its factory flat by setting each actuator to zero. Each actuator in turn was then set to 1 with the rest at 0 and an image taken of the surface via the SHWFS. The maximum displacement of the wavefront was then used as an estimate for the position of each actuator – when viewed from the SHWFS. Next the following iteration procedure was followed. First there was a pause for 1 min with the DM held in its current best flat pose in order to allow for any viscoelastic creep, (discussed later in this chapter). Next an image was taken with the SHWFS. This was used to identify the displacement of the mirror at each of the actuator positions. Since there should be no displacement if the mirror is flat (which was taken to be the $\lambda/10$ reference flat), these displacements were all errors. To flatten the mirror a correction needs to be made to the error across the surface. Care must to be taken not to overcorrect the error – as this would produce an error in the other direction. Therefore to reduce the error, a proportion (1/10, found by trial and error) of this measured error at each actuator position was subtracted from each actuator command signal to provide an updated command signal. The 1/10 figure enabled this iterative procedure to converge after 10 iterations to produce the best flat for the DM.

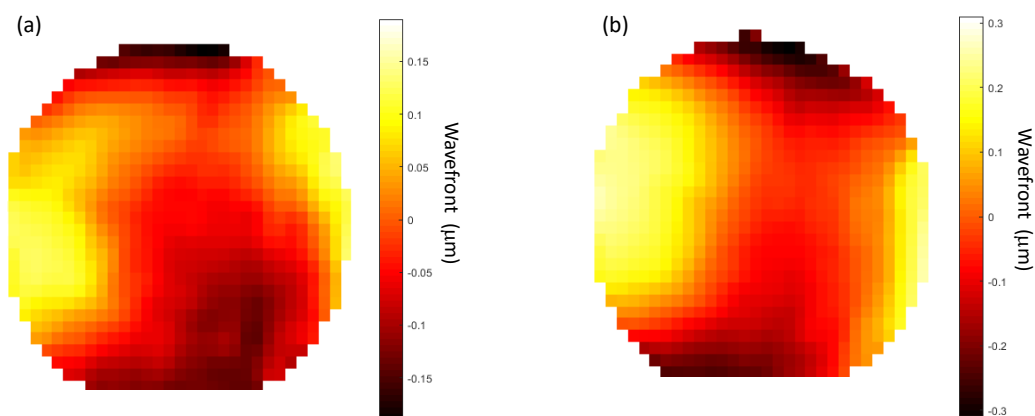


Figure 47 Wavefront measured by the Shack Hartman wavefront sensor (SHWFS) on consecutive days, 1 hour after being switched on after being off all night. The variation in surface is likely due to changes in ambient temperature and humidity. Note the scales of (a) and (b) are different.

The best flat achieved from this procedure had an RMS surface error of 13.5 nm. This is within the diffraction limit (34 nm) and is also consistent with the value of 20.5 nm as stated in the Alpao's manufacturer test report [131]. Figure 48 shows the SHWFS image of the DM mirror surface corresponding to the best flat which was used to obtain image Figure 43 (c) as described previously.

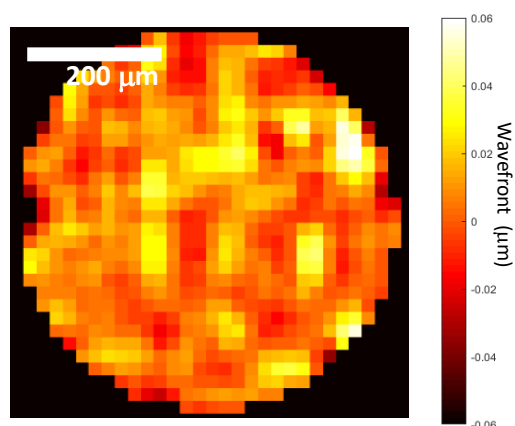


Figure 48 SHWFS image taken after 10 iterations of the procedure to flatten the mirror. Standard deviation = 0.014 μm , diffraction limit = 0.036 μm

The images in Figure 49 show the raw images of the central pinhole of the STM over consecutive days prior to the system being used. The DM had not been switched off overnight and was constantly on – in its best flat, in order to avoid viscoelastic creep (described later). It is clear that the factory flat can vary from day to day – most likely due to variations in temperature as described by reference [4].

This shows that it is necessary to use the SHWFS to find the best flat on a daily basis prior to use of the mirror for microscopy etc. The procedure for finding the best flat took 10 min.

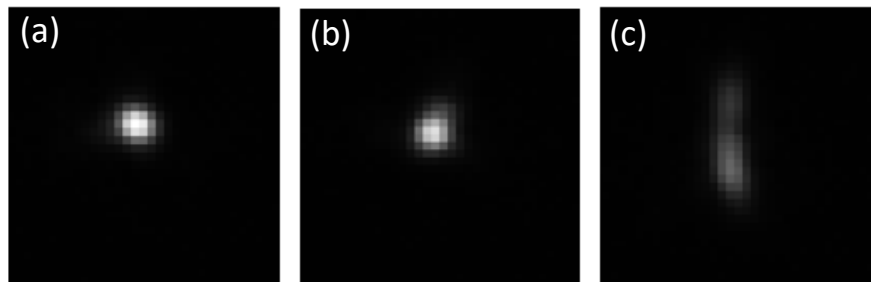


Figure 49 Raw images of the central pinhole of the STM with the mirror in the best flat. Images taken over 3 consecutive days with the DM constantly on an held when not used (e.g. at night) in the best flat.

3.11 Creep/hysteresis with the DM

The Alpao DM has a reflective surface with a shape that is controlled by magnetic actuators. This particular DM has linkages that connect the reflective surface with the actuators made of a material which contains polymer (Figure 26) and is subject to creep/hysteresis [referenced as a communication with Alpao in [4]]. Creep is the tendency of a material to deform over time when subjected to mechanical stress and the amount of creep usually depends on the amount of stress, exposure time, temperature and the type of material. A material that shows viscous and elastic properties is said to be viscoelastic; polymers are viscoelastic. Typically, a viscoelastic material has three characteristic stress-strain behaviours. First, it has a time-dependent increase in strain in response to constant stress, where initially there is a large rate of change of strain before levelling off. Secondly, it has a time-dependent reduction in stress as a material undergoes a constant strain. Finally, viscoelastic materials show hysteresis in a stress-strain plot, i.e. a difference in behaviour between loading and unloading the material which corresponds to a release of energy.

As a result of this viscoelastic behaviour, the current profile of the DM is dependent on the history of poses applied to the mirror. This is of crucial importance when using the DM in an open-loop configuration as it is essential that the mirror responds in a predictable manner to input commands in order that the mirror adopts the desired pose.

In the work by Bitenc et al. [4] an interferometer was used to show that if the mirror was held in one pose for several hours and then changed to a second pose, then the mirror would subsequently creep from this new mirror profile over the course of several hours. The RMS of the deviation in the final shape and the second pose could exceed 30 % of the RMS difference between the 2 poses. Bitenc et al. [4] developed a model of the correction that needed to be applied to the actuator commands in

order to allow for this creep which would allow the final surface to be within an RMS of 4 nm of the 2nd pose after a period of 6 min. The correction procedure requires characterising the mirror in advance of use and is dependent on the initial and final pose on the mirror, and also the length of time that the mirror was in the first pose and can have a time constant of the order of hours. This has a direct implication with regard to switching the DM and control electronics on and off. The mirror surface when unpowered is quite different to the powered state where actuator commands are all zero (the factory flat). To avoid creep, the DM was left permanently switched on, so any creep would naturally revert towards the factory flat. Reference [4] had showed that the ambient temperature and humidity could affect the behaviour of the mirror.

In the subsequent work by Bitenc et al. [5], an interferometer-based method was developed to mitigate further forms of creep behaviour and would compensate for 90-95% of the creep. This work characterised the 2 forms of creep; a long term creep which is a function of its history of poses – which is the viscoelastic creep – and a short-term thermal creep effect which is believed to be due to the warming up of the DM structure and has an effect which is related to the current flowing through the actuator coils. This thermal creep is reported to have a characteristic time of the order of 10s of seconds.

The viscoelastic creep with the current DM was illustrated with the following experiment. With the STM at the focal plane of the objective ($z = 0$), the DM was commanded to its best flat position for 1000 s. This was to ensure that there was no residual viscoelastic creep from previous work – an image was taken at the end of the 1000 s and a visual check made of the pinholes to ensure that they were sharply imaged. Then, 100 μm of high-NA defocus was applied to the surface of the mirror and this position was held for 60 s. Then the DM was then returned to its best flat again. The camera was then used to acquire a series of images each separated by 5 s with exposure time of 10 ms. The pinholes in Figure 50 (b), (c), (d) show progressively less defocus as the surface returns to being flat and back into focus. This data shows that the mirror is experiencing a creep effect and that its current shape is influenced by the history of the mirror shape.

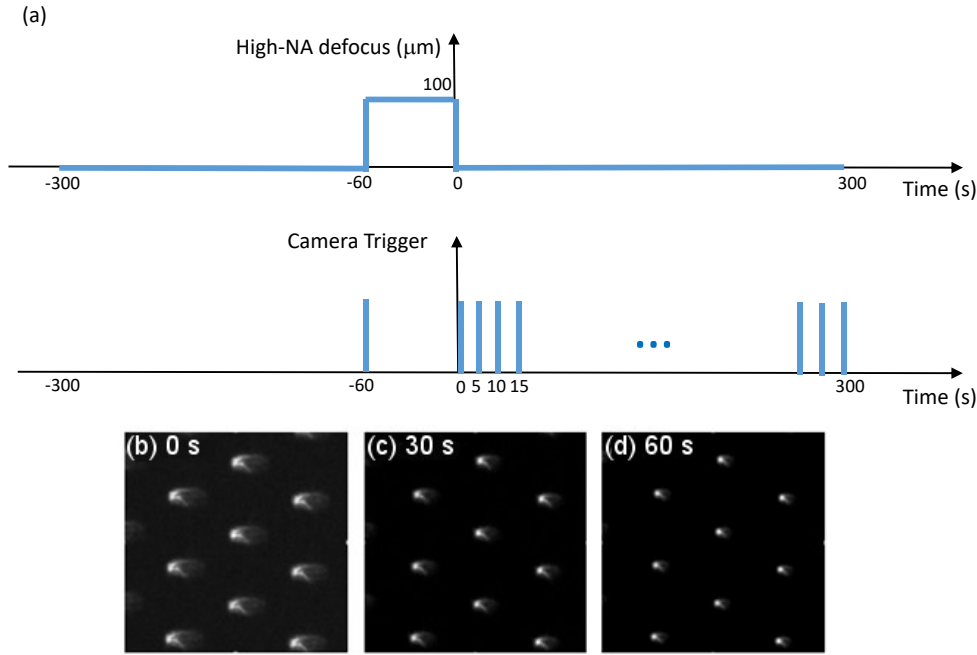


Figure 50 In (a) the DM is set flat for 240 s from -300 s to -60 s on the time axis, an initial image is taken with the camera at -60 s. Then 100 μm of high-NA defocus is applied to the mirror for 60 s until 0 s, and the DM is then set to flat. Images are captured every 5 s after the DM is flattened. Panels (b), (c), (d) show raw images of the pinholes demonstrating visco-elastic creep.

3.12 Characterisation of visco-elastic creep

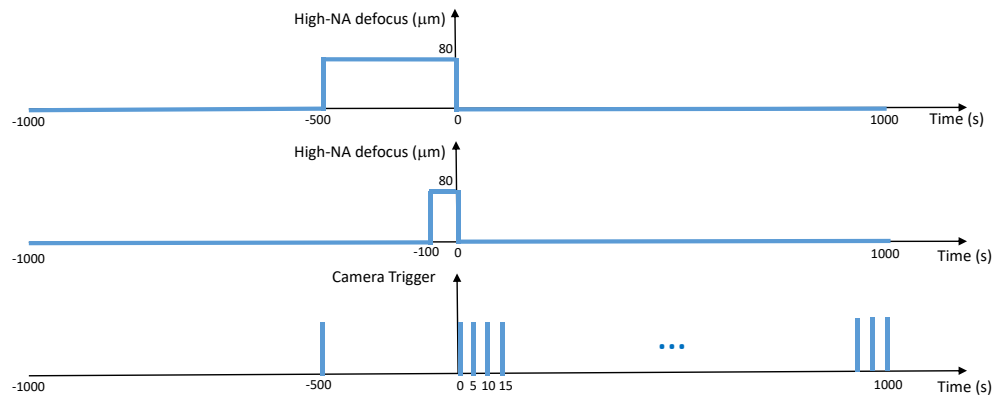
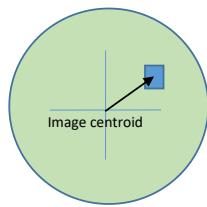


Figure 51 Timing diagram for experiment demonstrating that the characteristic time of the visco-elastic creep depends on the length of time that the DM is held in a particular pose. Top: the amount of high-NA defocus applied to the DM as a function of time. The DM is held flat from -1000 s to -500 s, and then an image taken (see bottom panel). The DM should now be free from visco-elastic creep. Then the DM is held at 80 microns for 500 s before returning to flat and an image is captured every 5 s for 1000 s. Middle: the procedure is repeated for the case where the mirror is held at 80 microns for 100 s. Bottom: the timings of the camera trigger for both experiments are shown.

The viscoelastic creep was characterised with a procedure with timing diagram shown in the schematic in Figure 51. The DM was first set to the factory flat setting for 500 s and an image taken to check that the pinholes were sharply in focus and did not appear to have significant aberrations (this had been found to be long enough to allow for previous creep effects). Then, 80 μm of high-NA defocus was put

onto the mirror for 500 s. Afterwards, the mirror was returned to the factory flat and the camera was used to acquire images of the star-test mask at a rate of 1 frame every 5 s for 1000 s. The procedure was repeated with the mirror being held in the defocused pose for 100 s. The central pinhole in the image of the star-test mask was used to measure the degree of aberration caused by the mirror not being flat. The 4th moment of the radial distribution of intensity about the centroid of the pinhole was chosen as a metric because this statistic is particularly sensitive to the spreading of light (Figure 52). Figure 53 shows that holding the mirror at 80 microns for 100 s has a relaxation time of about 200 s compared to holding the mirror at 80 microns for 1000 s has a relaxation time (time to reach 10 % of the limiting value) of about 1000 s. Increasing the length of time that the mirror is held in a position of high-NA defocus increased the amount of viscoelastic creep and also length of time that the mirror required to return to the factory flat.



$$4th\ moment = \frac{\sum r^4(x, y) I(x, y)}{\sum I(x, y)} \quad eq. 26$$

Figure 52 Estimation of the 4th moment about the centroid of the image of the pinhole.

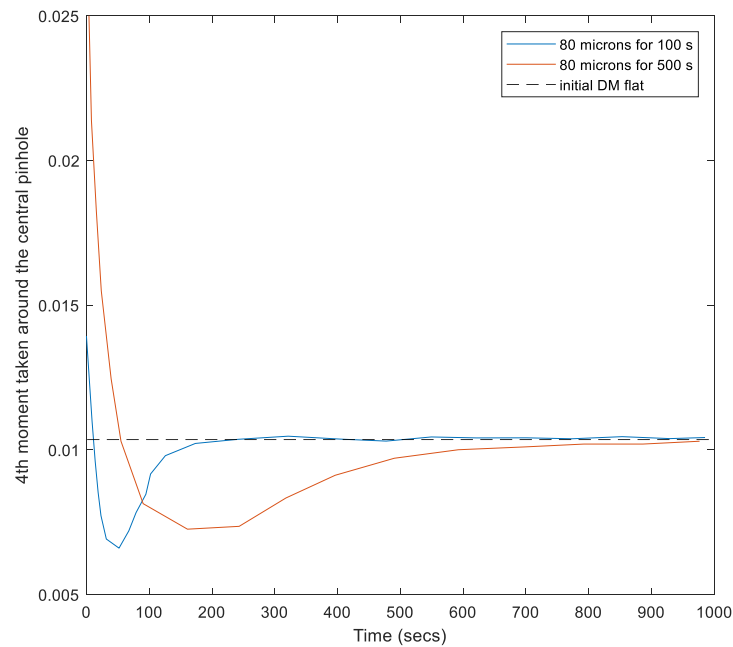


Figure 53 This plot compares the 4th moment about the image of the central pinhole of the STM image after the mirror has been held for 80 μ m of high-NA defocus for 100 s (blue line) compared with 80 μ m for 500 s (red line). The dashed line shows the 4th moment of the image of the central pinhole for the initially flattened DM. The 100 s step test takes about 200 s to return to flat compared to the 500 s step test, which takes about 1000 s to return to flat.

Viscoelastic creep means that the current mirror pose depends on the previous history of poses applied to the mirror. The next experiment examines the effect of keeping the average pose flat on the time constant of viscoelastic creep. As shown in the timing diagram in Figure 54, after an initial flattened period of 1000 s in order to ensure that there is no residual viscoelastic creep from previous use of the mirror, an image was captured at -1000 s to ensure that the DM is flat. Next the DM is held at 50 μm of high-NA defocus for 1000 s before flattening the mirror and then taking an image every 5 s for 1000 s. The procedure was then repeated but with the mirror oscillated from 50 to -50 μm for 1000 s. The symmetric oscillation of the mirror pose ensured that the time-average pose was flat. During the oscillation, each pose was held for 200 ms.

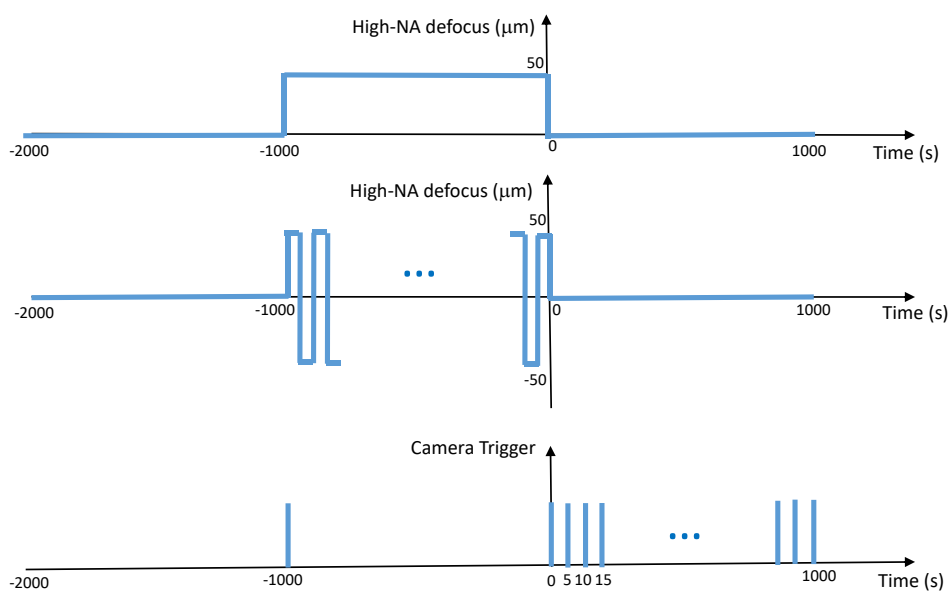


Figure 54 Timing diagram for experiment to show the difference in characteristic time between setting the DM to 50 μm of high-NA defocus for 1000 s compared with oscillating from 50 to -50 μm with the DM being on average flat, with each pose held for 200 ms, for a period of 1000 s. In both the constant and oscillating tests the mirror is initially held flat for 1000 s in order to ensure that there is no visco-elastic creep remaining and the mirror is flat, and an initial flattened image is taken. Then the mirror is either kept at a fixed displacement or oscillated for 1000 s and then the mirror is returned to flat and an image taken every 5 s for 1000 s.

Figure 55 shows that holding the mirror at 50 μm of high-NA defocus for 1000 s resulted in the DM taking 1000 s to return to flat. After oscillating from 50 to -50 μm for 1000 s the DM took about 100 s to return to flat. By keeping the average position of the surface flat the viscoelastic creep was reduced from 1000 s to 100 s. The goal of the project is to develop a focusing system which sweeps the focus of a microscope backwards and forwards through the volume of interest at high speed. This periodic series of poses would have a constant temporal average and so would avoid viscoelastic creep. After any period of oscillation the mirror would relax back to the temporal average pose. If that average pose is arranged to be flat, and the DM is kept permanently on, then viscoelastic creep can be avoided.

completely. The remaining creep will be thermal creep and would depend on the heat generated by the actuator coils which would be a function of the rate and amplitude of oscillation of the mirror.

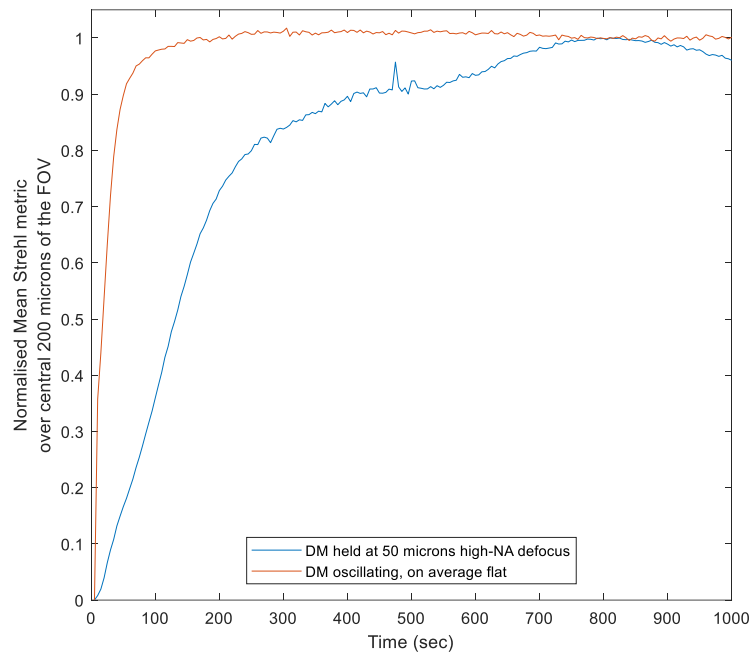


Figure 55 Plots showing the results of the oscillating mirror (brown) compared to the fixed mirror position (blue). It shows that the characteristic time for the oscillating mirror is much smaller than for the fixed mirror position, of the order of 1000 s compared to 100 s. This shows that the visco-elastic creep can be reduced by ensuring that the average pose of the mirror is flat. Figure reproduced from [134].

3.13 Characterisation of thermal creep

In order to characterise the thermal creep, the procedure was similar to the oscillation test described in the section above. An initial period of 1000 s of the mirror flattened ensured that there was no viscoelastic creep from previous work. The mirror was then oscillated for 1000 s from -50 to $50\text{ }\mu\text{m}$, where each pose was held for 100 ms. Finally, the mirror was flattened for 1000 s and an image taken each 5 s. The procedure was repeated for different amplitudes of oscillation of 10, 30, 50, 70, 90, $110\text{ }\mu\text{m}$ of high-NA defocus. Figure 56 shows the timing diagram. Figure 57 shows the relaxation of the mirror for 10, 30, $50\text{ }\mu\text{m}$ and that the greater the amplitude of oscillation the longer the time taken for the mirror to relax to a flattened pose. Figure 58 shows a summary of these results; that as the amplitude of oscillation increases the time taken to flatten increases; beyond $65\text{ }\mu\text{m}$ the relaxation time levels off.

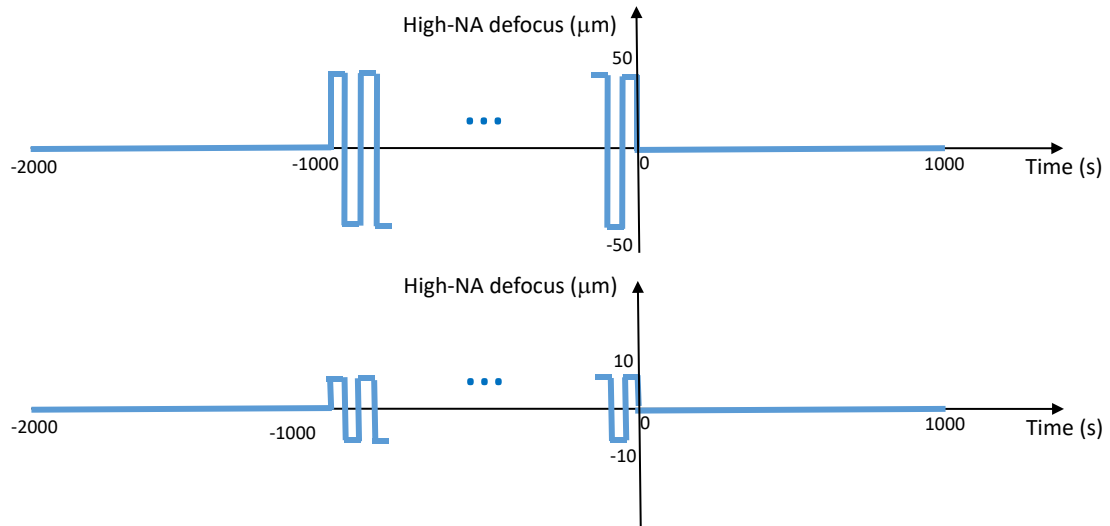


Figure 56 Timing diagram for the oscillating mirror experiment. This was repeated with different amplitudes of oscillation (10,30,50,70,90,110 μm), where each pose was held for 200 ms. (a) shows the amplitude for 50 μm of high-NA defocus and (b) for 10 μm .

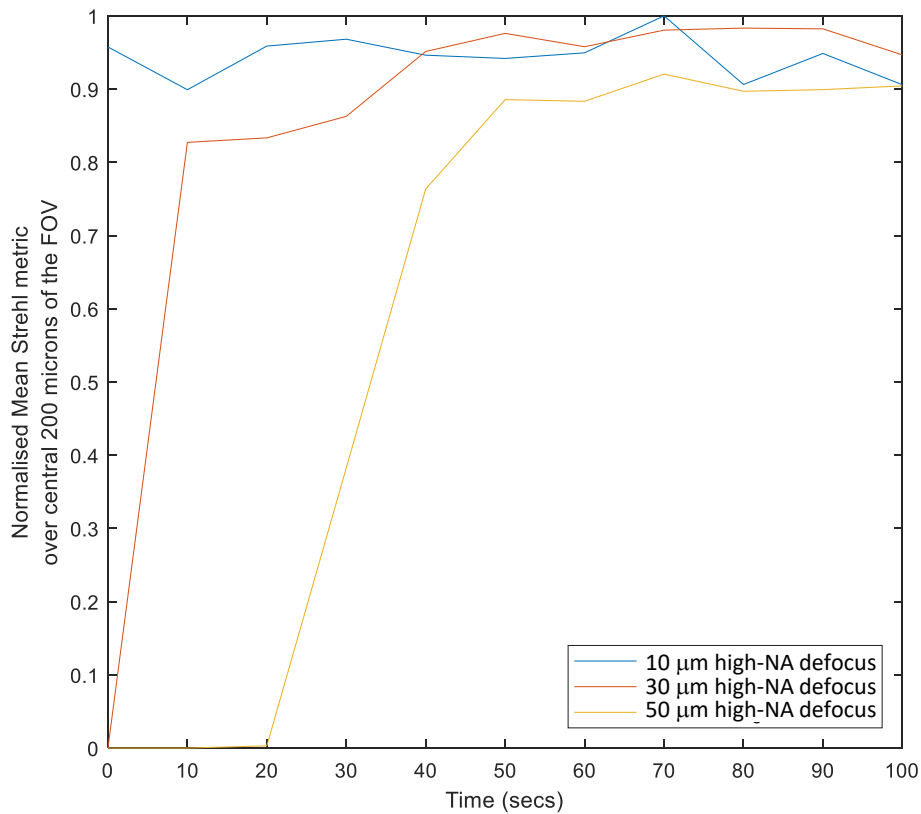


Figure 57 Normalised mean Strehl metric of the central 200 microns of the field of view against time for different amplitudes of oscillation, where the mirror was oscillated for 1000 s. These plots show that the time taken to return to flat increases as the amplitude of oscillation increases. This was attributed to the extra heat generated by the mirror causing thermal creep. Figure reproduced from [134].

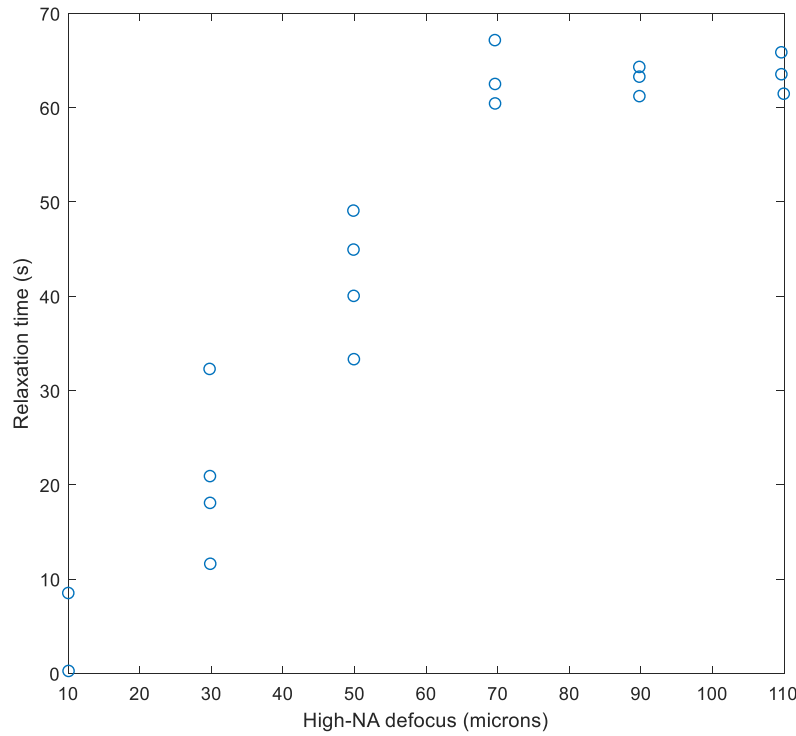


Figure 58 Plot showing the time taken for the DM to return to flat (relaxation time) after oscillating for 1000 s for different amplitudes of high-NA defocus. The relaxation time increase as the high-NA defocus increases until high-NA defocus of about 70 μm , after which the relaxation time levels off.

The general conclusions to these experiments is that viscoelastic creep can be avoided as long as the DM moves at a rate much faster than the characteristic time of the visco-elastic creep (100 s) and also that its mean profile is constant. By ensuring that the mean profile is flat and that the DM is constantly left on – ensures that viscoelastic creep can be avoided and an optimisation procedure needs to cope only with the thermal creep. For the thermal creep, there is no way of preventing the generation of heat by the actuator coils if fast movement of the DM surfaces is required. Therefore, in order to overcome thermal creep the mirror must be operated in a state of constant average actuator coil current in order to allow a thermal steady state to be reached. The constant effect of temperature on the mirror mechanical properties can then be overcome during the mirror shape optimization that is described in the next chapter.

3.14 Summary

This chapter described the development of an optical setup that will be used to develop a DM-based remote-refocusing scheme described in the next chapter. An estimated Strehl metric was presented and used to assess aberrations across the field of view of the system. This helped in the assessment of the accumulation of aberrations in the assembly of the setup when implemented with different

lens combinations. A Shack Hartman wavefront sensor and associated optics were added to the setup in order to flatten the DM as the factory flat was not found to be adequate, and previous work [4, 5] has reported that ambient temperature can have a significant impact on the factory flat and the best flat. The viscoelastic and thermal creep behavior of the DM were then characterized and led to the result that the mean DM profile would have to be the constant in order to avoid the unwanted effects of viscoelastic creep, with the DM remaining on and in a the chosen constant pose when not in use. In addition, this work showed that the DM would have to be moving continuously with constant average actuator coil currents during and after the DM optimisation procedure in order that the thermal creep could be managed.

Chapter 4: Optimisation of the DM for volumetric scanning

4.1 Introduction

For high speed volumetric imaging, it is necessary to rapidly refocus the imaging system successively to different depths within the object. Deformable mirrors (DM) are adaptive optical elements that can be used for this application, as they are able to apply the required phase correction to the pupil of the objective. Depending on the type of DM, they can change their profile at kHz rates and offer step-response times on the millisecond timescale. Additionally, they do not add chromatic aberration to the optical system. The simplest approach to volumetric imaging would be to find the best profile to apply to the DM corresponding to each level of defocus required within the sample. Volumetric scanning could then be achieved by applying a particular profile, or pose, to the mirror, waiting for it to settle - as there are likely to be vibrations or ringing due to the sudden change in profile (of the order of 0.4 ms for the Alpao DM used in this work [131]) - and then acquiring an image, before repeating at another depth within the sample. The z-stack of images could then be processed to create a 3D image of the sample. This 'move the DM, wait, and then take an image' approach requires that the camera acquisitions are carefully synchronized with the profiles sent to the DM, and the volumetric scan rate is fundamentally limited by the length of time it takes the mirror to settle after each pose change and the duration of camera exposure required. An alternative approach is instead to arrange for the DM to continuously change its profile through a range of defoci - whereby at any moment the DM surface corresponds to an optimized defocused plane within the sample. This approach eliminates the problem of ringing which occurs with sudden pose changes, as the DM can be guided smoothly through a series of surfaces. In this approach, the amount of defocus is scanned continuously and hence whenever an image is taken with the camera it will correspond to a particular refocus position within the sample. In this approach, the requirement for exact synchronization between camera acquisition and DM motion is relaxed. In this chapter, continuous motion of the DM was achieved by optimizing the DM for a particular set of defocus positions and then generating smoothly varying intermediate poses through linear interpolation.

The DM manufactured by Alpao suffers from viscoelastic creep and thermal creep, and so the response of the mirror surface to the actuator commands depends on the history of poses adopted by the mirror. These problems can be mitigated during an optimisation procedure by including pauses which are longer than the characteristic time of each kind of creep, and then the response of the DM to the actuator commands is repeatable. This is acceptable for situations where the mirror is comparatively static, however, for high-speed volumetric imaging both forms of creep have a significant effect. Viscoelastic creep can be avoided by ensuring that the mirror moves at a rate which

is much faster than the characteristic time of the viscoelastic creep and also that the average pose is constant. The thermal creep can be managed by ensuring that the mirror motion is much faster than the characteristic time for the thermal creep and that the mirror is driven through a constant set of poses in constant period so that it achieves thermal steady state.

The DM was first optimized for static use. This involved long pauses to allow for viscoelastic creep and to ensure repeatability of the actuator commands. Next, a quasi-static optimisation procedure was developed which had periods of rapid mirror motion. This served as a steppingstone to developing a method that was resilient to thermal creep as well as refocusing the optical system at high speed. This approach validated the optimisation algorithm developed and led to a fully dynamic optimisation procedure in which the mirror was constantly oscillating at the desired rate of volumetric imaging throughout the entire optimisation procedure in order to ensure that a thermal steady state was maintained. The average pose on the mirror was also maintained to be flat in order to avoid viscoelastic creep. This dynamic optimisation procedure could account for high-NA defocus, creep, system aberrations and dependencies between mirror poses; volumetric scanning at a rate of 26.3 vol/sec over a defocus range of 50 to -50 μm was achieved. The optimisation algorithm employed an image-based sensorless optimisation method that involved maximizing the Strehl ratio of a subset of images of pinholes of a star-test mask (STM) for a range of defocus positions.

4.2 Setup of the Optical System

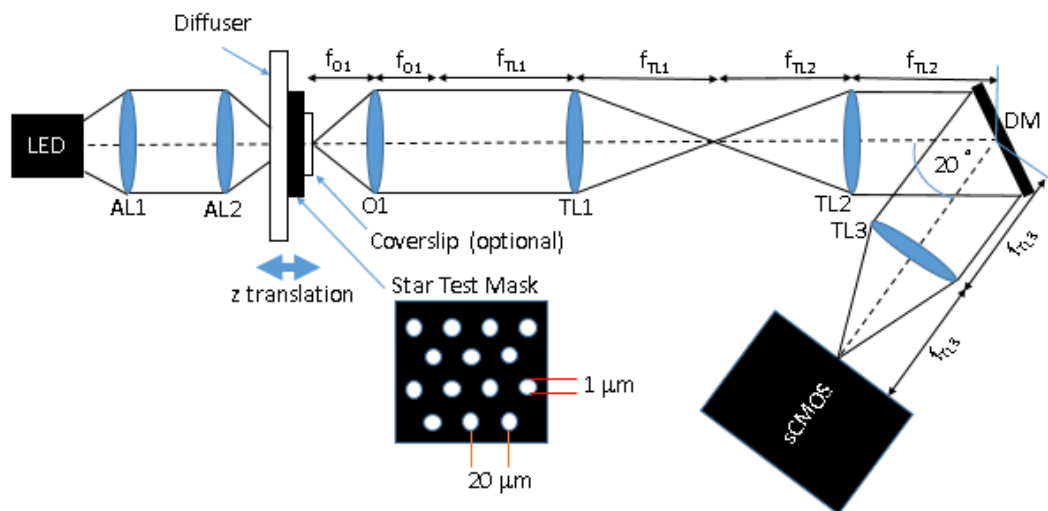


Figure S9 Optical setup used to optimise and test the deformable mirror for rapid refocusing. AL – aspheric lens; O – microscope objective, TL, tube lens; DM, deformable mirror. Light from the LED was imaged by aspheric lenses AL1, AL2 onto a Lambertian diffuser which illuminates a star test mask (STM). Light from the STM was collected by the objective O1 whose back focal plane was relayed lenses TL1, TL2 to the deformable mirror which applied a phase correction before tube lens TL3 brought the light to focus on the sCMOS camera.

Figure 59 shows the optical setup used for optimizing the DM for sweeping the amount of refocus. It does not show the Shack Hartman wavefront sensor (SHWFS) for clarity. For reference, optomechanics for the SHWFS is described in Chapter 3, Figure 44. Briefly, a pair of aspheric lenses imaged the chip of the LED onto the Lambertian diffuser that was in contact with and behind a star-test mask (STM). As before, the STM consisted of an array of 1 μm holes in a chrome mask on a silica substrate. The STM was used as the object during the DM optimisation procedure. Light transmitted through the STM was collected by objective O1, which was either a 40 \times /0.85 NA air objective or a 40 \times /0.80 NA water-immersion objective. For the water-immersion lens, as the system was aligned in a horizontal plane, ultrasound gel (UGEL250, Ana Wiz Ltd) was used as the immersion medium (which has a refractive index within 1% of that of water). The exit pupil of O1 was relayed via 4-f optical relay comprising a pair of tube lenses (TL1 and TL2) with a magnification of 2 \times , onto the DM which applied a phase correction. Ideally, the pupil of O1 (diameter 7.65 mm and 7.20 mm for the air and water immersion objectives respectively) would be imaged onto the DM so that the pupil image matches the size of the DM (diameter 13.5 mm). However, in this setup the image of the pupil overfilled the DM, thereby reducing the NA of the system to 0.75. In order to avoid using a beamsplitter (which would result in the loss of light when imaging unpolarised fluorescence), the DM was angled with its normal at 20° to the optical axis of O1 and TL1&2, and reflected the refocused wavefront to TL3, which produced an image on the sCMOS camera with an overall lateral magnification from the STM of 22.2 \times . To correct for the distortion introduced by the tilt of the DM with respect to the incident beam, the patterns applied to the DM were scaled by a factor of $1/\cos(20^\circ)$ in the direction parallel to the plane of the optical table. The value of 20° was the minimum angle needed in order to allow for the SHWFS to be inserted into the gap between TL1 and TL2. The SHWFS was needed in order to flatten the DM prior to each optimisation. It was found to be necessary to add this to the arrangement after it was discovered that the daily variation of ambient temperature was sufficient to alter the best flat, which was most noticeable for the optimized results for 0 μm of defocus.

4.3 Refocusing using high-NA defocus

As described in Chapter 1, Sine-condition obeying objectives have an expression for high-NA defocus given by,

$$\text{OPL} = z\sqrt{n^2 - \text{NA}^2\rho^2} \quad \text{eq. 27}$$

Objective lenses generally contain lens groups that precisely correct for spherical aberration, field curvature and chromatic aberration at the design conjugates [12, 13]. At non-design conjugates, these

aberrations are no longer corrected and become significant. It is also not necessarily the case for non-design conjugates that the system would still obey the Sine condition. A DM is able to apply a phase correction to the pupil in order to correct for the defocus, spherical aberration etc, however, it is not possible to correct for a field-dependent aberration such as field curvature from a Fourier plane.

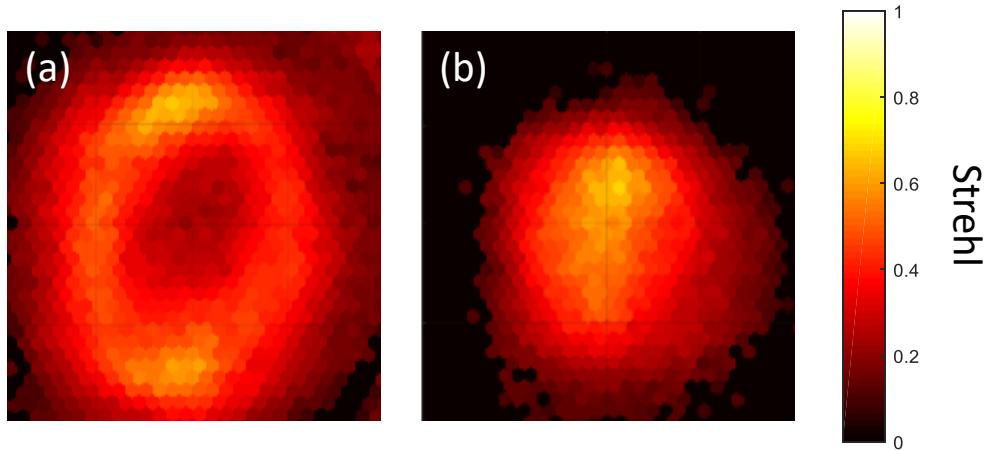


Figure 60 Panel (a) shows the Strehl map for high-NA defocus set to $30\ \mu\text{m}$ for a STM placed at a physical defocus of $30\ \mu\text{m}$. Panel (b) shows the Strehl map with $34\ \mu\text{m}$ of high-NA defocus applied to the DM and the stage at a physical defocus of $30\ \mu\text{m}$. The patterns observed in both panels are consistent with the presence of field curvature.

As an example, Figure 60 (a) shows the Strehl maps obtained with the air objective when moving the STM to a physical position of $30\ \mu\text{m}$ of defocus and then applying $30\ \mu\text{m}$ of high-NA defocus to the DM. The result is an annular pattern in the Strehl map which is consistent with field curvature plus defocus. Keeping the STM $30\ \mu\text{m}$ from the focal plane of the objective and applying $34\ \mu\text{m}$ of high-NA defocus to the mirror produces the disk-like Strehl map shown in Figure 60 (b) that shows that the 'bottom' of the bowl of field curvature has been reached causing the pinholes in the STM at the centre of the FOV to come into focus.

The amount of field curvature, after applying high-NA defocus onto the DM was found to be dependent on the objective used (as shown later in this chapter). The field curvature placed limits on the field of view achievable at different defocus positions. A difference in high-NA defocus corresponding to an axial displacement of the sample by $0.4\ \mu\text{m}$ is sufficient to break the Strehl limit. That is to say that the RMS over the pupil for the difference in high-NA defocus between 2 axial positions displaced by $0.4\ \mu\text{m}$ exceeds $\lambda/14$ and hence is not diffraction limited. Pinholes that only come into focus after an axial displacement of $0.4\ \mu\text{m}$ from the in-focus position of the STM due to field curvature can be regarded as being just diffraction limited. Hence this creates a circular diffraction-limited region. The greater the field curvature the smaller the radius of the diffraction-limited region.

The effect of using the objective in a non-design conjugate was therefore investigated in more detail. For a particular defocus, e.g. 20 μm , 20 μm of high-NA defocus was applied to the DM. The stage was moved to 20 μm . There was then a 60 sec pause in order to allow for thermal creep to occur and then an image was taken with the camera. The DM was then held in the negative pose (with all of the actuators being sent the negative of the previous signal). This was held for 60 sec before continuing. This way the average profile of the DM would be flat and so there would be no viscoelastic creep.

The procedure was repeated from -50 μm to 50 μm in steps of 5 μm . Each image was converted into a Strehl map and the results are shown in Figure 61. It can be seen that the Strehl metric is better for negative amounts of defocus compared to positive amounts of defocus for this optimisation.

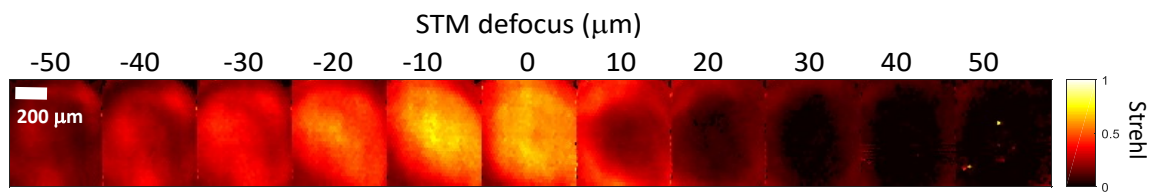


Figure 61 Strehl maps when high-NA alone is applied to the DM. The stage was moved from -50 μm to 50 μm in 5 μm intervals. Each pose was held for 60 s prior to taking an image (stage positions at multiples of 10 μm are shown in the figure). Results obtained using the air 40x/0.85 NA objective lens.

The performance of the system was then characterised in more detail. For each stage defocus position, e.g. 30 μm , the DM was set to 30 μm of high-NA defocus. The stage was then moved from 20 μm to 40 μm in steps of 1 μm with the camera taking an image at each position. Each of the 21 images associated with the 30 μm of DM defocus was then analysed to produce a Strehl map. The Strehl map was used to find for each pinhole in the STM the displacement of the STM that produced the maximum Strehl. These displacements were used to produce a map of field curvature shown in Figure 62. During

the procedure, 60 s pauses were used after changes in DM pose to avoid the unwanted effects of thermal creep.

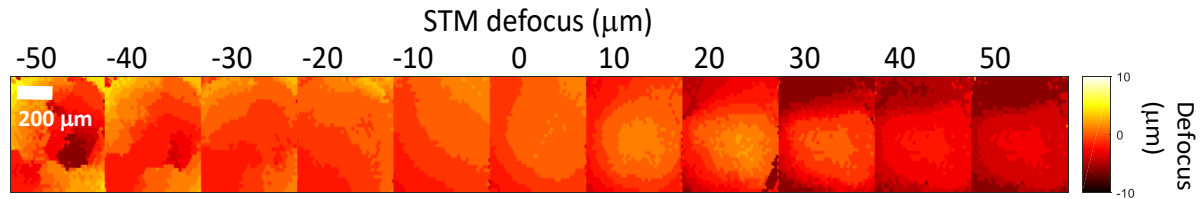


Figure 62 The stage was moved from -50 μm to 50 μm . High-NA defocus was applied to the mirror corresponding to each stage position. Then the stage was displaced in steps of 1 μm from -10 μm to 10 μm and a Strehl map obtained for each new stage position. For each stage position the displacement required to maximise each pixel in the Strehl map was used to create the images shown in the figure. The results indicate the presence of field curvature. Results were obtained using the air 40x/0.85 NA objective lens.

As can be seen in Figure 62, use of the Olympus 40x/0.85 objective at non-design conjugates by applying the high-NA defocus alone to the DM produces field curvature that increases with applied defocus. The difference in high-NA defocus between the centre of each map shown in Figure 62 and the amount on the righthand edge of the image was plotted against defocus in Figure 63, and provides an indication of how field curvature changes with defocus of the STM.

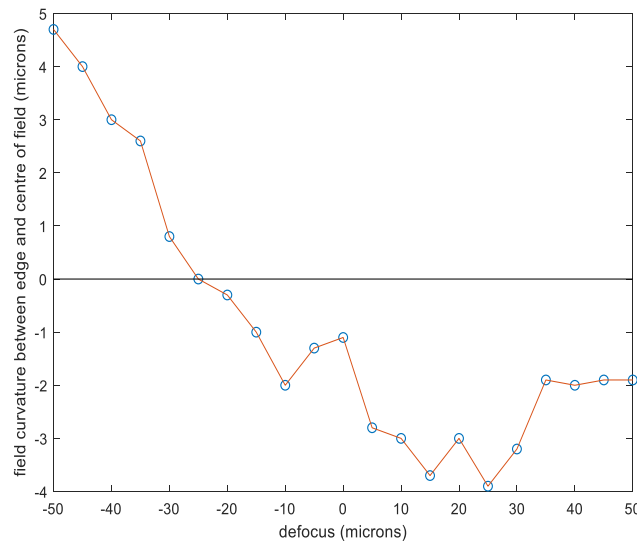


Figure 63 Estimated field curvature for Botcherby high-NA defocus for the 40x/0.85 air objective lens. Estimate was obtained by comparing best focus of the centre of the STM to best focus at the righthand edge of the STM image.

Also, for the 21 images associated with each control pose a best Strehl map was produced – corresponding to the best Strehl ratio achieved for each STM pinhole, which is shown in Figure 64.

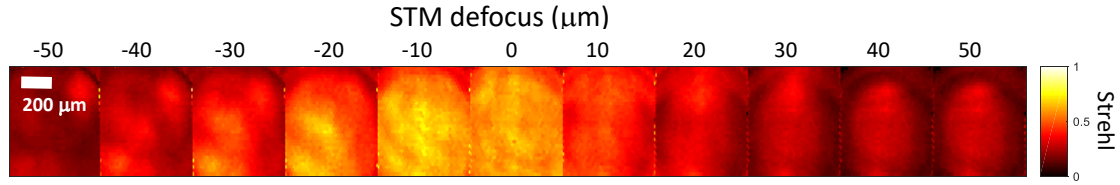


Figure 64 The stage was moved from -50 μm to 50 μm . High-NA defocus was applied to the mirror corresponding to each stage position. Then the stage was displaced in steps of 1 μm from -10 μm to 10 μm and a Strehl map obtained for each new stage position. The Strehl maps shown in the figure were obtained by taking the best Strehl value at pixel through the stack of 21 Strehl maps corresponding to each stage position. The results indicate the potential performance of the system if the field curvature could somehow be managed.

The best results occur in Figure 64 for STM defocuses of -10 and 0 μm , with a reduction in performance for other values. It was however possible to get close to the performance of the maximum Strehl maps in Figure 64 by tuning the amount of high-NA defocus applied to the DM for each STM defocus distance. For 30 μm of STM defocus, the amount of high-NA defocus applied to the DM was varied from 20 μm to 40 μm in steps of 1 μm and an image taken for each. That is to say, the position of the STM was fixed and different amounts of high-NA defocus were applied to the DM. The mean of the Strehl values of the pinholes in the central 100 μm square of the image were used to choose the optimal amount of high-NA defocus to apply to the DM. Strehl maps were obtained for all of the optimal high-NA defocus results corresponding to each defocus position from -50 to 50 μm in steps of 5 μm . The resulting Strehl maps for STM defocuses of multiples of 10 μm are shown in Figure 65.

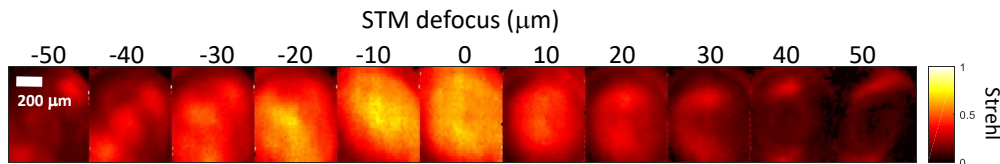


Figure 65 Strehl maps obtained for different amounts of high-NA defocus applied to the DM for the case where the amount of defocus has been chosen to maximise the mean Strehl metric obtained over the central 100x100 μm of the FOV.

A comparison between high-NA defocus alone, optimised high-NA defocus and also the best Strehl results are shown in Figure 66. None of the results were diffraction limited.

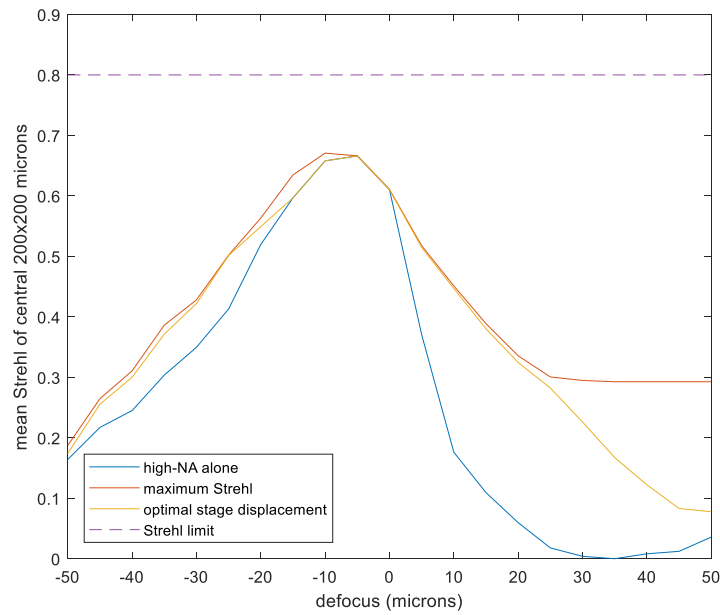


Figure 66 Comparison of high-NA alone, with optimised high-NA defocus, and the maximum Strehl projection obtained for each STM defocus position.

4.4 Static optimisation by optimizing high-NA defocus and also Zernike modes

Every DM pose can be represented as a set of Zernike amplitudes and the pose itself can be regarded a point in Zernike space, where each axis is the amount of each particular Zernike mode. Chapter 1 Figure 20 shows profile plots of the first 20 Zernike modes.

By exploring the region around the optimized high-NA defocus starting point, an improved local maximum can be found as shown schematically in Figure 67. Figure 67 shows how the optimised high

NA defocus can be regarded as a point in infinite dimensional Zernike space – which can be improved by successively optimizing along each Zernike dimension in turn.

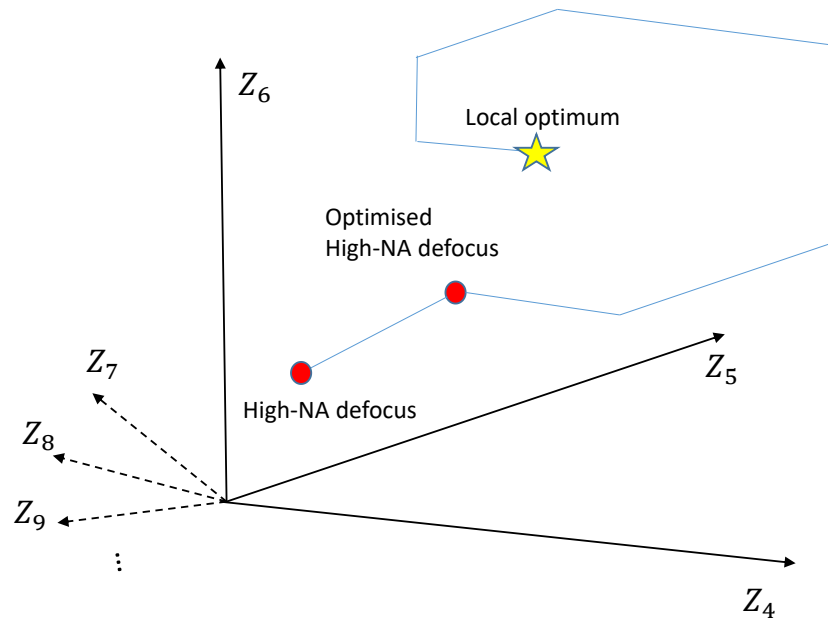


Figure 67 The search to find the best pose for the DM can be regarded as a search through Zernike space. Initially, the nominal amount of high-NA defocus is applied. The DM pose is then optimised as described in the previous section to produce the point marked as optimised high-NA defocus. Further optimisation then takes place along each dimension in turn. The whole procedure is then repeated in order to close in on an improved local optimum.

Initially, high-NA defocus corresponding to the defocus of the STM was applied to the mirror. This initial amount of high-NA defocus was then optimized as described in the previous section (4.3). This acted as the starting point for further optimisation using Zernike modes. The Zernike modes Z4 to Z28 were optimized in turn by successively applying a range of amplitudes of each mode to the mirror. After applying the initial high-NA defocus to the mirror, subsequent corrections with high-NA defocus or Zernike modes were an order of magnitude smaller as measurement by the maximum absolute displacement of the change in pose. It was found that it was not necessary to have a 60 sec thermal creep pause after each pose correction, 5 sec would suffice. So the procedure was to move the stage, apply appropriate high-NA defocus to the mirror, pause for 60 sec, take an image, then apply the negative pose with a 60 sec pause, then apply a high-NA defocus + high-NA/Zernike correction, pause for 5 sec, take an image, then apply the negative pose for 5 sec, and so on. For the optimisation of a particular stage position the drive current to the DM did not greatly vary, hence the reduced pauses to handle the thermal creep, however it was still necessary to include equal length pauses with the mirror holding the reverse pose in order to avoid viscoelastic creep.

With all of these pauses a typical optimisation for STM positions from $-50\text{ }\mu\text{m}$ to $50\text{ }\mu\text{m}$ in steps of $10\text{ }\mu\text{m}$ for modes of high-NA defocus and Z4 to Z28 would take 26 hours. During this time period the ambient temperature could sometimes change – which would change the behavior of the mirror, and therefore would cause the optimisation to go off course and fail. Z4 to Z28 was therefore found to be the largest range of Zernike modes that could practicably be optimised. However, this range of Zernike modes was found to be adequate and local optima were found to be present within the subspace formed by these modes.

The procedure described above used a brute-force optimization approach to determine the amplitude of a given Zernike mode that should be applied to the DM after each step. This involved measuring the mean Strehl for a central rectangle region $60 - 100\text{ }\mu\text{m}$ of the STM for a range of applied amplitudes and then interpolating to find the position of the maximum. As shown in Figure 68, 7 points, spanning 3 points on either side of the maximum, were then used to fit a parabola, which was used to estimate the amount of the Zernike mode required to maximize the score and so the performance at that step.

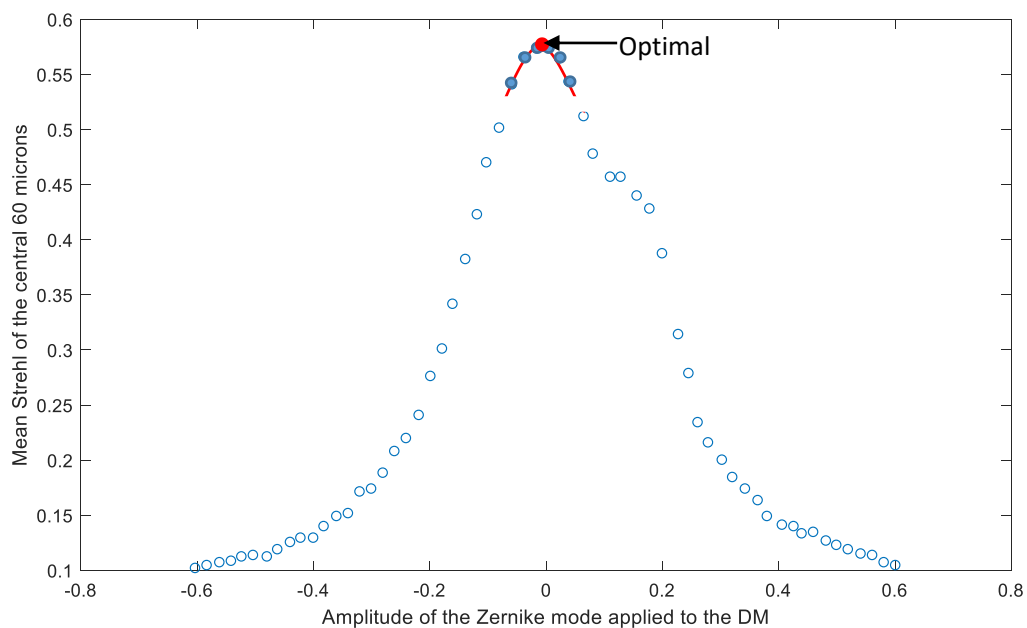


Figure 68 Optimisation of Z4 by applying different amounts of Z4 to the mirror, choosing the best 7 scores about the maximum and fitting a parabola to estimate the optimum. Figure reproduced from [134].

After optimizing the modes Z4 to Z28 the procedure was repeated until there was no further improvement in the score, which suggested that a local maximum had been reached (this usually took 3-4 repetitions).

The score used for the optimisation was the mean Strehl ratio for a square group of pinholes centred on the centre of the camera FOV. Too few pinholes and the statistical noise in the score would misdirect the optimization and the process would fail to find a maximum. Too many pinholes would extend the square region into parts of the FOV with field curvature and again result in a poor optimization result. A compromise of a $60 \times 60 \mu\text{m}^2$ square centred on the optical axis was found to be effective. Additionally, after the round of optimisation of high-NA defocus and the Zernike modes, increasing the square region up to a limit of $100 \times 100 \mu\text{m}$ would increase the area of the better-optimized region in the image, at the expense of slightly reducing the Strehl value at the centre of the FOV. If the optimisation rectangle did not contain the optical axis then the result would be an optimized annulus of pinholes – which was attributed to field curvature, as shown in Figure 69.

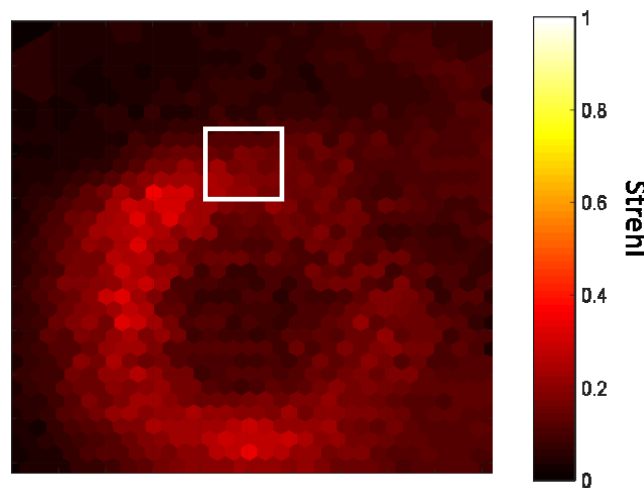


Figure 69 Optimisation thrown off course when the optimised rectangle of pinholes does not contain the optic axis, the white rectangle shows the region used to find the mean Strehl score.

A flowchart for the optimisation procedure used is shown in Figure 70. The outcome at the end of the procedure was a set of optimized amplitudes for each mode for each defocus. The results of the static optimisation procedure are shown in Figure 71.

During the development of the static optimisation procedure it was found that noise, vibration and changes in ambient temperature could have an adverse effect on the optimisation and easily throw it off course. As a result, a water-cooling system was installed instead of using air cooling of the Orca Flash camera in order to remove unwanted vibrations from an internal fan which could cause vibrations in the STM.

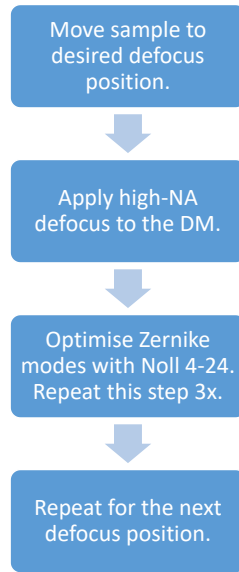


Figure 70 Flow chart for the static optimisation procedure.

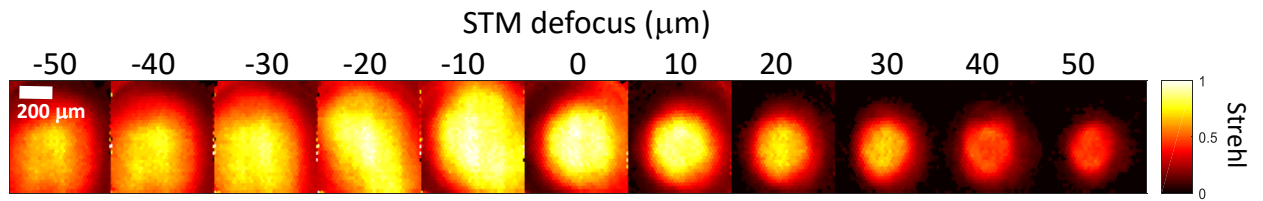


Figure 71 Strehl maps for the stage positions -50 μm to 50 μm after the DM was statically optimised firstly for high-NA defocus and then for the Zernike modes {Z4 ... Z28}. Figure reproduced from [134].

Figure 72 shows a plot of the mean Strehl ratio of pinholes within the central $200 \times 200 \mu\text{m}^2$ rectangle of the image against defocus. It shows a comparison of the results obtained for the DM optimised by tuning the amount of high-NA defocus followed by optimising the amplitudes of the Z4-Z28 Zernike modes compared with simply applying high-NA defocus calculated from the applied translation of the STM stage. As can be seen, the former procedure can achieve diffraction-limited performance over a

volume of $200 \times 200 \times 35 \text{ } \mu\text{m}^3$. The use of high-NA defocus alone was not able to achieve diffraction-limited performance.

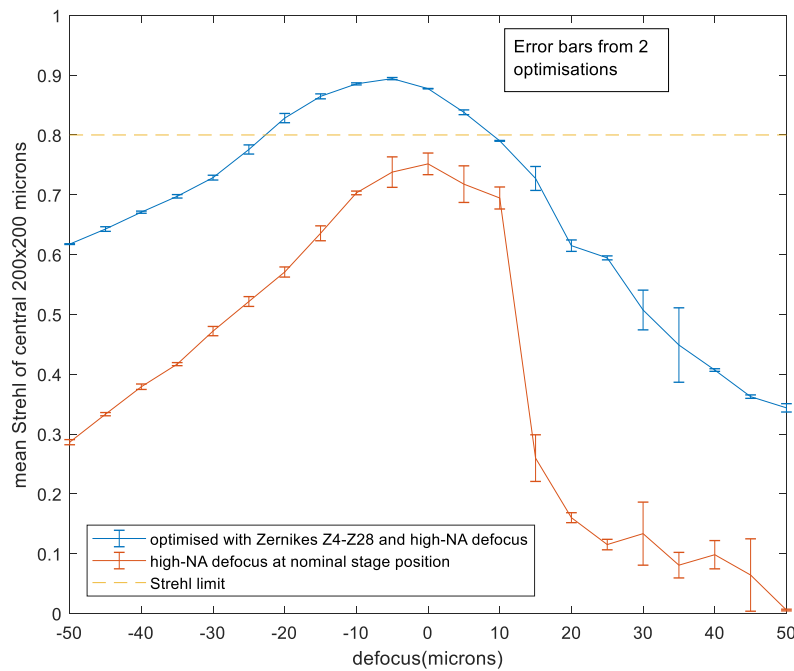


Figure 72 Comparison of DM statically optimised for high-NA alone compared with {high-NA defocus, Z4 ... Z28}. The error bars show the standard deviation calculated from two independent measurements. The high-NA defocus at nominal stage position curve is the same data as shown in figure 66.

4.5 Reducing the set of Zernike Modes

Given the time-consuming nature of the static optimisation procedure, it was natural to try to reduce the number of modes that are optimized. Linear models (order 2) were applied to each plot of Zernike amplitude against defocus and then F-tests were used to distinguish those models which had non-zero coefficients with $p < 0.01$. This suggested the reduced set of modes {optimized high-NA defocus, Z4,Z5,Z6,Z7,Z14}, with each having a statistically significant association with defocus. However, despite the use of the F-tests to identify the required subset of modes, optimisation of the DM using these modes did not produce a result superior to optimized high-NA defocus alone, and sometimes it was worse. However, the addition of a linear mode, $z = \rho$, resulted in a significant improvement in performance, although not as good as for the previous larger set of modes used for the static optimisation. This suggested that the small amplitudes of the neglected modes were still having a beneficial effect on the performance of the mirror. Optimisation with the reduced set of modes took only 6.5 hours and the results are shown in Figure 73.

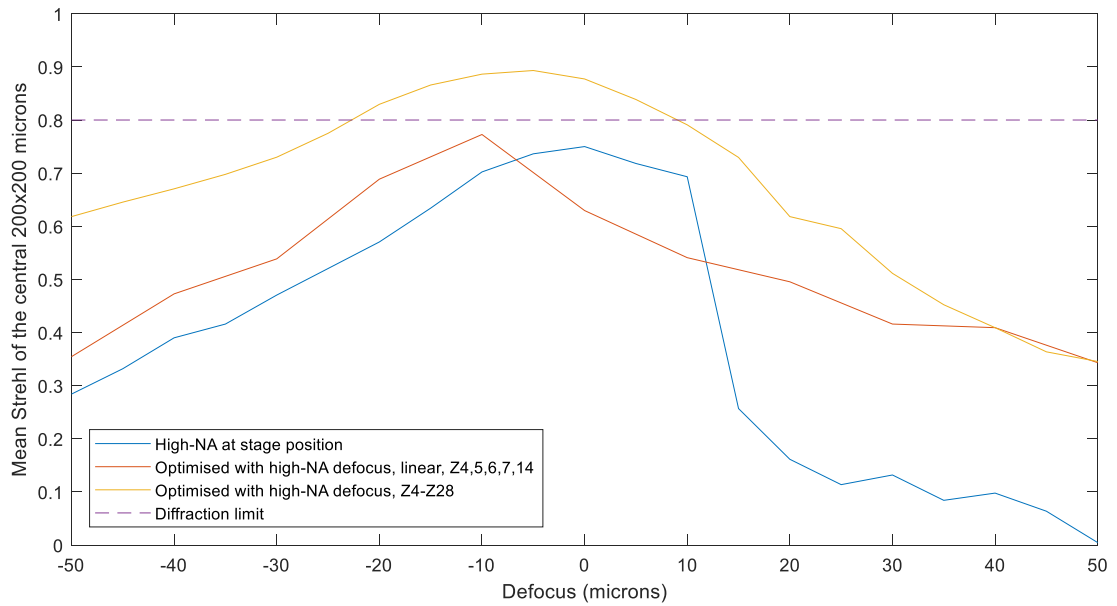


Figure 73 Comparison of the static optimisation results for {high-NA defocus, Z4..Z28} compared with the reduced set optimised {high-NA defocus, linear, Z4,5,6,7,14} and simply applying high-NA defocus for the stage position.

4.6 Quasi-Dynamic Optimisation

After optimizing the DM statically, the next series of experiments aimed to perform the first step in adapting the optimisation procedure, control software and hardware to successfully optimize the DM whilst it was moving through a discrete sequence of poses associated with rapid refocusing. This required a method capable of coping with the effects of the thermal creep associated with the actuator-induced heating of the DM.

The STM was first moved by the stage to the defocus position to be optimised. The idea was to oscillate the mirror at the desired rate of volumetric imaging long enough for thermal effects to have stabilized and then in the final cycle of poses capture an image of the STM at the appropriate defocus position. The mirror would then be held flat whilst Strehl ratios etc. were calculated and decisions made about optimizing the mirror surface (hence quasi-dynamic optimisation). The procedure would then be repeated for different amounts of the Zernike mode etc. added to the mirror surface. The optimisation algorithm itself was the same as for the static optimisation – the only difference was that the images of the STM were obtained in a procedure that periodically oscillated the mirror prior to the camera taking an exposure.

The DM was repeatedly moved through poses corresponding to -50, -40 ... 40, 50 μm of defocus (a ramp of poses). Each pose was held for a short period of time referred to as the interpose time – which was 10 ms – and corresponded to a refocus sweep rate of 9 sweeps/sec. The initial DM profiles

consisted of high-NA-defocus alone. In the last ramp of the sequence, following the change to the DM pose currently being optimised, there was then a 5 ms delay to allow for the DM to settle into its new pose, and then an image of the STM was taken with the camera using a 3 ms exposure time. For an interpose time of 10 ms, this left 2 ms before the next change of pose. This 2 ms was important and allowed for jitter in the software timing of the DM pose changes (e.g. in case the signal to change the pose came early causing it to occur during the camera exposure and hence leading to artefactual blurring of the image of the STM). The timing diagram for the DM and the camera are shown in Figure 74, and a flowchart for the procedure is shown in Figure 75.



Figure 74 Timing diagram for quasi-dynamic optimisation. The DM is oscillated through 300 ramps of defocus and then, when the mirror reaches the target pose on the last ramp cycle, an image of the STM is acquired by the camera when the mirror is defocused by the amount that is currently being optimised.

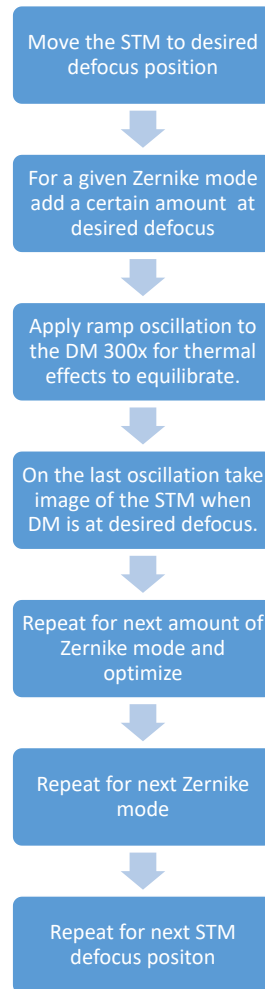


Figure 75 Flowchart for the quasi-dynamic optimisation procedure.

In terms of software, the DM was controlled by one MATLAB process and the Orca Flash camera was controlled via another MATLAB process. The 2 MATLAB processes were synchronized using the Windows operating system (OS) high resolution timer (HRT). By comparing logs of the HRT with the hardware timestamps provided by the Orca Flash camera (which is available in the meta-data associated with each image), it was clear that the median of the distribution of jitter in the HRT was 0.5 ms. Given that for an interpose time of 10 ms, this level of jitter was considered to be acceptable.

Once an image had been taken, the DM was held in a flat position (hence quasi-static optimisation) as the Strehl ratios were calculated and the next step in the optimisation process determined. A memory map was used to exchange data such as image statistics between the two processes. The mirror was then oscillated again and the procedure repeated. For this procedure and also the static optimisation, the camera was operated in SNAP mode – where resources are allocated and destroyed for each exposure – which is the simplest way to control the camera from MATLAB. In SNAP mode the resource allocation and deallocation associated with each image acquisition took 0.7 s.

The fact that each step in the optimisation required the mirror to be oscillated 300 times had the price of much longer optimisation times than for the static optimisation. As a result, the DM was only optimized for a small range of defocus positions spanning -20 to 20 μm in steps of 10 μm shown in Figure 76 (a) for an interpose time of 10 ms (9 sweeps/sec); Panel (b) shows the results for statistic optimisation with the larger set of Zernike modes for comparison.

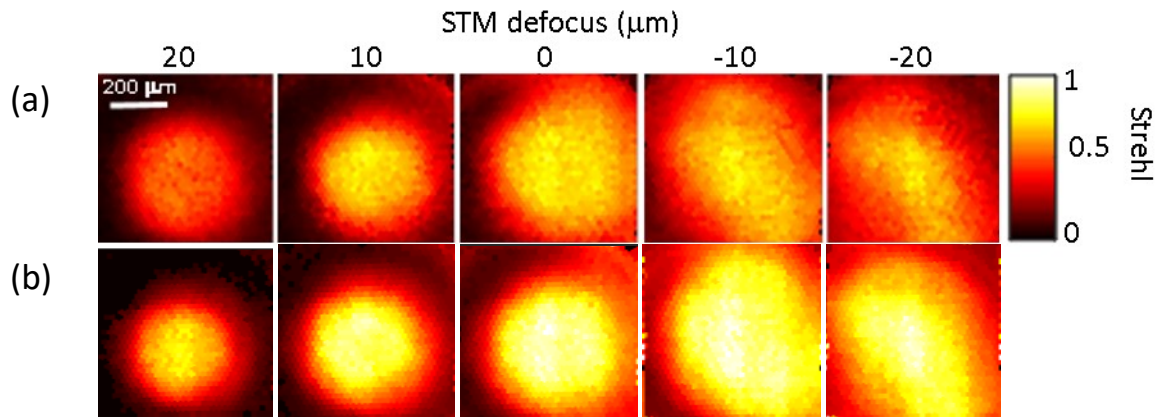


Figure 76 Panel (a) shows the results of quasi-dynamic optimisation with an interpose of 10 ms (9 refocus sweeps/sec). Prior to the acquisition of each STM image, the DM is oscillated 300 times in order to achieve a thermal steady state. Panel (b) shows the static optimisation results for these defocus positions taken from Figure 64 for comparison.

As can be seen, the optimisation results were not as good as the static optimisation, which was attributed to jitter in the timing of the 2 MATLAB processes. Although the HRT had a precision of 0.5 ms, the dependent MATLAB processes would wait in tight loops in order to trigger events at the right moment. These software-controlled procedures were observed to be disturbed by the operating system performing events such as process switching, and the occasional outlier jitter event could spoil the optimisation of the mirror. On the other hand, the results shown in Figure 76 do demonstrate the DM system operating at a refocus sweep rate of 9 sweeps/sec, albeit over a limited range of defocuses with the mirror oscillating through a range of refocus of 100 μm , and therefore does validate the quasi-dynamic optimisation approach.

4.7 Dynamic Optimisation

4.7.1 Initial approach with discrete DM pose changes

The approach in this section was to optimize the DM whilst it was oscillating at the desired refocus sweep rate. Following an initial warm up oscillation for the mirror to reach a thermal steady state (10 min), the average actuator coil currents were then maintained approximately constant throughout the entire process in order to minimize the effects of thermal creep. By keeping the average pose on the mirror flat, viscoelastic creep could also be avoided. Due to the symmetrical nature of the high-

NA defocus function and the fact that optimized corrections were an order of magnitude smaller, the mirror surface was sufficiently flat on average in order to avoid the effects of visco-elastic creep. The details of the optimisation algorithm were the same as for the static optimisation. A symmetrical sawtooth sequence of poses was applied to the DM, $\{-50, -40 \dots 40, 50, 40, \dots -40\} \mu\text{m}$, which was chosen to avoid additional complexities caused by ringing of the mirror surface due to large jumps in the mirror pose on the fly-back, as shown by Figure 77. The timing diagram is shown in Figure 78.

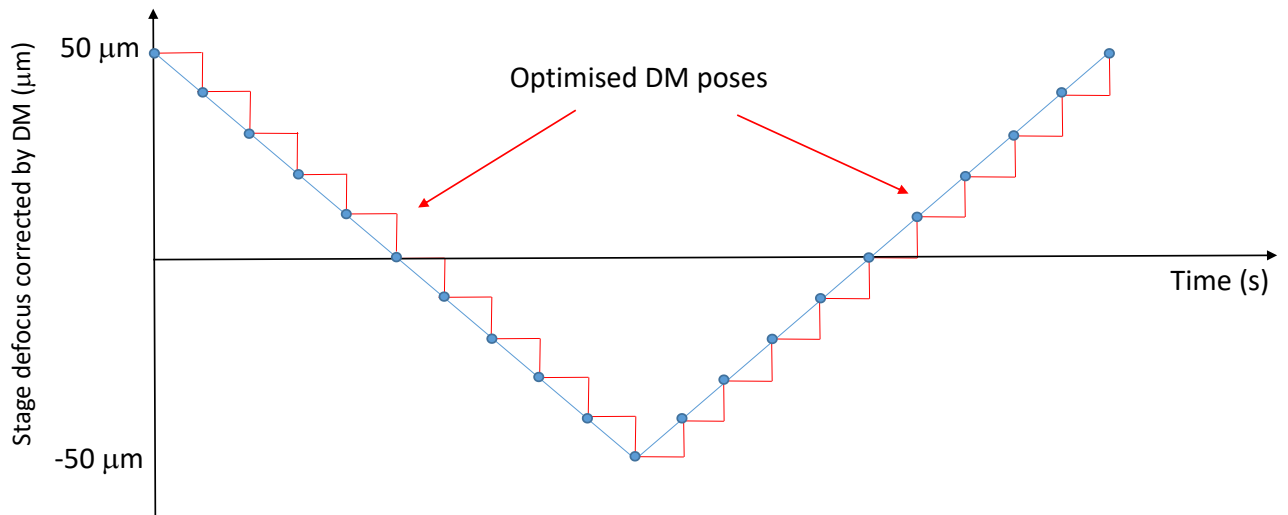


Figure 77 Symmetric saw-tooth of DM poses correcting for defocus of the stage for positions $\{50, 40, \dots, -50, \dots, 40\} \mu\text{m}$. Red line shows amount of defocus applied to DM and blue line is to guide the eye. Blue points indicate where DM pose is changed.

After each pose was applied to the mirror it was held stationary for a fixed length of time – the interpose time. The procedure was set up so that the camera was able to take images of the STM at particular defocus positions during the oscillation of the DM. For example, if the DM was being optimized at $30 \mu\text{m}$ defocus, then the camera would be synchronized to take an image whenever the mirror was in the $30 \mu\text{m}$ defocus pose. In this way the camera was arranged to acquire an image of the STM at a particular DM pose during the optimization procedure, with the exposure being triggered a set time after the pose change of the mirror. A flowchart for the optimisation procedure is given by Figure 79.

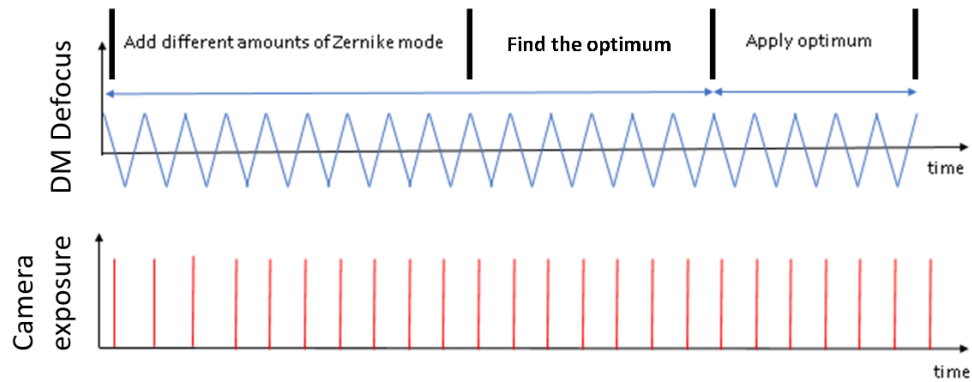


Figure 78 Timing diagram showing the DM defocus compared with the camera exposures. The DM is set to oscillate and the Orca Flash camera takes images are timed to occur for a particular DM defocus. During the first phase, varying amplitudes of a given Zernike mode were added to the particular pose that is being optimised. After capturing the optimisation images, the optimum is found during the second phase. The optimum is then tested through the acquisition of evaluation images during the third phase to check that the score does improve. If it does, then the change in pose is accepted. Otherwise it is rejected.

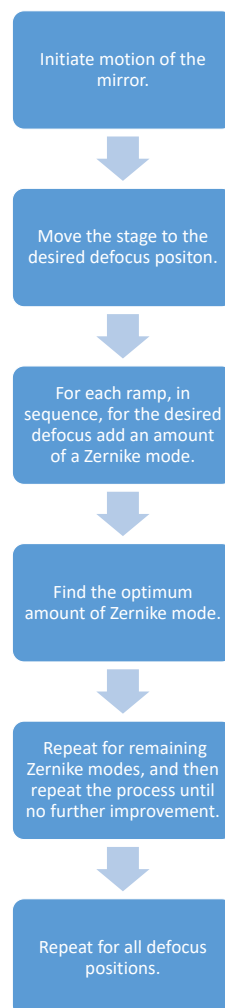


Figure 79 Flowchart for the dynamic optimisation procedure where the DM is continually oscillating through a set of discrete poses.

For the dynamic optimisation, the DM was controlled by one MATLAB process and the camera by another, and they were both synchronized with the Windows OS HRT. Information was exchanged between the processes via a MATLAB memory map. The MATLAB process controlling the camera calculated scores from the images captured and relayed the information to the DM controlling MATLAB process that directed the optimisation.

Figure 80 shows the results of optimisation for an interpose time of 20 ms with the exposure time of 5 ms at a delay of 12 ms after the DM pose change. The optimisation failed for -10 μm of defocus.

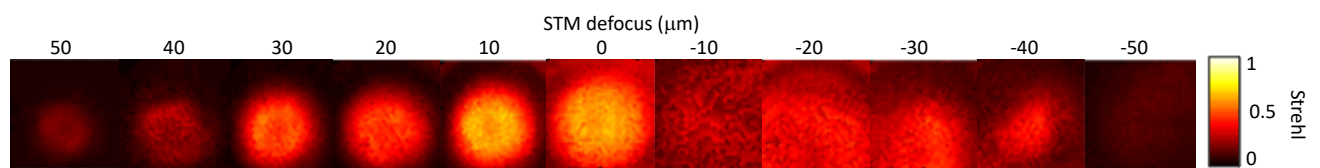


Figure 80 Results of dynamic optimisation for a set of discrete poses for an interpose time of 20 ms (5 Vol/sec), and an exposure time of 5 ms. The exposure was taken 12 ms after the pose change.

The poor performance of the optimisation was believed to be due to jitter in the software timing causing a variation in the delay between the pose change of the mirror and the exposure of the camera. The jitter also caused variations in the interpose time between DM pose changes.

4.7.2 Improvements to dynamic optimisation with discrete DM pose changes

As the optimisation process is very sensitive to noise, the system was therefore improved to introduce hardware electronic timing to remove the jitter associated with software timing. The DM control box outputs a TTL pulse after uploading a set of commands to the DM. This timing signal could be used as the basis for triggering the Orca Flash camera exposure electronically. Conveniently, the Orca Flash camera could be configured to provide a delay between receiving an input trigger and taking an exposure.

Up until now the Orca Flash camera had been used to capture images in SNAP mode, which had a 0.7 s overhead per acquisition as it allocated and deallocated resources. Since the dynamic optimisation needs to be able to run at video frame rate, this was no longer practicable. The Orca Flash camera was therefore configured to use multiple image buffers. A sufficiently large buffer was allocated on the Orca Flash camera to allow for the storage of each image in the optimisation and evaluation stages of the optimisation algorithm. The use of multiple buffers to store the images on the Orca Flash camera eliminated the need to continuously allocate and deallocate resources and substantially increased the speed of the optimisation from 5 hours to 1.5 hours.

In order to prevent every pose change on the DM triggering an exposure of the Orca Flash camera, a TTL pulse selector was used. This consisted of a National Instruments (NI) digital acquisition (DAQ) box (model 6008) connected to the PC and used to provide one of the inputs to a logical AND gate. The other input of the AND gate was connected to the TTL output from the DM. The output of the AND gate was used to trigger an image acquisition by the Orca Flash camera. Hence the PC could use this arrangement to select which DM trigger pulse would fire the Orca Flash camera. Figure 81 shows the corresponding wiring diagram.

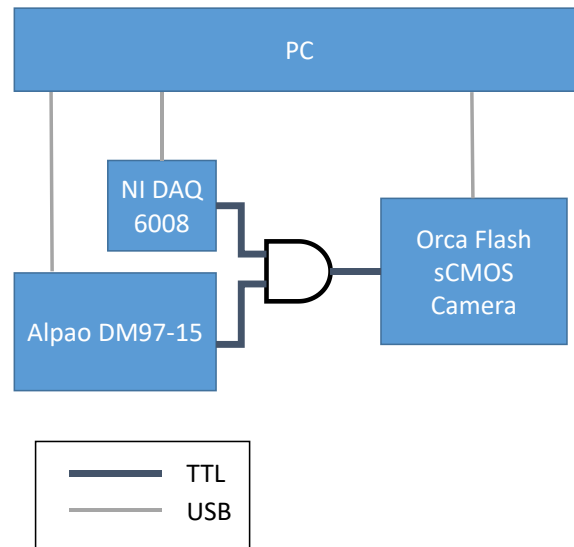


Figure 81 Wiring diagram for TTL pulse selector. A TTL pulse is output by the DM on each pose change. The desired DM pose change is selected by the AND gate when the output from the NI USB 6008 DAQ is high. Hence the DAQ can be used to enable the camera to receive only specific TTL pulses from the DM.

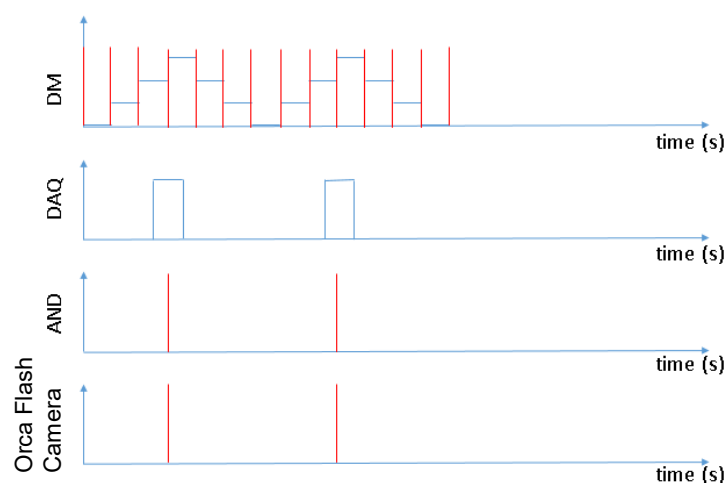


Figure 82 Timing diagram showing the symmetric staircase of poses being applied to the DM (blue). Each pose change is accompanied by a TTL output pulse (red). The DAQ is set to output a logical 1 for a period before and after the desired pose change. This causes the DM trigger to be transmitted through AND gate to trigger an image acquisition by the Orca Flash camera.

The PC controls the DAQ and so this output is still subject to 0.5 ms of jitter, however the DAQ is only used to select the period of time where the AND gate will allow pulses to go from the DM to trigger the Orca Flash camera. In this way, the timing of the camera acquisition is precisely controlled by the DM with no influence from the timing precision of the PC. The timing diagram between the DM, DAQ, AND gate and Orca Flash camera are shown in Figure 82.

The repeated triggering of multiple of images by the camera, e.g. a sequence of 40 images for the optimisation of the amplitude of one Zernike mode, was found to increase the background noise level of the camera. This effect is suspected to be due to the fact that each time an image is taken the readout process involves using amplifiers to determine the charge on each pixel, and this generates heat that increases the temperature and therefore background signal level output by the camera sensor. It was found that after a certain number of images a thermal steady state is achieved. Figure 82 shows the average brightness of the central 100 μm square of the Orca Flash camera's FOV for rapid sequences of images (rows) taken with the camera cap on. As can be seen, after several sequences a steady state is achieved.

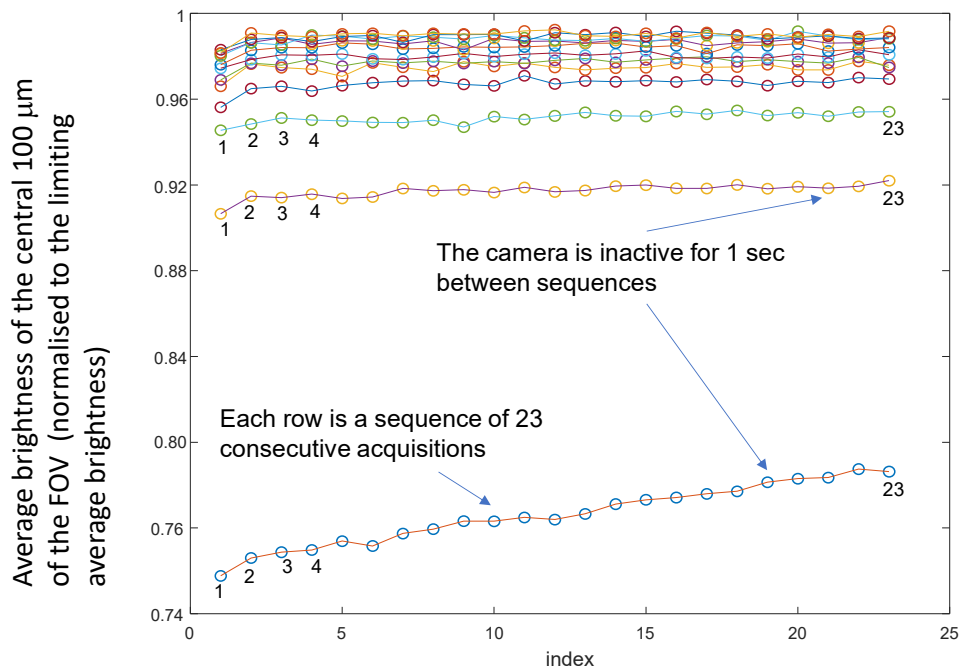


Figure 83 Sequences of 23 images taken consecutively (10ms exposure time, 20ms interpose time) by the Orca Flash camera with a 1 s delay between sequences. Each row corresponds to a sequence. After the 4th sequence, a thermal steady state has been reached by the camera. The cap was on during this experiment.

This heating effect could be managed by taking 5 sequences of optimisation images prior to the actual optimisation procedure for a particular mode. These images were taken only to allow the camera to achieve a thermal steady state and no change was made to the DM's oscillation. The same procedure

was followed when capturing images for evaluating the performance of an optimized mode. In the initial stages of the development of the optimisation algorithm background estimation was made by taking a series of images with the LED off, and so it was important that the camera be in a constant thermal state. This was not strictly necessary in later versions of the algorithm when a local correction for background was made for each pinhole.

It was then realised that the rolling shutter of the Orca Flash camera leads to different rows of the image being acquired at different delay times after the DM has changed its pose. This is illustrated in Figure 84, where the images were acquired with an interpose time of 25 ms and an exposure time of 2 ms. Panel (a) shows the Strehl map immediately after a pose change and (b) shows the map shortly before the next pose change.

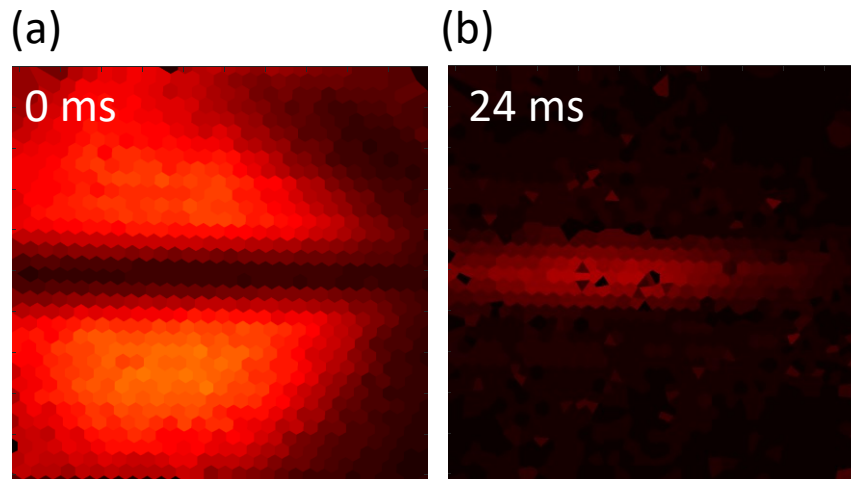


Figure 84 Strehl maps that show that near to a pose change a letterboxing artefact occurs – this is due to the rolling shutter of the Orca Flash camera. The interpose time was 25 ms and the exposure time was 2 ms. Note that in the Strehl map in Panel (a), the black stripe in the image at 0 ms is in a similar spatial location to the red stripe at 24 ms. It corresponds to part of the image corresponding to one pose and the rest corresponding to the next pose. However only one pose is in focus and has a good Strehl value. This is further illustrated by Panel (b) which is a raw image and only shows a horizontal stripe of in focus pinholes.

Due to the Orca Flash camera's rolling shutter, the exposure start time for each line on the camera has a delay of 10 μ s compared to the adjacent row due to the readout mechanism, and this occurs symmetrically starting from the horizontal midline of the sensor. The exposure of the horizontal midline of the camera therefore occurs at the same time as the pose change in Fig. 84(a). As the DM has not settled, then the STM pinholes near the midline are blurred and lower Strehl values are therefore measured in this region. As the mirror settles over time then the exposed lines roll up and down away from the midline and the Strehl values increase. This artefact can be prevented by using pulsed illumination timed to only illuminate the STM when the whole camera sensor is exposing. To implement this, the Global Reset mode of the Orca Flash camera was used, and the Global Exposure

TTL output on the Orca Flash camera was used to enable the LED light source. Then the Orca Flash camera sensor would only be illuminated by the LED when all rows were exposed. These settings on the camera remove the 'letterboxing' effect and Figure 85 shows the new electrical timing connections.

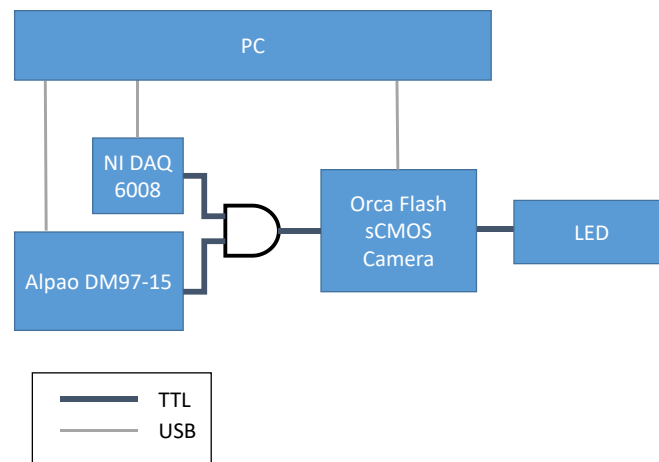


Figure 85 The Global Exposure output trigger of the Orca Flash camera is used to control an LED illumination source. In this way the LED is on only whilst the whole camera chip is being exposed.

The settling time of the mirror is specified by the manufacturer to be 0.39 ms [131]. However, this was measured from the step response from the central actuator. The time required for the measured Strehl metric to settle between high-NA defocus poses turned out to be longer, and this is studied below. To investigate the settling time of the DM, the delay between the DM pose change and the camera exposure was varied. The measured Strehl ratio then provided a readout of whether the mirror was still moving during the camera exposure. Figure 86 shows the mean Strehl ratio of the

central 200 μm square of the FOV following a step response from a 20 μm pose to a 30 μm pose and indicates that the mirror requires about 5 ms to finish moving.

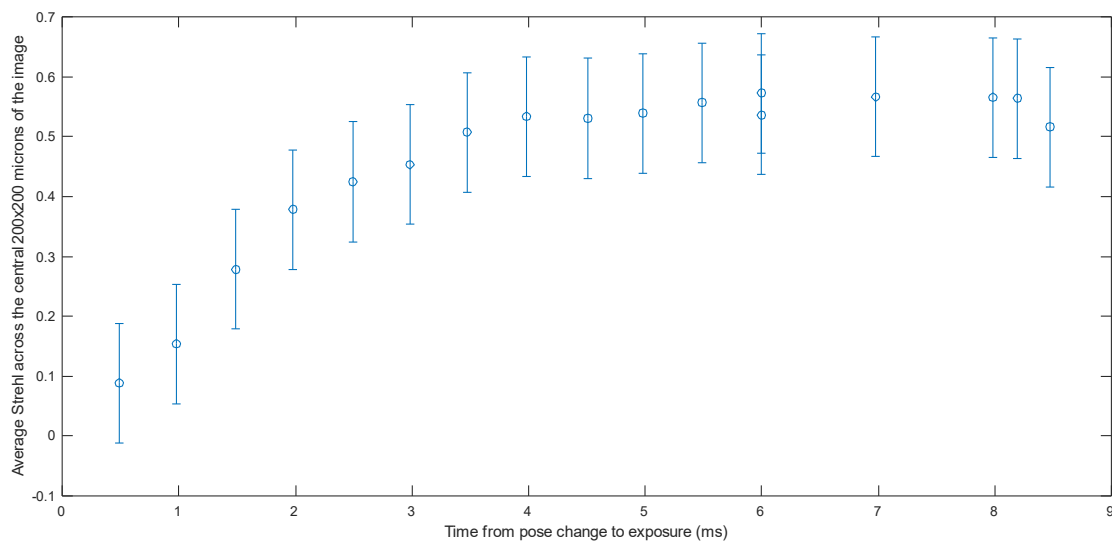


Figure 86 Average Strehl of the central 100 μm square as the time between the pose change and the exposure is varied. The mirror takes approximately 5 ms to settle.

If the mirror has not settled into its new pose when the camera acquisition is triggered, then this will blur the images of the STM pinholes, lower the measured Strehl metric and therefore affect the result of the optimisation. The optimisation results for different interpose times are shown in Figure 87 for a 1 ms camera exposure time and the exposure taking place 2 ms before the end of the interpose time in order to allow maximum time for the DM to settle. As expected, when the camera exposure takes place within 5 ms of the pose change, the optimisation is less successful. There is still some deterioration of the results when the camera exposure is within 8 ms of the pose change.

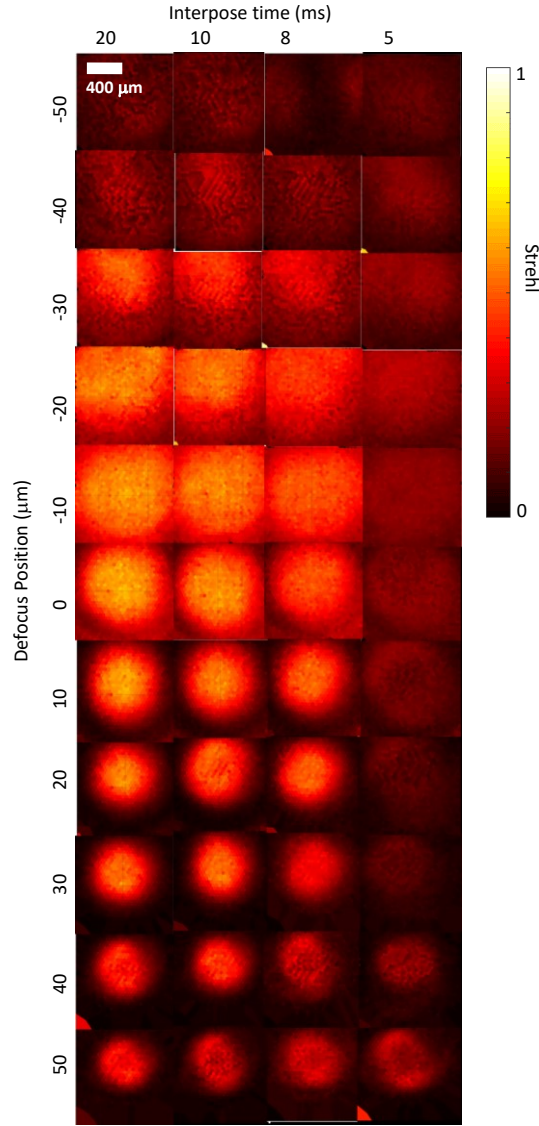


Figure 87 The effect of the settling of the mirror on the performance of the optimisation algorithm. The image was taken 2 ms before the end of the interpose interval and the exposure time was 1 ms.

Assuming the DM can settle in 5 ms and the refocus distance is 10 μm , this suggests that the fastest rate of change of high-NA refocus provided by the DM is changing is approximately 2 $\mu\text{m}/\text{ms}$. As the aim is to provide at least video-rate volumetric imaging over the maximum possible refocus range, it is clear that the settling time of the DM will limit the imaging performance that can be achieved if this method employing discrete pose changes is employed.

4.7.3 Asymmetric staircase pose sequence

The symmetric sawtooth staircase sequence of DM poses $\{-50, -40, \dots, 40, 50, 40, \dots, -40\}$ μm was chosen initially in order to avoid ringing of the mirror surface due to large jumps in the mirror surface upon fly-back. The symmetrical nature of the high-NA function with defocus meant that the time average of the mirror surface was on average flat (corrections introduced during optimisation were

an order of magnitude smaller than the largest high-NA defocus term). One advantage of this symmetric sawtooth was that there was no fly-back ‘dead-time’ and every mirror pose was used for imaging. However, the order of poses is reversed on each side of the staircase, and hence the time interval between a given refocus plane being imaged is not constant for all planes; this can lead to hard-to-compensate artefacts between neighbouring image volumes when imaging rapid events. To avoid this problem, an asymmetric sawtooth was investigated with a volumetric scan through the defocus positions {50, 40, ... , -40, -50}, followed by a comparatively fast flyback. The flyback would be ‘deadtime’ and not used for imaging. In addition, the return sequence must not move the mirror too quickly in order to prevent ringing effects. A convenient choice was found to be {50, 40, . . . , -40, -50} μm on the downward staircase with a flyback return of {-30, -10, 10, 30} μm , see figure 88. This choice was found to produce results as good as the symmetric pattern, data not shown. A bias was added to the return poses in order to ensure that the time average pose flat to prevent viscoelastic creep. The bias was found for a particular actuator by finding the sum of that actuator’s commands throughout the entire sweep. This was then divided by 4 and then subtracted from the {-30, -10, 10, 30} high-NA defocus actuator commands that were used for the fly-back. An advantage to applying the bias during the flyback was in debugging, in that it could be used to identify when an optimisation had gone off course, as this was often associated with a sudden change in the bias which could be identified by monitoring the flyback terms.

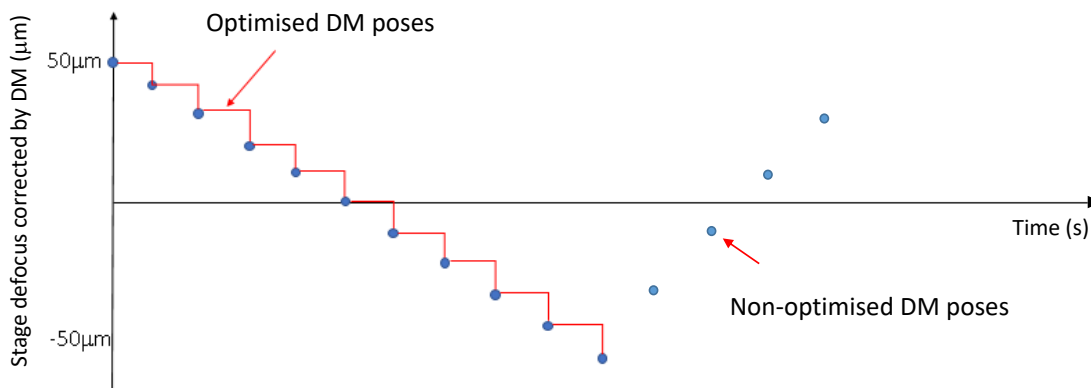


Figure 88 Sawtooth sequence of defocus positions, {50,40,30, ... -30,-40,-50,-30 -10,10,30} μm

4.7.4 Dynamic optimisation with continuous linearly interpolated DM sweep profile

Rather than stepping between discrete DM defocus positions, an improved approach was implemented to achieve an approximately smooth change of the DM’s pose over time. This required the DM pose update rate to be increased so that the DM update period was shorter or comparable to its settling time. Rather than waiting for the mirror to settle into each pose, a sequence of commands was sent to the mirror that were applied to the DM at 65 μs intervals, with each applying a short

impulse to the mirror surface. This allowed the mirror to be guided smoothly from one state to another and avoided sudden pose changes and ringing. The $65\ \mu\text{s}$ update interval was chosen as this is the device update rate of the Alpao DM and it provides a convenient mode of operation where a new pose can be set at this update interval.

At this higher DM pose update rate, a single sawtooth set of poses with a period of 10s of milliseconds requires 100s to 1000s of actuator commands, and it is not possible to optimise all of these poses in a reasonable amount of time. Therefore, the approach used was to optimize a subset of commands associated with the discrete set defocus positions used in the previous section, i.e. $\{50, 40, 30, \dots, -30, -40, -50\}\ \mu\text{m}$, which will be referred to as control poses, and then to linearly interpolate the intermediate commands as shown in Figure 89. Other interpolation approaches were tried such as quadratic interpolation and also interpolation via splines, however they were not found to offer a significant advantage in the optimisation and had a larger calculation overhead compared to linear interpolation.

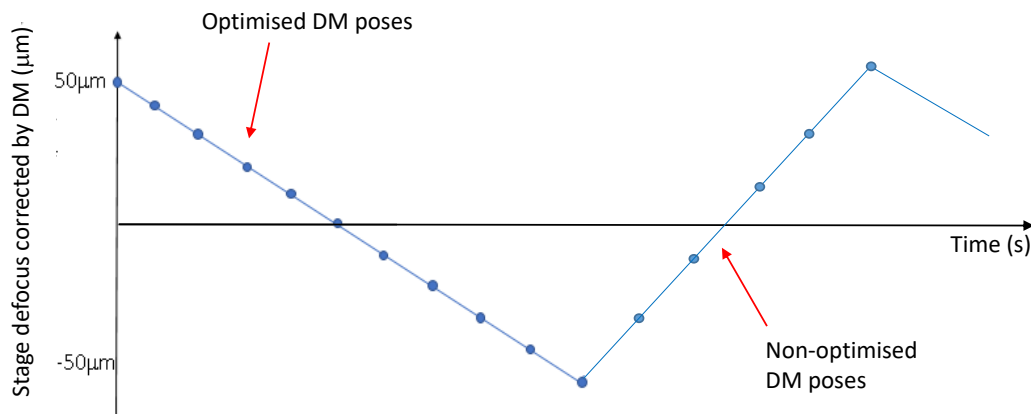


Figure 89 Command poses (blue dots) are explicitly optimised. The poses inbetween are linearly interpolated (blue line). The DM surface is updated with a new pose every $65\ \mu\text{s}$.

Figure 90(a) shows (a) the previous discrete and (b) the new continuous commands applied to an exemplar actuator during a single refocus sweep at $26.3\ \text{vol/sec}$.

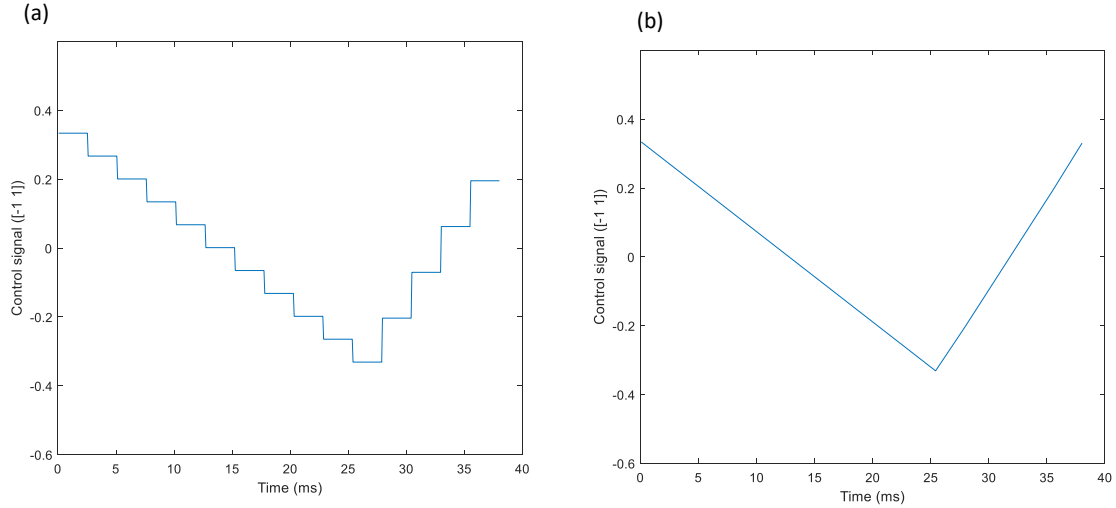


Figure 90 Panel (a) shows the saw-tooth of command values sent to an exemplar actuator during a discontinuous staircase sequence of poses where the mirror is moved and held. Panel (b) shows the saw-tooth command values for continuous movement of the mirror surface where the positions between the command values are linearly interpolated. In both (b) and (c) the return poses are used to apply a bias in order to ensure that the average command value is zero.

Once the actuator command data has been loaded to the DM it can be set to play the sequence repeatedly. At the beginning of each repeat the DM outputs a single TTL pulse. Previously, the DM commands had 0.5 ms of jitter as they were controlled by the Windows operating system's HRT. However, using the TTL pulse from the DM made full electronic timing possible and all jitter was removed. The Orca Flash camera was triggered at the beginning of the ramp sequence and was programmed with a sufficiently long hardware-timed delay so that the image acquired corresponded to the desired pose. Figure 91 shows the electronic triggering timing.

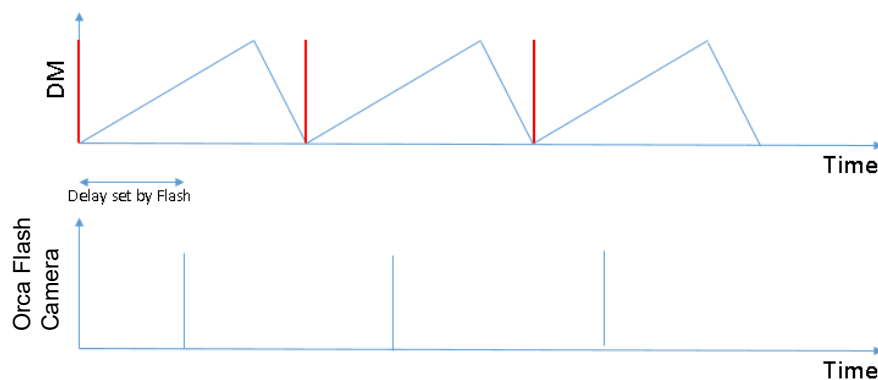


Figure 91 The DM is set to repeatedly play a sequence of commands corresponding to a full refocus sweep. At the beginning of the sequence, the DM outputs a TTL trigger pulse (red line on the DM timing diagram), which was used to trigger an exposure on the camera. The camera was set to introduce a delay between receiving the trigger from the DM in order to take an image of the mirror in the desired pose.

It was found that for interpose times between control poses smaller than 5 ms (13.3 refocus sweeps/sec) the optimisation would fail. This was due to the mirror surface moving during the camera exposure (the minimum exposure of the Orca Flash camera in this mode was 1 ms). The change in applied phase, due to motion of the DM during the camera integration, can be regarded as wavefront aberration. A change of high-NA defocus of $0.4\text{ }\mu\text{m}$ is enough to break the Strehl condition between 2 high-NA defocus poses. Since the mirror smoothly moves from one pose to another, a defocus change of $0.8\text{ }\mu\text{m}$ between the start and end poses would result in an average change in pose of $0.4\text{ }\mu\text{m}$. This means that over the integration time of the camera exposure the amount of change of high-NA defocus between the start and finishing pose must be no more than $0.8\text{ }\mu\text{m}$. With the Orca Flash camera running at its shortest exposure time (1 ms), this means the fastest speed that DM can move at most at $0.8\text{ }\mu\text{m/ms}$ in order for the image of the STM pinholes not to be blurred sufficiently by the motion of the DM to break the Strehl limit.

A refocus sweep rate of 26.3 sweeps/sec, which is an effective interpose time between the control poses of 2.535 ms, means the mirror is moving at $4.0\text{ }\mu\text{m/ms}$ (which is greater than $0.8\text{ }\mu\text{m/ms}$) and so there would be considerable blur and the resulting images would not be diffraction limited. In order that the defocus change of the mirror be only $0.8\text{ }\mu\text{m}$, the exposure time of the camera would need to be $0.8/4.0 = 0.2\text{ ms}$. This is shorter than the minimum exposure time of the Orca Flash camera and was achieved by reducing the duration of the illumination light pulse from the LED. A second National Instruments (NI) digital acquisition (DAQ) box (model 6363) was therefore added to the electronics controlling the system. It was configured to be triggered by the rising edge of the 1 ms TTL pulse output by the Orca Flash camera to produce a 0.20 ms pulse. With this reduced illumination pulse duration, the LED was at the limit of being bright enough to perform meaningful optimisation (the mean Strehl score was noisy and it was difficult to identify a maximum). Therefore, each round of the optimisation of a particular Zernike mode was conducted with a range of illumination pulse durations (found by trial and error), first at 0.5 ms, then 0.3 ms and finally 0.2 ms. This approach was able to optimize the mirror at a refocus sweep rate of 26.3 sweeps/sec.

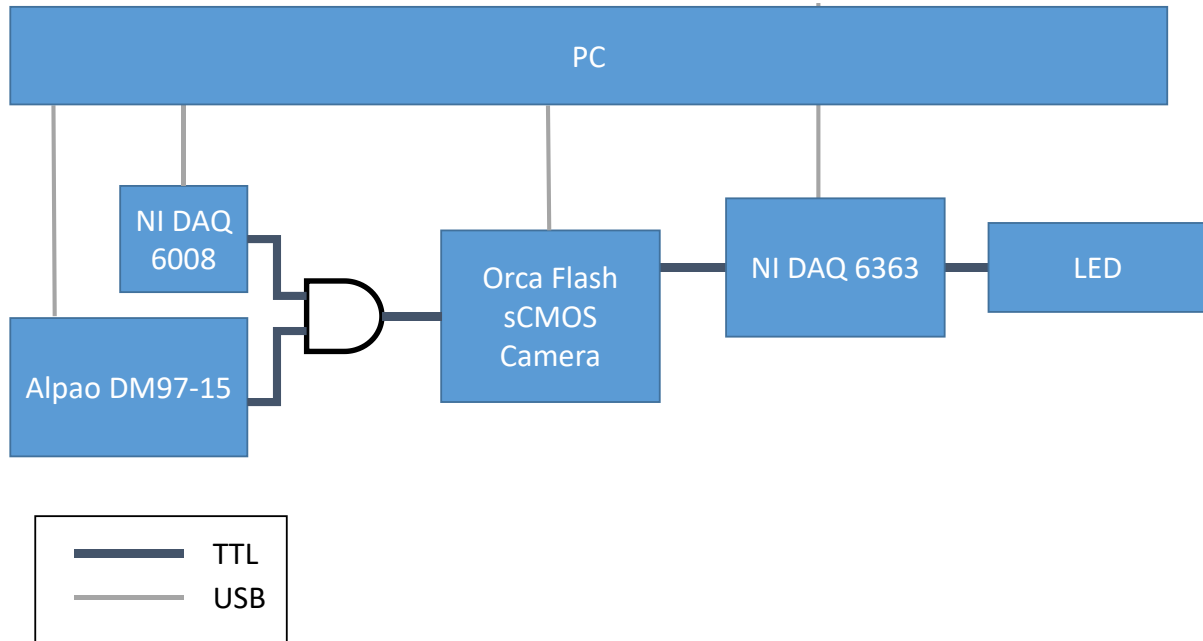


Figure 92 The output pulse from the Orca Flash camera is reduced from 1 ms to 0.3 ms by the NI 6363 DAQ. Figure shows the final electronic system used for linearly interpolated dynamic optimisation.

The organization of the electronic components is shown in Figure 92. The whole optimisation procedure for 11 control poses per sweep (585 poses in total including linearly interpolated poses), took approximately 90 minutes. Re-optimisation, along with re-flattening the DM, was found to be required probably due to variations in ambient temperature and humidity as investigated in reference [4]. However, often only a single round of optimisation was needed for each mode if the starting point was the previous day's set of commands, and the optimisation could immediately proceed with an LED pulse duration of 0.5 ms.

Following the optimisation, there was an evaluation step where images of the STM were obtained for each defocus position with the STM displaced by -2 to 2 μm from the position used during optimisation and Strehl maps obtained. Results for an Olympus 40x/0.85 air objective are shown in Figure 93 (a). The data from each defocus position were then combined to produce the best Strehl map for each optimised defocus position (Figure 93 (b)). The final column (Figure 93 (c)) shows the displacement of the STM at which the best Strehl value was obtained, and therefore indicates the amount of field curvature present at each optimised defocus position. The field curvature increases with defocus and reverses in sign through the focal plane.

The procedure was repeated for an Olympus water dipping 40x/0.80W – where ultrasound (US) gel was used as the immersion medium as the lens was mounted horizontally (the US gel has a refractive index within 1% that of water). One issue with using the US gel was with trapped bubbles of air; bubbles that were far from the plane being imaged could still produce significant aberrations – which

would negatively affect the Strehl map and could throw the optimisation off course, resulting in poor performance. A thorough check for bubbles prior to optimisation appeared to mitigate this issue. Also, the US gel would evaporate during the optimisation procedure, and ensuring that there was a large 'lump' of US gel around the lens reducing the surface area to volume ratio made this effect manageable. The results are shown in Figure 94 and also show increasing field curvature with defocus. This shows that for both objectives there is a limit to the amount of high-NA defocus that can be corrected with the deformable mirror in the configuration used in this setup. The DM in a Fourier plane is unable to correct for field dependent aberrations such as field curvature and the best that can be achieved is an average correction.

Figure 95 shows a plot of (a) the maximum Strehl metric over the central $200 \times 200 \mu\text{m}^2$ of the camera FOV for both objectives as a function of optimised defocus positions both for the static and the dynamic optimisations. For the water dipping objective, a mean Strehl of >0.6 was obtained over a defocus range of $80 \mu\text{m}$; for the air objective the range was $45 \mu\text{m}$. For the $40\times/0.85$ air objective the performance achieved with the dynamic optimisation was lower than that achieved with the static optimisation, which can be attributed to the motion of the DM during the 0.2 ms LED illumination and also the poor S/N. S/N was an important requirement for a successful optimisation and 0.2 ms was at the limit in terms of the brightness of the LED and better results would be expected in a future iteration with a brighter light source.

For both the air and water dipping objectives, the amount of each mode applied for each defocus position is shown in Figure 96. Beyond Z13, further Zernike modes provided no further improvement in the mean Strehl metric. The dashed horizontal lines in this figure show the amount of each mode alone that would be required to exceed the Strehl limit in order to give an indication of the scale of the applied correction.

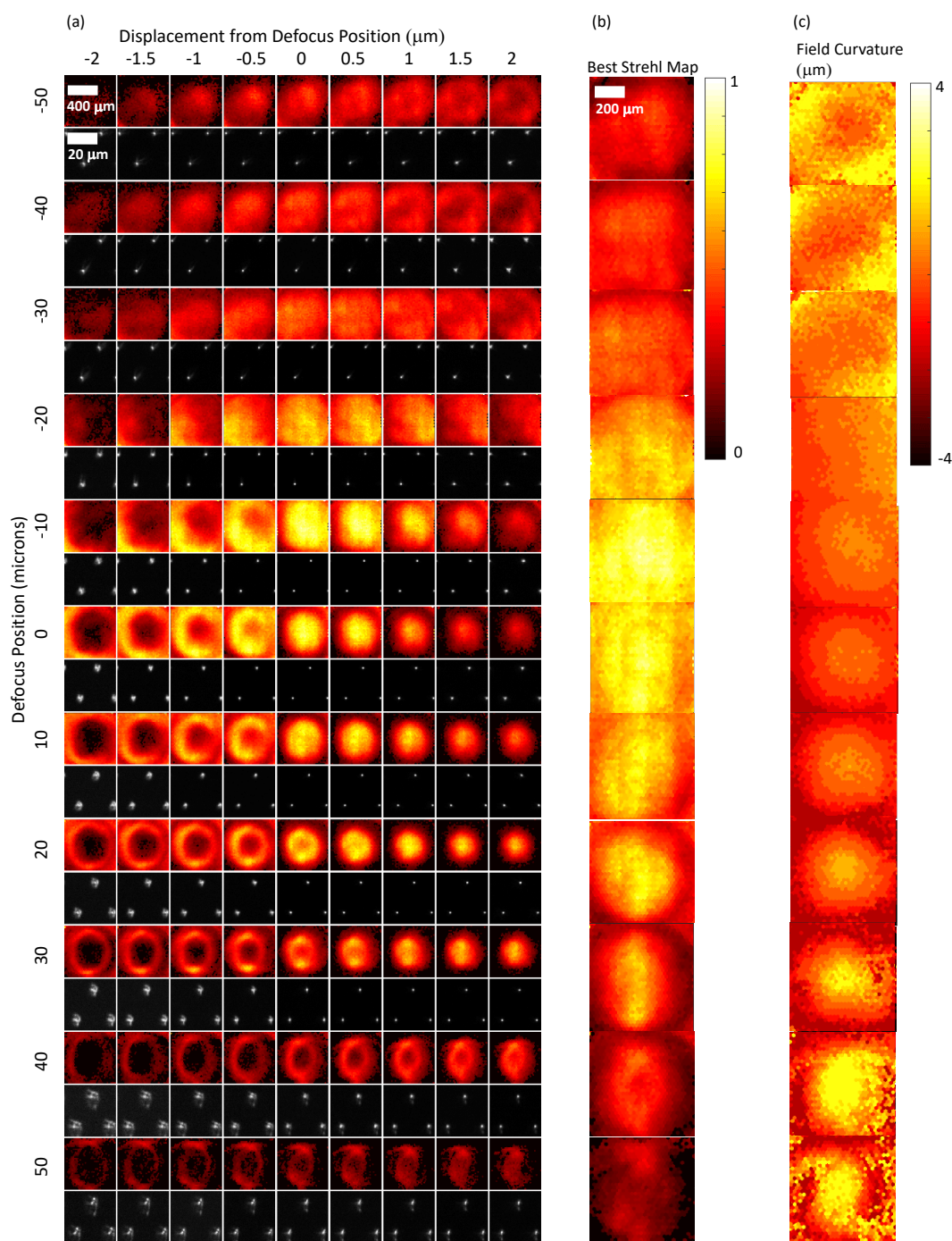


Figure 93 Results obtained from dynamic optimisation of the DM at 26.3 Hz with the 40 \times /0.85 air objective and coverslip. a) False-colour Strehl maps (upper row) and small ROI of raw star test mask image from the centre of the camera's FOV (lower row) for DM poses optimised to provide defoci of -50 to 50 μm in 10 μm steps (top to bottom). For clarity, the brightness of each raw star-test mask image has been individually scaled to the maximum for that image. For each optimised DM pose, data is shown for star test mask defocus positions Δz of -2 to 2 μm in 0.5 μm steps away from the defocus position used during DM optimisation (left to right). b) False-colour map of best Strehl value for each pinhole taken over all Δz values. c) False-colour map showing Δz location in units of μm of the best Strehl value for each pinhole, i.e. showing the curvature of the field imaged. *Figure reproduced from [134].*

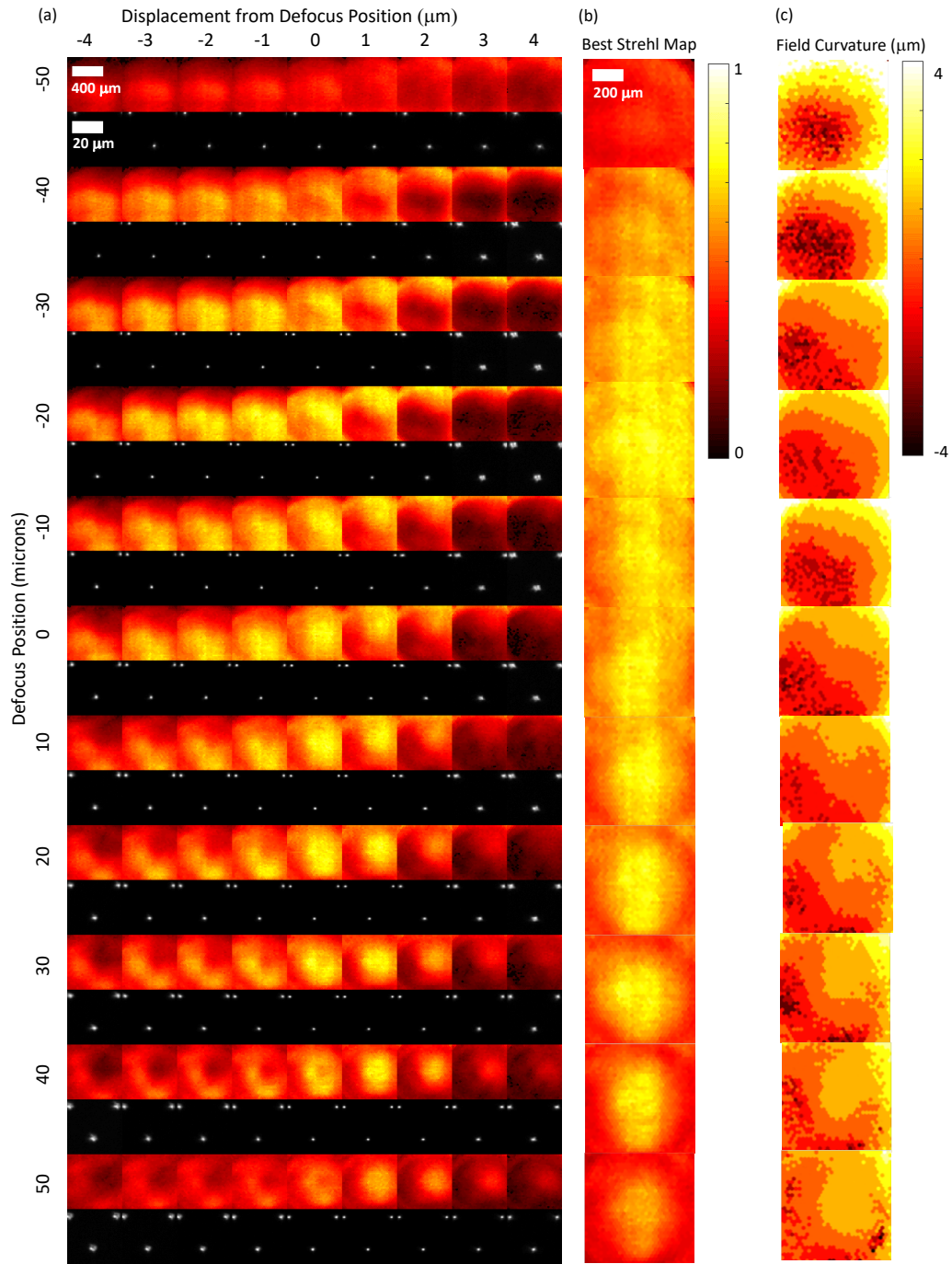


Figure 94 Results for dynamic optimisation of the DM at 26.3 Hz for the 40 \times /0.80 water dipping objective with ultrasound gel as the immersion medium. a) False-colour Strehl maps (upper row) and small ROI of raw star-test mask image from the centre of the camera's FOV (lower row) for DM poses optimised to provide defocuses of -50 to 50 μm in 10 μm steps (top to bottom). For clarity, the brightness of each raw star-test mask image has been individually scaled to the maximum for that image. For each optimised DM pose, data is shown for star-test mask defocus positions Δz of -4 to 4 μm in 1 μm steps away from the defocus position used during optimisation (left to right). b) False-colour map of best Strehl value for each pinhole taken over all Δz values. c) False-colour map showing Δz location in units of μm of the best Strehl value for each pinhole, i.e. showing the curvature of the field imaged. Figure reproduced from [134].

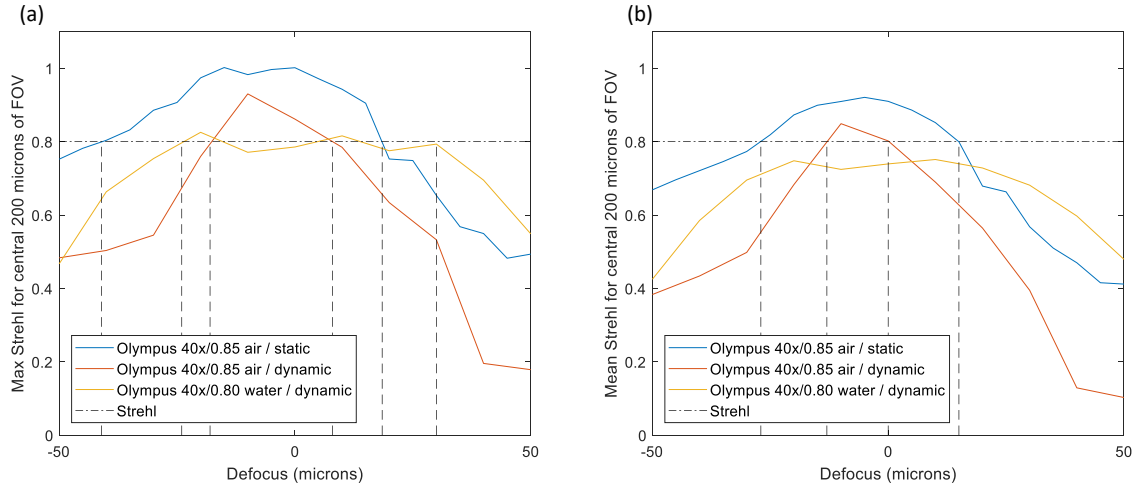


Figure 95 Maximum Strehl (a) and mean Strehl (b) of the central 200x200 μm square of the field of view for the statically optimised Olympus 40x/0.85 air objective, as well as the dynamically optimised (26.3 refocus sweeps/sec) Olympus 40x/0.85 air objective and Olympus 40x/0.80W water immersion objective. The dashed line shows the diffraction limit. Figure reproduced from [134].

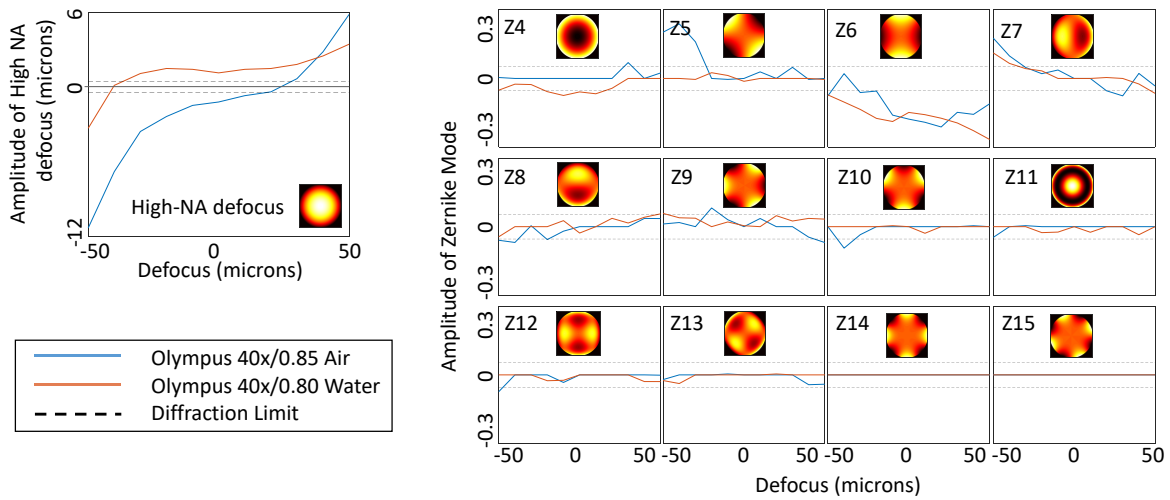


Figure 96 Plots showing the amplitude of the high NA defocus mode and Zernike modes (indexed by Noll index), for each defocus. Blue curve shows results for the 40x/0.85 lens with coverslip. Red curves show results for the 40x/0.8 water lens with ultrasound gel as the immersion medium. The black dashed lines show the Strehl limit above which the RMS wavefront aberration for that mode alone exceeds the diffraction limit of $\lambda/14$. Figure reproduced from [134].

To further validate the performance of the system for the 40x/0.80W objective, the DM was set to sweep at 26.3 Hz through the set of dynamically optimised poses with the camera acquiring an image of the star-test mask (with a reduced FOV) for every optimised DM pose, i.e. 11 images per oscillation of the mirror. During this process, the star-test mask was moved with a constant axial velocity from -50 to 50 μm at a rate of 6 μm s⁻¹ as shown in Figure 97. Figure 98 shows a montage of the data

acquired, with the images from each sweep (defocus position) shown as a column and with data from successive sweeps shown moving from left to right. It can be seen that the images where the star-test mask is in focus (diagonal) tracks the motion of the stage and validates the DM defocusing scanning at video frame rate.

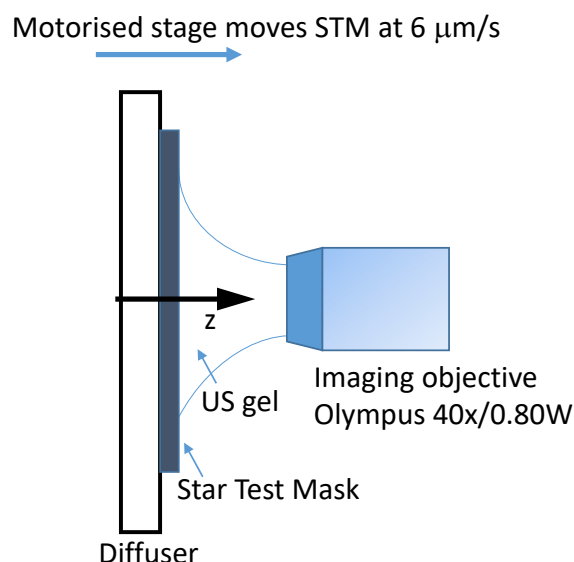


Figure 97 Schematic showing how the STM is moved towards the imaging objective at 6 $\mu\text{m/s}$ at the imaging objective is volumetrically refocused at a rate of 26.3 sweeps/sec through a range of -50 to 50 μm .

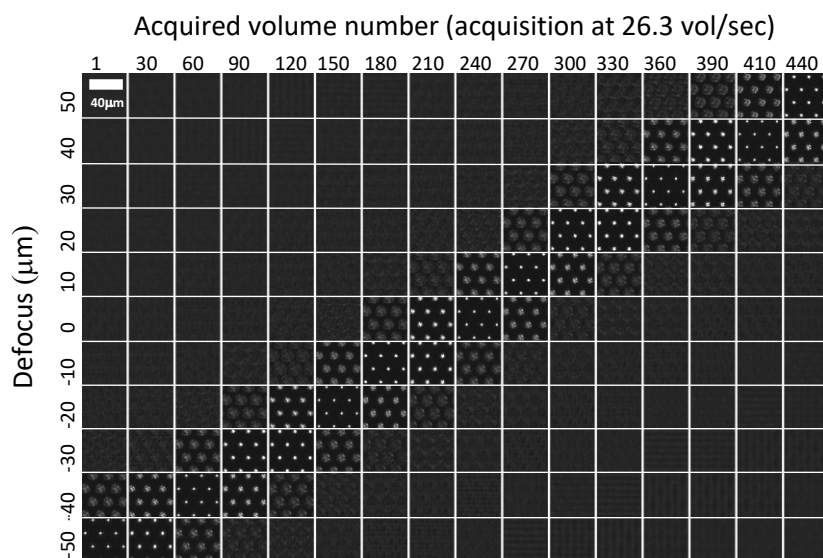


Figure 98 Image sequence acquired from every defocus position as a function of time as the star-test mask is translated at a constant velocity of 6 $\mu\text{m s}^{-1}$ towards the microscope objective. Data was acquired using the 40 \times /0.80W objective with ultrasound gel as the immersion medium. Refocus sweeps were performed at 26.3 Hz. Each column shows a sequential set of sCMOS images acquired at each of the 11 control poses of the DM, which correspond to refocus positions over the range -50 to 50 μm . Non-consecutive DM sweeps/volumes are shown moving left to right across the figure. Figure reproduced from [134].

4.8 Summary

This chapter has presented the development of an optimisation approach and algorithm to use the Alpao DM97-15 membrane deformable mirror to remotely refocus a microscope at 26.3 sweeps per second. The performance of the system was tested with a 40x/0.85 air objective and a 40x/0.80 water objective. The air objective enabled a mean Strehl metric of >0.6 over a field of view of $200 \times 200 \mu\text{m}^2$ and for a refocus range of $40 \mu\text{m}$. The water objective with ultrasound gel immersion fluid achieved a mean Strehl metric of >0.6 over $200 \times 200 \mu\text{m}^2$ over a larger refocus range of $77 \mu\text{m}$. These results showed increasing field curvature with defocus, which means that there is a limit to the amount of defocus that can be corrected with a single deformable mirror located in the plane conjugate to the pupil of the objective as it is unable to correct for field-dependent aberrations.

Initially, the DM was used in a static mode, however the optimisation was time consuming due to the need for pauses to cope with thermal creep. The optimisation algorithm involved first optimizing the amount of high-NA defocus on the mirror and then optimizing a set of Zernike modes until an improved local maximum is found. Next the mirror was optimized in a quasi-dynamic sense where the mirror was oscillated to achieve a thermal steady state and then the high-NA defocus and Zernike modes optimized. Next a fully dynamic optimisation procedure was developed. Initially, a discrete, step and settle approach was tested, however this was found to be limited by the settling time of the DM. Finally, the mirror was operated in a continuous manner where control defocus positions were optimized and poses between these determined by linear interpolation. The final optimisation procedure took 90 min.

The refocus rate of the DM was limited by the power of the LED light source used during the optimisation and much faster sweep rates should be achievable with a brighter light source.

In the next chapter this refocusing system will be used as the refocusing component of a LSFM to achieve volumetric imaging.

Chapter 5 : Deformable Mirror based Light Sheet Fluorescent Microscope

5.1 Introduction

In this chapter the development of a deformable mirror (DM) based light-sheet fluorescence microscope (LSFM) is presented. The DM was optimized for volumetric imaging in the manner described in chapter 4. These actuator commands were then used to refocus the imaging arm of a LSFM for volumetric imaging which was used to image corn and sunflower pollen, and the resolution of the system estimated with fluorescent beads (0.2 μm TetraSpeckK microspheres).

5.2 Deformable-mirror-based light-sheet fluorescence microscope

The system is made up of an illumination subsystem and an imaging subsystem, as shown in Figure 99 (a). Light from a laser diode (Oxxius, 40.0 mW, 488 nm laser diode), was collimated using a microscope objective (Olympus 10x/0.25), and then passed through cylindrical lens CY (50 mm focal length), to focus the beam in one direction. The galvo mirror was placed in the focal plane of the cylindrical lens and was used to add a linear phase profile to the wavefront. The inclination of the galvo mirror is proportional to the applied voltage – so the gradient of the linear phase profile was also proportional to the applied voltage. The galvo was made conjugate to the back focal plane of the illumination objective (Nikon 10x/0.30W) through the use of the afocal relay formed by plössl lenses L1 and L2, each with a focal length of 100 mm. The linear phase profile added by the galvo caused the light-sheet to move up and down through the sample, in the direction perpendicular to the illumination optical axis and parallel to the optical axis of the detection arm. Fluorescence was captured by the Olympus water immersion 40x/0.85 NA imaging objective (LUMPLFLN, Olympus), which had an optical axis that was perpendicular to the optical axis of the illumination objective. The back focal plane of the imaging objective was made conjugate to the deformable mirror (DM) through the use of a fold mirror and an afocal relay formed by tube lenses L3 (focal length 100 mm) and L4 (focal length 200 mm). The DM (DM97-15, Alpao) applied a phase correction for the high-NA defocus and system aberration as described in the last chapter. The light was then passed through an emission filter and finally L5 (focal length 200 mm) created an image on the sCMOS camera (Orca-Flash4.0 v3, Hamamatsu).

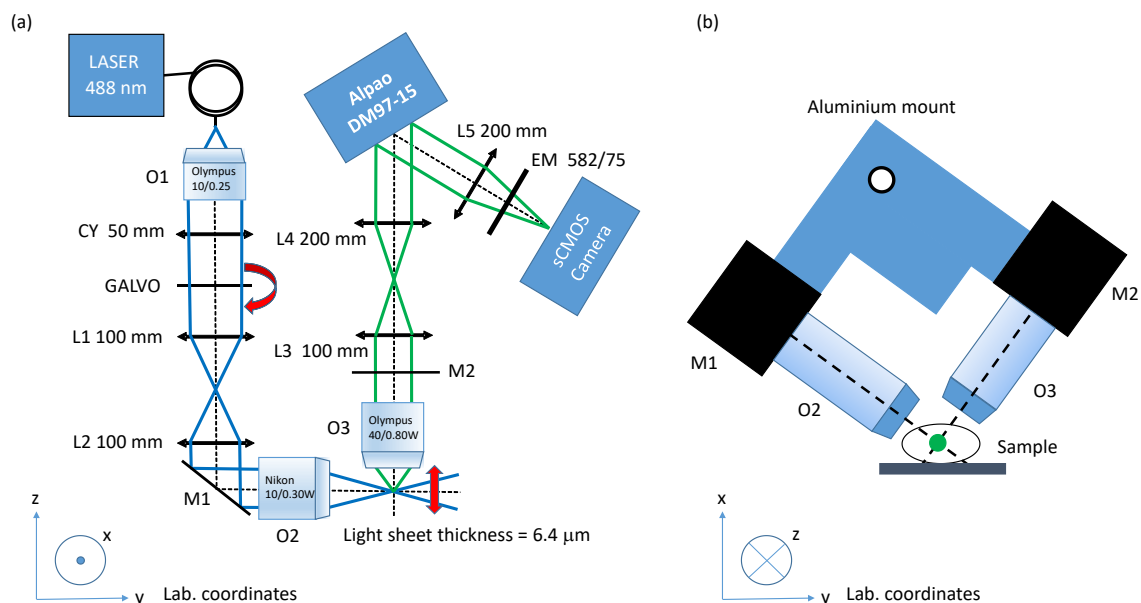


Figure 99 Panel (a) shows a schematic of the deformable-mirror-based light-sheet fluorescence microscope. Light at a wavelength of 488 nm produced by a laser diode is coupled to a mono-mode fibre and then collimated by an Olympus 10x/0.25 objective (O1). The light is then passed through a 50 mm focal length cylindrical lens CY which creates an focused line of illumination on the galvo mirror. This is relayed via a pair of plossl lenses (100 mm) to the back focal plane of the Nikon 10x/0.3W (O2) illumination objective which creates the light-sheet in the sample. The emitted fluorescence is then collected by the Olympus 40x/0.8W imaging objective (O3) whose back focal plane is relayed by the tube lenses L3 (100 mm), L4 (200 mm) to the DM, which applies a phase correction before being brought to focus by tube lens L5 (200 mm) onto the sCMOS camera. Panel (b) shows the V-shape iSPIM arrangement of the illumination and imaging objectives to an aluminium mount.

Laser diode	40.0 mW, 488 nm	Oxxius 40.0 mW, 488 nm laser diode and ND filters (Comar, 06 GN 25, 08 GN 25)
O1	Olympus 10x/0.25 objective	Olympus, PLN 10x/0.25 Plan Achromat
CY	50 mm cylindrical lens	Thorlabs, ACY254-050-A
G	Galvo mirror	Cambridge Tech, 6215MH40
L1, L2	100 mm Plössl lenses	Each Plössl lens made up from two 200 mm doublets each Thorlabs, AC254-200-A-ML
M1	Broadband dielectric mirror	Thorlabs, BB1 ED2
O2	Nikon 10x/0.3W objective	Nikon, MRH07120
Motion controller	Motion controller, to control stage	Newport, ESP 100
O3	Olympus 40x/0.80W objective	Olympus, LUMPLFLN
L3	100 mm tube lens	Thorlabs, TTL100A
L4, L5	200 mm tube lens	Thorlabs, TTL200A
EM	Emission filter	Semrock, EM 582/75
Camera	sCMOS Camera	Hamamatsu, OrcaFlash3v4

Table 6 A list of components used in the deformable-mirror-based LSFM shown in Figure 99.

This is then relayed via a pair of plössl lenses (L1 and L2) to the back focal plane of the Nikon 10x/0.3W (O2) illumination objective which creates the light sheet in the sample. The emitted fluorescence is then collected by the Olympus 40x/0.8W imaging objective (O3) whose back focal plane is relayed by a telescope composed of 100 mm (L3) and 200 mm (L4) tube lenses to the DM and a phase correction is made before the image is focussed onto the sCMOS camera by a 200 mm focal length tube lens (L5). O1, CY, GALVO, O2 and O3 are drawn in the plane of the diagram for clarity, but in practice were oriented at an angle to the plane of the diagram. Panel (b) shows the V-shape iSPIM arrangement of the illumination and imaging objectives attached to an aluminium mount and the angles of O2 and O3 in the x-y plane. The imaging and illumination objectives are inclined into a V-shaped iSPIM configuration and positioned in order to maximise the overall working distance and therefore convenience for sample mounting and imaging, as shown in Figure 99 (b). The imaging objective O3 along with fold mirror (M2) were attached to a rotating cage segment, which was able to rotate along the optical axis of the imaging arm. This enabled the imaging objective to be switched from being positioned for operation as a LSFM to a position that uses the star test mask (STM) to optimise the DM as described in Chapter 4 and is shown in Figure 100. At the beginning of each day the DM was flattened with the Shack-Hartman wavefront sensor (SHWFS) and then optimised for volumetric imaging at the desired rate. This full procedure took 90 min on average.

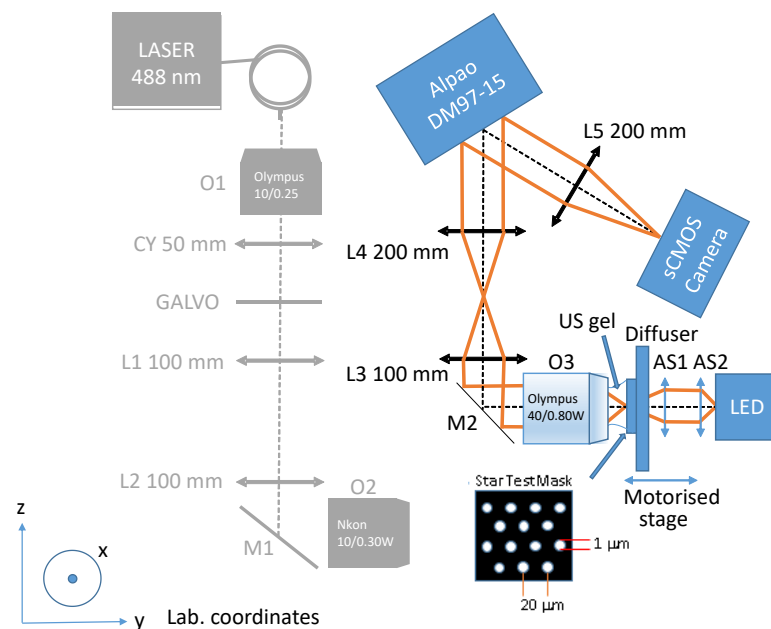


Figure 100 The LSFM in its optimisation mode. The imaging objective (O3) is unbolted from the aluminium mount and rotated to face the Star Test Mask (STM). The back focal plane of O3 is folded through 90 deg by M2 and then relayed to the DM by L3 and L4. The optimisation procedure of Chapter 4 is used to find the sequence of surfaces to apply to the DM in order to refocus the objective at video frame rates.

5.3 Imaging sub-system

The imaging arm is based on the experimental setup used for DM optimisation described in Chapter 4. In this previous setup, the imaging objective (Olympus 40x/0.80W) was mounted on a z-axis translation mount, and the 100 mm and 200 mm focal length tube lenses were mounted within a 60 mm Thorlabs cage as shown in Figure 101. For the LSFM setup, the previous setup was modified by putting a 60 mm to 30 mm cage adapter before the 100 mm tube lens and then a 30 mm rotating cage segment and finally a right-angle mirror before the objective, as shown in Figure 102. Since the setup of DM and camera had already been aligned in Chapter 4, the z-axis translation mount holding the imaging objective was positioned along the optical rail so that the 100 mm tube lens and imaging objective were in a 4-f arrangement, and this was determined with use of a shear plate and alignment laser.

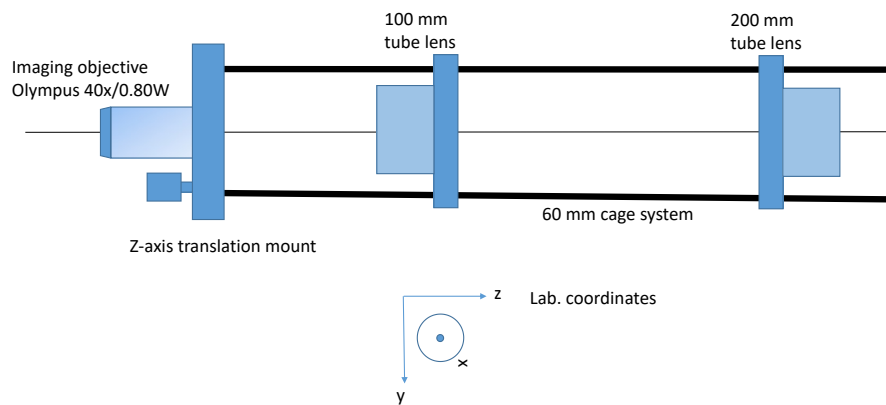


Figure 101 View along the z-axis of the opto-mechanics of the optical system as it was configured for the work described in Chapter 4.

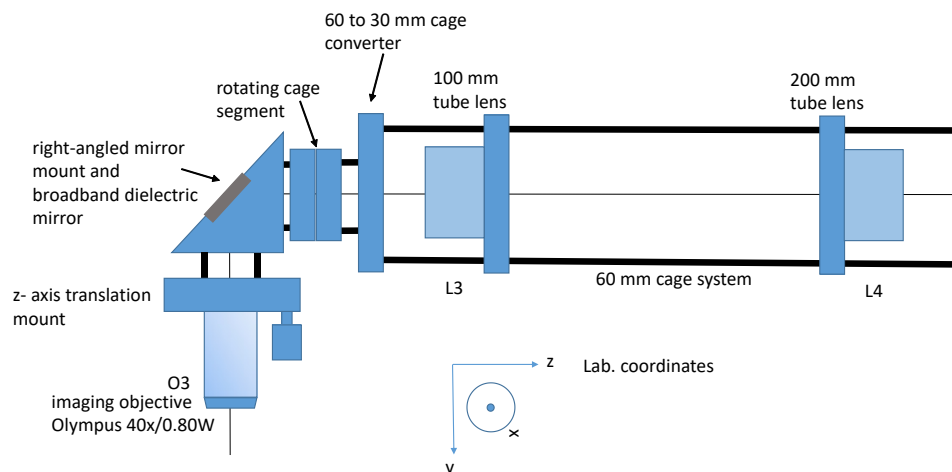


Figure 102 Changes in the opt-mechanics of the imaging arm showing the cage converter, rotating cage segment, right-angled mirror and z-axis translation mount.

In order to accommodate the V-shaped arrangement of the imaging and illumination objectives, an aluminium mount was introduced into optical system as shown in Figure 99 (b). The rotating cage segment was used to rotate the right-angled mirror mount about the optical axis of the imaging subsystem so that it could be bolted onto the aluminium mount when the system was to be used for LSM. When the setup was used to optimise the DM, the right-angled mirror mount was unbolted from the aluminium mount and then the rotating cage segment moved so that the imaging objective was horizontal and positioned to image the STM.

The introduction of the extra fold mirror into the imaging subsystem produces a slight reduction in the Strehl map across the field. Figure 103 (a) shows the results of optimisation when the components were arranged in a line as shown in Figure 101, as was used in Chapter 4. Figure 103 (b) shows the equivalent results obtained with the components arranged with the right-angled bend for LSM.

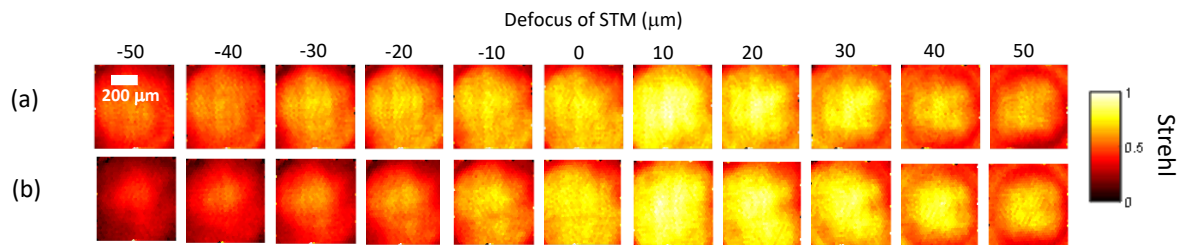


Figure 103 Panel (a) shows the Strehl maps obtained after the DM was optimised at 26.3 vol/sec with the imaging arm in the same configuration as Chapter 4 and shown in Figure 95. Panel (b) shows the results of optimisation with the rotating cage segment and fold mirror L2 as shown in Figure 96. These results show that there is a slight deterioration in the Strehl maps at each defocus after introduction of the fold mirror.

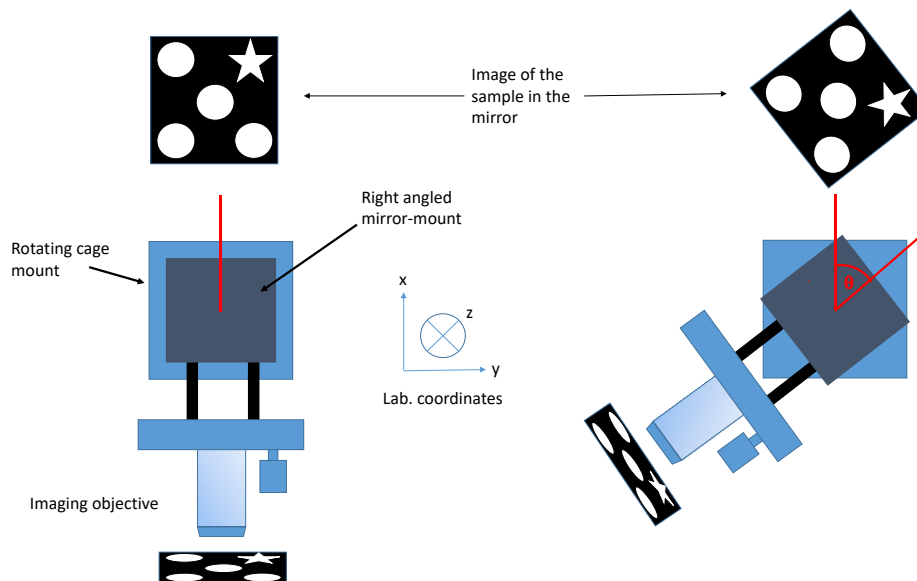


Figure 104 Figure shows that as the imaging objective (O3) is rotated (through angle θ), the image of the sample is also rotated through θ .

In the LSFM mode, the inclination of the rotating cage segment rotated the image captured by the Orca Flash camera through the angle of inclination, as shown schematically in Figure 104.

When the imaging objective was rotated by the rotating cage segment it also rotated the image of the pupil of the objective through the angle of rotation as shown in Figure 104. It was also found that the centre of the image of the pupil ‘walked’ as the objective was rotated, as shown in Figure 105. This was likely due to the finite tolerance of the rotating cage segment and also the precision of the attachment of the fold mirror to the imaging arm. It had been found that without the fold mirror – with all of the components arranged in a line that the image of the pupil was displaced by much less than with the right angle fold mirror as the objective was rotated. Ideally this issue could be eliminated in a further iteration of the system with a design which did not require moving the imaging objective. To provide a pragmatic solution to the problem, the objective was flooded with light by illuminating the diffuser with the LED such that the range of rays filled the NA of the lens. This resulted in a sharp edge to the image of the back focal plane on the DM. A camera fixed near to L4 captured an image of the fully illuminated back focal plane of O3 projected onto a white screen placed just in front of the DM for each of the two positions that the objective would be used. This showed that the centre of the image of the back focal plane moved 0.6 mm in the vertical direction and 0.1 mm in the horizontal direction as the objective was moved from its optimisation position with $\theta = 270^\circ$ deg, to being used for LSFM with $\theta = 41.4^\circ$ deg (this was determined by the method described in Section 5.7). These displacements would later be combined with the estimate for the displacement of the axis of the imaging system to the centre of the DM as described in chapter 3, along with a rotation of the pose profile, when the DM was used to refocus the objective lens in its LSFM configuration.

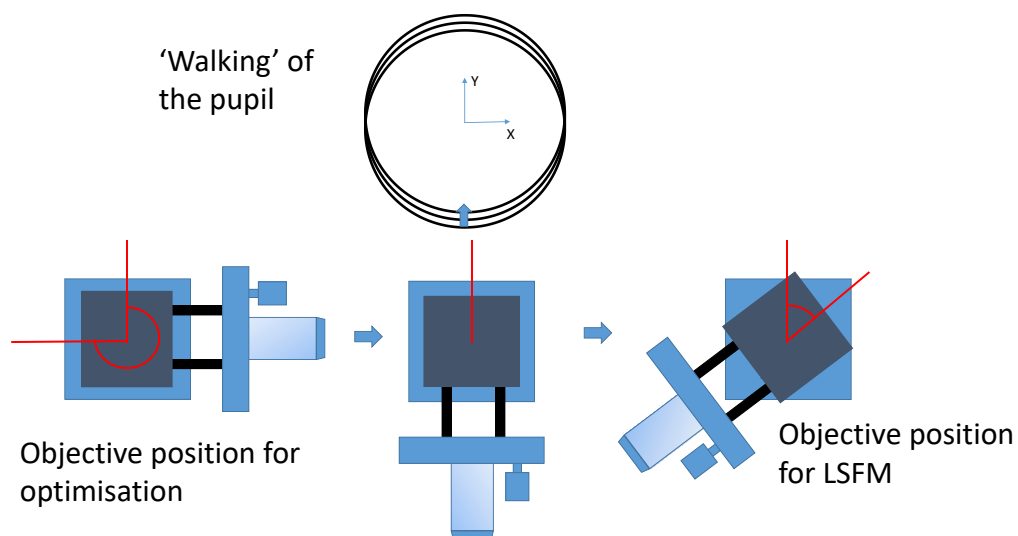


Figure 105 As the imaging objective (O3) moves from its optimisation position ($\theta = 270^\circ$) to its position in a LSFM configuration ($\theta = 41.4^\circ$), the centre of the image of the pupil of O3 changes. It was found that the pupil walked 0.1 mm in the y direction and 0.6 mm in the x direction.

5.4 Illumination sub-system

The illumination subsystem created a light-sheet and scanned it up and down in the direction parallel to the axis of the imaging optical system. The illumination was created using a beam from an Oxixus 40.0 mW, 488 nm laser diode and coupled into a single mode fibre using a kineFLEX (Qioptic) fibre delivery system. When carrying out alignment, the output from the laser was passed through 2 ND filters of optical densities 0.6, 0.8 (06 GN 25 and 08 GN 25, Comar), to reduce the optical power to 1.6 mW. Collectively, these components reduced the power output from the fibre to 0.65 mW. As shown in Figure 106, the light output from the fibre was collected and collimated by an objective O1 (Olympus 10x/0.25) objective. The Gaussian beam waist of the fibre was previously measured to be $2.9\ \mu\text{m}$ [119]. This beam was then passed through a 50 mm cylindrical lens CY (ACY254-050-A, Thorlabs), which produced a line focus on the galvo mirror G. The plane of the galvo was conjugated via 2 pairs of Plössl lenses, (each made of 200 mm focal length doublets, AC254-200-A-ML, Thorlabs), L1 and L2 each with effective focal length of 100 mm see specification in Table 6, to the back focal plane of the objective O2 (Nikon 10x/0.3W). Prior to passing through the objective, the beam was folded through 90° with a broadband dielectric mirror (Thorlabs BB1 ED2). The axial position of O1 and O2 could both be controlled via their own z-axis translation mounts. The illumination line produced by the cylindrical lens on the GM was imaged onto the back focal place of O2 and produced the light-sheet in the sample. The optical power output from O2 was measured to be 0.45 mW. Figure 106 shows a schematic of the illumination system for the focusing (Panel (a)) and non-focusing (Panel (b)) axes of the cylindrical lens.

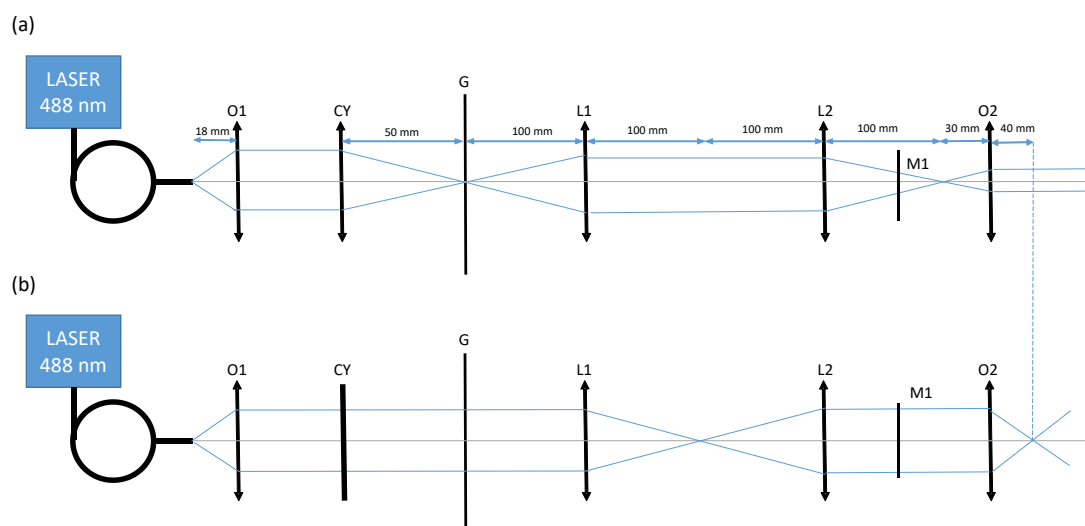


Figure 106 (a) schematic of the imaging arm in the focusing plane of the cylindrical lens CY. Light from a mono-mode fibre is collimated by O1 then focused by the cylindrical lens CY onto the Galvo G. The Galvo is made conjugate to the back focal plane of O2 using a pair of Plössl lenses. Panel (b) shows the imaging arm in the non-focusing plane of CY. (b) schematic of the imaging arm perpendicular to the focusing plane of CY.

A schematic for the optomechanics of the illumination arm are shown in Figures 107 and 108. The setup is arranged so that the illumination objective rotates about the optical axis of L1 and L2. For LSM, the right-angled mirror mount connected to the illumination objective was bolted onto the aluminium block as shown in Figure 99 (b).

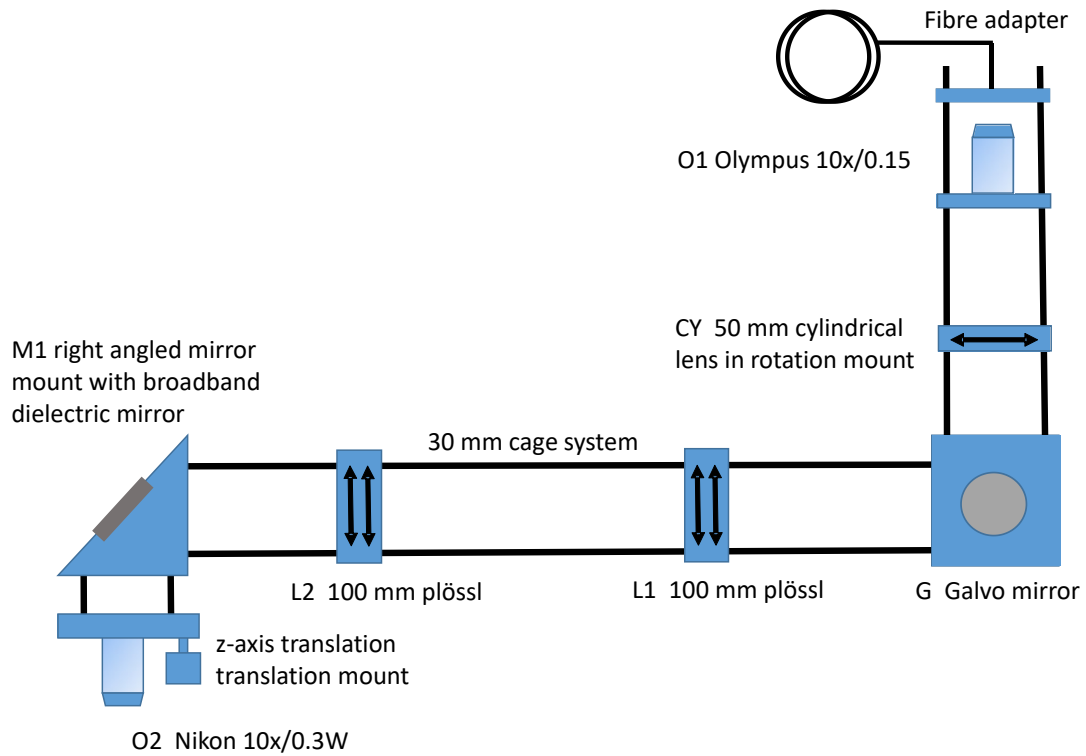


Figure 107 Schematic of the opto-mechanics of the illumination arm

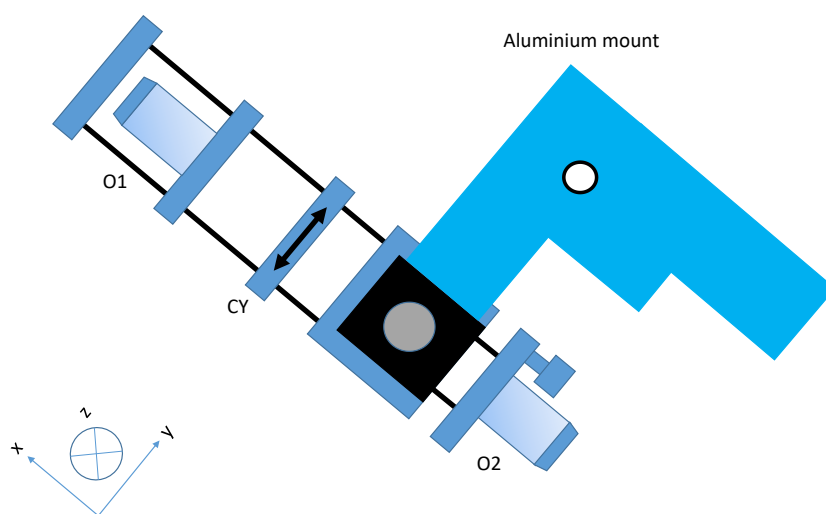


Figure 108 Schematic of the illumination arm showing how the aluminium mount is attached to the right-angled mirror mount.

5.5 Light sheet dimensions

Gaussian beam optics can be used to estimate the dimensions of the light sheet which are shown in Figure 109. The single-mode optical fibre feeding into O1 was measured in reference [133] to produce a Gaussian beam waist of $2.9\ \mu\text{m}$. In the non-focusing plane the cylindrical lens produces a calculated beam waist of $3.2\ \mu\text{m}$ and a Rayleigh range of $66\ \mu\text{m}$ at the sample. The focusing plane of the cylindrical lens the beam has a final calculated waist of $390\ \mu\text{m}$ and a Rayleigh range of $0.98\ \text{m}$ at the sample. This results in a FWHM of intensity of illumination of $132\ \mu\text{m}$ parallel to the direction of the illumination axis and $460\ \mu\text{m}$ perpendicular to the direction of the illumination axis and in the plane of the light sheet.

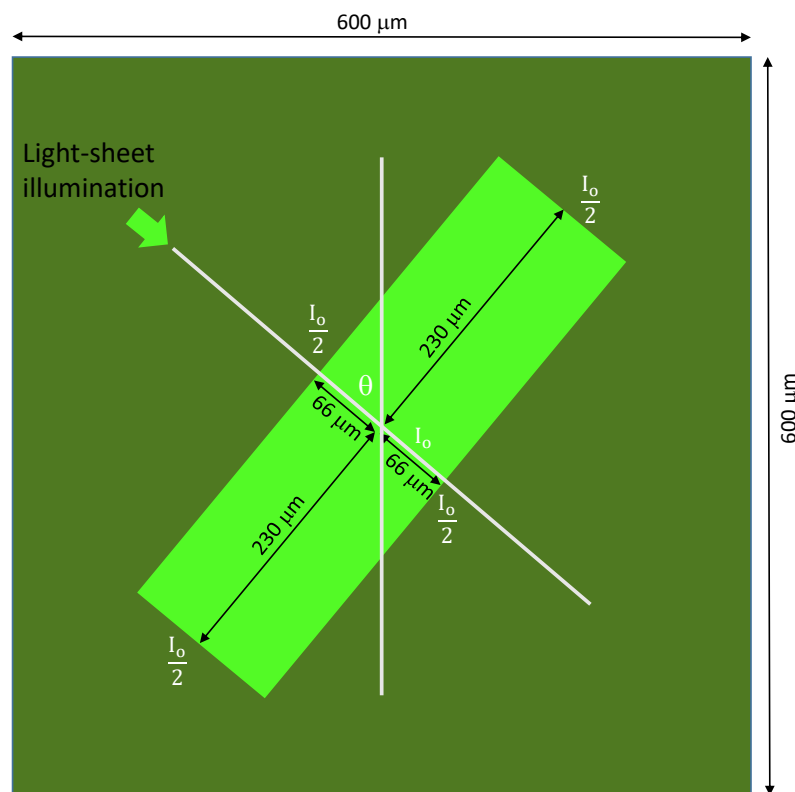


Figure 109 Schematic of the light-sheet showing the intensity variation within the focal plane of the imaging objective O3. The intensity is maximum at the centre with a FWHM of $132\ \mu\text{m}$ in direction of propagation of the light-sheet (which is the confocal parameter of the Gaussian beam in the non-focusing plane of the cylindrical lens), and $460\ \mu\text{m}$ in the perpendicular direction (which is the confocal parameter in the focusing plane of the cylindrical lens).

5.6 Alignment of the illumination subsystem

Initially, the lenses were removed from the optomechanical assembly. O1 was then inserted and its axial position was adjusted in order to obtain a collimated beam. Collimation was confirmed by measuring the diameter of the beam exiting the objective over several meters. Next, a pinhole was placed before the cage unit containing the galvo to produce a pencil beam. The voltage to the galvo

was adjusted in order to tip the mirror so that the pencil beam passed through 2 pinholes in the horizontal cage system where L1 and L2 would be located. Next, two pinholes spaced by 20 cm were placed onto rods after the right-angle mirror mount used to hold the illumination objective. The tip, tilt and piston of the fold mirror were then adjusted until the beam went through both pinholes and so as to ensure that the beam had been accurately folded through 90° .

Next, O2 and L2 were added to the system and a shear plate and alignment laser used to position L2 so that they were in 4-f configuration. O2 was then removed and L1 added and L1 moved until L1 and L2 were in 4-f. The next task involved arranging the galvo mirror so that it was at the focal planes of both L1 and CY. Figure 110 shows a schematic of the procedure.

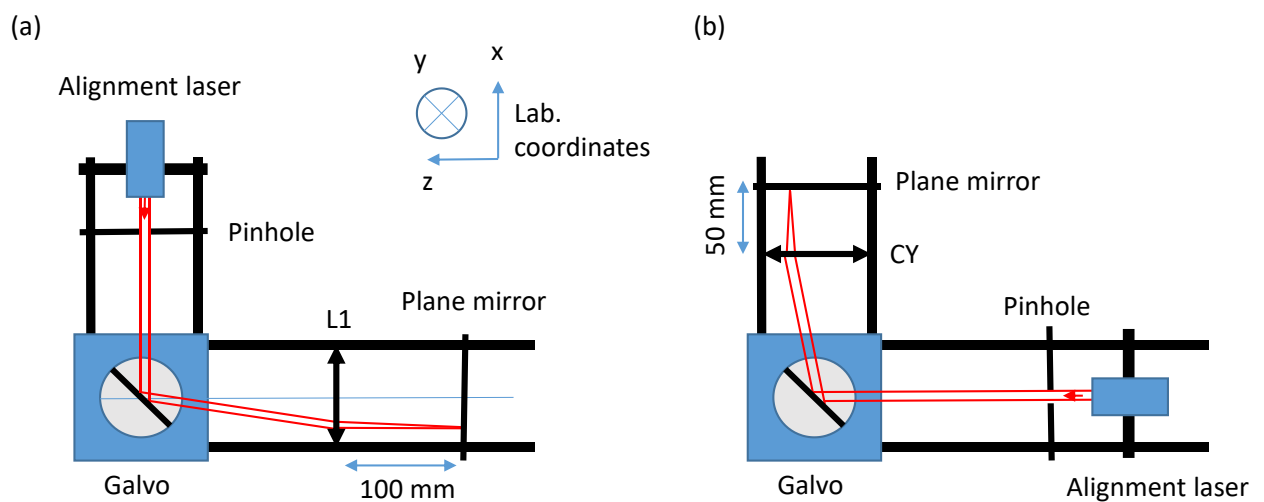


Figure 110 Panel (a) shows the setup for aligning the position of the galvo so that it is at the focus of L1. Panel (b) shows the setup for aligning the position of the cylindrical lens CY so that the galvo is at its line focus. Further details of the procedure are in the text.

Light from an alignment laser was passed along the optic axis and through a pinhole where it was reflected by the galvo, passed through a lens (either CY or L1) and incident on a plane mirror placed normal to the rail system, where it was retroreflected. If the galvo mirror was in the focal plane of the lens, then the light would be reflected back along the same path taken by the light on its outward path. For L1, the retroreflected beam would be a spot that can be focused onto the back of the pinhole by adjusting the axial position of the mirror. For CY, the beam would be a stripe that can be focused by adjusting the axial position of the mirror. The key point is that even if the galvo mirror is oscillating, the beam will still be reflected back to produce a stationary spot or a line on the back of the pinhole. If the galvo was not in the focal plane of the lens, then position of the spot or line would oscillate as the galvo mirror changes its angle. The procedure was initially carried out as shown in Panel (a) to ensure the correct spacing of L1 and the galvo. Here, the galvo cage was carefully moved along the cage system whilst the galvo mirror was oscillating until no lateral oscillation of the reflected spot was

detected. The procedure was repeated as shown in Panel (b) using an alignment laser propagating in the opposite direction to allow the distance between CY and the galvo mirror to be set.

Finally, a 582/75 emission filter was attached to the tube in front of the Orca Flash camera.

5.7 Combining and aligning the illumination and the imaging subsystems

The right-angled mirror mounts for the illumination and the imaging arms were bolted onto the aluminium mount as shown in Figure 99 (b). The angle of the imaging side of the right-angled mount relative to the optical table was set to 50° which maximized the working distance between the imaging and illuminating objective and the slide as shown in Figure 111. Two alignment lasers were used to visibly check that the optic axis of each subsystem overlapped in the region between both objectives.

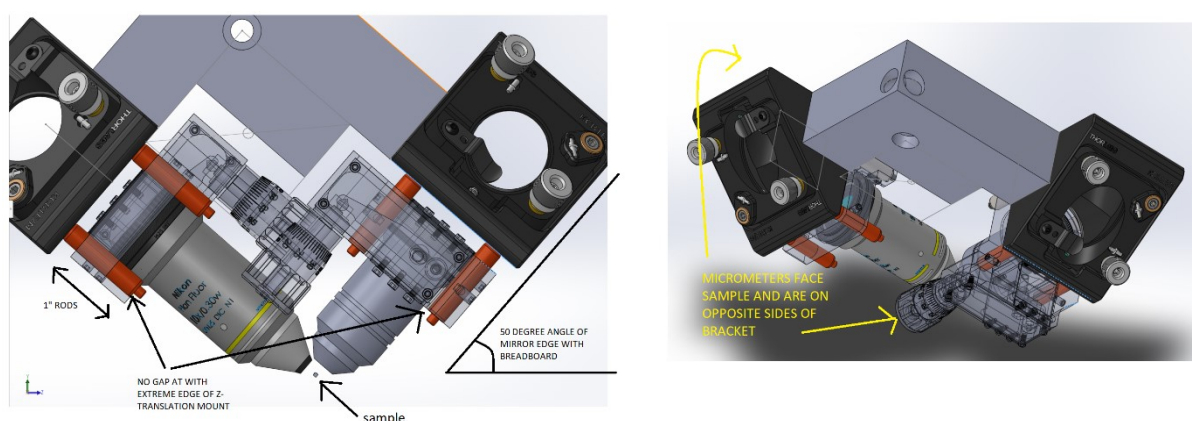


Figure 111 SolidWorks model showing the arrangement of the illumination and imaging objectives attached to the aluminium mount. This arrangement maximises the working distance of the system. (Image credited to Dr. Hugh Sparks)

Next, a silicone rubber sheet with a thickness of 3 mm and with a rectangular section cut out was stuck onto a slide with superglue as shown in Figure 112 in order to make a bath of fluorescein.

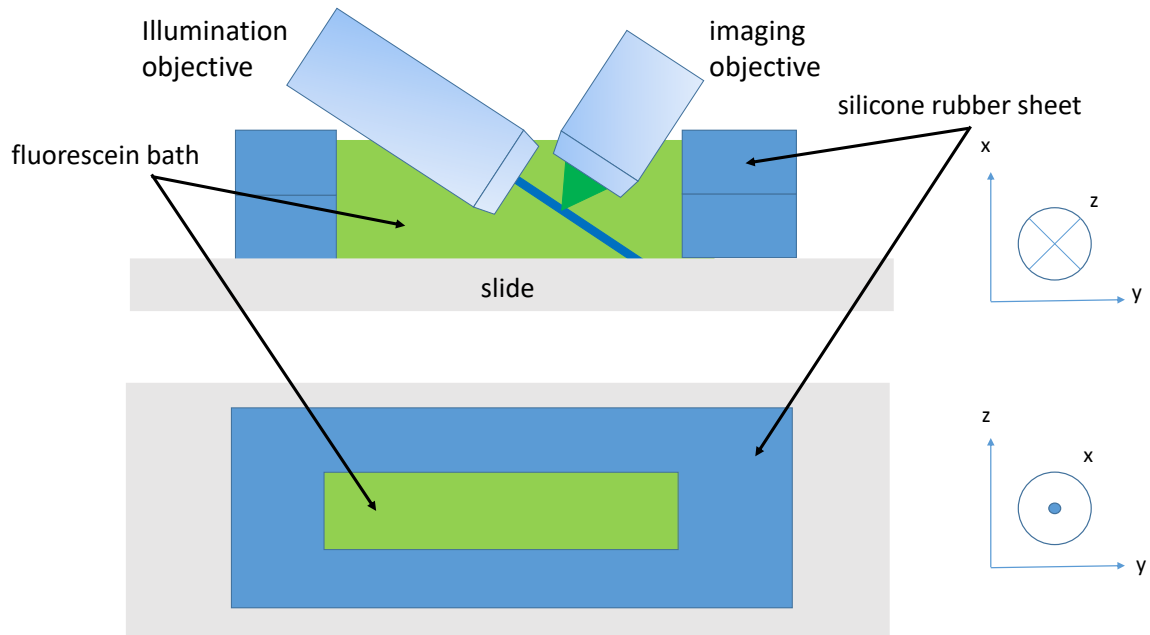


Figure 112 Schematic showing the silicone structure which contains a fluorescent sea along with the relative positions of the illumination and imaging objectives.

By adjusting the voltage applied to the galvo the light sheet was moved until it was in the focal plane of the imaging objective. This produced the image shown in Figure 113.

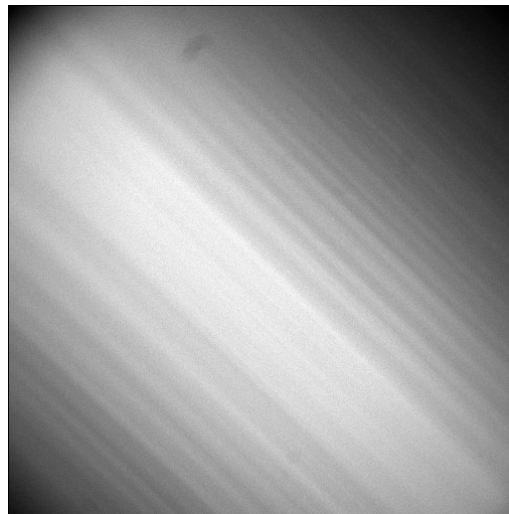


Figure 113 Image showing an in-focus image of the light-sheet collected by objective O3. The long in-focus shadow artefacts indicate that the light-sheet is in the front focal plane of the imaging objective. The FOV is $600 \times 600 \mu\text{m}$. The light sheet is propagating in the direction from the top left towards the bottom right of the image.

The image showed shadow artefacts caused by speckle in the illumination beam. The position of the light-sheet was adjusted via the command voltage applied to the galvo until the shadow artefacts were as sharply in focus as possible. This showed that the plane of the light-sheet was aligned to the front focal plane of the imaging objective. If the light-sheet was tilted with respect to the front focal plane of the imaging objective, then the result would be that the extent of the region where the stripes

were in focus would be reduced. The long shadows shown in Figure 114 (a) show that the light-sheet's plane is parallel with the focal plane of the imaging objective. With a situation like Figure 114 (b), the inclination of the light-sheet needs to be adjusted until the shadows maximize in length.

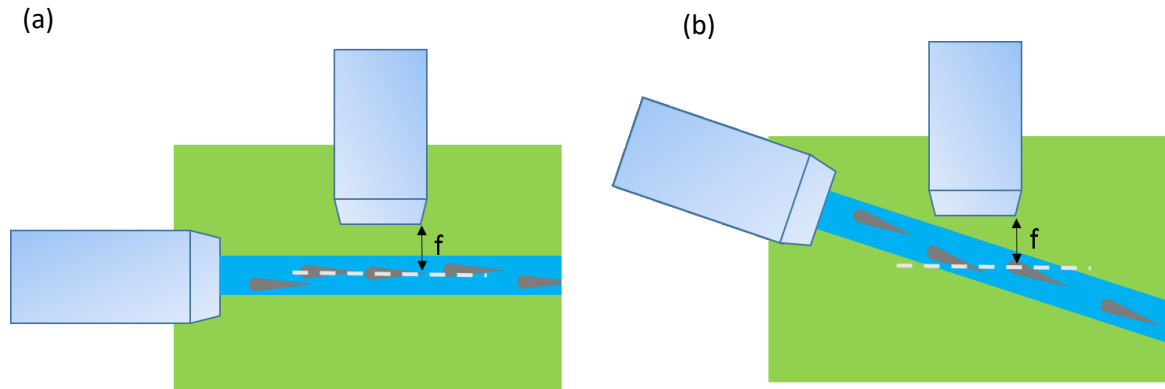


Figure 114 Shadow artefact are longer when the light-sheet is (a) parallel to the focal plane of the imaging objective compared with (b) a tilted light sheet which will result in shorter shadow artefacts.

Raising the slide, which does not fluoresce, creates a step function in the detected fluorescence signal and a straight edge between the fluorescent sea and the non-fluorescent glass as shown in Figure 115.

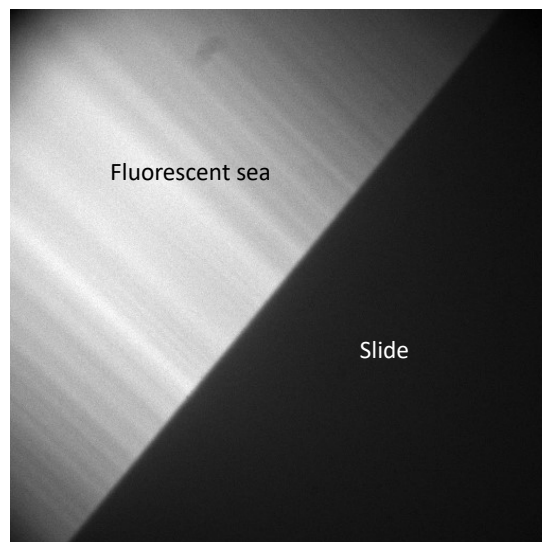


Figure 115 Raw camera image showing signal from the fluorescent sea (top left) and the slide (black, bottom right). The edge of the slide can be used to align the light-sheet. FOV is 600x600 μm .

The light-sheet can be rotated about the optical axis of the illumination axis by rotating the cylindrical lens in its rotation mount. The cylindrical lens was rotated until the edge was as sharp as possible along its full length, at which point the plane of the light-sheet could be assumed to be parallel to the plane of the imaging objective's focal plane.

The working distance, i.e. the limiting distance between the sample and either the illumination or imaging objective is determined by the relative positions of the imaging and the illumination objectives. Figure 116 shows the two extreme examples. In (a) the slide is touching the illumination objective and in (b) the slide is touching the imaging objective. In (a) the working distance is small as the intersection of the illumination beam and the optical axis of the imaging objective is only just inside the field of view of the imaging objective. In (b) the imaging objective is touching the slide, but the working distance is greater, as the fraction of the field of view of the imaging objective occupied by the sample (fluorescent sea in figure) is larger. Hence, the alignment of the objectives must be adjusted carefully so as not to unnecessarily limit the available working distance.

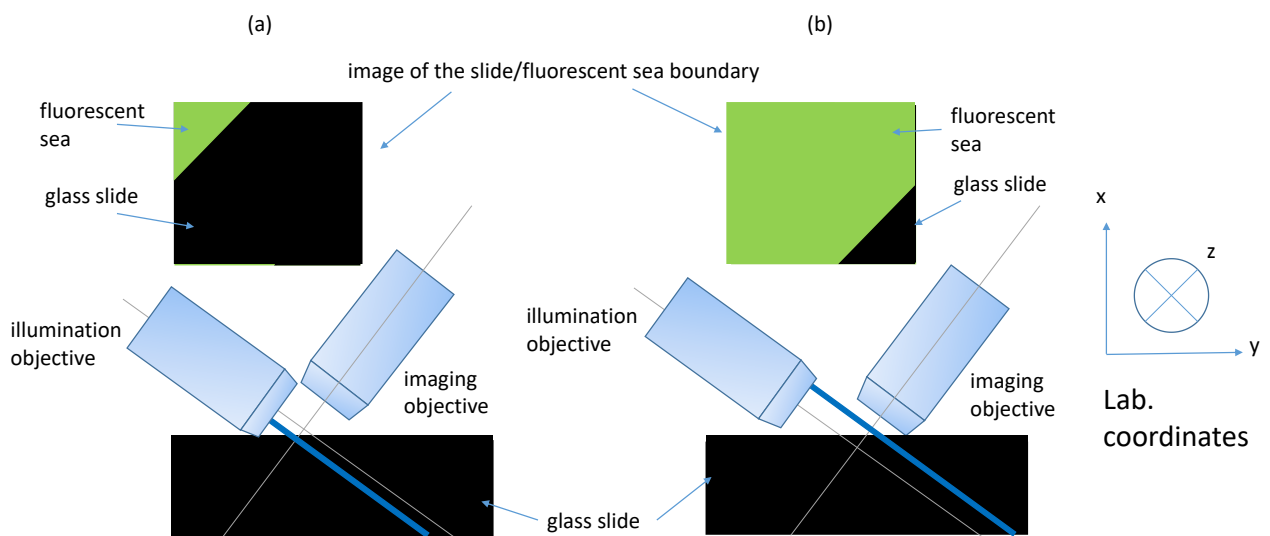


Figure 116 Panel (a) shows that the working distance of the system is limited by the illumination objective. Panel (b) shows that the working distance is limited by the imaging objective.

The position of the edge of the slide seen on the camera was adjusted by moving the sample stage until the edge crossed the centre of the FOV. Next, the waist of the light-sheet had to be adjusted in order to ensure that it was located on the optical axis of the imaging objective. In Figure 117 (a) the waist is misaligned because of the larger illumination beam width at the slide boundary and its intersection with the optical axis of the imaging objective. In this case the axial resolution of the imaging system would be reduced and so the edge would appear to be more blurred than the case of Panel (b) where the waist is aligned to the optical axis of the imaging objective. The illumination objective was moved along its axis by the z-axis translation mount until the edge of the slide appeared to be sharpest at which point the position of the waist was assumed to be at the optical axis of the illumination objective.

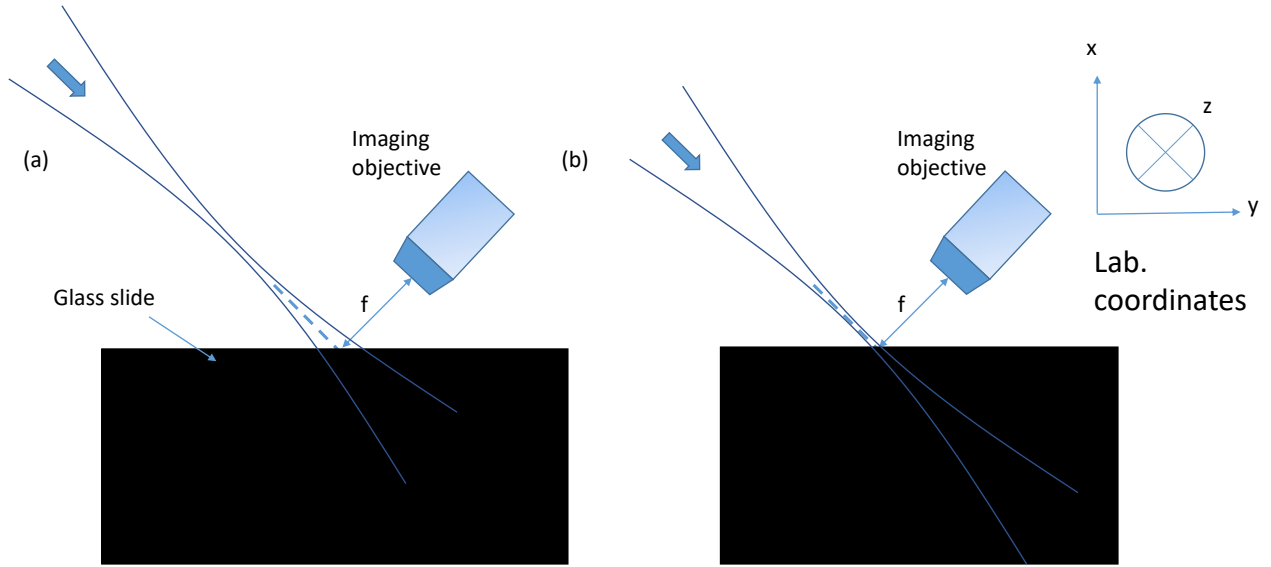


Figure 117 Schematic showing the alignment of the waist. In Panel (a) the waist is not aligned and as a result the axial resolution is worse than in the case of Panel (b); hence the edge of the slide is blurrier in the case of (a) than (b).

The angular resolution of the rotating cage segment in the imaging arm of the system was only 2 deg, and so the angle of inclination of the imaging objective was estimated from images of the edge of the slide relative to the FOV of the camera, as shown in Figure 118. The angle of inclination of the objective was $\theta = 48.6 \pm 0.4^\circ$.

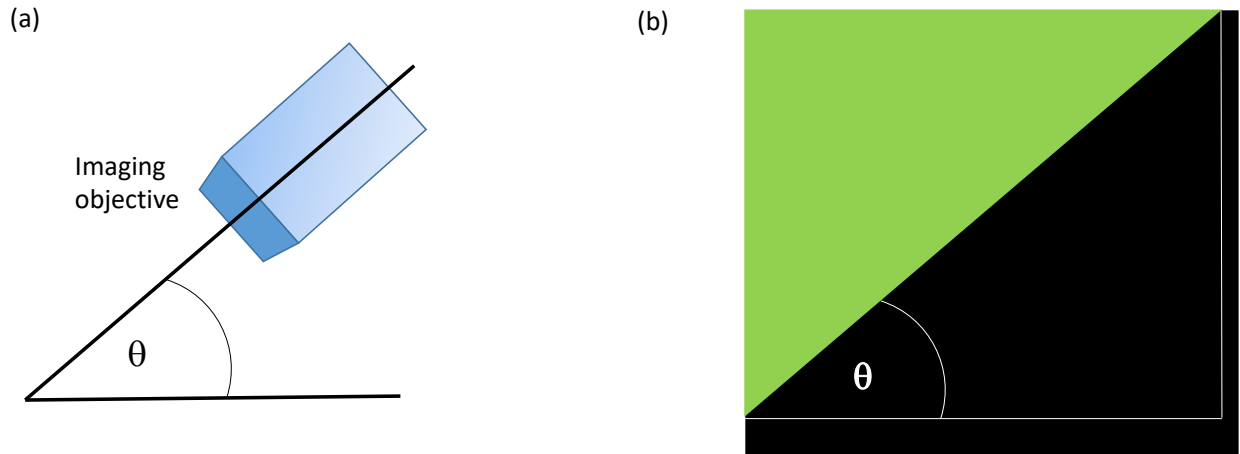


Figure 118 (a) Diagram defining the inclination of the imaging arm θ . (b) illustration of how θ defines the angle of the image of the edge of a slide (black) with a fluorescent sea above (green) on the camera.

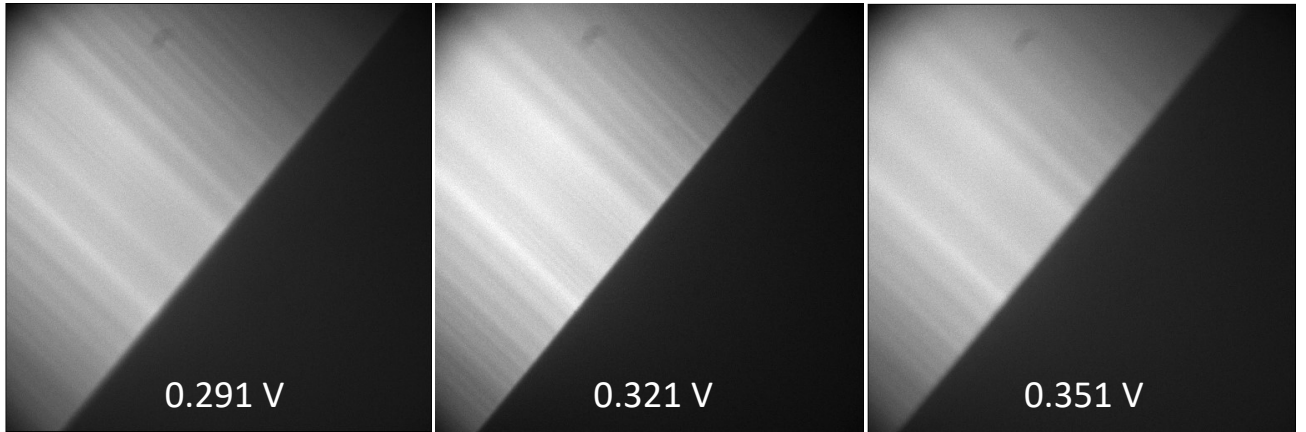


Figure 119 Images show the edge between the slide of the fluorescent sea for different voltages applied to the galvo. FOV of 600x600 μm .

The relationship between the voltage applied to the galvo V , and the displacement of the light sheet from the focal plane of the imaging objective z was determined.

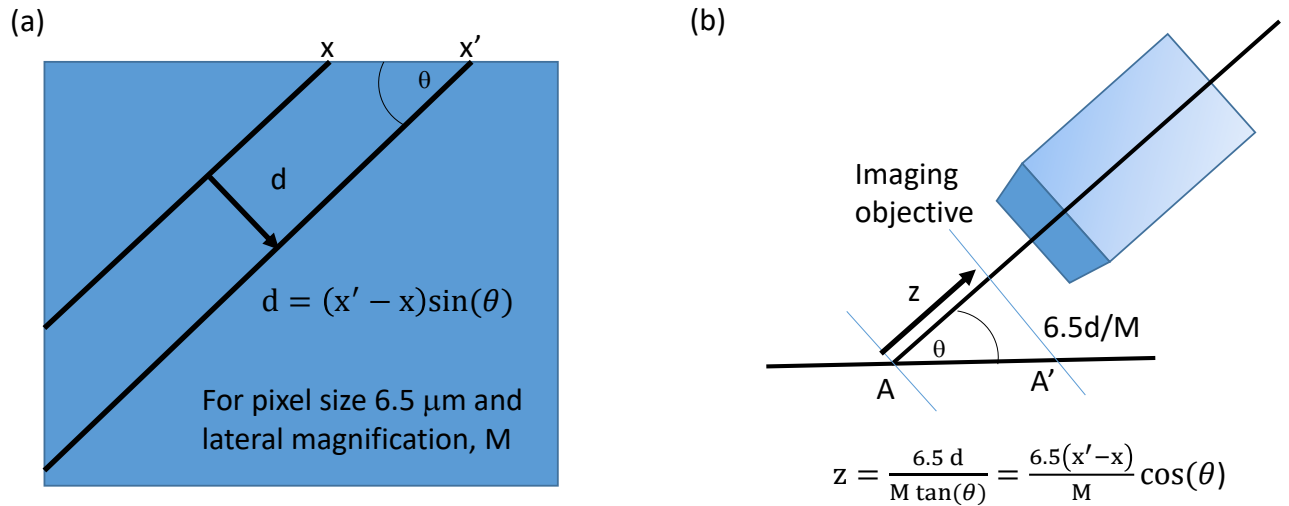


Figure 120 Panel (a) shows that measurements of the x and x' positions of the edge of the slide on the camera as the light-sheet moves from A to A' enables the displacement d of the edge of the slide to be determined. Panel (b) shows how this is related to the axial displacement of the objective O3, z .

A series of command voltages were applied to the galvo and images taken as shown in Figure 119. Each one produced a z displacement of the light sheet from the focal plane of the imaging objective and so a different position of the image of the edge of the slide on the camera. A line was fit to the edge between the glass slide and the fluorescent sea. Figure 120 (a) shows how the pixel value at the point of interception of the fit line with the top edge of the image could be used to find the displacement from a datum level corresponding to the voltage for the in-focus plane. The perpendicular displacement d between the edges could then be related directly to the axial displacement z as shown in Figure 120 (b), given the camera pixel size and lateral magnification M .

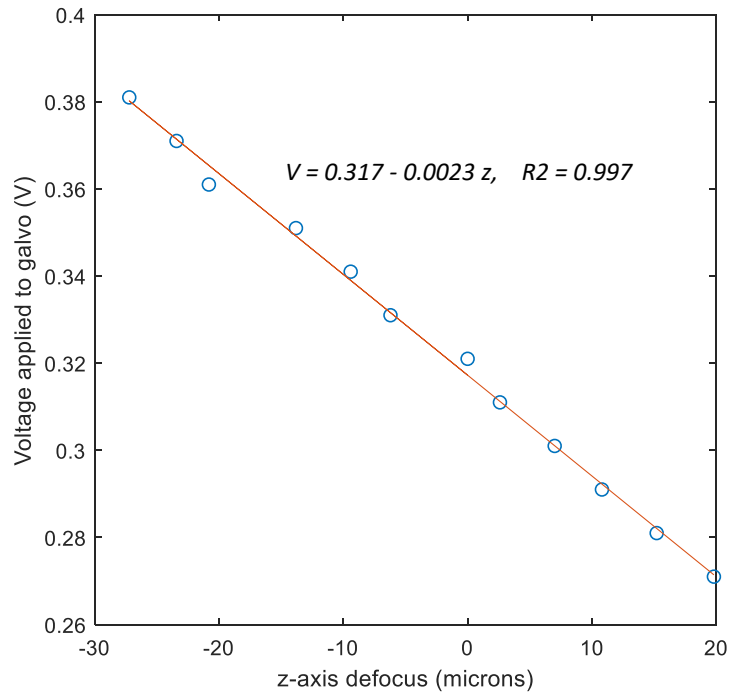


Figure 121 Relationship between the galvo voltage and the displacement z of the slide as viewed by O3.

The result of the regression using the previous estimate for the position focal plane is shown in Figure 121. The rate of change of voltage with axial displacement of the light-sheet was $-0.0023 \text{ V}/\mu\text{m}$ and the relationship was linear. Later work with beads suggested that the best estimate for the galvo voltage in the focal plane was 0.321 giving a relationship between voltage and light sheet position of

$$V = 0.321 - 0.0023z$$

Now that the light sheet had been crudely aligned and the galvo calibrated, it was now necessary to fine tune the light sheet positioning in order to ensure that it was not defocused, or the waist displaced or tilted. Figure 122 shows a schematic of the different ways in which the light-sheet could be misaligned.

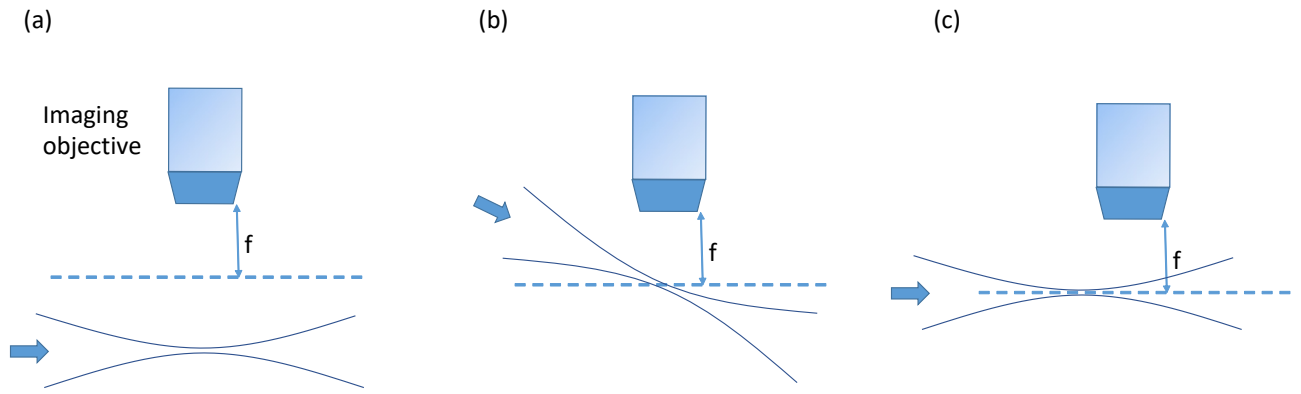


Figure 122 Different ways in which the light-sheet can be misaligned. Panel (a) shows a defocused light-sheet, Panel (b) shows a tilted light-sheet and Panel (c) shows misalignment of the waist of the light-sheet.

TetraSpeck 0.2 μm fluorescent beads in agarose were used for the fine adjustment of the light sheet. Initially the slide was raised until visible in the camera and a recognizable cluster of beads identified on the slide edge. This cluster was brought into focus in the centre of the FOV. This is shown in Figure 123.

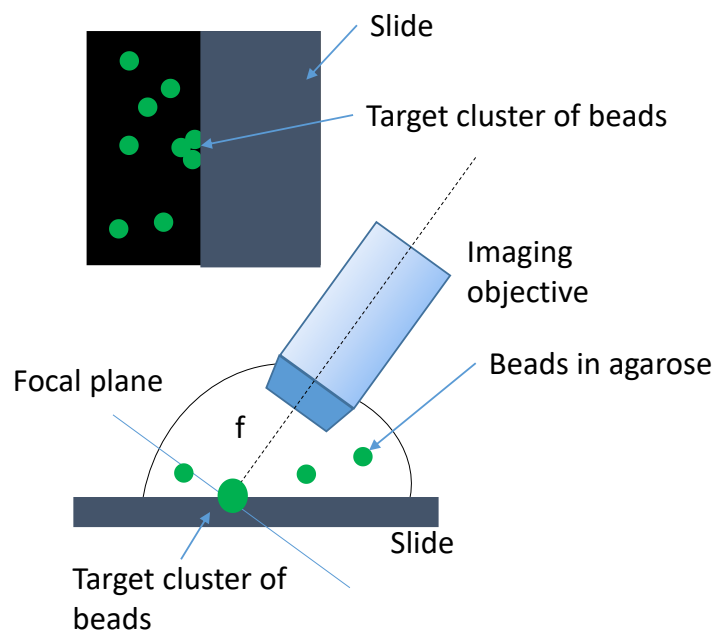


Figure 123 Top: cartoon of the image acquired when imaging beads in agarose on a microscope slide. Bottom: side-on view cartoon of a cluster of beads positioned into the focal plane and on the optical axis of the imaging objective.

This meant that the cluster of beads was on the optical axis of the imaging objective and on the focal plane (to within the axial resolution of the imaging objective). The voltage to the galvo was then adjusted in order to maximize the brightness of the cluster of beads as shown in Figure 124. The beads will be at their brightest when they are on the axis of the light-sheet. This was found to be with a galvo voltage of 0.321 V.

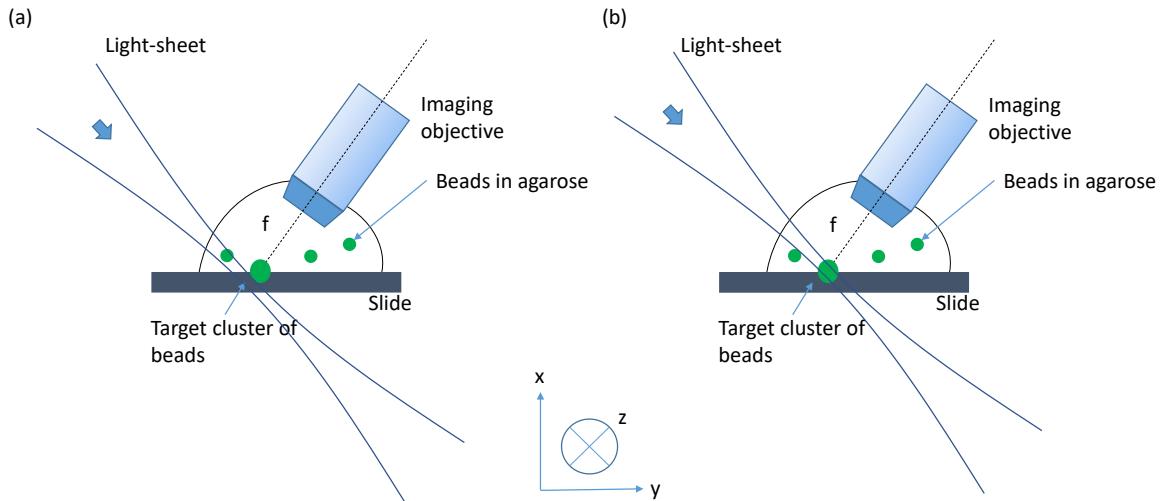


Figure 124 Panels (a) and (b) show the light-sheet being moved axially along the imaging axis until the cluster of beads has maximum intensity. At this point the propagation axis of the light-sheet is assumed to intercept with the focal point of the imaging objective.

The light sheet could also be translated in the z-direction the fold mirror (M1) prior to the illumination objective in order to maximize the brightness of the beads and to ensure that the axis of the light-sheet intercepted with the bead cluster.

The slide was then adjusted vertically down (the x-axis) so that only beads were visible in the FOV. In order to fluoresce the bead must be within the light-sheet. The bead will be brighter if it is in a more intense region of the light-sheet, and will fluoresce most strongly at the waist and on the axis of the illumination objective. To be imaged with minimal lateral FWHM, the bead needs to be within the depth of field of the imaging objective. Figure 125 shows a schematic of an image of in focus beads (small green circles) as well as out-of-focus beads (larger green circles). If the Gaussian beam is running perpendicular to the imaging objective with the light-sheet plane the same as focal plane then we would expect the beads to look as shown in Figure 125 with the distribution of out-of-focus beads being equal on either side of the diagonal.

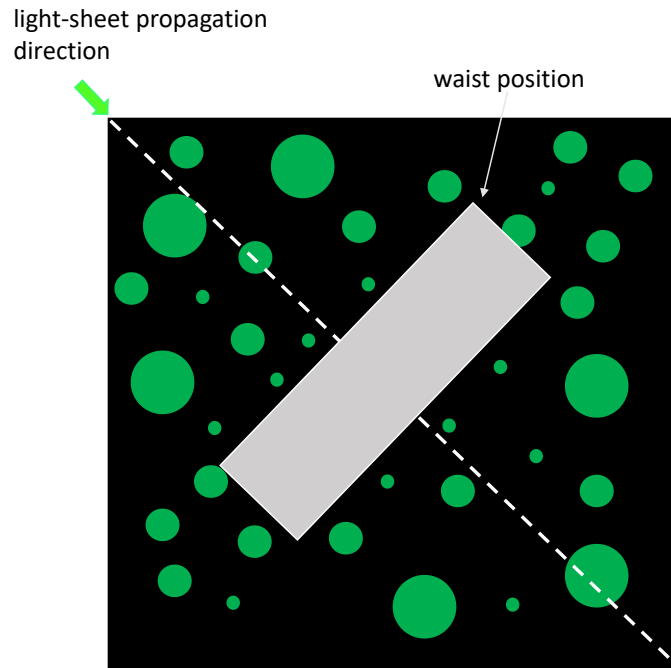


Figure 125 Schematic of the image of the beads when the light-sheet is correctly aligned, running along the focal plane of the imaging objective and normal to the optical axis of the imaging objective.

If the plane of the light-sheet is in the plane of the focal plane of the imaging objective but the waist of the light-sheet has been displaced along the axis of the illumination objective, then one would expect to see something like Figure 126.

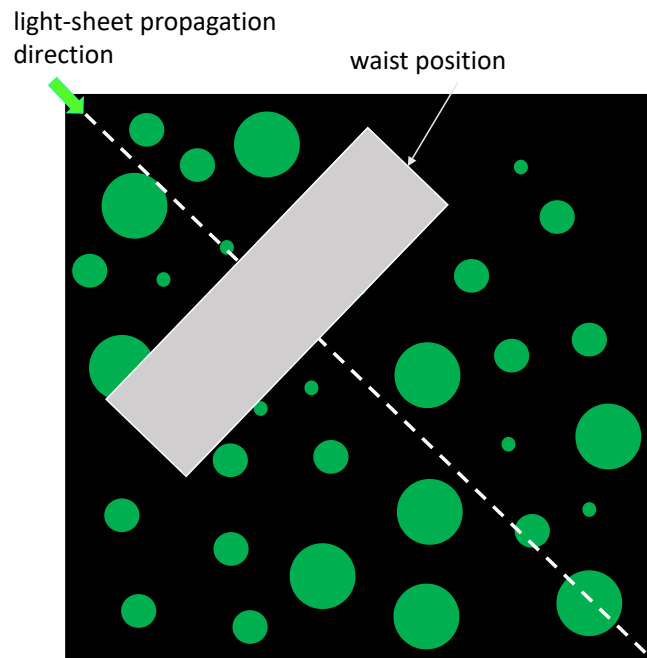


Figure 126 Schematic of the image if the light-sheet is displaced in the axial direction of the illumination object, as shown in Figure 122 (c).

Displacement of the light sheet through the focal plane of the imaging objective (yet keeping the planes parallel) would have the effect shown in Figure 127. (This should not happen if field-of-view-length shadow artefacts were previously observed when imaging a fluorescent sea of fluorescein above the microscope slide.) By smoothly moving the light-sheet up and down the imaging axis using the voltage applied to the galvo it is possible to check that the voltage offset previously determined for the focal plane is symmetrically between 2 situations like Panel (b) in Figure 127.

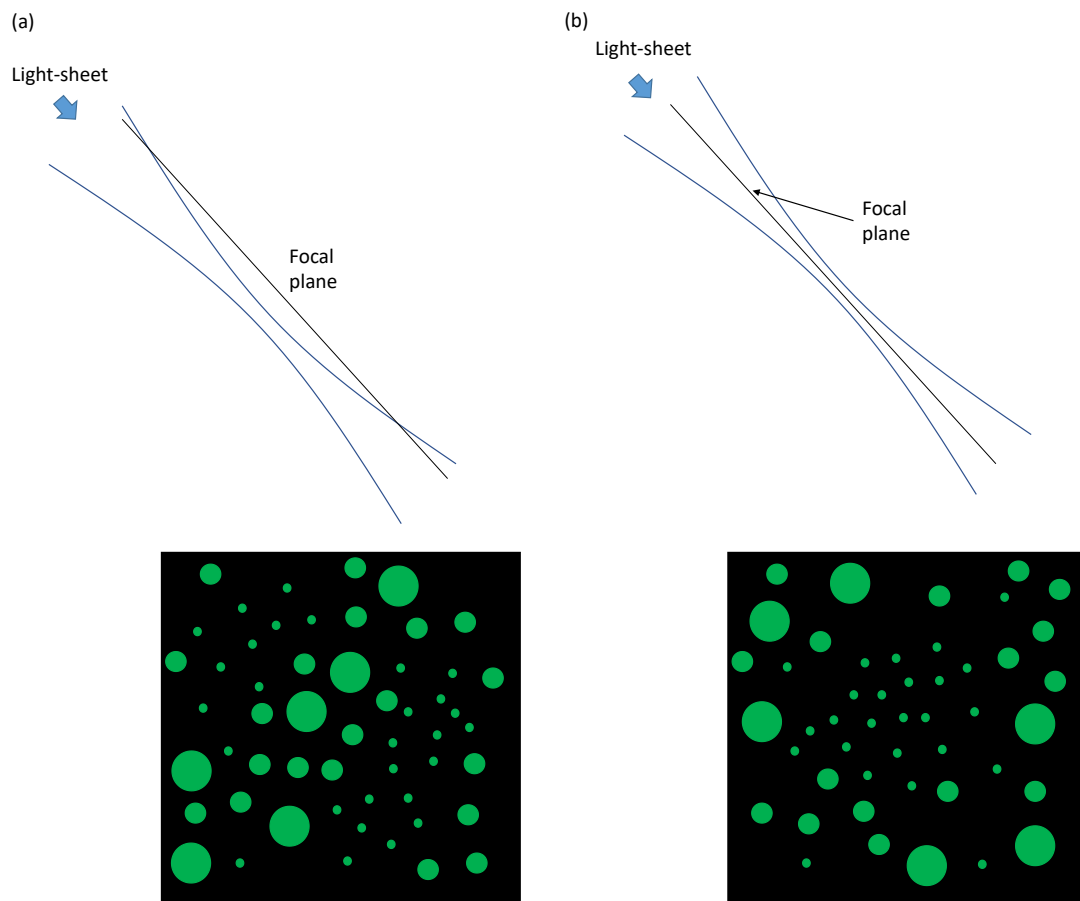


Figure 127 Panel (a) shows a schematic of the appearance of the beads if the light-sheet is defocused compared to (b) where the light-sheet is in the focal plane. In (a) there is an absence of in-focus beads along the central diagonal. In (b) there is an absence of out-of-focus beads along the central diagonal.

If the light-sheet is not parallel to the focal plane then we would expect the in-focus central stripe of beads to be translated in the direction of the illumination axis as the light sheet is displaced in the direction of the imaging objective optic axis. This should be unlikely if field-of-view-length shadow artefacts were previously observed when imaging a sea of fluorescein on a microscope slide.

Similarly, if the light-sheet has any 'roll' along the direction of propagation, then we would expect the in-focus stripe of beads to be translated in a direction perpendicular to the illumination axis as the

slide is displaced in the direction of the imaging objective. The roll of the light sheet could be corrected by rotating the cylindrical lens.

An experimentally-acquired image of fluorescent beads in agarose following the above alignment steps is shown in Figure 128.

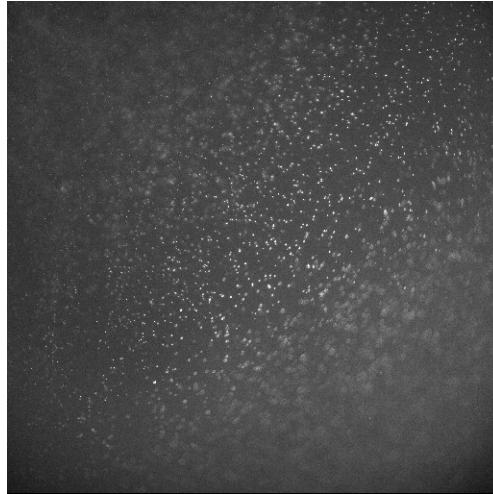


Figure 128 Raw image of fluorescent beads in agarose once the light-sheet has been aligned. The intensity and contrast of the image has been adjusted to make the beads more visible. FOV was 600x600 μm .

Individual beads in the image were used to estimate the geometry of the light-sheet. The image shown in Figure 128 was divided up into blocks of 64x64 pixels. In each block, the bead with the highest intensity was identified. This bead was assumed to be located closest to the centre of the light sheet in the direction perpendicular to the plane of the light sheet. The FWHM of the intensity of the illumination light sheet along its direction of propagation (confocal parameter) was determined using the intensities of the brightest beads in blocks lying on the line passing through the centre of the FOV and in the direction of propagation of the light-sheet. The FWHM of the intensity of the illumination light sheet along the direction perpendicular to its direction of propagation was determined using the intensities of the brightest beads from a line of blocks taken perpendicular to the propagation direction and passing through the centre of the FOV. The process was repeated for 5 full FOV images of beads. The FWHM of the intensity of the light sheet in the direction of propagation of the light sheet was $(130 \pm 10) \mu\text{m}$ and in the direction perpendicular to the propagation direction in the plane of the light sheet was $(400 \pm 100) \mu\text{m}$. These values compare well with the theoretical values of 132 μm and 460 μm shown in Figure 109. The confocal parameter was used to estimate the light sheet waist, which returned a value of $(3.3 \pm 0.1) \mu\text{m}$. This compares well with the expected waist of 3.2 μm described above. To provide another estimate for the waist of the light-sheet, several in focus beads were chosen in the centre of the field of view and the waist swept through them in the axial direction

of the imaging lens (by varying the voltage applied to the galvo). The estimated waist mean and standard deviation estimated this way was $(3.3 \pm 0.3) \mu\text{m}$.

The beads were also used to find the lateral resolution of the static system. A sample of five beads were analysed from the centre of the FOV. For each bead the light-sheet was adjusted to a position which maximised the intensity. The FWHM was found through the vertical direction (which is perpendicular to the direction of propagation of the light sheet), passing through the brightest pixel and in the same way horizontally (which is the direction of propagation of the light-sheet). The mean and standard deviations in the horizontal and vertical directions FWHMs were found to be $(0.6 \pm 0.1) \mu\text{m}$ and $(0.4 \pm 0.2) \mu\text{m}$ respectively. On a sample of five beads the mean and standard deviations of the axial FWHM was $(2.20 \pm 0.07) \mu\text{m}$. At the peak emission wavelength of fluorescein (517 nm) and for the $\text{NA} = 0.75$ used in this project the lateral FWHM of the imaging objective PSF was $0.347 \mu\text{m}$ and axial FWHM was $2.16 \mu\text{m}$. For a LSM the lateral FWHM of the system is the same as the FWHM of the imaging objective. This axial FWHM is less than the $6.2 \mu\text{m}$ thickness of the light-sheet at the beam waist and hence the axial PSF FWHM of the system will be dominated by the PSF of the imaging objective. The axial FWHM of the imaging objective can be combined with the light-sheet thickness to provide an estimate for the axial FWHM of the system according to eq.3 in Chpt 2, which is $2.1 \mu\text{m}$. In order to compare these estimates with the measurements taken from the 200 nm diameter fluorescent beads, under scalar wave optics (which is appropriate when polarization is not important), assuming that the bead is uniformly fluorescent, transparent and its refractive index is close to the refractive index of the surrounding agarose then the theoretical 3D PSF of the imaging objective obtained must be convolved with a sphere of diameter 200 nm representing the fluorescent bead, in order to obtain the expected 3D image of the bead (further explained in the Appendix). In order to simplify the calculation, the 3D PSF of the imaging objective was modelled with a Gaussian with the same lateral and axial FWHM as the actual PSF. This produced estimated of resolution of the system for the lateral and axial FWHM of $0.375 \mu\text{m}$ and $2.03 \mu\text{m}$ respectively, which compare well with the experimentally measured values.

5.8 Timing of the DM, Camera and Galvo

In order to achieve volumetric image acquisition, the approach was to play a sequence of commands repeatedly on the DM corresponding to sweeping the focus through a sawtooth-shaped range of defocus positions as described in Chapter 4 and shown with the red line in Figure 129. At the beginning of each sawtooth the DM emits a TTL pulse which was used to coordinate the other devices.

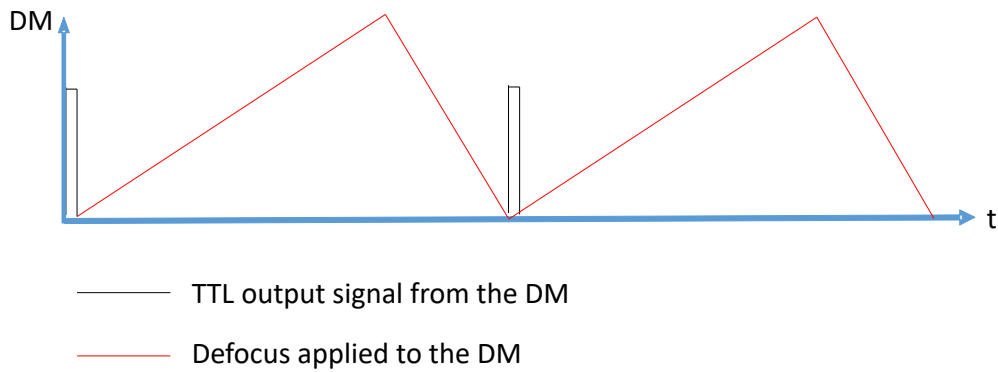


Figure 129 Timing diagram showing the relationship of the sequence of poses used to scan a volume to the TTL pulse produced by the DM; which is used for electronic timing in the system.

As shown in Figure 130, the TTL pulse from the DM is passed to an AND gate with the other input being a NI DAQ 6008, which allowed software to be able to select specific pulses from the DM. This approach meant that the DM could continuously oscillate and so manage thermal creep. The output of the AND gate went into a NI DAQ 6363 which produced a sawtooth output for the galvo as well as a second output that was used to trigger the Orca Flash camera. The output to the Orca Flash camera also triggered the laser.

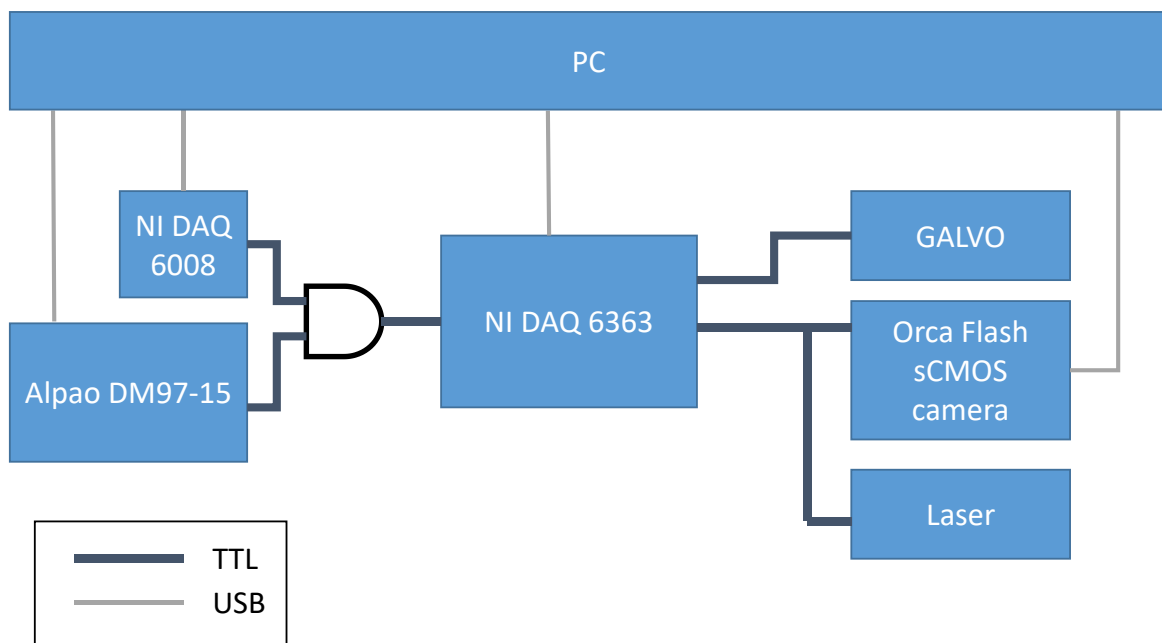


Figure 130 Schematic showing the how the different elements of the system are connected. The DM produces a single pulse for each volume scan which triggers the NI DAQ 6363 to produce a sequence of commands for the galvo and also triggers the camera and switches on the laser for the desired exposure time.

As shown in Figure 131, the rising edge of the second output trigger would cause the Orca Flash camera to take an image and the length of the pulse would be the length of time that the laser would be illuminate the sample. The Orca Flash camera was configured to operate in Global Exposure and Global Reset modes, which are explained in section Chapter 4.

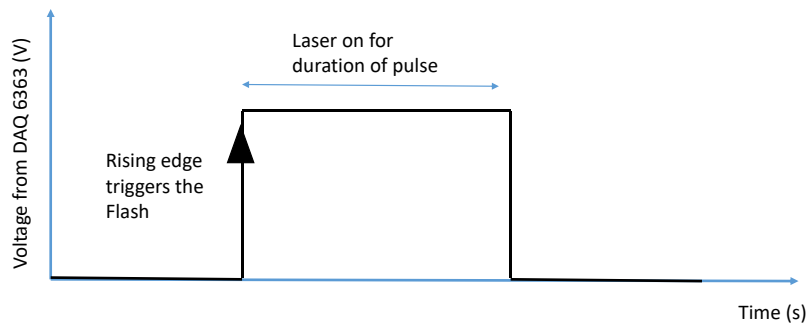


Figure 131 Pulse from the NI DAQ 6363 used to trigger the Orca Flash camera and the laser. The rising edge of the pulse triggers the camera and the length of the pulse is used to modulate the output of the laser and determines the length of time that it is switched on.

Since the mirror smoothly moved through defocus positions, any defocus within the volume could be chosen. Figure 132 shows how the system was used so that a particular defocus position could be strobed within each volume. The strobe mode was particularly useful for debugging the system. It was also useful when performing volumetric imaging when the whole FOV of the camera was required, and this could be captured with the camera acquiring a full-frame at much lower frame rates than required to capture every individual pose change from the DM.

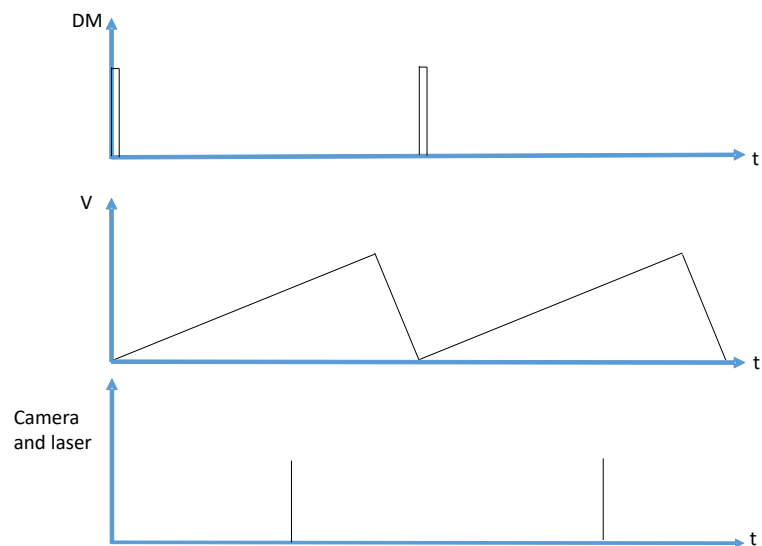


Figure 132 System timing diagram for the DM refocusing LSFM. Top: the DM emits a TTL pulse prior to playing a sequence of poses corresponding to scanning a single volume. Middle: a voltage ramp is applied to the galvo mirror. Bottom: a single image is taken at the same time within each volume.

Figure 133 shows how a series of images could also be captured within each volume. The size of each image was limited by the maximum frame rate that could be achieved by the Orca Flash camera at the given image region-of-interest size.

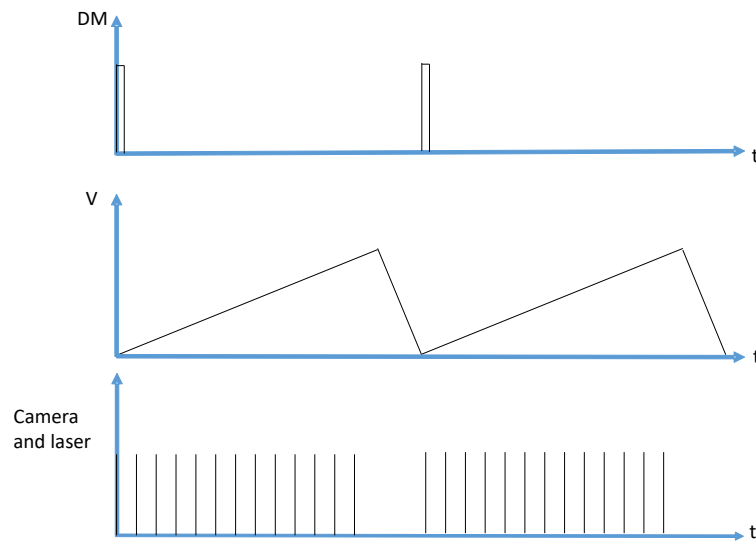


Figure 133 System timing diagram for the DM refocusing LSM. The DM emits a TTL pulse prior to playing a sequence of poses corresponding to scanning a single volume. A voltage ramp is applied to the galvo mirror and a sequence of images acquired by the camera. The images can be taken at any stage within the capturing of the volume as the DM and Galvo are synchronised with each other.

5.9 Imaging corn pollen

The DM-based LSM was used to volumetrically image corn pollen which had been attached to a microscope slide by nail varnish. The mirror oscillated at a rate of 26.3 vol/sec using the previously optimized commands. Initially the system was operated in a strobe mode where a single image was captured per volume with images captured every 5 μm from -50 μm to 50 μm . The exposure time was 2 ms and used in this way the entire FOV (600x600 μm) could be captured through a USB3 connection between the Orca Flash sCMOS camera and the PC. Figure 134 shows the central 160x160 μm region of interest (ROI) of the FOV containing several pollen grains. The system was then used to capture a series of images 10 equally spaced images in each volume from -50 μm to 50 μm , which required a camera frame rate of 263 fps. At this rate of image acquisition the bandwidth of the USB 3 connection to the camera limited the maximum image size to 256x128 pixels, which corresponded to the central 75x38 μm of the FOV. Each image had an exposure time of 2 ms.

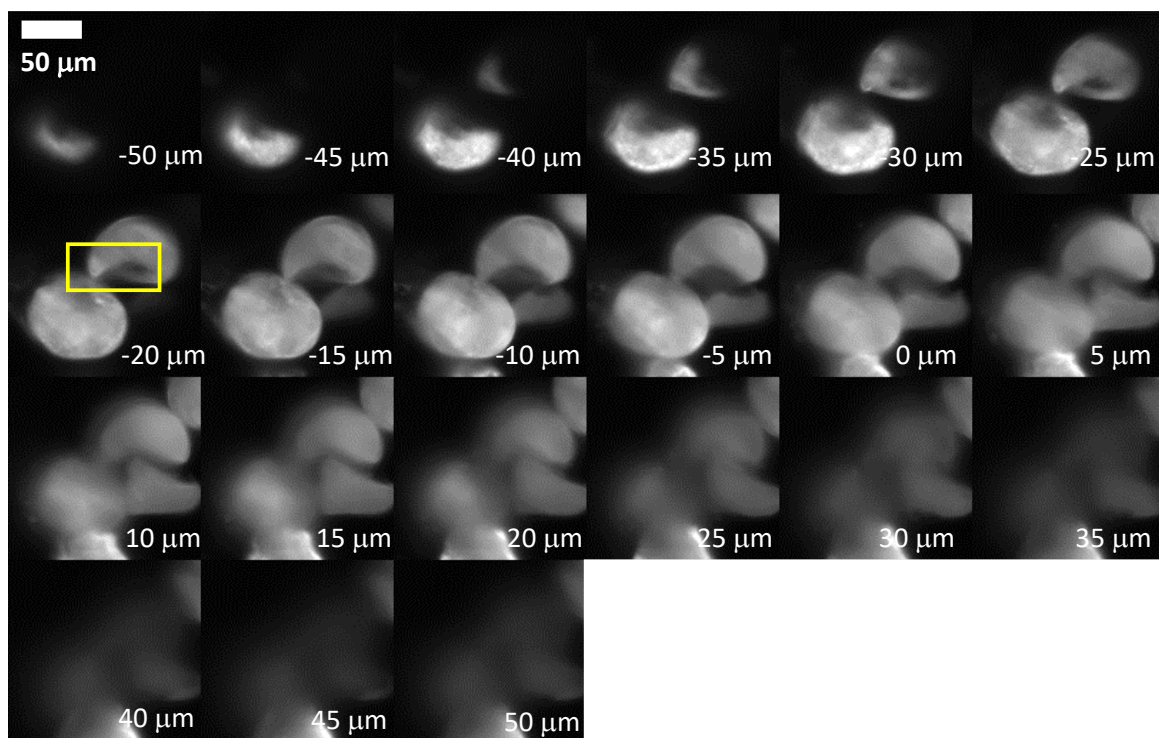


Figure 134 Optically-sectioned images of corn pollen (which is auto-fluorescent) taken with the DM refocusing the LSFM in strobe mode at 26.3 volts/sec. The exposure time of the camera was 2 ms and the laser was set to maximum power of 40 mW. Used in a strobe mode the system captures a single image per volume and so the entire FOV of the LSFM can be examined. The figure shows just the central 160x160 μm region of the camera FOV. The yellow rectangle in the image at -20 μm corresponds to the FOV used in Figure 129 where a series of 10 images were taken per volume.

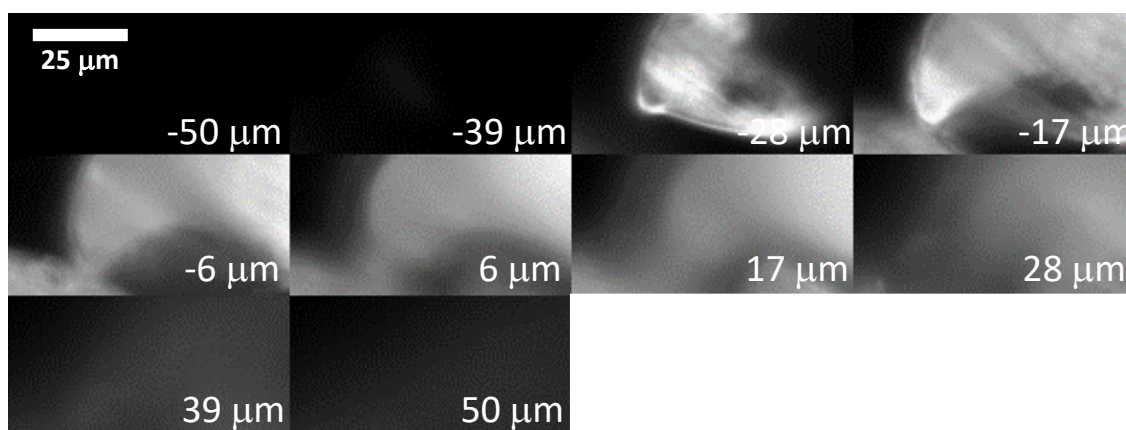


Figure 135 Optically-sectioned images of corn pollen taken with the DM refocusing the LSFM at 26.3 vol/sec. In each volume a series of 10 images equally spaced from axial range -50 μm to 50 μm were acquired with an exposure time of 2 ms. Due to bandwidth limits of the USB 3 connection between the Orca Flash camera and the PC the FOV was limited to the central 75x38 μm , which corresponds to 256x128 pixels. The FOV in this figure is identified in Figure 128 by the yellow rectangle.

5.10 Imaging sunflower pollen

Sunflower pollen (attached to a slide via nail varnish) was observed at 26.3 vol/sec with a 2 ms exposure time; firstly in a stobe mode with the entire FOV of the camera with 26 equally spaced planes per volume over the range -50 to 50 μm . Figure 136 shows a central 120x120 μm ROI from this data. The sunflower pollen grains were then imaged with a 2 ms exposure time with the system capturing 10 exposures per volume equally spaced from -50 μm to 50 μm and a FOV of the central 75x38 μm , with results from 2 different locations shown in Figure 137 (a) and (b).

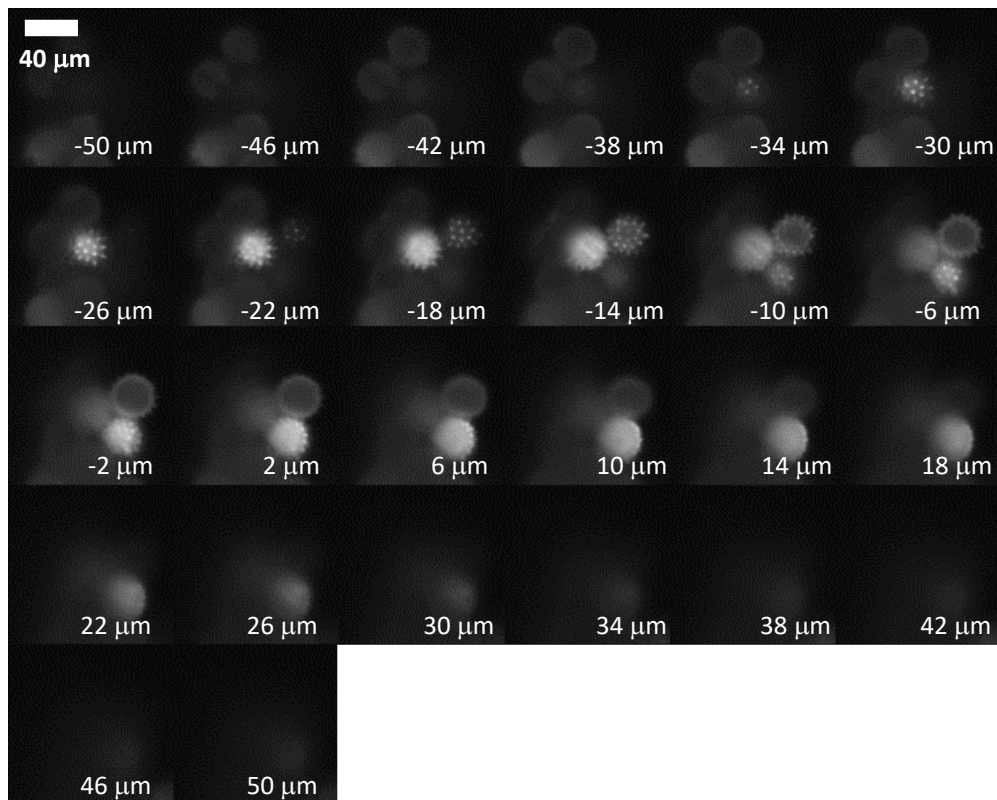


Figure 136 Central 120x120 μm ROI with the system in stobe mode with one camera frame acquired per sweep with LSFM operating at 26.3 vol/sec and with an exposure time of 2 ms.

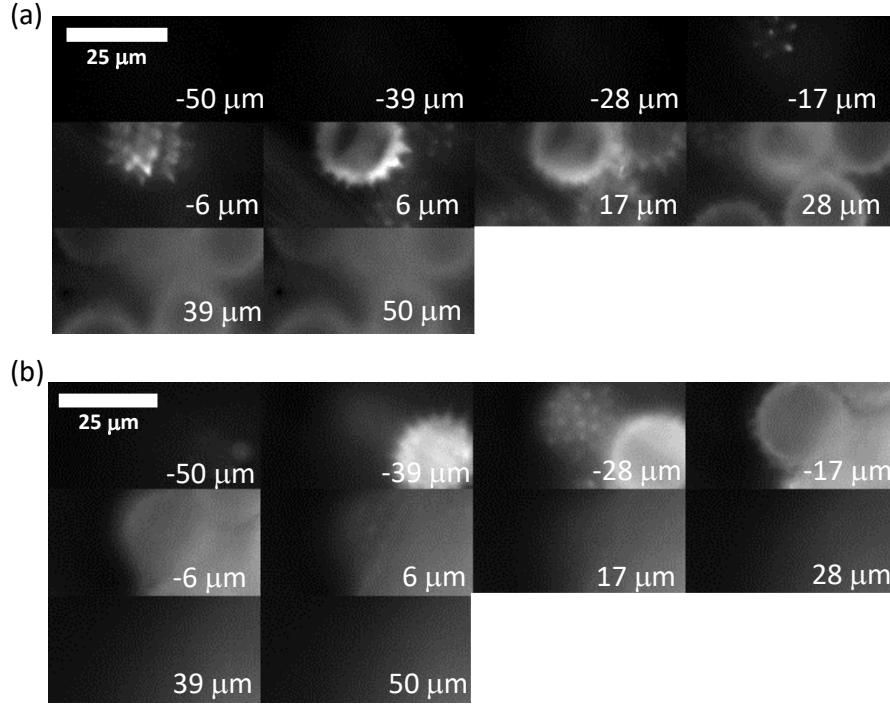


Figure 137 Sunflower pollen with the LSM volumetrically imaging at 26.3 vol/sec capturing 10 images per volume equally spaced between -50 μm to 50 μm . Panel (a) and (b) show images of the central 70x38 μm from 2 different preparations of sunflower pollen. The FOV is limited by the bandwidth of the USB 3 connection between the Orca Flash sCMOS camera and the PC.

5.11 Resolution estimation using beads

The spatial resolution of the DM-based LSM system operating at 26.3 volumes/sec was estimated using 200 nm diameter fluorescent beads (TetraSpeck microspheres) mounted in agarose for each defocus plane from -50 μm to 50 μm in intervals of 5 μm . Each image was obtained using the system in strobe mode in order to acquire the full 600x600 μm camera FOV. An exposure time of 2 ms was used for each image with the laser operating at its full power of 40 mW. For each defocus the images of 20 beads were identified in the central 100x100 μm of the FOV. The FWHM was found for the x and y direction along with lines angled at 45 deg and -45 deg which passed through the pixel with maximum intensity for each selected bead image. The mean of these 4 estimates were used as the estimate for FWHM for the bead. The predicted lateral FWHM of the imaging objective, accounting the size of the bead was 0.375 μm . The mean FWHM for each defocus are shown in Figure 138. The mean FWHM was 0.835 μm across all of the defocus positions.

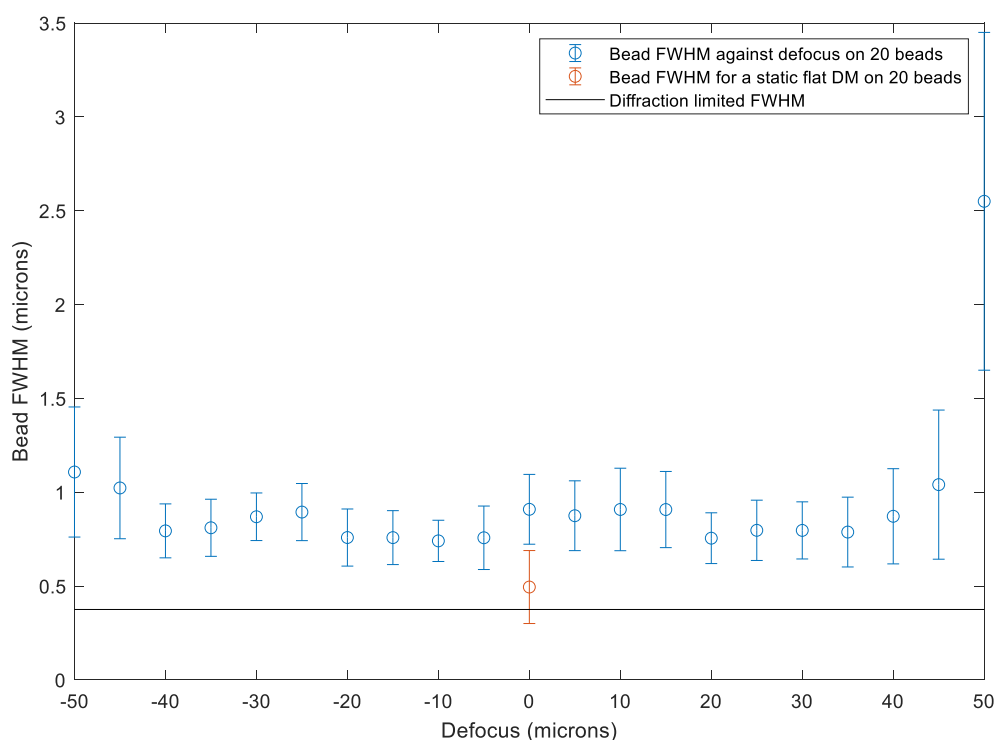


Figure 138 The lateral spatial resolution of the system was estimated with 200 nm fluorescent beads. The FWHM was estimated from 20 beads within the central 100x100 μm at each defocus position. The points indicate the mean FWHM over the 20 beads and the error bars indicate the standard deviation.

5.12 Summary

This chapter has described in detail the imaging and illumination arms of the deformable-mirror-based light-sheet fluorescence microscope and also how they are combined and aligned. The implementation consisted of an illumination arm to create and control the light-sheet – which collimated light (488 nm) from a single mode fibre was passed through a cylindrical lens and then tilt applied via a galvo – which was relayed via a 4f system onto the back pupil of the illumination objective. This axial position of the light-sheet (as viewed along the imaging arm) was controlled by the voltage applied to the galvo. This voltage was generated by a NIDAQ 6363 and simultaneously controlled the galvo, laser and triggered the Orca Flash camera. The imaging system used the DM based refocusing system developed in previous chapters. The illumination and imaging objectives were bolted onto an aluminium mount when the system was to be used as a LSFM. When the DM was being optimized the illumination arm was unbolted and the imaging objective rotated into a horizontal position in order to image the STM as described in previous chapters.

The workflow for daily useage of the LSFM was as follows. Initially the DM must be flattened by the Shack Hartman wavefront sensor. Next the objective must be disconnected from the aluminium

mount and rotated with a rotating cage segment into its optimisation position and a 90 minute optimisation procedure used to determine the commands to correct the mirror for high-NA defocus at each control pose. The illumination arm is then rotated back and reconnected to the aluminium mount that holds the imaging objective at 90° to the illumination objective. The displacement of the image of back focal plane on the DM as the objective was rotated was measured and a correction made in software. During this rotation, the imaging and illumination arms are likely to have come out of alignment and so an alignment laser is passed through the illumination arm and the cylindrical lens from the illumination arm removed and the illumination arm adjusted until the illumination beam crosses the centre of the imaging system. Next a fluorescent sea is used to find the galvo voltage needed to position the light-sheet in the focal plane of the imaging objective. This is then refined by adjusting the cylindrical lens and the axial displacement of the illumination objective. Next the bottom edge of the fluorescent sea is used to find the angle of inclination of the imaging objective and relationship between voltage of the galvo and defocus found. Next 200 nm beads were used to fine tune the alignment of the light sheet and also confirm the confocal parameter etc.

With the mirror flattened the resolution in the focal plane was found to be 0.6 μm and 0.4 μm in the directions corresponding to x,y in Figure 91. This compares well with 0.375 μm which is the predicted lateral FWHM resolution accounting for the finite size of the beads.

The system was used in both a strobe mode and also capturing a z-stack of images through each volume at a rate of 26.3 vol/sec. In strobe mode, the camera took a single image per volume and so the full FOV of the camera could be used. When taking multiple images per volume the USB 3 connection between the Orca Flash camera and the PC limited the FOV to 70x38 μm . Corn pollen and sunflower pollen were both imaged in both strobe and continuous volumetric imaging modes. Finally, the lateral spatial resolution of the system was characterized using 200 nm fluorescent beads while it was operating in volumetric imaging mode and the mean lateral bead FWHM was found to be 0.835 μm over the range from -50 to 50 μm .

This work is an advance on prior art such as reference [6] where membrane DM had been used under open loop control to provide higher-order defocus correction for rapid adaptive focusing and also compensation for sample aberrations on a multiphoton microscope to image a labelled pollen grain and also a live fruit fly brain. This system achieved an axial displacement of 50 μm at a rate of 2 volumes/sec compared with 100 μm at 26.3 volumes/sec in this work.

In [7] a high speed extended depth of field system (EDOF) is presented using a DM to axially sweep the focus through a single exposure and the apply deconvolution to recover the 3D image. The authors imaged 4 μm fluorescent beads with a 40x/0.8NA objective at 472 volumes/sec with an extended

depth of field of 41 μm . This is a smaller axial depth than this work of 100 μm however the large rate of acquisition is mitigated by the need to deconvolution which requires significant computation and potentially time and also can degrade in performance with thickly labelled samples – where as this system, once the mirror is optimised can immediately and robustly acquire images.

Overall, the work presented in this chapter has demonstrated a DM-based LSFM system capable of video-rate volumetric refocusing and this has been demonstrated using fluorescent bead and pollen grain samples, and its performance characterized with fluorescent beads.

Chapter 6: Future work and conclusions

This project developed the first light-sheet fluorescence (LSFM) microscope which uses a membrane deformable mirror (DM) to refocus the imaging objective (Olympus, 40x/0.80NA water immersion) and to volumetrically scan at video rates. It was able to volumetrically image through an axial range 50 to -50 μm about the focal plane of the imaging objective at 26.3 vol/sec. This approach could be used in the future to study high speed biological processes such as the generation of calcium waves in cardiomyocytes.

In order to achieve this, we first chose a membrane deformable mirror primarily based on its ability to provide the maximum possible refocusing range; an Alpao DM97-15 was chosen because of its large stroke. It was then necessary to characterize this DM to understand its properties and this work was reported in chapter 3. The DM was found, as previously published [4 5], to exhibit viscoelastic and thermal creep. The viscoelastic creep has a time constant on the order of 100s and the thermal creep had a time constant on the order of 10 s. These effects mean that the DM's current pose is affected by the recent history of poses adopted by the mirror. Rather than developing algorithms that compensate for the previous history of DM poses, we sought simpler solutions. To reduce the effects of viscoelastic creep, we used an approach where the DM was continuously oscillated at the refocus rate required for the imaging application and so that the time-average pose adopted by the mirror was constant and hence avoiding viscoelastic creep. To reduce the effects of thermal creep, we chose to use an initial warm-up period prior to any measurements to ensure that the DM had come to thermal equilibrium. We found that this approach worked for our application, but it does have the disadvantage that a new optimisation had to be performed if the amplitude of the refocus sweep range is changed or the rate of volumetric imaging changed.

In chapter 4, we developed a method for optimizing the DM using a performance metric derived from an image of a star-test mask, where each pinhole was used to make an estimate for the Strehl ratio at that point. These Strehl maps provided information on the performance of the refocusing system over the whole field of view of the imaging system and also allowed us to assess field-dependent aberrations such as field curvature. Used statically this refocusing approach allowed for diffraction limited performance with the Olympus 40x/0.85NA air objective over an axial refocus range of 35 μm . Used dynamically the method was not able to achieve diffraction limited results but the Olympus 40x/0.80NA water immersion objective could achieve a mean Strehl ratio over the central 200x200 μm of the FOV of >0.7 for an axial refocus of 52 μm and >0.6 through a refocus of 77 μm . For the Olympus 50x/0.85NA air objective the procedure achieved a mean Strehl over the central 200x200 μm of >0.6 through an axial refocus of 40 μm . The difference between static and dynamic performance

likely due to the fact that the mirror was moving during the exposure of the camera – creating blur which would affect the optimisation procedure. With a brighter light-source and reduced exposure time this problem would become less significant. The next limiting factors are concerned with the fidelity of the mirror at representing higher Zernike modes with issues such as the number of actuators and inter-actuator distance. One would imagine that it should be possible for the dynamic refocusing performance to be equivalent to the static performance if the mirror can be made to effectively fit the difference in the mirror surface associated with the thermal effects due to the high-speed motion. Objectives are carefully designed to balance aberrations such as spherical aberration and field curvature at the design conjugates. At non-design conjugates the spherical aberration can be corrected through high-NA defocus however field curvature, a field dependent aberration, cannot be corrected with a single adaptive optic at a Fourier plane, and ultimately limits the performance of this kind of system.

It was found that it was necessary to re-optimize the command sequence for the DM each day even once the best flat had been obtained. Often, DM refocusing commands were re-optimized starting from the previous day's commands. The changes were small but significant. If there is no change in the alignment of the system or sample, then any change in response must be due to the DM. The behavior of the DM is determined by its best flat set of commands and also its influence matrix. It is likely that the thermal changes to the mechanical properties of the DM are causing the influence matrix to vary slightly in addition to changing the best flat. Therefore, an alternative to reoptimizing the command sequence each day may be to measure the influence matrix of the DM each day using a Shack Hartman wavefront sensor. With a correctly measured influence matrix and best flat the previously measured set of Zernike modes and correction to high-NA defocus might then be able to be applied and so enable daily changes in mirror response to be corrected without the need for time-consuming re-optimisation.

Once the DM-based refocusing system had been demonstrated, we then incorporated it into a LSFM system and this was described in chapter 5. LSFM imaging at 26.3 vol/sec over the axial range 50 μm to -50 μm was demonstrated using both a stroboscopic camera acquisition – where the whole field of the camera could be used – and using direct volumetric imaging of multiple planes per volume. The system was used to image corn and sunflower pollen and also its performance characterized with 200 nm fluorescent beads; it was found to have a mean lateral FWHM of 0.835 μm over then central 100x100 μm of the field of view (FOV) throughout the axial refocus range, with diffraction limited performance being 0.375 μm .

There are several ways in which the performance of the instrument could be improved in a next iteration. The need to rotate the imaging objective from an optimisation position to the LSM position, and the tolerances of the rotating cage segment causing the image of the back focal plane of the objective on the DM to move, was a likely source of aberrations. Rotation of the imaging objective also meant that the illumination system had to be completely realigned each time prior to use which was very time consuming. Ideally, the imaging objective should not be moved at all after it has been aligned. This could be achieved by raising the level of the entire system by 10 cm so that the STM, diffuser and LED could fit underneath the imaging objective for the optimisation procedure. This would mean that after an initial alignment there would be no further need to move either the illumination or the imaging sub-systems. Another improvement could be made to the positioning of the DM in the optical train of the imaging system. A correction was made in this system due to the fact that the centre of the DM was slightly displaced from the axis of the imaging system. An engineering solution would obviate this need, possibly a DM mount which locks into the cage system of the imaging arm.

Another weakness of the system was that the image of the back focal plane of the imaging objective on the DM overfilled the pupil of the DM. This reduced the effective NA of the system from 0.80 or 0.85 (for the water and air objectives used respectively) to 0.75 with the DM acting as the aperture stop. This reduction in NA was due to the limited range of magnifications that could be achieved using a pair of commercially available tube lenses. We also established that it was necessary to use better-corrected tube lenses rather than achromatic doublets in order to prevent the accumulation of aberrations in the system. In the future, it may be possible that another pair of tube lenses could be designed or chosen which do match the pupil of the objective to that of the DM without limiting the NA. Another approach might be to replace one of the tube lenses with a pair of achromatic doublets or a doublet and a tube lens. The spacing between the lenses would then permit adjustment of the magnification of the back focal plane until it matched the DM, but would create additional aberrations which would need to be corrected by the DM.

The tilt of the DM means that its pupil will always present as an ellipse from the point of view of the imaging objective. If the pupil of the DM is smaller than the image of the back focal plane of the objective, then it will clip the light in an elliptical shape. As a result, the optical system will have a slightly lower NA in the plane of the optical table than the plane perpendicular to the optical table. If on the other hand the pupil of the DM over-fills the image of the back focal plane then no light is lost so there is no reduction or difference in NA between the 2 axes – however this comes at the expense of not using all of the active surface of the DM.

Another improvement to this system would be to use a brighter LED for optimisation. Ideally the LED should be on for no more than 0.2 ms in order for the DM movement not to create blur at 26.3 vol/sec. In this project the signal level at 0.2 ms was inadequate and would at times cause the optimisation procedure to be less than effective. Another improvement would be to connecting the Orca Flash camera to the computer via a frame grabber rather than a USB connection, which would then be able to acquire full frames at a rate of 100 fps, or a reduced FOV at much greater frame rates. This would mean that a greater number of images with a greater FOV could be captured through each volume.

After optimisation for the defocus of the STM there was still remaining stroke which could be used to correct for sample-induced aberrations. This would require using a sensorless optimisation approach based on e.g. an image-based metric such as brightness or contrast associated with an imaged feature. After a single initial correction for the sample-induced aberrations the system could then be run at high speed for volumetric imaging. One type of sample-induced aberration, which can be expressed in analytical form, is that due to a refractive index mismatch between the immersion medium and the sample; in the future it may be possible to introduce a programmatic method to compensate this aberration automatically using the DM.

This project has demonstrated a first iteration of a high-speed, video-rate deformable mirror based LSFM. The project demonstrated a novel solution for how visco-elastic and thermal hysteresis associated with the Alpao DM97-15 membrane mirror could be managed by optimizing with the mirror vibrating at the desired rate of volumetric imaging. The project also showed that it was mostly field curvature that limited the ability of a DM in the Fourier plane to correct for high-NA defocus of the objective.

The central achievement of the project has been the demonstration of high optical throughput with video rate volumetric scanning without the loss of light associated with approaches to remote refocusing – with a robust 90 min optimisation procedure prior to use for imaging. This is an advance on prior art in several ways. It provides a robust and simple solution to dealing with the visco-elastic and thermal creep associated with Alpao membrane deformable mirrors which had previously required interferometry [4,5]. The rapid refocusing with a DM in the multiphoton microscope in reference [6] achieved an axial displacement of 50 μm at a rate of 2 volumes/sec compared with a superior 100 μm at 26.3 volumes/sec in this work. The DM based extended depth of field system in reference [7] achieved an axial displacement of 41 μm at 472 volumes/sec. The large rate of acquisition is mitigated by the fact that deconvolution is required with each volume – which requires computation/time and will likely not perform well with thickly labelled samples, whereas once the mirror has been optimized (90 min) it can robustly acquire images for the rest of the day.

Published work and proceedings

- 4/2018 EMBO Practical course in advanced optical microscopy for cell biology, poster presentation, “Video-rate remote refocusing via continuous oscillation of a membrane deformable mirror”, Terry Wright, Hugh Sparks, Carl Paterson and Chris Dunsby.
- 11/2019 Microsoft Research PhD workshop, poster presentation, “Video-rate remote refocusing via continuous oscillation of a membrane deformable mirror”, Terry Wright, Hugh Sparks, Carl Paterson and Chris Dunsby.
- 4/2020 Accepted to give oral presentation at FOM 2020, but cancelled due to Covid19
- 9/2020 RMS LSFM 2020, oral presentation, “Video-rate remote refocusing via continuous oscillation of a membrane deformable mirror”, Terry Wright, Hugh Sparks, Carl Paterson and Chris Dunsby.
- 10/2020 IOP Photon 2020, oral presentation, “Video-rate remote refocusing via continuous oscillation of a membrane deformable mirror”, Terry Wright, Hugh Sparks, Carl Paterson and Chris Dunsby.
- 4/2021 FOM 2021, oral presentation, “Video-rate remote refocusing via continuous oscillation of a membrane deformable mirror ”, Terry Wright, Hugh Sparks, Carl Paterson and Chris Dunsby.
- 10/2021 Accepted for publication, “Video-rate remote refocusing via continuous oscillation of a membrane deformable mirror ”, Terry Wright, Hugh Sparks, Carl Paterson and Chris Dunsby. *J. Phys. Photonics*, 2021. **3** 045004 <https://doi.org/10.1088/2515-7647/ac29a2>

References

1. E.J. Botcherby, R. Juškaitis, M.J. Booth and T. Wilson, *Aberration-free optical refocusing in high numerical aperture microscopy*. Optics Letters, 2007. **32**.
2. B. Grewe, F.V., M. van 't Hoff, and F. Helmchen, *Fast two-layer two-photon imaging of neuronal cell populations using an electrically tunable lens*. Biomed. Opt. Express 2011. **2**: p. 2035-2046.
3. P.Y. Madec, *Overview of deformable mirror technologies for adaptive optics and astronomy*. Proc. SPIE, Adaptive Optics System III, 2012. 844705.
4. U. Bitenc, N.B., T. Morris, R. Myers, *Assessing the stability of an ALPAO deformable mirror for feed-forward operation*. Opt Express, 2014. **22**: p. 12438-12451.
5. Bitenc, U., *Software compensation method for achieving high stability of Alpao deformable mirrors*. Opt Express, 2017. **25**: p. 4368-4381.
6. M. Žurauskas, O. Barnstedt, M. Frade-Rodriguez, S. Waddell, and M. Booth, *Rapid adaptive remote focusing microscope for sensing of volumetric neural activity*. Biomed. Opt. Express, 2017. **8**: p. 4369-4379
7. W. J. Shain, N. A. Vickers, B. B. Goldberg, T. Bifano, J. Mertz, *Extended depth-of-field microscopy with a high-speed deformable mirror*. Opt Lett, 2017. **42**(5): p. 995-998.
8. M. Born, E. Wolf, *Principles of Optics*. 1983: Pergamon Press.
9. A.H. Bennet, *The development of the microscope objective*. Journal of the Optical Society of America, 1943. **33**(3): p. 123-128.
10. C. Fink, F. Morgan, L.M. Leow, *Intracellular fluorescent probe concentrations by confocal microscopy*. Biophysical Journal, 1998. **75**(4): p.1648-1658
11. C. Wenzel et al., *3D high-content screening for the identification of compounds that target cells in dormant tumor spheroid regions*. Cancer Research, 2015. **75**.
12. Y. Zhang, and H. Gross, *Systematic design of microscope objectives. Part I: System review and analysis*. Advanced Optical Technologies, 2019. **8**(5): p. 313-347.
13. Y. Zhang, and H. Gross, *Systematic design of microscope objectives. Part II: Lens modules and design principles*. Advanced Optical Technologies, 2019. **8**(5): p. 349-384.
14. J.C. Deiman, *MRes dissertation, Imperial College, Microscope optics and JJ Lister's influence on the development of the chromatic objective, 1750-1850*. 1992.
15. R. Kingslake, *Lens Design Fundamentals*. 1978: Academic Press, New York.
16. H. Boegehold, *US 1578259*, 1940.
17. A.H. Shoemaker, *US 3700311*, 1972.
18. J.W. Lichtman, Jose-Angel Canchello, *Fluorescence microscopy*. Nature Methods, 2005. **2**: p. 910-919.
19. J. Nakai, M. Ohkura, K. Imoto, *A high signal to noise Ca²⁺ probe composed of a single green fluorescent protein*. Nature Biotechnology, 2001. **19**: p. 137-141.
20. K.R. Gee, K.A. Brown, W.N.U. Chen, J. Bishop-Stewart, D. Gray, I. Johnson, *Chemical and physiological characterisation of fluo-4 Ca²⁺ indicator dyes*. Cell Calcium, 2000. **27**: p. 97-106.

21. O. Shimomura, F.H. Johnson, and Y. Saiga, *Extraction, Purification and Properties of Aequorin; a Bioluminescent Protein from the Luminous Hydromedusan, Aequorea*. Journal of Cellular and Comparative Physiology, 1962. **59**: p. 223-239.
22. M. Chalfie, Y. Tu, G. Euskirchen, W.W. Ward and D.C. Prasher, *Green fluorescent protein as a marker for gene expression*. Science, 1994. **263**: p. 802-805.
23. D.C. Prasher, V.K. Eckenrode, W.W. Ward, F.G. Prendergast, and M.J. Cormier, *Primary structure of the Aequorea victoria green-fluorescence protein*. Gene, 1992. **111**: p. 229-233.
24. R.Y. Tsien, *The green fluorescent protein*. Annual review of biochemistry, 1998. **67**: p. 509-522.
25. T. Xian, N. Li, X. Fang, *Single molecule fluorescent imaging in living cells*. Annual review of physical chemistry, 2013. **64**: p. 459-480.
26. T. Wilson, *Optical sectioning in fluorescence microscopy*. Journal of Microscopy, 2010. **242**(2): p. 111-116.
27. M. Minsky, *Microscopy apparatus (published 1961)*. 1957.
28. T. Wilson, *Resolution and optical sectioning in the confocal microscope*. Journal of Microscopy, 2011. **244**(2): p. 113-21.
29. T. Wilson, *Optical sectioning in confocal fluorescent microscopes*. Journal of Microscopy, 1989. **154**: p. 143-156.
30. T. Wilson and C. J. R. Sheppard, *Theory and Practice of Scanning Optical Microscopy*. 1984: Academic Press, New York, 1984.
31. B.F. Grewe, D. Langer, H. Kasper, B.M. Kampa, and F. Helmchen, *High-speed in vivo calcium imaging reveals neuronal network activity with near-millisecond precision*. Nat Methods, 2010. **7**(5): p. 399-405.
32. G. Duemani Reddy, K. Kelleher, R. Fink, and P. Saggau, *Fast three-dimensional laser scanning scheme using acousto-optic deflectors*. J Biomed Opt, 2005. **10**.
33. P. Lanigan, *Application of confocal and multiphoton microscopes to multidimensional fluorescence imaging*. 2006, Thesis, Imperial College.
34. K.B. Im, S. Han, H. Park, D. Kim, and K.M. Kim, *Simple high-speed confocal line-scanning microscope*. Optics Express, 2005. **13**.
35. E. Mei, P. A. Fomitchov, R. Graves, M. Campion, *A line scanning confocal fluorescent microscope using a CMOS rolling shutter as an adjustable aperture*. J Microsc, 2012. **247**: p. 269-76.
36. T. Tanaami, S. Otsuki, N. Tomosada, Y. Kosugi, M. Shimizu, H. Ishida, *High-speed 1-frame/ms scanning confocal microscope with a microlens and Nipkow disks*. Applied Optics, 2002. **14**.
37. E. Wang, C.M. Babbey, K.W. Dunn, *Performance comparison between the high-speed Yokogawa spinning disc confocal system and single-point scanning confocal systems*. Journal of Microscopy, 2005. **218**: p. 148-159.
38. A. Mayer, H. P. Thomas, H. Vogel, T. A. Steitz, D. M. Engelman, D. B. McKay, A. Steitz, J. Wyman, J. P. Changeux, T. A. Hardt, W. F. Mangel, C. Livingston, L. L. Melhado, S. W. Peltz, B. P. Schoenborn, G. Zaccai, C. Sutherland, J. Desmond, Z. Takacs, J. C. Sutherland, P. C. Keck, K. P. Griffin, P. Z. Takacs, D. Toledo,

- W. Denk, J. Strickler, and W. W. Webb, *Two-photon laser scanning fluorescence microscopy*, Science, 1990. **248**: p. 73–76
39. P. So, H. Kim, and I. Kochevar, *Two-photon deep tissue ex vivo imaging of mouse dermal and subcutaneous structures*, Opt. Express, 1998. **3**: p. 339–350
 40. F. Helmchen and W. Denk, *Deep tissue two-photon microscopy*, Nat. Methods, 2005. **2**: p. 932–940
 41. D.S.C. Biggs, *3D Deconvolution Microscopy*. Current Protocols in Cytometry, 2010. **52**(1).
 42. R. Gonzalez, R. Woods, S. Eddins, *Digital Image Processing Using Matlab*. 2003: Prentice Hall.
 43. M.A.A. Neil, R. Juškaitis, T. Wilson, *Method of obtaining optical sectioning by using structured light in a conventional microscope*. Optics Letters, 1997. **22**.
 44. M.G. Gustafsson et al., *Three-dimensional resolution doubling in wide-field fluorescence microscopy by structured illumination*. Biophys J, 2008. **94**(12): p. 4957-70.
 45. M.G. Gustafsson, *Surpassing the lateral resolution limit by a factor of two using structured illumination microscopy*. Journal of Microscopy, 2000. **198**: p. 82-87.
 46. H. Siedentopf, R. Zsigmondy., *Über Sichtbarmachung und Grossenbestimmung ultramikroskopischer Teilchen, mit besonderer Anwendung auf Goldrubinglaser*. Annalen der Physik, 1902. **315**.
 47. A.H. Voie, D.H.B., F.A. Spelman, *Orthogonal-plane fluorescence optical sectioning: Three-dimensional imaging of macroscopic biological specimens*. HJournal of Microscopy, 1993. **170**: p. 229-236.
 48. E. Fuchs, J.S. Jaffe., *Thin laser light sheet microscope for microbial oceanography*. Optics Express, 2002. **10**.
 49. J. Huiskens, J. Swoger, F.D. Bene, J. Wittbrodt, E. H. K. Stelzer., *Optical Sectioning Deep Inside Live Embryos by Selective Plane Illumination Microscopy*. Science, 2004. **305**.
 50. P. J. Keller and H. U. Dodt, *Light sheet microscopy of living or cleared specimens*. Curr Opin Neurobiol, 2012. **22**(1): p. 138-43.
 51. P. J. Keller, et al., *Fast, high-contrast imaging of animal development with scanned light sheet-based structured-illumination microscopy*. Nat Methods, 2010. **7**(8): p. 637-42.
 52. P. J. Keller and E.H. Stelzer, *Quantitative in vivo imaging of entire embryos with Digital Scanned Laser Light Sheet Fluorescence Microscopy*. Curr Opin Neurobiol, 2008. **18**(6): p. 624-32.
 53. J.M. Taylor, M. John, J. M. Girkin, G. D. Love., *High-resolution 3D optical microscopy inside the beating zebrafish heart using prospective optical gating*. Biomedical Optics Express, 2012. **3**: p. 3043-3053
 54. O. Svelto, *Principles of Lasers*. 2010: Springer.
 55. F. O. Fahrbach, et al., *Self-reconstructing sectioned Bessel beams offer submicron optical sectioning for large fields of view in light-sheet microscopy*. Opt Express, 2013. **21**(9): p. 11425-40.
 56. F. O. Fahrbach, P. Simon, and A. Rohrbach, *Microscopy with self-reconstructing beams*. Nature Photonics, 2010. **4**(11): p. 780-785.
 57. Fahrbach, F.O., et al., *Light-sheet microscopy in thick media using scanned Bessel beams and two-photon fluorescence excitation*. Opt Express, 2013. **21**(11): p. 13824-39.

58. T. A. Planchon, et al., *Rapid three-dimensional isotropic imaging of living cells using Bessel beam plane illumination*. Nat Methods, 2011. **8**(5): p. 417-23.
59. L. Silvestri, A. Bria, L. Sacconi, G. Iannello, F. S. Pavone, *Confocal light sheet microscopy: micron-scale neuroanatomy of the entire mouse brain*. OPTICS EXPRESS, 2012. **20**.
60. P. Zhang, M.E.Phipps, P.M. Goodwin, J.H. Werner, *Confocal line scanning of a Bessel beam for fast 3D imaging*. Opt. Lett., 2014. **39**: p. 3682-3685.
61. T. Vettenburg, et al., *Light-sheet microscopy using an Airy beam*. Nat Methods, 2014. **11**(5): p. 541-4.
62. J. Nytk, K. McCluskey, S. Aggarwal, J. A. Tello, K. Dholakia, *Enhancement of image quality and imaging depth with Airy light-sheet microscopy in cleared and non-cleared neural tissue*. Biomed Opt Express, 2016. **6**: p. 4021-4033.
63. I. Golub, T.M., J. Nuttall, D. Shaw, *The taming of absorption: generating a constant intensity beam in a lossy medium*. Optics Letters, 2012. **37**.
64. J. Nytk, K. McCluskey, M. A. Preciado, M. Mazilu, Z. Yang, F. J. Gunn-Moore, S. Aggarwal, J. A. Tello, D. E. K. Ferrier, K. Dholakia, *Light-sheet microscopy with attenuation-compensated propagation-invariant beams*. Science Advances, 2018. **4**.
65. T. Cizmar, K.Dholakia, *Tunable Bessel light modes: Engineering the axial propagation*. Opt.Express, 2009. **17**: p. 15558-15570.
66. M. Zamboni-Rached, *Stationary optical wave field with arbitrary longitudinal shape by superposing equal frequency Bessel beams:Frozen waves*. Opt Express, 2004. **12**: p. 4001-4006.
67. S. Preibisch, S.Saalfeld, J. Schindelin, P. Tomancak, *Software for bead-based registration of selective plane illumination microscopy data*. Nat. Methods, 2010. **7**: p. 418-419.
68. J. Huiskens, D.Y.R. Stainer, *Even fluorescence excitation by multidirectional selective plane illumination microscopy (mSPIM)*. Opt. Lett., 2007. **32**: p. 2608-2610.
69. J. Swoger, J. Huiskens, E.H.K. Stelzer, *Multiple imaging axis microscopy improves resolution for a thick sample*. Opt. Lett., 2003. **15**: p. 1654-1656.
70. J. Swoger, P.J. Verveer, K. Greger, J. Huiskens, *Multi-view image fusion improves resolution in three-dimensional microscopy*. Opt Express, 2007. **15**: p. 8029-8042.
71. Y. Wu, P. Wawrzusin, J. Senseney, R. S. Fischer, R. Christensen, A. Santella, *Spatially isotropic four-dimensional imaging with dual-view plane illumination microscopy*. Nat. Biotechnol., 2013. **31**: p. 1032-1038.
72. A. Kumar, Y. Wu, R. Christensen, P. Chandris, W. Gandler, E. McCreedy, *Dual-view plane illumination microscopy for rapid and spatially isotropic imaging*. Nat. Protoc., 2014. **9**: p. 2555-2573.
73. R. McGorty, et al., *Open-top selective plane illumination microscope for conventionally mounted specimens*. Opt Express, 2015. **23**(12): p. 16142-53.
74. M. Tokunaga, N. Imamoto, K. Sakata-Sogawa, *Highly inclined thin illumination enables clear single molecule imaging in cells*. Nature methods, 2008. **5**: p. 159-161.
75. C. Dunsby, *Optically sectioned imaging by Oblique Plane Microscopy*. Optics Express, 2008. **16**: p. 20306-20316.

76. E. J. Botcherby, R. Juškaitis, M. J. Booth, T. Wilson, *An optical technique for remote focusing in microscopy*. Optics Communications, 2008. **281**(4): p. 880-887.
77. S. Kumar, D. Wilding, M. B. Sikkell, A. R. Lyon, K. T. MacLeod, C. Dunsby, *High-speed 2D and 3D fluorescence microscopy of cardiac myocytes*. OPTICS EXPRESS, 2011. **19**.
78. M. B. Sikkell, S. Kumar, V. Maioli, C. Rowlands, F. Gordon, S. E. Harding, A. R. Lyon, K. T. MacLeod, C. Dunsby, *High speed sCMOS-based oblique plane microscopy applied to the study of calcium dynamics in cardiac myocytes*. J Biophotonics, 2016. **9**(3): p. 311-23.
79. M.B. Bouchard, V. Voleti, C.S. Mendes, C. Lacefield, W.B. Gruber, R.S. Mann, R.M. Bruno, E.M.C. Hillman, *Swept confocally-aligned planar excitation (SCAPE) microscopy for high-speed volumetric imaging of behaving organisms*. Nature Photonics, 2015. **9**: p. 113-119.
80. T. Li, S. Ota, J. Kim, Z. J. Wong, Y. Wang, X. Yin and X. Zhang, *Axial plane optical microscopy*. Sci Rep, 2014. **4**: p. 7253.
81. M. B. M. Meddens, S. Liu, C. D. James, T. Edwards and K. A. Lidke, *Reflected Beam Light-Sheet Microscopy for Whole-Cell 3D Super-Resolution Imaging*. Biophysical Journal, 2015. **108**(2).
82. E. J. Botcherby, R. Juškaitis, T. Wilson, *Scanning two photon fluorescence microscopy with extended depth of field*. Opt. Commun., 2006. **268**: p. 253-260.
83. G. Hausler, *A method to increase the depth of focus by two step image processing*. Opt. Commun., 1972. **6**(38-42).
84. P. Török, Fu-Jen Kao , *Optical Imaging and Microscopy*. 2007: Springer.
85. E.J. Botcherby, M. J. Booth, R. Juškaitis , *Real time extended depth of field microscopy*. Opt Express, 2008. **16**(26).
86. W. J. Shain, N. A. Vickers, A. Negash, T. Bifano, A. Sentenac, J. Mertz, *Dual fluorescence-absorption deconvolution applied to extended-depth-of-field microscopy*. Opt Lett, 2017. **42**(20): p. 4183-4186.
87. J. Edward, R. Dowski, W. T. Cathey, *Extended depth of field through wave-front coding*. Appl Opt, 1995. **34**: p. 1859-1866.
88. O.E. Olarte, J. Andilla, D. Artigas, P. Loza-Alvarez, *Decoupled illumination detection in light-sheet microscopy for fast volumetric imaging*. Optica, 2015. **2**(8).
89. R. K. Tyson, *Introduction to Adaptive Optics*. 2000: SPIE Press.
90. V. Tuchin, *Tissue Optics*. 2007: SPIE Press.
91. M. J. Booth, M. A. A. Neil, R. Juškaitis, T. Wilson, *Adaptive aberration correction in a confocal microscope*. PNAS, 2002. **99**(9).
92. P.N. Marsh, D. Burns, J. Girkin , *Practical implementation of adaptive optics in multiphoton microscopy*. Opt Express, 2003. **11**: p. 1123-1130.
93. L.Sherman, J.Y. Ye, O. Albert, T.B. Norris, *Adaptive correction of depth-induced aberrations in multiphoton scanning microscopy using a deformable mirror*. J Microsc, 2002(206): p. 65-71.
94. B. Sherlock, S. Warren, J. Stone, M. Neil, C. Paterson, J. Knight, P. French, C. Dunsby , *Fibre-coupled multiphoton microscope with adaptive motion compensation*. Biomed Opt Express, 2015. **6**(5).

95. L.A. Roger, W.C. Lemon, R.K. Chhetri, Y. Wan, M. Coleman, E.W. Myers, P.J. Keller , *Adaptive light-sheet microscopy for long-term, high-resolution imaging of living organisms*. 34, 2016: p. 1267-1278.
96. C. Bourgenot, C. D. Saunter, J. M. Taylor, J. M. Girkin, G. D. Love, *3D adaptive optics in a light sheet microscope*. Optics Express, 2012. **20**(12): p. 13252-13261.
97. M. J. Booth, *Adaptive optical microscopy: the ongoing quest for a perfect image*. Light: Science and Applications, 2014.
98. A. J. Wright, D. Burns, B. A. Patterson, S. P. Poland, G. J. Girkin, M.J. Padgett, *Dynamic closed-loop system for focus tracking using a spatial light modulator and a deformable mirror*. Opt Express, 2006. **14**: p. 222-228.
99. O. Azucena, J. Crest, S. Kotadia, W. Sullivan, X. Tao, M. Reinig, D. Gavel, S. Olivier, J. Kubby , *Adaptive optics wide-field microscopy using direct wavefront sensing*. Optics Letters, 2011. **36**(6).
100. R. Jorand., *Deep and clear optical imaging of thick inhomogeneous samples*. PLoS 2012. **7**.
101. A. J. Wright, D. Burns, B. A. Patterson, S. P. Poland, G. J., *Exploration of the optimiation algorithms used in the implementation of adaptive optics in confocal and multiphoton microscopy*. Microsc Res Tech, 2005. **64**(36).
102. M. J. Booth, *Wavefront sensorless adaptive optics for large aberrations*. Opt. Lett., 2007. **32**(5-7).
103. D, Débarre , *Image-based adaptive optics for two-photon microscopy*. Opt. Lett., 2009. **34**: p. 2495-2497.
104. R.A. Gonsalves, *Phase retrieval and diversity in adaptive optics*. Opt. Eng., 1982. **21**.
105. P. Kner, L. Winoto, D. A. Agard, J. W. Sedat , *Closed loop adaptive optics for microscopy without a wavefront sensor*. Proc. SPIE, 2010.
106. P. Kner, *Phase diversity for three dimensional imaging*. J. Opt. Soc. Am. A, 2013. **30**.
107. K. Wang, *Direct wavefront sensing for high-resolution in vivo imaging in scattering tissue*. . Nat. Commun., 2015. **6**: p. 7276.
108. N. Ji., T. Sato, R. Betzig, *Characterization and adaptive optical correction of aberrations during in vivo imaging in the mouse cortex*. Proc. Natl. Acad. Sci. USA, 2012. **109**.
109. K. Wang, *Rapid adaptive optical recovery of optimal resolution over large volumes*. Nat. Methods, 2014. **11**: p. 625-628.
110. C. Wang, *Multiplexed aberration measurement for deep tissue imaging in vivo*. Nat. Methods, 2014. **11**: p. 1037-1040.
111. H. Sparks, L. Dvinskikh, J. M. Firth, A. J. Francis, S. E. Harding, C. Paterson, K. T. MacLeod, C. Dunsby, *A flexible light-sheet fluorescence microscope for high-speed 3D imaging of calcium dynamics and 3D imaging of cellular microstructure*. J Biophotonics, 2020. **13**(6): p. e201960239.
112. M. Mansuripur, *Classical Optics and Applications*. 2009: Cambridge University Press.
113. M. Mansuripur, *Abbe's Sine Condition*. Optics and Photonics News, 1998. **9**(2).
114. W.T. Wetford , *Aberrations of optical systems*. 1986: CRC Press.
115. F. Zernike, *Beugungstheorie des Schneidenverfahrens und seiner verbesserten Form, der Phasenkontrastmethode*. . Physica (Utrecht). 1934. **1**: p. 689-704.

116. M.V. Svechnikov, N.I.Chkhalo, M.N. Toropov, N.N. Salashchenko, *Resolving capacity of the circular Zernike polynomials*. Optics Express, 2015. **23**.
117. R. J. Noll, *Zernike polynomials and atmospheric turbulence*. Opt. Soc. Am., 1976. **66**.
118. F.O. Fahrbach, F. F. Voigt, B. Schmid, F. Helmchen, J. Huisken, *Rapid 3D light-sheet microscopy with a tunable lens*. Opt Express, 2013. **21**(18): p. 21010-26.
119. J. Jabbour, B. Malik, C. Olsovsky, R. Cuenca, S. Cheng, J. Jo, Y. Cheng, J. Wright, K. Maitland, *Optical axial scanning in confocal microscopy using an electrically tunable lens*. Biomed. Opt. Express 2014. **5**.
120. M. Gu, *Advanced Optical Imaging Theory*. 2000: Springer.
121. L.Philipp, F Lemke, S. Scholz, U. Wallrabe, M.C. Wapler, N. Koukourakis, J.W.Czarske *Diffraction-limited axial scanning in thick biological tissue with an aberration-correcting adaptive lens*. Scientific Reports, 2019. **9**: p. 9532.
122. W. Torres-Sepúlveda, J. Henao, J. Morales-Marin, A. Mira-Agudelo, E. A. Rueda-Muñoz, *Hysteresis characterization of an electrically focus-tunable lens*. Opt. Eng., 2020. **59**.
123. J. S. Goodman, *Introduction to Fourier Optics*. 1996: McGraw-Hill.
124. J.M. Girkin, S.P. Poland, A.J. Wright, *Adaptive optics for deeper imaging of biological samples*. Curr. Opin. Biotechnol., 2009. **20**: p. 106-110.
125. B. Thomas, A. Wolstenholme, S. N. Chaudhari, E. T. Kipreos, P. Kner , *Enhanced resolution through thick tissue with structured illumination and adaptive optics*. J. Biomed. Opt., 2015. **20**.
126. E. Auksoorius, B.R. Boruah, C. Dunsby, P.M. Lanigan, G.Kennedy, M.A.A. Neil, P.M.W. French, *Stimulated emission depletion microscopy with a supercontinuum source and fluorescence lifetime imaging*. Optics Letters, 2008. **33**(2): p. 113-115.
127. M.O. Lenz, H.G. Sinclair, A. Savell, J.H. Clegg, A.C. Brown, C. Dunsby, M.A.A. Neil, P.M.W. French, *3-D stimulated emission depletion microscopy with programmable aberration correction*. J Biophotonics, 2014. **7**: p. 29-36.
128. T.J. Gould TJ, E.B. Kromann, D. Burke, M.J. Booth, J. Bewersdorf, *Auto-aligning stimulated emission depletion microscope using adaptive optics*. Optics Letters, 2013. **38**: p. 1860-1862.
129. H. W. Babcock, *The possibility of compensating astronomical seeing*. Pub, Astron. Soc. Pac., 1953. **65**: p. 229-36.
130. D. Malacara, *Optical shop testing*. 2007: John Wiley and Sons, Inc.
131. Alpao, *Deformable mirror test report: DM97-15 HSDM97-15-014*, 2017.
132. D. MacKay, *Information Theory, Inference and Learning Algorithms*. 2003: Cambridge University Press.
133. R. F. Barry, *MRes dissertation, Imperial College, Investigation of the implementation of laser-scanning light-sheet formation for the OPM*. 2014.
134. Terry Wright, Hugh Sparks, Carl Paterson and Chris Dunsby, *Video-rate refocusing through continuous oscillation of a deformable mirror*. 2021. *J.Phys. Photonics* **3** 045004 <https://doi.org/10.1088/2515-7647/ac29a2>

135. E. Abbe, *A contribution to the theory of the microscope and the nature of microscopic vision*. 1874. Proceedings of the Bristol Naturalists Society **1**: p. 200-261
136. E. Abbe, *On the estimation of aperture in the microscope*. 1881. Journal of the Royal Microscopical Society **1**: p. 388-423
137. H. von Helmholtz, *On the limits of the optical capacity of the microscope*. 1876. The Monthly Microscopical Journal. **16**: p. 15-39
138. W. V. Houston, *A compound interferometer for fine structure work*. 1927. Physical Review. **29**: p. 478-484
139. H. Hopkins, *The aberration permissible in optical systems*. 1957. Proceedings of the Physical Society B, **70**: p. 449-470

Appendix

A1 All Scripts and Code for this thesis:

All of the code is available via GitHub, DOI: 10.5281/zenodo.5732850

Where possible an Object Orientated approach has been used. Each piece of hardware is represented by a software object, and where multiple types of hardware are used e.g. cameras or stage actuators the objects are arranged into hierarchies. The precise manner in which the piece of hardware is accessed is hidden within the object however will either be via a SDK or by issuing RS232 commands. In the case of the Orca Flash camera the Matlab camera object calls a dynamic link library (DLL) which then calls into the Hamamatsu DCAM dynamic link library – which is the generic library for PVCAM cameras. This intermediate DLL is referred to as a Relay DLL as in most cases it relays commands from Matlab to call C++ functions within DCAM.dll. In some cases, due to the limitations of Matlab, in terms of accessing pointers, the Relay.dll needed to slightly change the function however this is explained in detail in the code in various ReadMe.docx files. All of this complexity of calls to DLLs etc., is hidden inside the Orca Flash object. The Shack Hartman Wavefront Sensor is handled in a similar manner.

The following is a brief summary of all of the key Matlab scripts:

1. **Script to measure centre of optical axis on DM** – acquires two images, one each side of focus and checks for lateral shift. It performs a grid-search for different positions of the optical axis on the disk of the DM and chooses the point that has the minimum displacement.

DMLSFM_ALIGN_DM_WITH_OPTICAL_AXIS.m

2. **Scripts for flattening the DM** – uses the Shack-Hartmann and DM. Initially pokes each activator in turn and identifies their location as viewed by the Shack Hartman. Then flattens the mirror with the current factory flat. An image is taken with the Shack Hartman, any displacement of the surface of the mirror from being flat is taken to be an error. A small amount of this error is reversed – and sent to each actuator of the DM, in order to move the mirror surface closer to flat. This negative feedback is then repeated, taking an image with the SHWFS, subtracting an proportionate amount from the DM commands, until the mirror's RMS of the surface displacement has converged.

DMLSFM_FLATTENING_THE_DM_WITH_SHACK_HARTMAN.m

3. **Script for control of the stage.** Many scripts need to move the stage, rather than each having a Stage object this script runs constantly in the background in an instance of Matlab. This script initialised and manages the stage. It monitors a file, stage_config.xml, and if the stage position element changes (as changed by another program), then it will move to the new stage position. In this way programs only need to change this single entry in stage_config.xml and not need to home the stage etc.

DMLSFM_SCRIPT_STAGE_CONTROLLER.m

4. **Optimisation of the DM and evaluation of the set of command generated.** The DM will play a sequence of poses – at the beginning of the sequence the DM produces a trigger pulse. When the Flash takes an image it produces an output pulse which is high for the length of the exposure (1ms). This is fed into a NIDAQ 6363 which chops down the length of the pulse, which is then attached to the laser, which is implemented by DMLSFM_PULSE_REDUCER_FOR_OPTIMISATION.vi. The Matlab processes running simultaneously, MASTER and _SLAVE control the optimisation and the evaluation between them. The 2 Matlab processes communicate via a memory map. The memory map contains details about the exposure time and the number of frames per second etc. The MASTER is responsible for the behaviour of the mirror and the SLAVE is responsible for acquiring images with the Orca Flash camera and also evaluating and controlling the optimisation.

DMLSFM_OPTIMISATION_AND_EVALUATION_MASTER.m

DMLSFM_OPTIMISATION_AND_EVALUATION_SLAVE.m

DMLSFM_PULSE_REDUCER_FOR_OPTIMISATION.vi

Imaging script – for strobed images at a particular defocus while the DM is oscillating continuously (includes galvo for LSFM). Within each volumetric sweep 1 image is taken with the full FOV of the Orca Flash camera. The associated LabVIEW script determines the pulses to send to the Orca Flash camera to trigger the exposure and also to the laser. The DMLSFM_STROBE_MASTER Matlab script controls the DM. The control of the DM is separate

to the camera and the camera could be controlled with the Hamamatsu HCI application or micromanager or the the above Matlab script:

DMLSFM_OPTIMISATION_AND_EVALUATION_SLAVE.m

There are two sets of scripts for strobed image. The following Matlab and LabView scripts allow you to change the position of the strobed image at runtime – however the interpose time must be less than 5ms.

DMLSFM_STROBE_MASTER.m

DMLSFM_STROBE.vi

The following Matlab and LabView scripts can be used for interpose time longer than 5 ms, however the position of the strobed image cannot be changed at runtime.

DMLSFM_STROBE_MASTER_SIMPLE.m

DMLSFM_STROBE_SIMPLE.vi

5. **Imaging script – to take a sequence of images within a volume.** The number of images which can be acquired per volume is subject to the bandwidth of the connection between the Orca Flash and the PC.

The following 3 processes must be run in parallel.

DMLSFM_SCAN_MASTER.m

DMLSFM_SCAN_SLAVE.m

DMLSFM_SCAN.vi

6. Script to calibrate galvo voltage to actual axial position of illumination sheet

DMLSFM_CONTROL_GALVO.vi

7. **Mathematica scripts** deriving formula to investigate the ability of primary defocus to compensate for high-NA defocus.

highNA_cf_Prim_defocus.nb

A2 Derivation of expressions lateral FWHM and axial FWHM.

The ability of an optical system to create images can be understood by decomposing the object into a Fourier series. Abbe [135, 136] considered the object to be a set of periodic diffraction elements and showed that at least 2 orders of diffraction have to be collected by the optical system in order to barely resolve the periodic grating. This led to an estimation of the resolution of an optical system for incoherent light to be,

$$d = \frac{\lambda}{2NA} \quad eq. 28$$

Where d is the smallest resolvable feature. In 1876 H. von Helmholtz [137] theoretically confirmed Abbe's theory including the $\frac{1}{2}$ factor for incoherent light (and not for coherent). Reference [138] suggested that the full-width half maximum (FWHM) of the diffraction pattern of a point source was a useful method for measuring the lateral resolution as it could be usefully applied to diffraction patterns which do not fall off to zero. Hopkins [139] promoted the use of the Optical Transfer Function (OTF), to evaluate spatial frequencies as they pass through an optical system to assess the quality of optical systems.

In an optical system either made up of a single lens or a complicated system of lenses, the exit pupil (pupil function), is responsible for the diffraction of an optical system. As described in detail in reference [123], the image of a point source, is the Point Spread Function (PSF) of the optical system. The PSF can also be shown to be a scaled version of the Fourier transform of the pupil function. The *imaging equation of Fourier optics* states that the image of an object can be found by convolving the field in the object plane with the PSF and then scaling the result with the magnification of the system. The location of the image and lateral magnification, is given by the standard formulae of Geometrical Optics. In the case of coherent imaging – the amplitude PSF is used and in the case of incoherent imaging it is the intensity PSF (which is the squared absolute value of the amplitude PSF).

The amplitude PSF in object space for a circular pupil in normalised transverse optical coordinates is,

$$U(v) \propto \frac{2J_1(v)}{v}, \quad v = k NA r \quad eq. 29$$

Where $k = \frac{2\pi}{\lambda_0}$ and r is the radial coordinate in the pupil. For the intensity,

$$I(v) \propto \left(\frac{2J_1(v)}{v} \right)^2 \quad eq. 30$$

This provides the following lateral FWHM expression with λ the vacuum wavelength,

$$FWHM_{lateral} = \frac{0.51\lambda}{NA} \quad eq. 31$$

Fresnel propagating the field with an axial displacement about the focal plane shows the field axially along the optic axis which is given by a function of the form, for axial displacement z and normalised axial coordinate u ,

$$U(u) \propto \frac{\sin\left(\frac{u}{4}\right)}{\left(\frac{u}{4}\right)}, \quad u = k NA^2 z \quad eq. 32$$

For the intensity,

$$I(u) \propto \left(\frac{\sin\left(\frac{u}{4}\right)}{\left(\frac{u}{4}\right)} \right)^2 \quad eq. 33$$

This provides the following axial FWHM expression λ the vacuum wavelength and n the refractive index of the immersion media.

$$FWHM_{axial} = \frac{1.77\lambda n}{NA^2} \quad eq. 34$$

A3 Derivation of lateral FWHM and axial FWHM for a finite sized bead.

In the assessment of resolution of the system beads of diameter 0.2 microns were used, which have a finite size and so produce an image which is not the PSF of the system. Rather it will be a convolution between the 3D PSF of the system and the 0.2 micron diameter spherical bead, assuming that the material of the bead was uniformly fluorescent, transparent and that the refractive index of the bead was not significantly different to the agarose. This scalar wave-theory approach is acceptable for situations where the vectorial nature of light is not significant – such as away from concentrated focal points of light and where the polarization of light is unimportant, which is the case in this work.

The lateral FWHM of the system corresponds to the imaging objective, whereas the axial depends on both the thickness of the light-sheet and also the axial FWHM of the imaging objective. As previously described (chp 2 eq. 2) can be accounted for with the expression:

$$w_{\text{system}} = \sqrt{\frac{1}{\left(\frac{1}{\Delta z}\right)^2 + \left(\frac{1}{w_{LS}}\right)^2}} \quad \text{chp2 eq.2}$$

The relatively complicated 3D PSF of the system can be approximated by a 3D Gaussian with FWHM in the x and y the same as the lateral FWHM and FWHM z taken from the axial. This is then convolved with a sphere of diameter 0.2 microns to find the lateral and axial FWHM of the resulting intensity distribution.

A4 Derivation of expressions related to the Strehl limit.

In reality imaging systems have optical aberrations, which can reduce the performance of the system. Karl Strehl attempted to define a metric which would define practically aberration free focusing [8]. This ratio, known as the Strehl ratio (S), is the ratio of the aberrated to aberration-free central intensity value. A Strehl ratio greater than 0.8 is considered to be practically aberration free, and is said to be diffraction limited. A Strehl ratio less than 0.8 is said to be aberration limited.

It can be shown that the field at the centre of the focal plane of an optical system with exit pupil diameter a and focal length f and normalized radial coordinate ρ and azimuthal coordinate γ is given by [123],

$$U_f(0, 0, 0) = -\frac{ia^2 \exp(ikf)}{\lambda f} \int_0^1 \int_0^{2\pi} \exp(ikW(\rho, \gamma)) \rho d\rho d\gamma \quad \text{eq.35}$$

Where $W(\rho, \gamma)$ is the aberration function and is the deviation of the wavefront emerging from the exit pupil to the ideal converging spherical wavefront for an ideal image point. For small aberrations,

$$\exp(ikW(\rho, \theta)) \approx 1 + ikW - \frac{k^2 W^2}{2} \quad \text{eq.36}$$

Hence the nth moment of W is given by,

$$\langle W^n \rangle = \frac{1}{\pi} \int_0^1 \int_0^{2\pi} W^n r dr d\gamma \quad \text{eq.37}$$

Thus from eq xxxx,

$$I'(0,0,0) = \frac{1}{\pi} \left| \int_0^1 \int_0^{2\pi} \left(1 + ikW + \frac{1}{2}(ikW)^2 \right) r dr d\gamma \right|^2 \approx 1 - k^2(\langle W^2 \rangle - \langle W \rangle^2)$$

$$= 1 - k^2 \sigma_W^2 \quad eq. 38$$

When the Strehl ratio is 0.8 this gives a value,

$$\sigma_W \approx \frac{\lambda}{14} \quad eq. 39$$

A5 Derivation of expressions for the optimum correction for high-NA defocus achievable with primary defocus alone.

Mathematica scripts via GitHub, DOI: 10.5281/zenodo.5732850

The amount of primary defocus (corresponding to an axial displacement z_1) that best corrects for high-NA defocus of z – in terms of minimising the RMS difference between applied primary defocus and desired high-NA defocus over the pupil of the objective – i.e. the function:

$$f(\rho; z, z_1) = z\sqrt{n^2 - NA^2\rho^2} - nz + \frac{z_1 NA^2 \rho^2}{2n} \quad eq. 40$$

Here, n is the refractive index of the immersion medium and NA is the numerical aperture. The term $-nz$ is constant when z is constant and so is simply piston not affecting the optimization but convenient for simplification of the algebra. The RMS of the difference was obtained with the integral,

$$\sqrt{\left[\int_0^{2\pi} \int_0^1 f^2 \rho d\rho d\theta \right] - \left[\int_0^{2\pi} \int_0^1 f \rho d\rho d\theta \right]^2} \quad eq. 41$$

The RMS difference is minimized at z_1 ,

$$z_1 = - \left[\frac{8n(4n^5 - 5n^3 NA^2 + \sqrt{n^2 - NA^2}(NA^4 + 3n^2 NA^2 - 4n^4))}{5 NA^6} \right] z \quad eq. 42$$

At this value of z_1 , the standard deviation (StdDev) of the difference between the optimal primary defocus and the high-NA defocus at a particular defocus z is,

$$StdDev(z) = - \left[\frac{768n^{10} + 30n^2NA^8 - 384n^8(5NA^2 + 2n\sqrt{n^2 - NA^2}) + NA^6(NA^4 + 160n^3\sqrt{n^2 - NA^2}) + 64n^6(25NA^4 + 24nNA^2\sqrt{n^2 - NA^2}) - 32n^4(15NA^6 + 29nNA^4\sqrt{n^2 - NA^2})}{480 NA^8} \right]^{\frac{1}{2}} \quad z \text{ eq. 43}$$

According to A2 above, the system is no longer diffraction limited when this standard deviation exceeds $\lambda/14$ where λ is the wavelength of light. This corresponds to a maximum defocus that can be achieved before the optimum amount of primary defocus (z_1) no longer provides a diffraction-limited approximation to the high-NA defocus

$$z_{Strehl} = \max\{StdDev(z) \leq \lambda/14\} \quad \text{eq. 44}$$

is,

$$z_{Strehl} = \frac{\pm 15\lambda \sqrt{\left(30n^2 + \frac{768n^{10}}{NA^8} - \frac{1920n^6}{NA^4} - \frac{480n^4}{NA^2} + NA^2\right) + \sqrt{n^2 - NA^2} \left(\frac{768n^9}{NA^8} - \frac{1536n^7}{NA^6} + \frac{928n^5}{NA^4} - \frac{160n^3}{NA^2}\right)}}{7\sqrt{2}\sqrt{60n^4 - 60n^2NA^2 - NA^4}} \quad \text{eq. 45}$$